

# Investigation of the adsorption and reaction of small molecules on the NiO/Pd(100) system

Der Naturwissenschaftlichen Fakultät  
der Friedrich-Alexander-Universität  
Erlangen-Nürnberg

zur

Erlangung des Doktorgrades Dr. rer. nat

vorgelegt

von Oliver Höfert  
aus Lingen (Ems)

Als Dissertation genehmigt  
von der Naturwissenschaftlichen Fakultät  
der Friedrich-Alexander-Universität Erlangen-Nürnberg

Tag der mündlichen Prüfung: 08.05.2014

Vorsitzender des Promotionsorgans: Prof. Dr. Johannes Barth

Gutachter: Prof. Dr. Steinrück  
Prof. Dr. Libuda

# Contents

<b>1</b>	<b>Introduction</b>	<b>7</b>
<b>2</b>	<b>Theoretical Background</b>	<b>11</b>
2.1	Photoelectron Spectroscopy . . . . .	11
2.1.1	Chemical Shifts . . . . .	12
2.1.2	Final state effects . . . . .	13
2.1.3	Signal Damping . . . . .	14
<b>3</b>	<b>Experimental Setup</b>	<b>17</b>
3.1	Setup . . . . .	17
3.2	Transfer System . . . . .	18
3.2.1	Inserting a new sample . . . . .	19
3.3	Time Resolution in the microsecond regime . . . . .	21
3.3.1	Experimental Setup . . . . .	21
3.3.2	Open and closing time of the molecular beam . . . . .	25
<b>4</b>	<b>CO</b>	<b>27</b>
4.1	Surface Core Level Shift at different excitation energies . . . . .	27
4.2	Oxygen . . . . .	28
4.3	CO . . . . .	29
4.4	NiO/Pd(100) . . . . .	31
4.5	Structure of NiO on Pd(100) . . . . .	31
4.5.1	Data analysis of the Ni 2p spectrum . . . . .	31
4.5.2	Growth . . . . .	33
4.5.3	Thermal stability . . . . .	34
4.6	CO Oxidation on Nickel Oxide . . . . .	36
4.6.1	Reduction of thin NiO films . . . . .	36
4.6.1.1	Comparison of film thickness reaction . . . . .	36

4.6.1.2	Wetting layer: 1 monolayer . . . . .	38
4.6.1.3	Two monolayers . . . . .	40
4.6.1.4	Reoxidation and 2nd reduction cycle . . . . .	45
4.7	CO on Pt(111) at higher temperatures . . . . .	49
4.7.1	Measurements and data analysis . . . . .	50
4.7.2	Simulation . . . . .	58
4.8	Conclusion . . . . .	60
4.8.1	CO Oxidation on nickel oxide . . . . .	60
4.8.2	CO Adsorption and Desorption at higher temperatures . . . . .	60
<b>5</b>	<b>H<sub>2</sub>O</b>	<b>61</b>
5.1	H <sub>2</sub> O on Pd(100) . . . . .	61
5.1.1	Adsorption . . . . .	61
5.1.2	Reaction . . . . .	64
5.2	H <sub>2</sub> O on O/Pd(100) . . . . .	65
5.2.1	Adsorption . . . . .	65
5.2.2	Reaction . . . . .	67
5.3	H <sub>2</sub> O on NiO/Pd(100) . . . . .	69
5.3.1	1 ML . . . . .	69
5.3.1.1	Adsorption . . . . .	69
5.3.1.2	Reaction . . . . .	71
5.3.2	2 ML . . . . .	73
5.3.2.1	Adsorption . . . . .	73
5.3.2.2	Reaction . . . . .	75
5.3.3	6 ML . . . . .	77
5.3.3.1	Adsorption . . . . .	77
5.3.3.2	Reaction . . . . .	79
5.4	Conclusion . . . . .	81
<b>6</b>	<b>C<sub>2</sub>H<sub>2</sub></b>	<b>83</b>
6.1	C <sub>2</sub> H <sub>2</sub> on Pd(100) . . . . .	83
6.1.1	Adsorption . . . . .	84
6.1.2	Simulation . . . . .	89
6.1.3	Reaction . . . . .	92
6.2	C <sub>2</sub> H <sub>2</sub> on O/Pd(100) . . . . .	97
6.2.1	Adsorption . . . . .	97
6.2.2	Reaction . . . . .	99

---

6.3	C <sub>2</sub> H <sub>2</sub> on NiO/Pd(100)	101
6.3.1	NiO film: 1 ML	102
6.3.1.1	Adsorption	102
6.3.1.2	Reaction	104
6.3.2	NiO film: 2 ML	107
6.3.2.1	Adsorption	107
6.3.2.2	Reaction	108
6.3.3	NiO film: 6 ML	109
6.3.3.1	Adsorption	109
6.3.3.2	Reaction	111
6.4	Conclusion	113
<b>7</b>	<b>C<sub>2</sub>H<sub>4</sub></b>	<b>115</b>
7.1	C <sub>2</sub> H <sub>4</sub> on Pd(100)	115
7.1.1	Adsorption	115
7.1.2	Reaction	119
7.2	Coadsorption with CO	121
7.3	Coadsorption with O	124
7.3.1	Adsorption	124
7.3.2	Reaction	126
7.4	Conclusion	127
<b>8</b>	<b>C<sub>6</sub>H<sub>6</sub></b>	<b>129</b>
8.1	C <sub>6</sub> H <sub>6</sub> on Pd(100)	129
8.1.1	Adsorption	130
8.1.2	Reaction	133
8.2	C <sub>6</sub> H <sub>6</sub> on O/Pd(100)	134
8.2.1	Adsorption	134
8.2.2	Reaction	135
8.3	Conclusion	137
<b>9</b>	<b>TEB</b>	<b>139</b>
9.1	TEB on Pd(100)	139
9.1.1	Adsorption and Reaction from 180 K	139
9.1.1.1	Adsorption	139
9.1.1.2	Reaction	144
9.1.2	Adsorption at 120 K	150

---

9.1.3	Adsorption and Reaction from 300 K . . . . .	153
9.1.3.1	Adsorption . . . . .	153
9.1.3.2	Reaction . . . . .	156
9.2	Conclusion . . . . .	159
<b>10</b>	<b>Summary</b>	<b>161</b>
<b>11</b>	<b>Zusammenfassung</b>	<b>165</b>
<b>12</b>	<b>Attachment</b>	<b>169</b>
12.1	C <sub>6</sub> H <sub>6</sub> on NiO/Pd(100) . . . . .	169
12.1.1	NiO film: 1 ML . . . . .	169
12.1.1.1	Adsorption . . . . .	169
12.1.1.2	Reaction . . . . .	172
12.1.2	NiO film: 2 ML . . . . .	174
12.1.2.1	Adsorption . . . . .	174
12.1.2.2	Reaction . . . . .	176
12.1.3	NiO film: 6 ML . . . . .	178
12.1.3.1	Adsorption . . . . .	178
12.1.3.2	Reaction . . . . .	180
12.1.4	Conclusion . . . . .	182
12.2	Coverage Simulation . . . . .	184
12.3	Transfer System Blueprints . . . . .	186

# Chapter 1

## Introduction

The best tested and commonly used way for energy storage up to now is in chemical bonds, especially in hydrocarbons. One of the key technologies of the 21st century will be heterogeneous catalysis<sup>1</sup>, due to its efficiency in transforming chemical substances, including fuels, without a change of the catalyst itself. The growing importance of synthetic fuel production can be seen in the approach to produce fuel using the Fischer-Tropsch-Synthesis by the U.S. Air force<sup>2</sup>. Hydrocarbons are produced by the Fischer-Tropsch-Process from carbon monoxide and hydrogen in so called X-to-liquid-facilities, where the liquid is the synthetic fuel and the X stands either for coal, gas or biomass. Recently, it was shown that biomass-FT-facilities can reach an energy efficiency of 60 to 80%<sup>3</sup>, and that the efficiency depends on the choice of the right catalyst. This is just one example of the importance of catalysts. Among many potential catalysts, nickel oxide has turned out to be applicable for a wide range of applications: water splitting<sup>4,5</sup>, ethylene dimerization<sup>6-10</sup>, butane isomerization<sup>6,10</sup>, oxidation of azodyes<sup>11</sup>, hydrogenation of benzene and unsaturated fatty acids<sup>12,13</sup>, and generation of H<sub>2</sub> from biomass<sup>14</sup>.

Present-day research concerning in catalysis often concentrates on developing new catalysts, or optimizing either the selectivity or the reactivity, or both of existing catalyst. In the following, two approaches are introduced: the more technical screening approach and the knowledge-driven approach. With the screening approach, a large variety of differently prepared catalysts is empirically tested towards their behavior and performance for a chemical process. Often there is a lack of knowledge about the exact catalyst structure, and therefore it is not possible to predict the properties of these catalysts before testing. Nevertheless, the advantage of this method is the direct eval-

uation of the performance and the guarantee of the reproducibility, due to the test runs. In the other mentioned approach, the engineering approach, a catalyst is designed bottom up with all effects of every single reaction step in mind. This is only possible when all interacting partners are identified and quantified. Often, this approach is still a vision in the scientific community. Nevertheless, the goal of the major research efforts in this direction is at the end, to design completely new catalysts on demand, fulfilling technical and economic requirements, but with significantly less effort, due to the avoidance of testing unsatisfactory candidates.

Generally, it is very difficult and time-consuming to identify single steps in a complex reaction mechanism. One successful route to bring some light into darkness was evolved by the growing field of surface science over the past decades. Here, the research concentrates on identification and clarification of the elemental process steps with model systems. These systems are often simplified systems as compared to the real technical applications, or are even complete different systems. A very common problem is the deactivation or contamination of the studied system by the residual gases in the atmosphere. To avoid such contamination effects ultra-high vacuum is used. The drawback of this approach is the immense technical effort on the one hand, and on the other hand the fact that there is a gap concerning the pressure use in the model studies and in real catalysis, the so called "pressure gap". This gap describes the fact that a system could behave completely different at high pressures, i.e. normal atmosphere or even higher, compared to vacuum pressures, due to different equilibria, and transport effects in the gas phase. One approach to at least partly overcome the pressure gap is using a molecular beam, in order to achieve higher pressures on the probed surface. Another big challenge is the complexity in real technical approaches, where normally powders and mixtures of different elements with an often uncontrolled structure are used as catalyst. This additional difficulty is avoided by studying an ordered single crystal surface; some examples underlining the success of this approach, reaching from adsorption of CO and H on Pd(100)<sup>15-17</sup> over the adsorption of oxygen on Ni(100)<sup>18</sup> to the CO oxidation at well defined surfaces<sup>19</sup>. Additional studies were made for the adsorption and reaction on the well defined NiO(100) surface<sup>20-22</sup>. The results of these and further studies lead to the insight that the adsorption and reaction of ethylene on

---

Pt(100) is structure sensitive<sup>23</sup> and therefore nano-size structured materials play an important role.

Introducing nanomaterials, i.e. structures in the size of nanometers, can be used to tune a catalyst or open completely new reaction pathways. These structures often have different properties than the bulk material, due to finite size effects or the different coordination and thus electronic and chemical properties of surface and bulk atoms. For nanostructures the ratio of the surface to the bulk is much higher and therefore surface effects play a bigger role. Different self assembled structures have been investigated from complete monolayers (SAMs)<sup>24</sup> to nanowires<sup>25</sup>, revealing a significant effect on the adsorption and reaction behavior. Also structures with metal clusters supported on oxides have been a subject of interest<sup>26-28</sup>. Recently it was suggested that the thickness of an oxide film supported by a metal can be used as switch between the regimes of nanomaterials and bulk materials<sup>29</sup>, ranging from enhanced reactivity for thin films (1-5 layers) to less reactive bulk-like behavior (5-10 layers). In this thesis, nickel oxide films supported by a Pd(100) surface were chosen as substrate because the growth mode and the structure was studied before, revealing that the first layer is a wetting layer with ordered nickel vacancies. From the second layer on, complete layers grow and at  $\sim 6$  ML the film shows a bulk-like behavior<sup>30-35</sup>. Additionally, for thin oxide films supported on metal substrates a mechanism was proposed where a charge-transfer of an electron from the metal-oxide interface to the adsorbing molecule has a stabilizing effect<sup>36</sup>.

After discussion the importance of heterogeneous catalysis in nowadays industry and the role of model studies in surface science, in the following the methods to study such systems are shortly introduced. A variety of different methods to explore single steps of surface processes were developed in the past, reaching from diffraction and reflection methods (LEED, XRD, XRR) and microscopic (STM, TEM, AFM) to spectroscopic methods (FTIR, XPS, TPD). The list is by far not complete and a lot of more specialized methods were introduced. In this thesis, XPS at the synchrotron radiation facility BESSY II in Berlin was used to measure high resolution XP spectra with a high temporal resolution, allowing to record spectra during adsorption and during a temperature ramp, applied to the sample during a temperature programmed experiment (TPXPS). This method gives the possibility to identify and quantify surface species and also to distinguish between different species

qualitatively. In Chapter 2 a short introduction is given in the fundamental aspect of photoelectron spectroscopy.

Chapter 3 deals with the experimental setup. The apparatus is briefly explained and two important modifications made during this thesis are discussed in greater detail. The first improvement is the design of a transfer system necessary for sample preparation outside the vacuum chamber. Here, the concept and the steps for sample transfer are described. The second improvement is the improvement in time resolution by a factor of 2000 and its technical implementation.

Chapter 4 deals with the adsorption of CO. It addresses the growth of nickel oxide and its characterization and thickness calibration, followed by kinetic analysis of the CO oxidation by nickel oxide films on Pd(100). It is completed by the analysis of the experiments with high time resolution, namely the adsorption and desorption of CO on Pt(111).

The chapters 5 - 9 deal with different molecules, namely H<sub>2</sub>O, C<sub>2</sub>H<sub>2</sub>, C<sub>2</sub>H<sub>4</sub>, C<sub>6</sub>H<sub>6</sub> and Triethyleboran (TEB). These molecules are ordered by their complexity. Water is studied on the clean and oxygen precovered Pd(100) and on nickel oxide films with different thickness on Pd(100). Acetylene as the next molecule is studied on the same substrates as water. A simple simulation of the adsorption process on the clean palladium is presented. For the adsorption of C<sub>2</sub>H<sub>4</sub> on Pd(100) suggestions for the adsorption sites are made, based on coadsorption experiments with carbon monoxide and oxygen. The adsorption and reaction behavior of benzene is shown on clean and oxygen-precovered Pd(100), and on the differently thick nickel oxide films in the attachments. The last molecule, TEB, is the most complex one in this work and therefore only studied on the clean Pd(100) surface.

# Chapter 2

## Theoretical Background

### 2.1 Photoelectron Spectroscopy

Photoelectron spectroscopy is an extensively used method to probe the chemical composition of a sample. It is used for more than one hundred years and makes use of the photoelectric effect, where a photon impinges on matter and transfers its energy completely to a bound electron resulting in its emission. According to the energy conservation the remaining energy of the photon, which was not needed for the liberation of the electron is carried away by the latter as its kinetic energy. This energy can be measured using a suitable energy analyzer. A schematic energy diagram of the photoelectron process is presented in Figure 2.1, which illustrates that the kinetic energy differs, depending on the observed core level and the energy of incident light.

The equation to describe the most simple case is:

$$E_{kin} = h\nu - E_b - \Phi_S \quad (2.1)$$

with  $E_{kin}$  as kinetic energy,  $\nu$  as the frequency of light and  $\Phi_S$  as the work function of the sample. To measure the kinetic energy of an electron it is not only necessary to overcome the work function of the sample but also the work function difference of the detector. Subtracting the difference  $\Phi_{Spec} - \Phi_S$  from equation 2.1, the work function of the sample is compensated and only the work function of the spectrometer  $\Phi_{spec}$  has to be accounted for. This work function can be determined by measuring the Fermi edge of a metal using a well-known photon energy (e.g. He-I radiation)

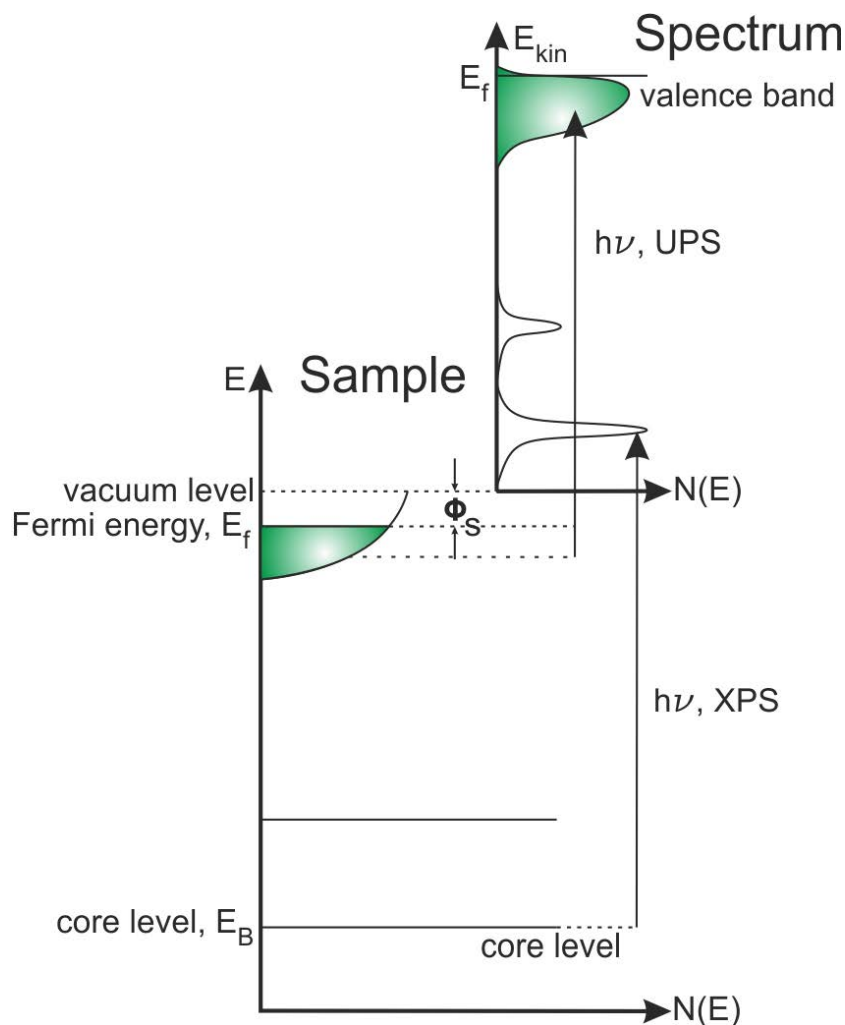


**Figure 2.1:** The energy diagram of the photoemission process. The part which is marked with sample shows the energetic situation in the sample, where an electron is excited by light and leaves the atom or in this case the solid. According to Hüfner<sup>37</sup>.

In general, the photoemission signal is not plotted against kinetic energy but against binding energy; this type of presentation does not depend on the photon energy used.

### 2.1.1 Chemical Shifts

Shifts in binding energy of the photoemission lines of the same material due to different chemical surroundings are called chemical shifts. A typical example would be the higher binding energy of a metal oxide in comparison to the pure metal. In a simplified picture, oxygen attracts the electrons from the metal resulting in a lower electron density around the metal atom. This

lower electron density does not screen the core as effective as in the pure metal case and therefore the binding energy is higher<sup>37</sup>.

Another example is the different chemical situation of an atom in a bulk crystal to an atom on the surface. Here the so called surface core level shift (SCLS) is visible<sup>38</sup>.

### 2.1.2 Final state effects

In XPS the final state is measured. As a consequence, several so called final state effects can occur. Examples are shake off or shake up effects, where a second electron is excited to leave the atom (shake off) or it is excited typically to the unoccupied valence band (shake up). An explicit example for these effects is the 6 eV satellite of the Ni which is formed due to different screening of the core hole from the changed bands<sup>39</sup>.

One specific class of final state effects are vibrational excitations during the photoemission process<sup>40</sup>. The transition is described by the Franck-Condon-Principle. The intensity of a specific vibrationally excited final state is described by:

$$I(0 \rightarrow \nu) = e^{-S} \frac{S^\nu}{\nu!} \quad (2.2)$$

with  $\nu$  as the vibrational level in the final state ion. The S factor describes the ratio between the electronic transition to the vibrationally excited state and the vibrational ground state in the final state ion (adiabatic transition). The S factor for  $\nu = 1$  is given by

$$S = \frac{I(0 \rightarrow 1)}{I(0 \rightarrow 0)} \quad (2.3)$$

and can easily be obtained experimentally<sup>41</sup>. The S factor can be calculated according to

$$S = \frac{\mu\omega m(\Delta r)^2}{2\hbar} \quad (2.4)$$

with  $\mu$  as the reduced mass,  $\Delta r$  the change of the minimum in the potential energy curve upon excitation, and  $m$  the number of equivalent bonds, e. g. in this thesis the number of C-H-bonds. Detailed information can be found in<sup>41,42</sup>.

### 2.1.3 Signal Damping

The signal intensity is depending on the inelastic mean free path (IMFP) of the electrons in a solid. This value is the mean distance an electron can travel through a solid without losing energy due to inelastic scattering processes within the solid. It depends on the kinetic energy of the electron. In Figure 2.2 the "universal curve" for the IMFP is depicted for several elements.

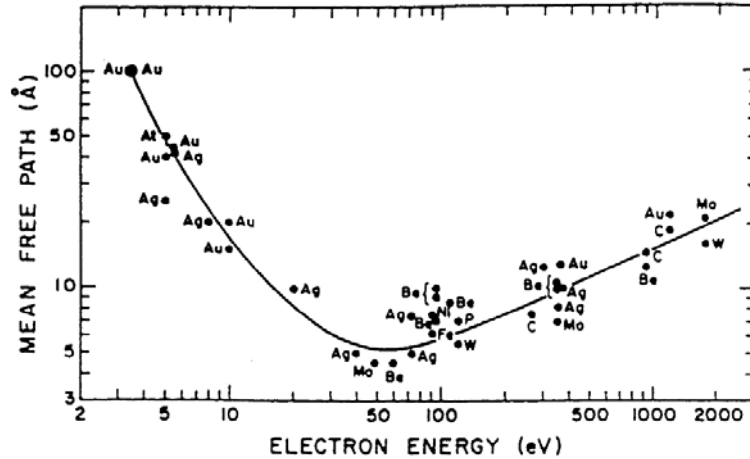


**Figure 2.2:** Inelastic mean free paths of several materials, taken from<sup>43</sup>

The curve shows a local minimum at  $\sim 50 - 100$  eV. This can be used to perform highly surface sensitive measurements by choosing a kinetic energy around these energy values. To do this for different elements an X-Ray source with tunable photon energy is necessary. Up to date this is only possible at a synchrotron radiation facility, like BESSY II.

The intensity after transmission through a layer with thickness  $d$  is given by

$$I = I_0 \cdot e^{-\frac{d}{\lambda}} \quad (2.5)$$

with  $I$  as the attenuated intensity,  $I_0$  as the original intensity without damping and  $\lambda$  for the IMFP.  $\lambda$  is material dependent.

In the following, a special case is discussed, where the thickness and the substrate area covered by clusters change the intensity of the supporting substrate. For simplicity, the clusters are modeled here as rectangular blocks with an average height (cf. Figure 2.3). This model is used later to estimate the cluster thickness of nickel oxide clusters in Chapter 4.6.1.4.

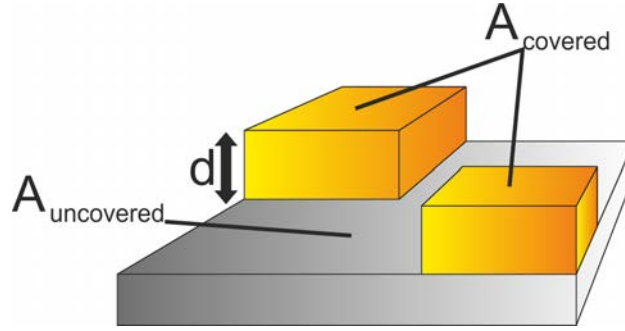


**Figure 2.3:** Model of clusters covering an area  $A$  with a thickness  $d$ . The clusters are assumed to form rectangulars for simplicity.

The complete signal intensity  $I_{total}$  of the substrate signal is given by

$$I_{total} = A_{covered} \cdot I_{covered} + (1 - A_{covered}) \cdot I_{uncovered} \quad (2.6)$$

with  $A_{covered}$  as covered area in percent. Now solving for  $A_{covered}$  gives:

$$I_{total} - I_{uncovered} = (I_{covered} - I_{uncovered}) \cdot A_{covered} \quad (2.7)$$

$$\Leftrightarrow A_{covered} = \frac{I_{total} - I_{uncovered}}{I_{covered} - I_{uncovered}}. \quad (2.8)$$

Inserting equation 2.5 for  $I_{covered}$  results in

$$\Leftrightarrow A_{covered} = \frac{I_{total} - I_{uncovered}}{I_{uncovered} \left( e^{\frac{-d_{clusters}}{\lambda_{clusters}}} - 1 \right)}. \quad (2.9)$$

From the knowledge of either the thickness or the covered area the respective other mean value is available.



# Chapter 3

## Experimental Setup

In this chapter the setup of the apparatus is briefly introduced, a detailed discussion can be found in [44,45]. The modifications made during this PhD thesis are described in two sections.

### 3.1 Setup

All measurements presented in this thesis were performed in a transportable UHV setup at the 3rd generation synchrotron source BESSY II at beamline U49/2-PGM-1. The setup has two main chambers. The first is used for the preparation of the sample and is equipped with a low energy electron diffraction (LEED) instrument, several ports for metal evaporators and a doser connected to a dosing system for gases; also a sputtergun for sample cleaning is installed in this part. The other chamber is the so called analysis chamber with a connection to the synchrotron beamline via a separately pumped connection with a shutter for the x-ray light. This chamber has also one port for mounting additional evaporators. This port is also pumped separately which permits to exchange this evaporator for maintenance reasons without venting the whole analysis chamber. The centerpiece is the Omicron EA-125 kinetic electron analyzer (see Section 3.3 for more details). Additionally a quadrupole mass spectrometer (QMS) is installed to monitor residual gases and to perform temperature programmed desorption (TPD) experiments.

In addition, a supersonic molecular beam is connected to this analysis chamber. It consists of a classical three stage setup. In the first stage the expansion of the gas from the nozzle takes place. The gas is supplied by two

flow controllers (MKS), one for flows up to 50 sccm and one for 500 sccm. The second stage is connected via a skimmer, cutting out the silent zone. This stage is also equipped with a pneumatic flag. An aperture arrangement in the third stage gives control over the beam size. Ideally, the molecular beam, the synchrotron light and the focus of the analyzer cross at the same spot on the sample. For this purpose, several calibration and adjustment tools are installed in the analysis chamber, like a pressure gauge for the molecular beam and a phosphorizing metal plate for the x-ray beam.

The sample can be heated in two different ways. The first method is resistive heating to maximum temperatures of 1400 K, but with the drawback of changing the electromagnetic field in front of the sample drastically leading to a massive change in the intensity of the recorded electrons. To avoid this behavior, the second heating setup is a filament behind the sample. With this filament it is possible to reach temperatures up to 600 K without significant disturbance of the measurement. The complete sample holder can be cooled down to 100 K. In the experiment, typically a temperature around 120 K was used during the adsorption of gases. The sample temperature is measured with a K-type thermocouple spot welded to the sample.

## 3.2 Transfer System

As described above, the crystal is spotwelded to the manipulator head. This setup makes it inevitable to vent the chamber and remove the whole manipulator to change the crystal. To lower the maintenance time, a manipulator head with transferable sample was implemented during this work. The used setup described in<sup>45</sup> had to be extended with the goal to achieve a maximum flexibility. The blueprints are shown in the Appendix. Three main tasks has to be fulfilled with this setup:

1. Direct temperature measurement of the sample:

In commercially systems this problem is often solved by measuring the temperature on a point on the sample holder and not on the crystal itself. This is done due to the easier construction but the cost for this practical approach is lack of the exact information on temperature. For preparation this setup may be sufficient, but not for TPXPS or TPD experiments.

2. Direct heating and cooling via the sample connections itself:

The most critical task was the part responsible for cooling, because every connection lowers the heat conductivity strongly. In this case the heat is transferred through a connection of copper on aluminum, yielding a minimal temperature of 160 K. This is higher by  $\sim 40$  K in comparison to the fixed crystal in the former setup, but still very helpful, since not all systems need such low temperatures.

3. An indirect heating via heat radiation in the back of the sample with a filament:

The filament is located on the part of the manipulator head which remains in the UHV chamber upon sample change. This is the only fragile part which can not be repaired by extracting the transferable sample holder.

### 3.2.1 Inserting a new sample

The sample transfer is not as straight forward as in commercially available systems, and therefore the procedure to install and change a sample is demonstrated in this section. First of all, the inner part of the sample holder (depicted in Figure 3.1) is isolated against the outer guidance by a thin mica plate (cf. Figure 3.2). The electric pathways and thermocouple wires are shown in Figure 3.1.

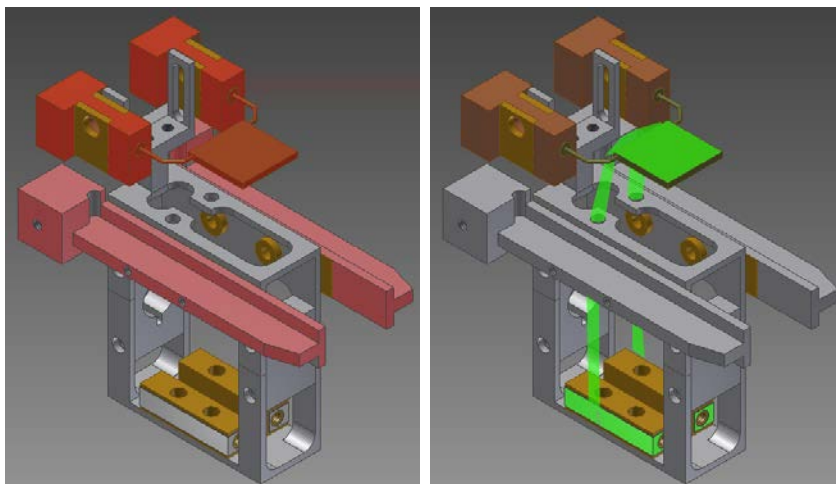


**Figure 3.1:** Sample holder drawings: The conduction of electricity and heat is colored in red. The thermocouple wires and connections are colored in green.

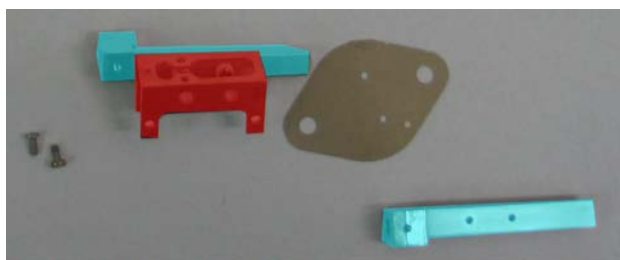


**Figure 3.2:** Sample holder and the insulating mica foil. Blue and red parts are insulated from each other.

After the sample is installed on the sample holder like in the drawings, the transfer can be performed. A position of the sample holder and the sample port like in Figure 3.3 is needed. After the sample holder is completely shifted into the bay screws on the top site and on the thermocouple connection have to be tightened (cf Figure 3.4).

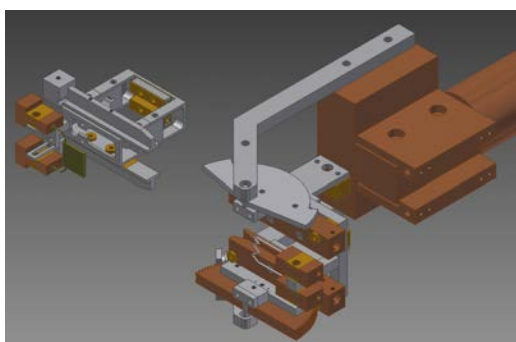


**Figure 3.3:** Scheme of the positioning of the sample holder and the sample port.

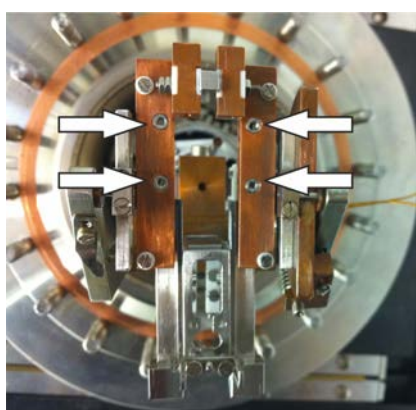


**Figure 3.4:** Photo of the sample port with the sample holder half installed from the top. The four threaded holes, marked with arrows, in the middle are for fixing the sample by screws.

## 3.3 Time Resolution in the microsecond regime

In Chapter 4.7 XPS measurements with the enhanced time resolution are presented. The necessary setup is explained in the following. One specific advantage of the here proposed approach is its high flexibility, since the original electron analyzer setup is conserved, and only commercially available standard components are added, which makes the implementation highly cost effective.

### 3.3.1 Experimental Setup

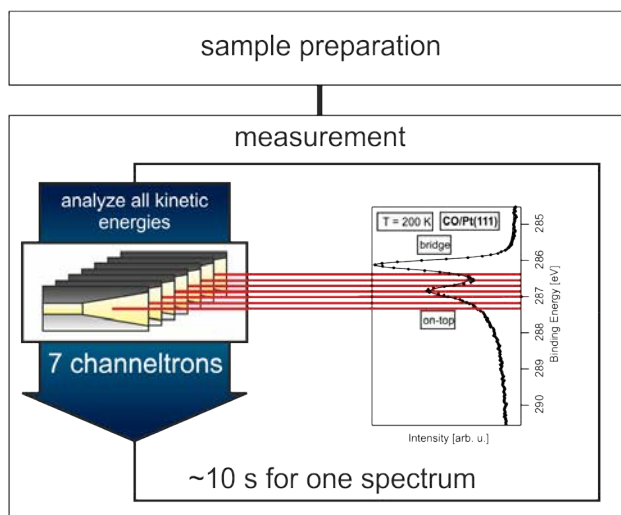
In the analyzer chamber a 7 channeltron hemispherical analyzer (Omicron EA 125 U7 HR) is installed. In the past, this analyzer was routinely operated with acquisition times down to  $\sim 1.5$  s for a 6 eV wide energy window. A three stage supersonic molecular beam (SSMB) is attached to the analysis chamber for well-defined gas dosing. The SSMB is controlled by a shutter with opening / closing times of about  $\sim 50$   $\mu$ s for a spot size on the sample of 125  $\mu$ m; thus a controlled time structure is available. A specific additional advantage of using the SSMB is the high local pressure of  $2 \times 10^{-6}$  mbar on the surface, while keeping the surrounding pressure in the chamber at  $2.6 \times 10^{-8}$  mbar. This is particularly important as an "instant" increase/drop in the pressure by a factor of  $\sim 77$  on the sample surface results, when the shutter is opened/closed. For further details on the general setup please look at Ref. [44].

In the following, the changes of the experimental setup to obtain a higher time resolution are introduced. The original operation mode is the so called "swept mode", with a single spectrum acquired in a few seconds. Thereby, the kinetic energy of the detected electrons is swept, so that each channeltron collects electrons at the desired kinetic energy for a certain time (dwell time). The spectra of the individual channeltrons (in this case 7) are added appropriately after acquisition (see Figure 3.5a). In the here presented approach, the channeltron detector in the style of the "snapshot" mode of CCD camera detectors is used. This means that kinetic energy is not changed, but data is acquired with a fixed kinetic energy in every channeltron; this approach is schematically sketched in Figure 3.5b.

In principle a whole spectrum is obtained by repeating the experiment with the analyzer set to different kinetic energies. However, if the peaks of

the investigated surface species do not shift in binding energy during the observed surface processes this is not necessary, and the information can be derived from measuring at only one kinetic energy. This is the case in our model system (see Chapter 4.7)

a) swept mode - full spectrum:



b) snapshot mode:

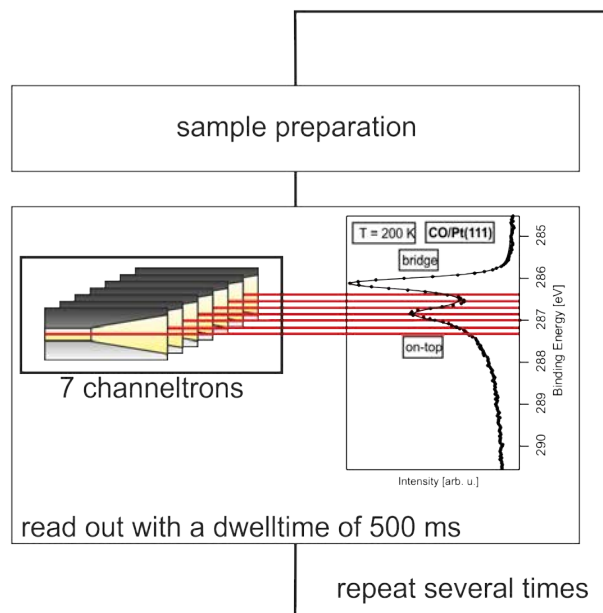


**Figure 3.5:** a) Conventional PES setup; one spectrum is measured completely with in the swept mode, with a lower time resolution. b) No shift in analyzer energy with gain in higher time resolution.

After this general description, the actual layout of the fast XPS experiment is described in Figure 3.6 and the signal processing is discussed. In the original setup the amplifiers of the 7 channeltrons in the analyzer generate an electric pulse for each electron detection event. This pulse is translated into optic signals and transferred by fiber optic cables (FOC) to a translator; there it is transformed to a TTL (transistor-transistor logic) signal, which is registered by a counter card. In the modified setup, a Y-switch is inserted after the translator allowing to record the counts with another digital acquisition board (National Instruments, NI PCI6602) with 8 counting/pulsing channels. This hardware replacement was due to the restrictive software design by Omicron. Seven of the eight channels are used to read out the channeltrons by tapping the TTL-signals at the Y-switch. The eighth channel gives the timer signal for synchronization of channel readouts. This process is controlled by a LabView program. The trigger for the dwell time, which determines the time resolution, is provided by a 2 kHz signal from a signal generator ( $500 \mu\text{s}/\text{channel}$ ); its rising edge triggers the readout of the channels to the onboard memory. The latter is copied to the main memory of the computer every 0.5 s in the background, while the counting of the TTL-signals continues. The LabView program also controls the opening and closing of the molecular beam shutter.

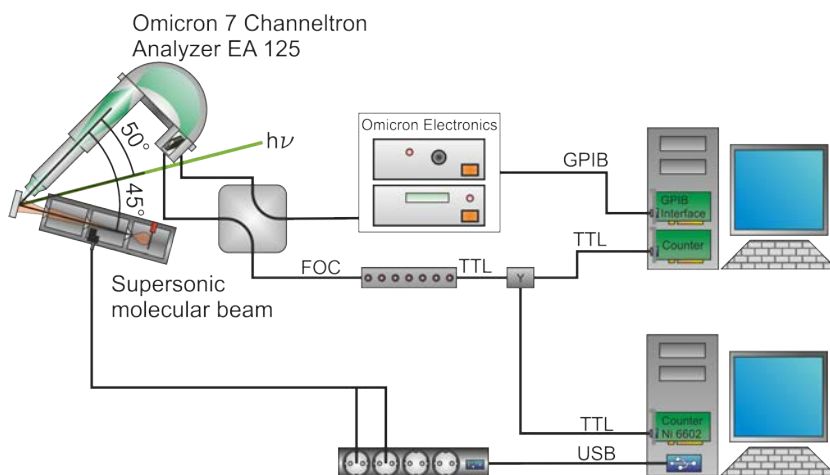


**Figure 3.6:** Setup of the experiment and the added setup for fast XPS

In Figure 3.7, a typical experiment, taken with this setup is shown. The data is recorded, while a Pt(111) surface at 460 K is exposed to the molecular beam for 7.5 s. In order to achieve a sufficient signal to noise ratio, the experiment (which lasted 20 s) was repeated 100 times, so that the total

experiment lasted for 2000 s ( $\sim 33$  min). The data shows the signal from one channeltron set to the binding energy of CO adsorbed at an on top site (286.8 eV) vs. time (Figure 3.7a). At the starting time ( $t=0$  s) a constant background signal is observed. Upon opening the molecular beam at  $t = 1.5$  s, the signals rapidly increases due to adsorption of CO at on top and bridge sites, respectively. After  $\sim 0.5$  s (see Section 4.7 for details on the adsorption experiments) a plateau is reached, which corresponds to the equilibrium coverage at this given temperature and pressure (i.e.,  $\Theta = 0.137$  ML at  $T = 460$  K and  $p = 2 \times 10^{-6}$  mbar). At  $t = 9$  s the shutter of the molecular beam is closed, leading to a rapid drop in intensity, due to the isothermal desorption of CO. After 11 s, the signal has decreased to a value of below 2% of the maximum signal.

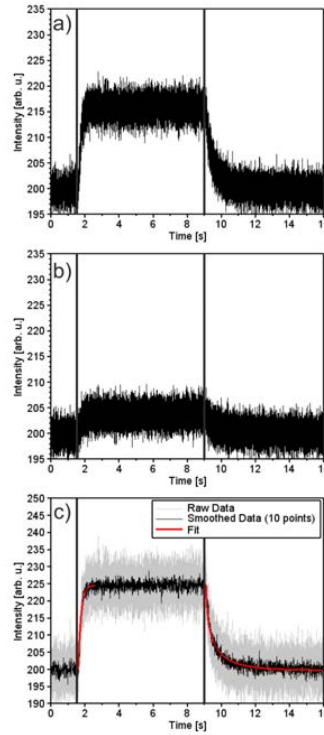


**Figure 3.7:** a) A complete measurement with a dwell time of 500 microseconds and 100 times repeated on the binding energy of the on top site and b) on the bridge site. c) Light Grey curve shows both channels from a) and b) added and scaled similar to [46]. Lightest grey gives a time resolution of 500 microseconds. The darker grey gives 5 ms of time resolution. Black bars show the opening and closing of the molecular beam shutter. ( $\Theta_{tot} = 0.14$  ML,  $T = 460$  K,  $p_{CO} = 2 \times 10^{-6}$  mbar)

### 3.3.2 Open and closing time of the molecular beam

The above discussed setup for fast measurements requires an estimation about the opening and closing time of the molecular beam. This is made in the following by measuring the velocity of the molecular beam shutter.

To measure the reaction time two switches are installed, which react by contact with a bolt connected to the linear shift. The setup is shown in Figure 3.8

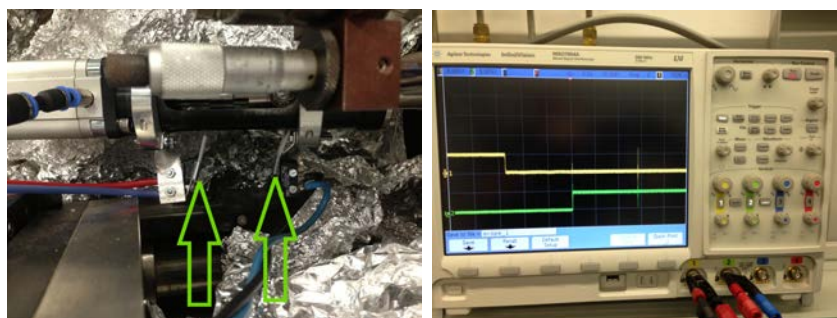


**Figure 3.8:** Test system for the measurement of the velocity of the molecular beam. Two switches give a signal on an oscilloscope.

The time for the bolt to travel the distance between both switches is 51.8 ms: as this is the time it takes from releasing one switch and pressing the other switch. The moving distance of this bolt is 50 mm, thus its velocity is  $\sim 1$  m/s (cf. Figure 3.9).

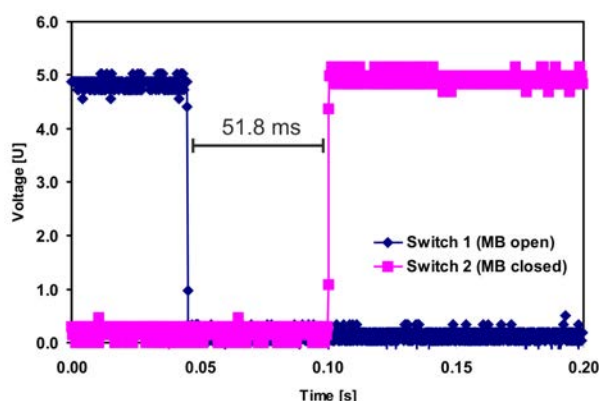


**Figure 3.9:** Time of the travel distance of the bolt between the two switches.

The distance from the source of the molecules, that is the tip of the skimmer to the shutter is 77 mm and from the source to the sample is 489 mm (see Figure 3.10). The ratio between these two distances is 0.157.

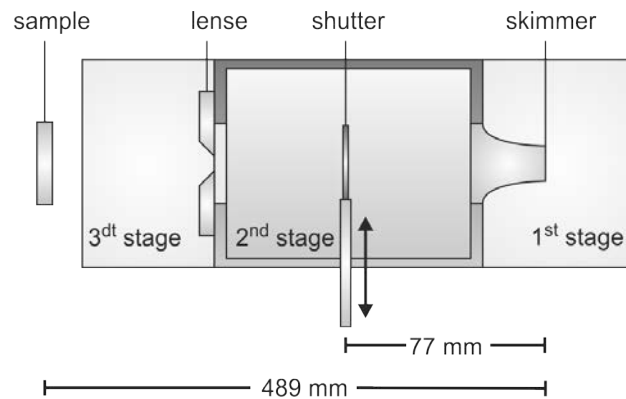


**Figure 3.10:** Scheme of the setup of the molecular beam with respective dimensions.

The specification of the beam U49/2-PGM-1 says that the spotsize is  $60 \mu\text{m}$ ; because the measurements were performed at an angle of  $50^\circ$  the spotsize increases to  $93 \mu\text{m}$ . An additional factor, which enlarges the spotsize, is the fact that the machine is not exactly in the focus of the light beam. This factor is assumed by roughly 30% resulting in a spotsize of  $125 \mu\text{m}$ .  $125 \mu\text{m}$  on the sample corresponds to  $19.7 \mu\text{m}$  on the shutter and therefore a closing or opening time of  $20 \mu\text{s}$ . This  $20 \mu\text{s}$  are small compared to the dwelltime of the measurements ( $500 \mu\text{s}$ ) and the time of the surface process.

# Chapter 4

## CO

This chapter begins with the calibration measurements of the Pd  $3d_{5/2}$  of a clean Pd(100) surface and the adsorption of CO and O<sub>2</sub> on this surface for calibration purposes. It is followed by the studies of the growth of nickel oxide on a Pd(100) surface by XPS. Films of different thickness are then tested concerning their CO-oxidation in the next section. To conclude the studies about the CO-oxidation, kinetic analysis of 1 and 2 ML thick films are shown.

### 4.1 Surface Core Level Shift at different excitation energies

The Pd  $3d_{5/2}$  peak of a clean crystal Pd(100) surface shows not only a single peak but also a distinct shoulder on the lower binding energy side (cf. Figure 4.1). The shoulder is an additional peak originating from the so called surface core level shift (SCLS)<sup>38,47</sup> as mentioned in Section 2.1.2. This effect occurs from the different geometric (and then also electronic) environment of the first and second layer atoms compared to the bulk atoms of the single crystal.

The surface sensitivity can be enhanced by lowering the excitation energy and changing the ratio between the bulk and surface contributions. The overall intensity itself depends on the excitation energy due to the beamline setup. Nevertheless, the ratio of the two peaks only depends on the surface sensitivity. Consequently, the analysis of the surface core level shift depends on the excitation energy<sup>47,48</sup>. Interestingly, the intensity of the surface species is higher than the intensity of the bulk species between excitation energies of

400 and 390 eV. This cannot be explained by the enhanced surface sensitivity, and photoelectron diffraction is assumed to be responsible for this effect.

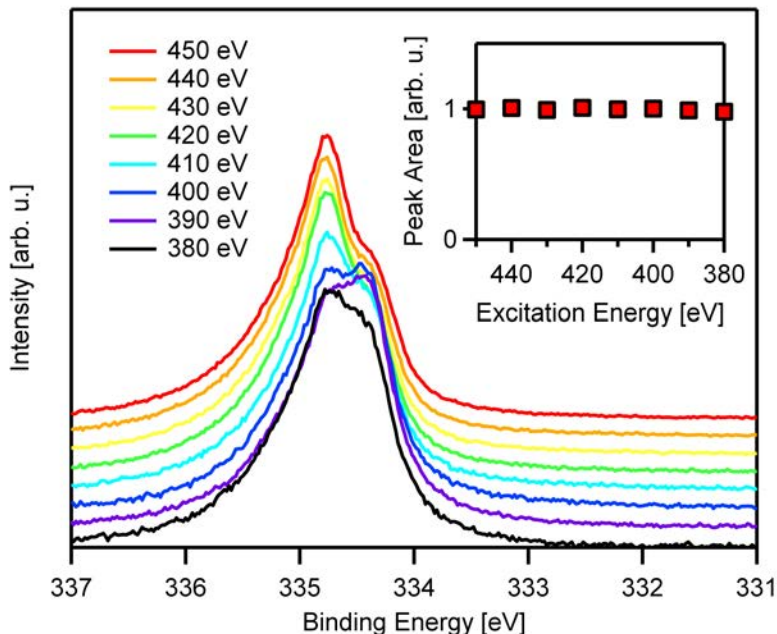


**Figure 4.1:** Spectra of the Pd<sub>5/2</sub> core level at different excitation energies. The inset shows the total peak area in dependency of the excitation energy.

## 4.2 Oxygen

The calibration of all oxygen coverages was done by a comparison to the experiment of the adsorption of O<sub>2</sub> at 300 K, where it dissociates on the palladium surface<sup>49</sup>. The complex phase diagram of oxygen adsorption shows that after an exposure of more than 10 L at 300 K the surface is covered with 0.5 ML of oxygen<sup>50</sup>. So oxygen was adsorbed at 300 K at an pressure of  $1 \cdot 10^{-6}$  Torr for 10 minutes, with an overall exposure of 600 L. The shape of the spectrum shown in Figure 4.2, which was taken after the adsorption, is very similar to the one measured from Gladys et al<sup>51</sup>. However, the coverage is denoted as 0.2 ML of oxygen; thus here is a difference between the phase diagram of Uvdal and the coverage of Gladys. To clarify this issue, a LEED pattern was measured and is shown in Figure 4.3. This pattern corresponds to a p(2x2) superstructure and is at a coverage of 0.25 ML. Because of the similarity to the spectrum of Gladys and the unmistakable diffraction pat-

tern, the amount of oxygen, stated as 0.25 ML, is used for calibration in this work.

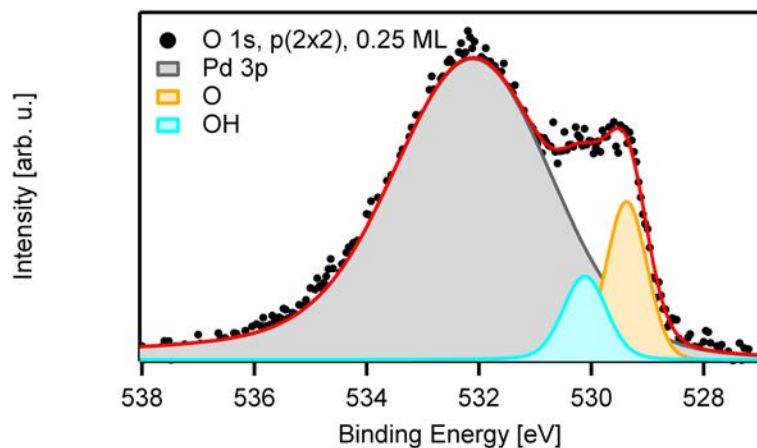


**Figure 4.2:** O1s spectrum of 0.25 ML O after adsorption of 600 L

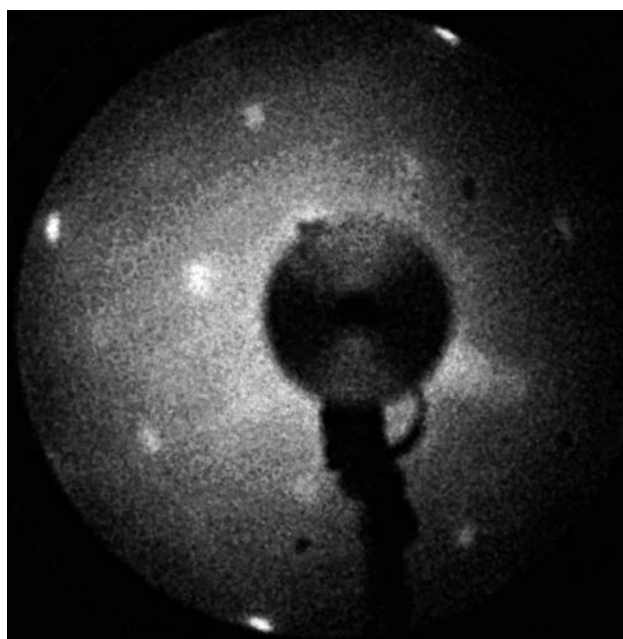


**Figure 4.3:** p(2x2) LEED pattern of adsorbed oxygen at 82.2 eV

## 4.3 CO

The system of CO on Pd(100) is well known from literature<sup>52,53</sup>. The adsorption studies showed that the coverage depends on the temperature such that for lower temperatures higher coverages are found. Altogether, three

structures are recognizable: at 350 K the  $p(2\sqrt{2} \times \sqrt{2})R45^\circ$  pattern is observed with a coverage of 0.5 ML. The next structure is seen at 240 K with a  $p(3\sqrt{2} \times \sqrt{2})R45^\circ$  pattern and gives an overall coverage of 0.67 ML. The last structure ( $p(4\sqrt{2} \times \sqrt{2})R45^\circ$ ) comes with an coverage of 0.75 ML. The low coverage system was prepared by dosing CO at  $3 \cdot 10^{-9}$  Torr to get to an coverage of 0.5 ML and the  $p(2\sqrt{2} \times \sqrt{2})R45^\circ$  structure. The corresponding XP spectra of this experiment are shown in Figure 4.4. They show a sharp single peak at the typical binding energy for CO of 286 eV. The occurrence of a single peak means that only one adsorption site is occupied in contrast to CO on platinum<sup>45,46,54</sup> at these conditions.

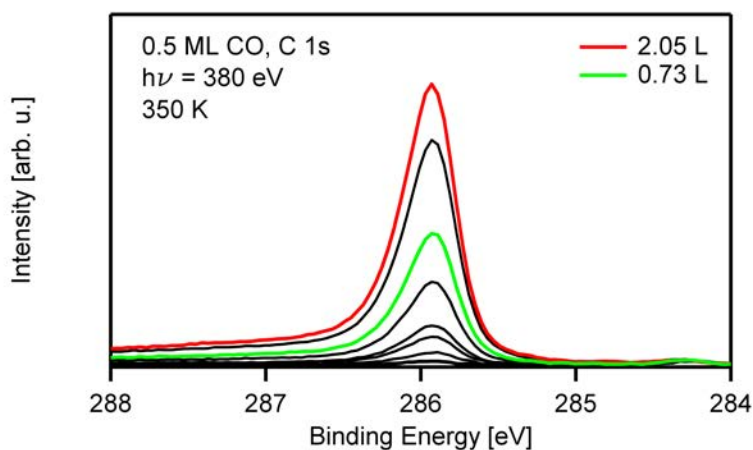


**Figure 4.4:** C 1s XP spectra of the CO adsorption.

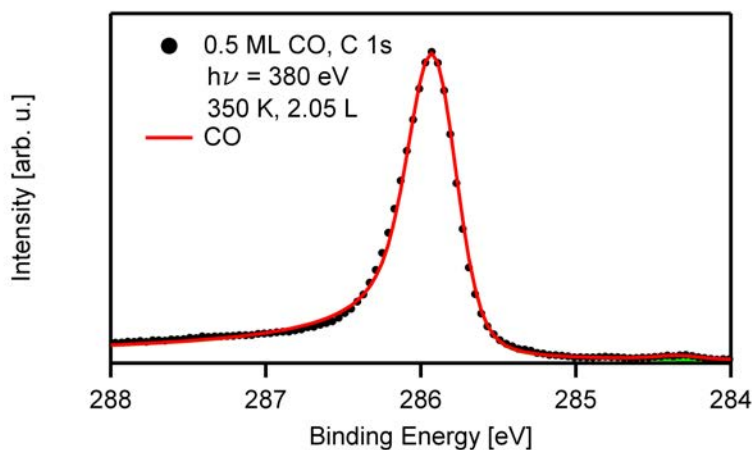


**Figure 4.5:** Fit of the spectra of the saturated CO layer adsorbed on Pd(100) at 350 K (topmost spectrum in Figure 4.4)

The fit of the saturated spectrum is shown in Figure 4.5. This spectrum was used for calibration in all later experiments to determine the amount of carbon on the surface.

## 4.4 NiO/Pd(100)

A crystalline nickel oxide film which is grown by reactive deposition, i.e. deposition of metallic nickel under oxygen atmosphere,<sup>31,35</sup> on a Pd(100) single crystal ( $a_{Pd} = 3.9 \text{ \AA}$ ) has a lattice mismatch ( $a_{NiO} = 4.2 \text{ \AA}$ ) of 7.8%. Because of this lattice mismatch the first layer is a wetting layer to relieve stress in the system<sup>55</sup>. Its calculated height is  $2.13 \text{ \AA}$ <sup>56</sup>, which is lower than the lattice constant of the strained second layer, which is  $2.34 \text{ \AA}$ <sup>55</sup>. The wetting layer has the stoichiometry of  $Ni_3O_4$  by forming a layer with missing nickel atoms generating a  $c(4 \times 2)$  overlayer<sup>33,35</sup>. From the second layer on the nickel oxide film grows stoichiometrically 1:1 in a Stranski-Krastanov mode with a strained lattice. This strain induces mosaics and for films thicker than 6 ML a bulk like nickel oxide is formed. The RMS-roughness lies between 0.6 and  $1.9 \text{ \AA}$  depending on the layer thickness between 0.5 and 6 ML. The average terrace size is  $66 \times 66 \text{ \AA}^2$ <sup>55</sup>. In contrast to the reactive deposition post oxidation was examined by Sambhi et al<sup>57</sup>. These films do not show a long range ordering and particles/islands are formed.

In this work all nickel oxide films were grown at 300 K in oxygen atmosphere of  $1 \cdot 10^{-6} \text{ mbar}$ <sup>35</sup>. As nickel source an electron beam evaporator was used. For the ex situ preparation, the evaporation rate was calibrated with a quartz micro balance before each film preparation. The film thicknesses of the in situ grown films were calibrated in relation to the ex situ films.

## 4.5 Structure of NiO on Pd(100)

### 4.5.1 Data analysis of the Ni 2p spectrum

In the following sections, the growth and the reduction of several nickel oxide films are described. In the following, the fit procedure of Ni 2p is discussed.

To fit these spectra it is necessary to understand the Ni 2p spectrum, see Figure 4.6. It consists of three contributions at 852.9, 854.2 and 856.0 eV.

Calculations by Veenendaal et al have shown that the shoulder on the high binding energy site does not appear until neighboring clusters are included in the calculations<sup>58</sup>. This effect is called a non-local screening effect, because the surrounding atoms screen the local core hole<sup>39</sup>. The NiO unit is embedded in a large NiO cluster, i.e., the neighbor in next environment are as further NiO shells included. So the screening depends on the amount of the clusters and should be reflected by the ratio between the main peak and its shoulder<sup>59-61</sup>. The examples in Figure 4.6 are fitted with the same ratio between the main peak (854.2 eV) and its shoulder (856.0 eV) obtained on the thicker film (3.2 ML). One can easily see that a fixed ratio does not work very well for the thinner film (1.8 ML). To accomplish a good fit, the ratio will be varied for low coverages. The peak at 861.8 eV is a satellite of nickel, similar to the 6 eV satellite in nickel. The binding energy decreases with lower film thickness as mentioned before by Rizzi et al<sup>62</sup>.

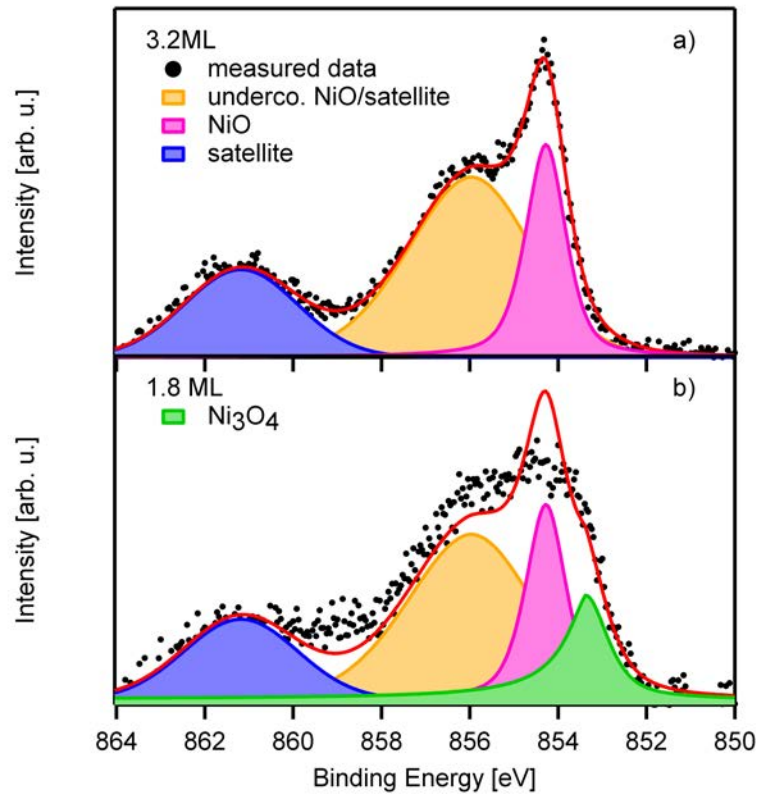


**Figure 4.6:** Change in the ratio between the NiO main peak and its shoulder. Ratio between the main peak and the shoulder obtained from (a) put in (b) giving a substandard line shape. This change in ratio is explained in the text.  $T = 300$  K,  $h\nu = 950$  eV

### 4.5.2 Growth

During deposition, XP spectra of the Ni 2p region were continuously measured; in Figure 4.7 typical spectra are shown along with corresponding fits. At low coverages, i.e., below one monolayer (see Figure 4.7b), the Ni 2p spectra show a dominant peak at a binding energy of 853.3 eV. This peak is assigned to the wetting layer with a stoichiometry of  $\text{Ni}_3\text{O}_4$ <sup>33</sup>. In addition to the dominating peak, two broad features are observed at  $\sim 857$  eV and  $\sim 861$  eV; the first feature originates from the non local screening effects, the second is a satellite<sup>63</sup>.

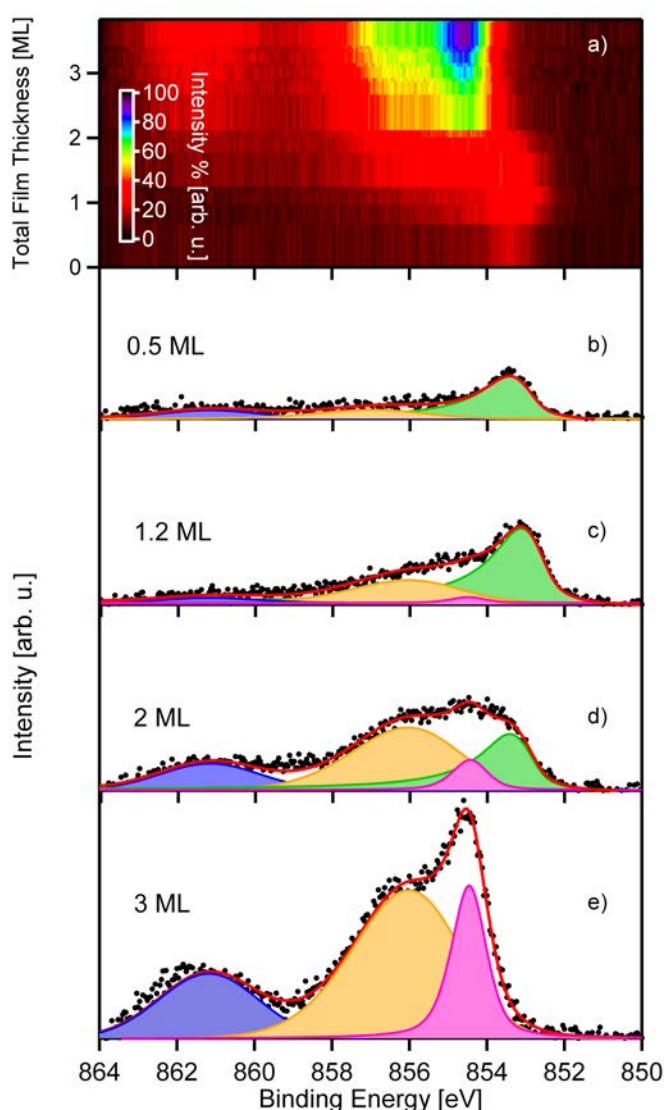


**Figure 4.7:** a) Ni 2p spectra of the growth of NiO on Pd(100). All data shown in a color coded density plot; b), c), d) and e) show fits at the denoted thicknesses

For a coverage of 3 ML (cf. Figure 4.7e), the spectrum shows three peaks, with the main peak at 854.2 and two satellites at 856.0 and 861.5 eV (interpretation as above). This spectrum is characteristic for bulk-like NiO<sup>63,64</sup>. For coverages between 1 and 3 ML, situations intermediate between the wetting layer and the bulk-like nickel oxide layers are observed. This is in line with observations in literature, where the growth of NiO islands on the wetting layer have been reported<sup>31</sup>.

In Figure 4.8 the quantitative analysis of the spectra at different coverages is shown: at low coverages, first the growth of the wetting layer is found. Around 1 ML, the intensity of bulk-like NiO starts to increase; simultaneously, the intensity of the wetting layer saturates and thereafter starts to decrease, due to damping by the bulk-like NiO-islands on top. In this experiment, the surface sensitivity is very pronounced due to the low kinetic energy of the photoelectrons leading to an inelastic mean free path of 5.1 Å<sup>65</sup>. This, and the emission angle of 70° with respect to the surface normal, reduce the signal of the first layer to < 10 % of the initial value by two monolayers of NiO with a thickness of ~4.2 Å on the wetting layer (total of 3 ML).

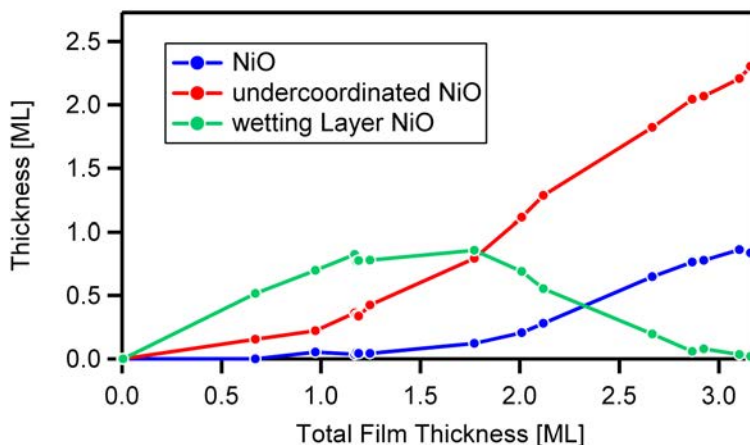


**Figure 4.8:** Quantitative analysis of the experiment shown in Figure 4.7.

### 4.5.3 Thermal stability

The reactivity of the prepared nickel oxide layers towards CO was studied between 475 and 550 K. Upon prolonged heating (up to one hour at 450 K) no changes in the intensities of the different Ni 2p peaks were observed (Figure 4.9). Upon annealing at 550 K (Figure 4.10), a very slow decrease of the

NiO features occurs with time, accompanied by an increase of a metallic Ni species. These changes are partly attributed to the desorption of minor amounts of OH, adsorbed during the preparation process, and partly to a reduction of the NiO film by CO in the residual gas. Note that the increase in the residual CO-pressure in the chamber due to heating and the related changes in the spectra are much smaller than those observed in the reduction experiments.

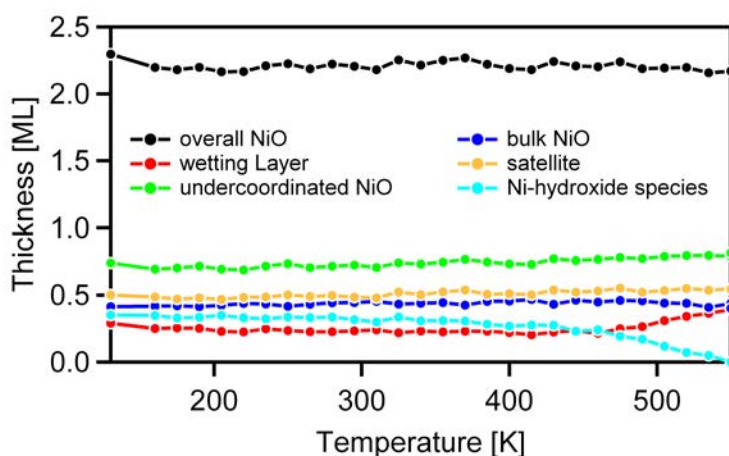


**Figure 4.9:** Thermal stability of 2 ML NiO film at rising temperature (0.5K/s)

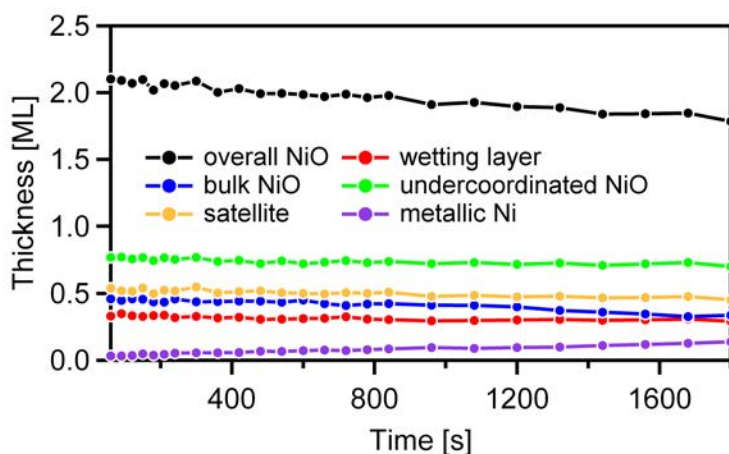


**Figure 4.10:** Isothermal experiment of the film at 550 K

The decrease of the overall NiO coverage of  $\sim 0.1$  ML NiO (cf. Figure 4.10) can be explained by two effects. The first effect is the flattening of the film and a reduced signal due to the damping of lower nickel oxide film

parts. The other effect can be the diffusion of nickel into the Pd crystal. Nevertheless, this loss can be neglected because of the time frame in which this decrease takes place and the small amount, when compared to later experiments.

## 4.6 CO Oxidation on Nickel Oxide

### 4.6.1 Reduction of thin NiO films

CeO<sub>2</sub> is a reactive oxide and is often used in catalysis<sup>26,66</sup>. Several theoretical and experimental studies show that it can be reduced and also be oxidized. It has been shown that the reduction of ceria is based on surface vacancies and the process is exothermic for the (110) and (310) surfaces<sup>67</sup>. This result was also found for nanostructured ceria powders with a partially reduced surface<sup>68-70</sup>. For comparison, now the reduction of NiO by CO was studied.

#### 4.6.1.1 Comparison of film thickness reaction

To analyze the general potential of NiO films as oxygen source, we investigated the activity towards oxygen release for different thicknesses of the NiO films, namely 0.5, 1, 2, 3, 4 and 6 ML. In Figure 4.12, the normalized intensity of the nickel oxide signals is plotted against time for a reaction temperature of 500 K at a CO pressure of  $1 \cdot 10^{-6}$  mbar. For the thin films of 0.5 and 1 ML we find complete and fast reduction to metallic nickel. At intermediate coverages the reaction becomes increasingly slower until for 6 ML no measurable changes occurs. At this thickness the layer is considered to behave like bulk-like NiO.

To investigate, whether the interface between Pd and NiO, related edge or border sites or free Pd sites are responsible for the observed reactivity at low coverage, 0.1 ML Pd were deposited on the non-reactive 6 ML thick NiO layer. From the fact that no change or increase in reactivity was observed, it can be ruled out that Pd-related sites are responsible for this reaction.

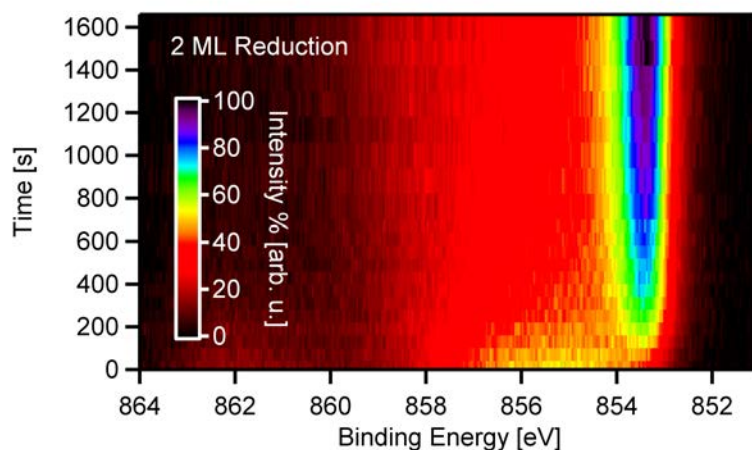


**Figure 4.11:** Reduction of 2 ML NiO/Pd(100) at 500 K in a color coded density plot

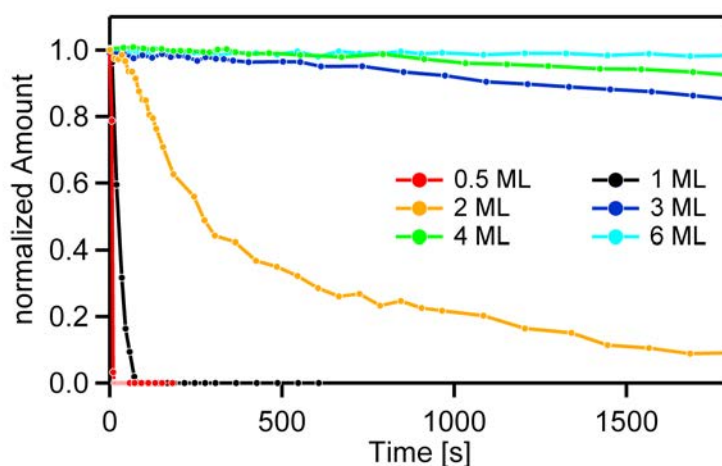


**Figure 4.12:** Quantitative analysis of the reduction of NiO films.

From the experiments, it cannot be ruled out that the reactivity is also related to the mere thickness of the oxide film: For other oxides, it has been proposed<sup>36,71,72</sup> that a charge transfer from the underlying metal is responsible for an enhanced reactivity. Such a behavior was found for adsorbates with a high electron affinity as e.g.  $\text{NO}_2$  adsorbed on oxides as e.g.  $\text{MgO}$ ,  $\text{BaO}$ , and  $\text{Al}_2\text{O}_3$  supported on Ag or Pt. On the other hand, it is interesting to note that in other studies<sup>31,55,73</sup> the existence of polar borders, i.e. steps and kink sites on highly strained films, did not seem to be responsible for the reactivity of these films, as the roughness typically rises with thicker films having more steps and kinks<sup>31</sup>. Thus for a roughness-induced mechanism the

reactivity should increase with film thickness, which is not observed here. At 20 ML thick films the RMS is about  $3.8 \text{ \AA}$  where it is only  $1.9 \text{ \AA}$  of it at 6 ML NiO.

#### 4.6.1.2 Wetting layer: 1 monolayer

To obtain further insight, the reduction process at various temperatures was investigated by isothermal experiments. First the 1 ML thick NiO wetting layer is discussed at temperatures between 350 and 500 K. In Figure 4.13, the corresponding spectra collected during the reduction process at 500 K are shown in a color coded density plot. The spectra show the dominating peak of the wetting layer at 853.3 eV with its satellites at 857 and 861 eV (see above). Upon exposing the surface to  $1 \cdot 10^{-6}$  mbar CO, the appearance of a new peak at 852.7 eV due to metallic nickel is observed, reflecting the reduction of nickel oxide. At the end of the experiment, the film is completely reduced, as shown by the quantitative analysis in Figure 4.14. Plotting the logarithm of the amount of NiO vs reaction-time yields a straight line, as is evident from Figure 4.15. Experiments at other temperatures also result in straight lines, indicating a pseudo first order reaction behavior; overall the rate constants (i.e., the negative slope in Figure 4.15) increase with temperature. From the Arrhenius analysis in Figure 4.16 the activation energy for the reduction process was determined to be 0.64 eV.

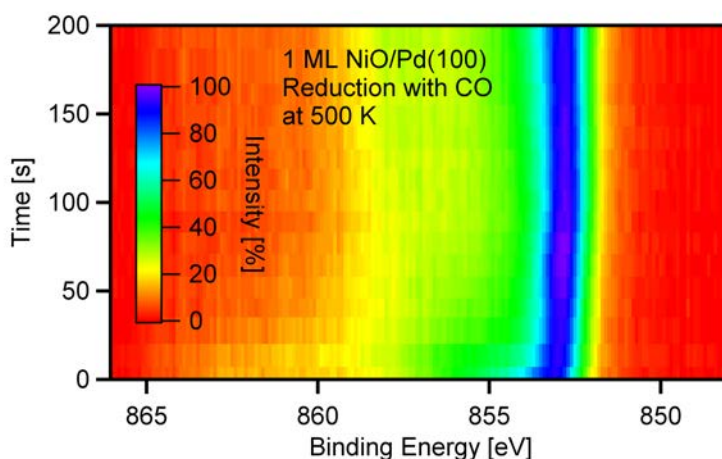


**Figure 4.13:** Reduction of 1 ML thick NiO film by CO at 500 K studied in the Ni 2p regime.  $1 \cdot 10^{-6}$  mbar CO was dosed onto a 1 ML thick nickel oxide film for 100 seconds

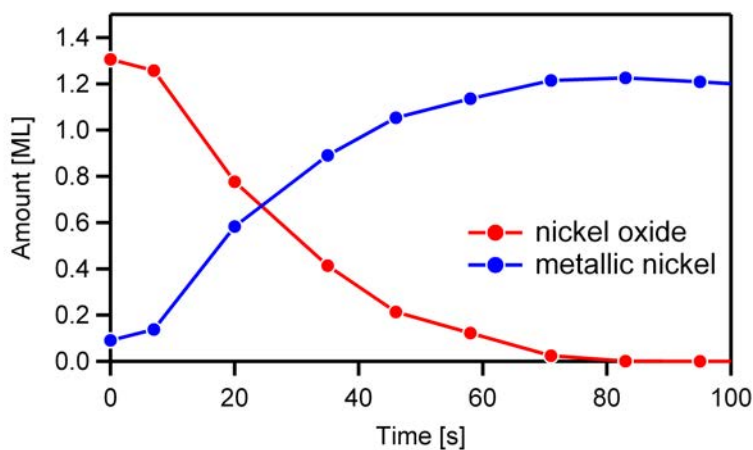


**Figure 4.14:** Quantitative analysis of the reduction of 1 ML NiO/Pd(100) at 500 K with CO at a pressure of  $\cdot 10^{-6}$  mbar CO

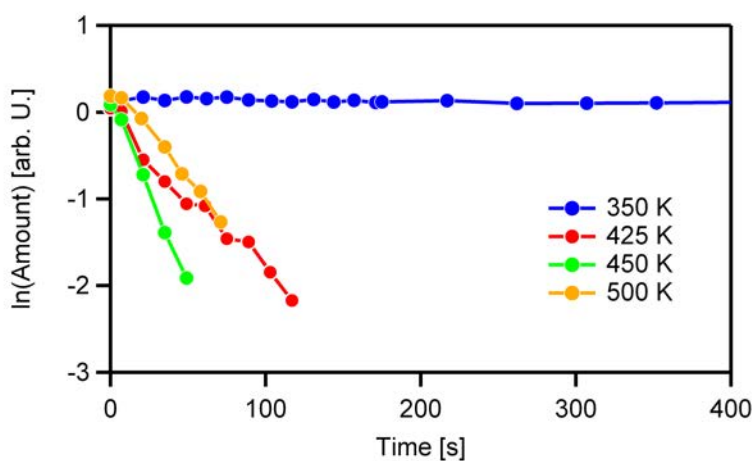


**Figure 4.15:** Quantitative analysis of the reduction of 1 ML NiO/Pd(100) at different temperatures. The logarithm of the data is used to show the straight line indicating the 1st order reaction.

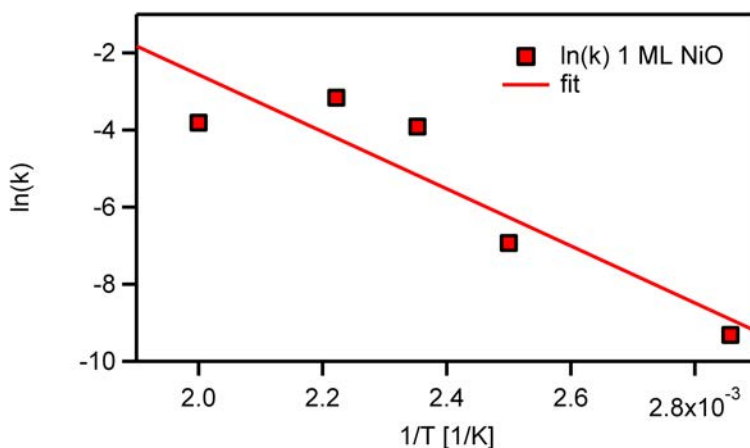


**Figure 4.16:** Arrhenius plot of the reduction of 1 ML NiO film via CO Oxidation. The activation energy is 0.64 eV.

#### 4.6.1.3 Two monolayers

As a next step, the reduction of 2 ML thick NiO film was investigated. Typical XP spectra and the corresponding analysis are shown in Figure 4.17 and 4.18, respectively. The spectrum before exposure to CO shows the superposition of the signal from the wetting layer and one layer of bulk-like NiO (see above). Note that these experiments were performed at normal emission, leading to a higher information depth and consequently a smaller damping of the wetting layer than in the growth experiment shown in section 4.5.2. The exposure to  $1 \cdot 10^{-6}$  mbar CO at 500 K (Figure 4.17) leads to a rapid decrease in NiO intensity and to the evolution of the metallic Nickel peak at 852.7 eV with its satellite at 858 eV.

In Figure 4.17, the Ni 2p spectra before and after 1500 s CO exposure are shown, for comparison. A quantitative analysis of this isothermal reduction experiment along with experiments at different temperatures is shown in Figure 4.18. For 475 K, a slow decrease of the NiO signal is found. The curves at the higher temperatures (500 - 550 K) show a steep initial decrease down to a coverage of  $\sim 1$  ML; thereafter the slope becomes more shallow. Such a behavior is not in line with a simple exponential decay that was reported e.g. by Agnoli et al.<sup>74</sup> for the isothermal reduction of NiO/Pd(100) with hydrogen. The deviation from a simple first order reaction becomes even more evident from the plot of the logarithm of the signal versus time in Figure 4.19: Obviously, the data cannot be fitted with a single straight line.

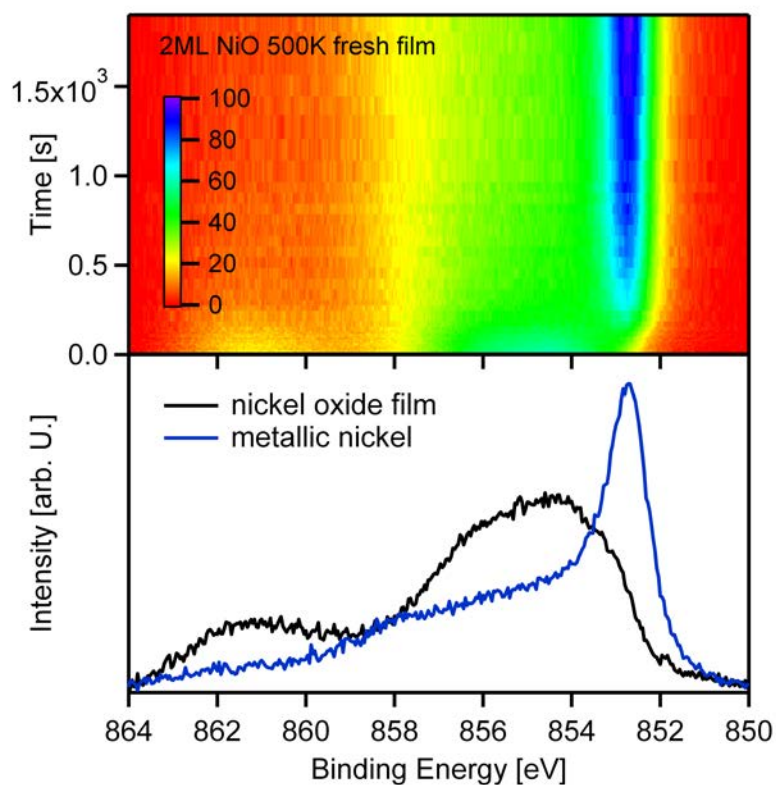


**Figure 4.17:** Reduction of a 2 ML NiO film on Pd (100) with CO: a) experiment in a color coded density plot; b) first and last spectrum

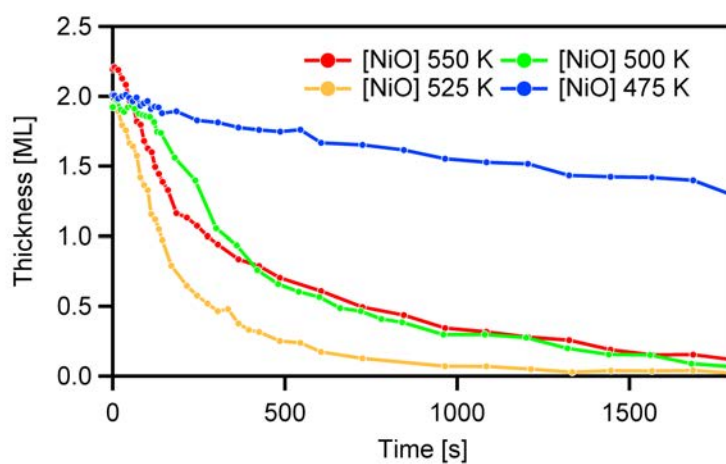


**Figure 4.18:** Quantitative analysis of the reduction of NiO at temperatures from 475 to 550 K.

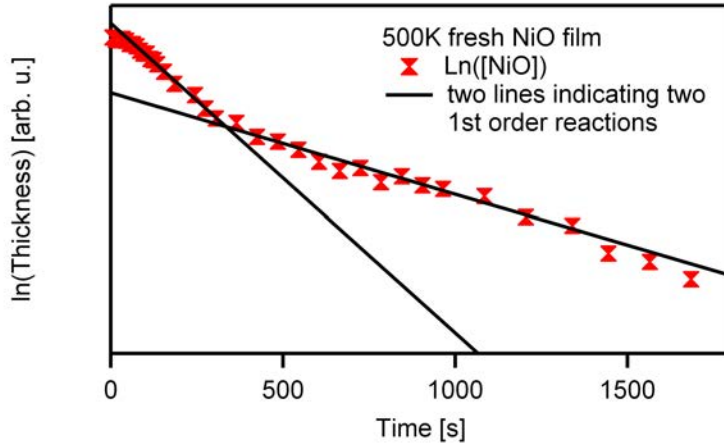
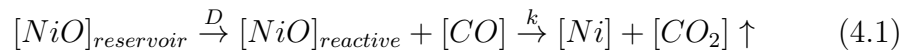


**Figure 4.19:** Linear regression model for the reaction of NiO with CO at 550 K.

A more complex model is needed and presented in the following: a knee in the logarithmic curve of the thickness vs. time is a strong hint that two first order reactions are involved (cf Figure 4.19). From this, the diffusion in a thin film, described by a first order process in the terms of lattice hopping<sup>75,76</sup> and a first order reaction of the oxygen with CO to CO<sub>2</sub> at reactive sites is assumed (cf. Figure 4.20a). The corresponding thickness curves are shown in Figure 4.20b. The assumption of the diffusion as hopping processes is justified, because the film is so thin that no reasonable concentration gradient is applicable.

The model reaction scheme for two serial coupled first order reaction would look like this:



with D as the diffusion rate constant and k as the reaction rate constant. The nickel oxide thickness, i.e. the amount of NiO, is described with  $[NiO]_{reservoir}$  for the non reactive reservoir and  $[NiO]_{reactive}$  for the reactive sites.  $[Ni]$  is the produced metallic nickel. Due to the relatively high pressure, a pseudo first order reaction for the CO oxidation can be assumed.

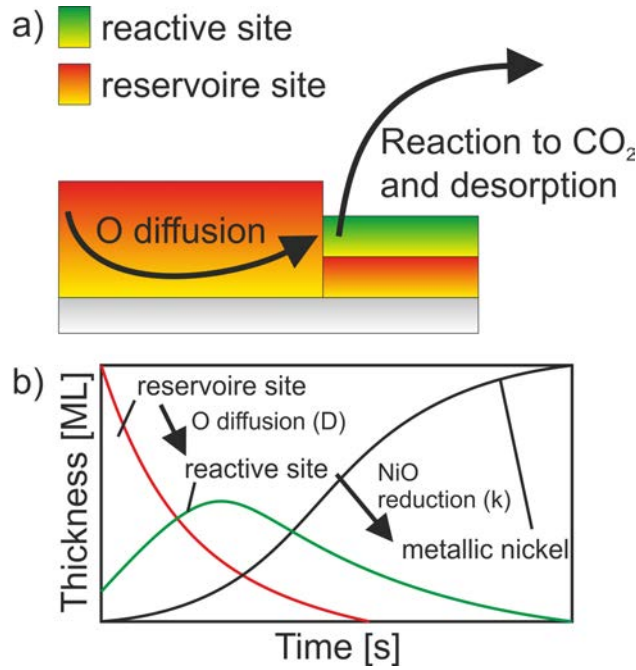


**Figure 4.20:** a) Model of the processes in a 2 ML thick nickel oxide film supported on Pd(100). Two processes happen: diffusion of oxygen from a reservoir to a reactive site and reduction of these sites by CO b) Thickness, i.e. amounts, of nickel oxides vs. the time.

Following, the textbook approach for a consecutive reaction from the reactant via an intermediate to the product the thickness of the NiO in the reservoir reactant evolves according to<sup>77</sup>

$$[NiO]_{reservoir} = [NiO]_{reservoir,0} \cdot \exp(-Dt) \quad (4.2)$$

with  $t$  as the time and  $[NiO]_{reservoir,0}$  as the initial thickness of the  $[NiO]_{reservoir}$ . The equation for the amount of the reactive sites is given by<sup>77</sup>

$$[NiO]_{reactive} = \frac{D \cdot [NiO]_{reservoir,0}}{k - D} \cdot (\exp(-Dt) - \exp(-kt)) + [NiO]_{reactive,0} \cdot \exp(-kt) \quad (4.3)$$

with  $t$  as time,  $D$  and  $r$  as the rate constants for the diffusion and reaction and  $[NiO]_{reactive,0}$  as the initial thickness of the reactive nickel oxide species. Here the term in the first line of equation 4.4 gives the thickness, i.e. the

amount, of reactive nickel oxide due to diffusion of oxygen from the oxygen reservoir and the term in the second line gives the initial thickness of the reactive nickel oxide sites which was formed during the growth process.

One has to mention that the amount of oxygen which is not on a reactive site can still be seen with XPS, but it is not possible to distinguish exactly between the two mentioned oxygen species by the fitting procedure. To compensate this imprecision both thicknesses,  $[NiO]_{reservoir}$  and  $[NiO]_{reactive}$ , are added, which leads to

$$[NiO]_{complete} = \frac{D \cdot [NiO]_{reservoir,0}}{k - D} \cdot (exp(-Dt) - exp(-kt)) \quad (4.4)$$

$$+ [NiO]_{reactive,0} \cdot exp(-kt) + [NiO]_{reservoir,0} \cdot exp(-Dt)$$

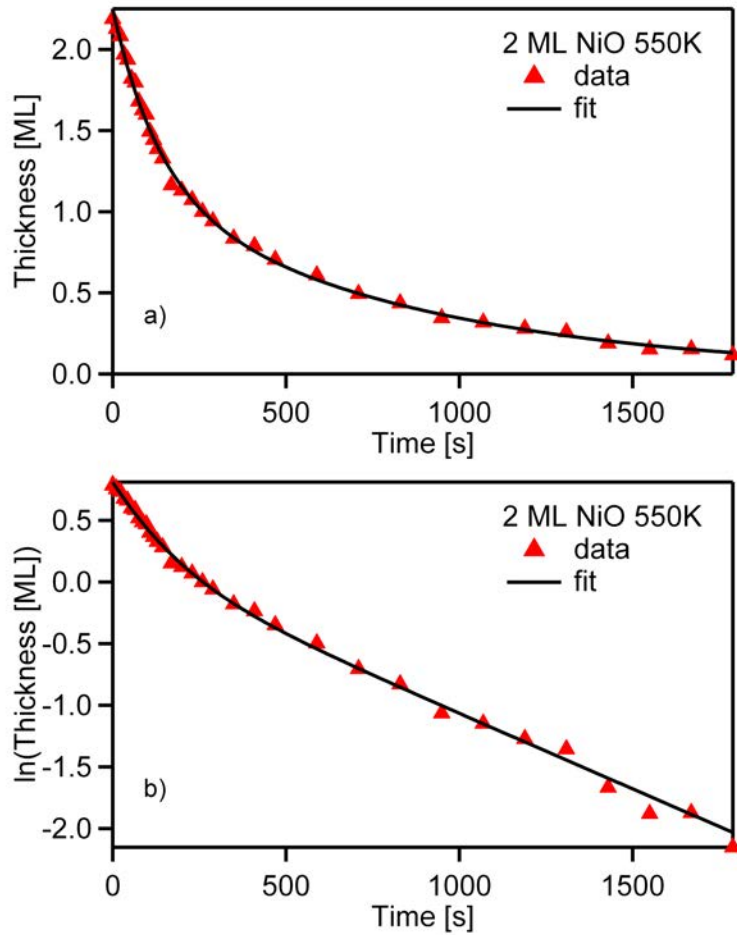


**Figure 4.21:** a) Model for the reduction of 2 ML nickel oxide at 550 K. b) as logarithmic plot

An exemplary fit with this model to the data for 550 K is shown in Figure 4.21a (linear scale) and Figure 4.21b (logarithmic scale), showing an excellent match to our data, during the whole experiment, especially in the thickness region around 1 ML, where the change in slope occurs. The respective Arrhenius analysis for the complete data set is shown in Figure 4.22. The activation energies for the rate determining steps, i. e. reaction and diffusion are found to be 0.22 and 0.33 eV, respectively.

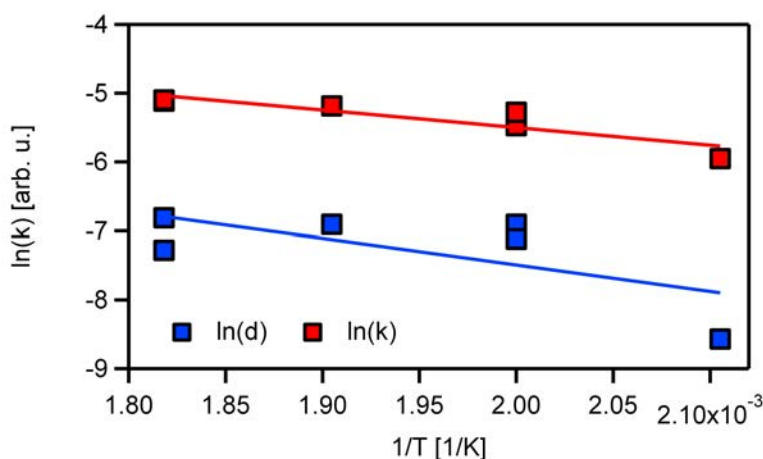


**Figure 4.22:** Arrhenius analysis of the model. Blue (d) describes the results of the diffusion and red (k) the result of the reaction.

A first model of the character of the reactive sites could lead to the assumption that these sites are uncovered reactions sites from the wetting layer. This assumption is unlikely because the activation energy is only 1/3 in comparison to the reaction of the wetting layer. Thus no explanation can be given at the moment.

#### 4.6.1.4 Reoxidation and 2nd reduction cycle

For an effective use of this system as an oxygen source in reactions it would be highly beneficial to restore the initial oxide film; in the following, the behavior for the case of the 2 ML NiO films was analyzed. After reduction with CO, the Ni film was reoxidized at 550 K. This procedure can also be regarded as a alternative route to produce thin NiO films, namely the deposition of a metallic Ni layer, which is oxidized subsequently<sup>57</sup>.

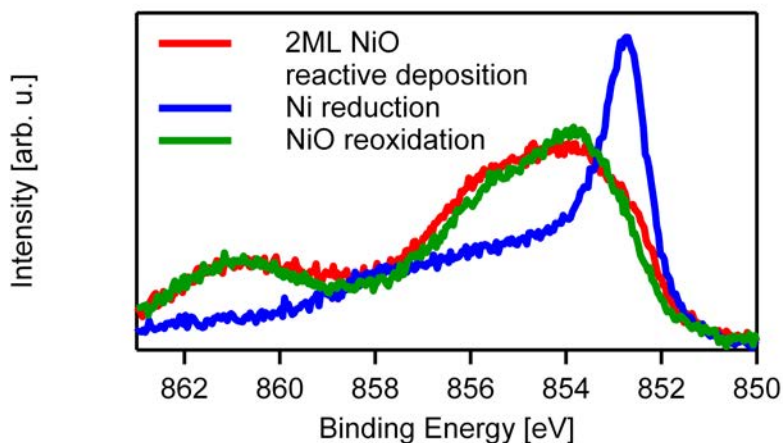


**Figure 4.23:** Ni 2p spectra of the NiO film grown with reactive deposition, after reduction and after reoxidation at 550 K.

The analysis of the Ni 2p spectra in Figure 4.25 shows that the NiO species formed by reoxidation shows a spectrum that is very similar in shape to the spectrum obtained after the initial reactive oxidation process. However, there is a significant difference in the intensity of the Pd 3d substrate signals, which shows a higher intensity due to a change in damping by the NiO film: For the reactive grown nickel oxide film the Pd signal is reduced to 53% as compared to 61% for the reoxidized film (the value for the clean Ni film was 68%) see Figure 4.24.

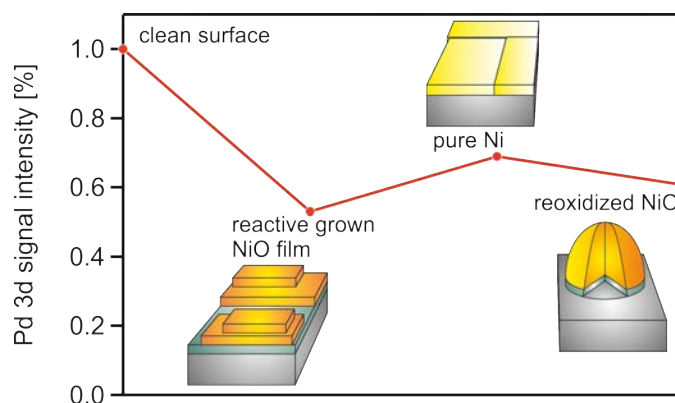


**Figure 4.24:** Respective Pd 3d signal intensities of a fresh and reoxidized NiO film and a correlated model

The higher value for the reoxidized film, i.e. the lower degree of damping implies that the reoxidized NiO films form islands and thus the Pd 3d signal becomes stronger, compared to the case of the reactive deposition, where

films are formed<sup>57</sup>. From the damping and with the model from section 2.1.3 an estimation shows that islands with about twice the height, i.e. 4 ML are formed, which cover only half the surface.

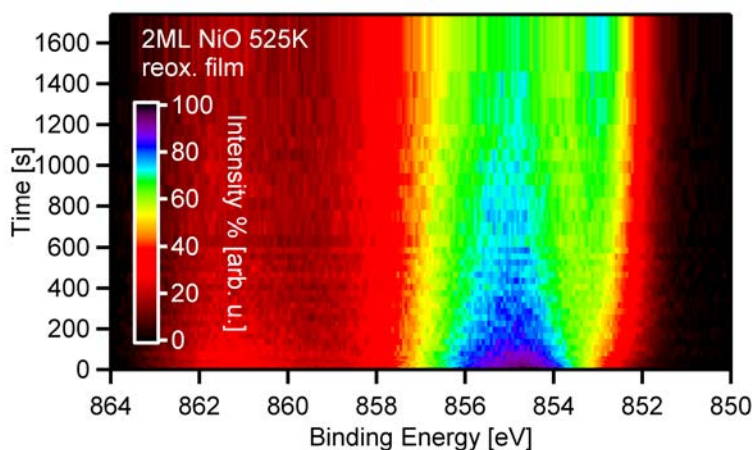


**Figure 4.25:** Ni 2p spectra of the 2nd isothermal reduction of a reoxidised 2 ML NiO layer.

The kinetics of the reduction of the reoxidized layers was studied in a similar way as described above for the layers prepared by reactive deposition. A typical experiment is shown in Figure 4.25. Overall, the quantitative analysis shows a similar behavior to the reaction on the freshly prepared 2 ML films. The major difference is the observation that the reaction does not lead to complete reduction, but slows down at a coverage of  $\sim 1.5$  ML. The activation energies, determined using the two coupled first order reactions (see above) are 0.39 and 0.40 eV.

The observation that in case of the reoxidation only  $\sim 0.5$  monolayers of the NiO are reduced is in contrast to the situation for the reactive deposition, where a full reduction was found. This is in line with the result from the analysis of the damping of the Pd 3d signal, which indicated the formation of islands that also contain thicker parts that are not reduced, or are too thick so that the oxide can't diffuse to the reactive sites. A model of the structure of the whole cycle is given in Figure 4.28. First, a fresh 2 ML nickel oxide film is produced. As reported in<sup>35</sup>, a wetting layer (green) and some islands with steps occur. Reduction of this film leads to a strained nickel film. After reoxidation with oxygen, the nickel oxide film exhibits higher structures, probably clusters, covering on average only half of the surface. It is not possible to completely reduce these structures again.

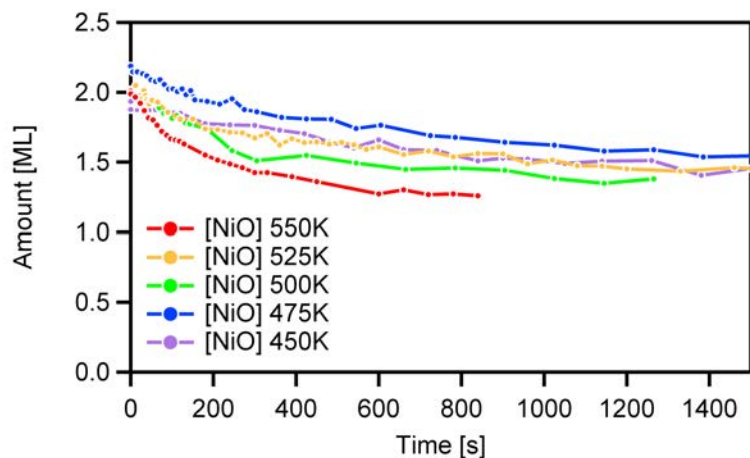


**Figure 4.26:** Quantitative analysis of different reaction temperatures of the reoxidized 2 ML NiO films.

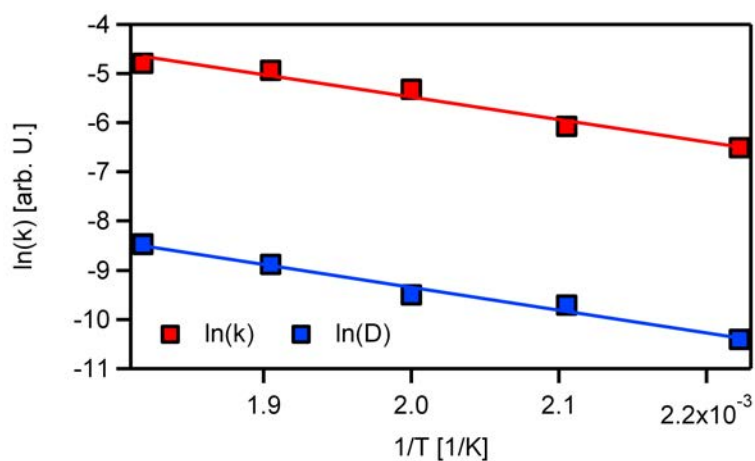


**Figure 4.27:** Arrhenius plot of the isothermal reactions.

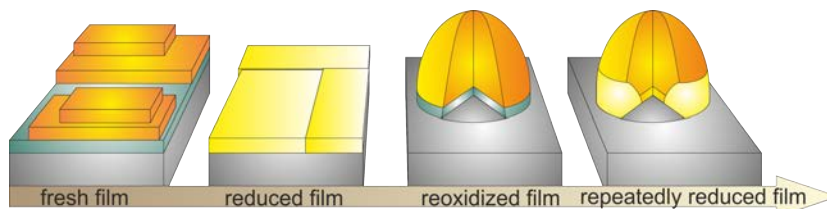


**Figure 4.28:** Reduction Oxidation cycle of 2 ML NiO on Pd(100): for details see text.

## 4.7 CO on Pt(111) at higher temperatures

Photoelectron spectroscopy has benefitted strongly from the improvements of synchrotron radiation sources<sup>78</sup>. Especially the high flux and tunable energy allows for using spectroscopic methods such as XPS as an in situ measuring tool for determining the surface composition<sup>79</sup>. Thereby, not only a much better energy resolution but also much shorter data acquisition times than in typical lab experiments was achieved<sup>80</sup>. Using laboratory X-ray sources, the typical measuring times in the order of several minutes up to hours allow only for a very limited picture of time-dependent changes occurring on a surface. When using synchrotron radiation, the time resolution is significantly improved, such that high-resolution XP spectra can be taken in a few seconds<sup>54</sup>. With this improvement, it became possible to study time-dependent surface processes in situ, i.e. to follow adsorption as function of time or reaction as function of temperature. This gain in time resolution not only opens the possibility to access the kinetics of surface reactions<sup>81,82</sup>, but also to greatly improve the output in measurement data per time. On top of that, further improvements were achieved by new technological efforts: The development of new detectors and the operation of electron analyzers in the so called snap shot mode enables a time resolution of down to  $\sim 100$  ms in the case of analyzers with a CCD camera as detector, while times down to 1 ms are projected for delay line detectors<sup>83</sup> and other advanced detector designs<sup>84</sup>. As examples one should mention the detector from Bussat et al.<sup>85</sup> and the company Omicron (128 channel stripe anode detector). The improved time resolution for XPS, and also for other X-ray based techniques, was used to study, e.g. surface reactions<sup>81,86-89</sup>, giving insights to reaction intermediates and reaction kinetics<sup>82,90,91</sup>, the growth of different adsorbate layers<sup>54,92</sup>, including (metal) oxides<sup>35,93,94</sup>, graphene<sup>95,96</sup> and small hydrocarbons<sup>96-99</sup>.

In addition to the mentioned applications, which all make use of synchrotron radiation in the "multi bunch mode", for pump and probe-type experiments with much shorter timescales in the nanosecond regime or below, the synchrotron facility must be operated in the single bunch mode, i.e. the pulsed time structure of the synchrotron radiation is made use of<sup>100</sup>. Typical setups for the detection of the electrons are either gated analyzers<sup>101,102</sup> or time-of-flight analyzers<sup>103</sup>. In these cases, the incident photon numbers

are significantly smaller and thus the detected overall number of electrons is lower. The aims of experiments with time resolution down to the few femtosecond range are quite different, leading to information on molecular motion and electron movements, e.g. the photovoltaic effects in the valence bands of semiconductor surfaces<sup>104</sup>. These type of experiments will not be addressed here, but are only listed for the sake of completeness.

Herein, a new approach is presented, which still uses the "continuous" flux of synchrotron radiation in the multi bunch mode, with only minimal losses due to analyzer read out times. Thereby, the accessible temperature range for time-dependent spectroscopic studies of surface reactions can be significantly extended to higher temperatures; e.g. up to 500 K for CO on Pt(111), at low surface coverages of only  $\sim 0.1$  ML and below. The presented data were collected with a time resolution of 500  $\mu$ s, and one extrapolate that for the appropriate adsorption/reaction systems measurements with a time resolution of down to 20  $\mu$ s should be possible. CO adsorption on Pt(111) has been chosen as model system, since it has been well characterized in literature, in particular also with high-resolution XPS. We study the adsorption and transient desorption of CO at temperatures between 460 and 500 K, and compare the results to data obtained at lower temperatures with a time resolution of  $\sim 4$  s. Please note that the isothermal adsorption/desorption of CO on Pt(111) was up to now only studied up to temperatures of 450 K, as at higher temperatures the desorption is too fast, not allowing the required number of data points before complete desorption<sup>54</sup>.

#### 4.7.1 Measurements and data analysis

For an overview, first the adsorption of CO on Pt(111) is briefly recapitulated: In Figure 4.29a, C 1s XP spectra of the adsorption at a temperature of 200 K are shown up to a total coverage of 0.5 ML, which displays a well ordered c(4x2) LEED pattern (reproduced from<sup>45,54</sup>). The spectra show two peaks at 286.1 and 286.8 eV, due to CO adsorbed at bridge and on top sites, respectively, with coverages of 0.25 ML each. The difference in the intensity of the two peaks is attributed to photoelectron diffraction effects. The binding energies of the two peaks show only minor changes with coverage ( $\sim 0.07$  eV<sup>45</sup>). Consequently, the occupation of a particular site can be measured by following the intensity at a particular (fixed) binding energy for this site (e.g.

286.8 eV for the on top site), rather than by acquiring a "full spectrum". The spectrum of the  $c(4 \times 2)$  layer in Figure 4.29b served as a reference for the CO coverage calibration, e.g. for the C 1s intensity in the equilibrium state in Figure 4.30 (plateau from 2.5 - 9 s). During this adsorption experiment, the pressure of CO was  $1.7 \cdot 10^{-9}$  mbar to achieve a reasonable number of data points.

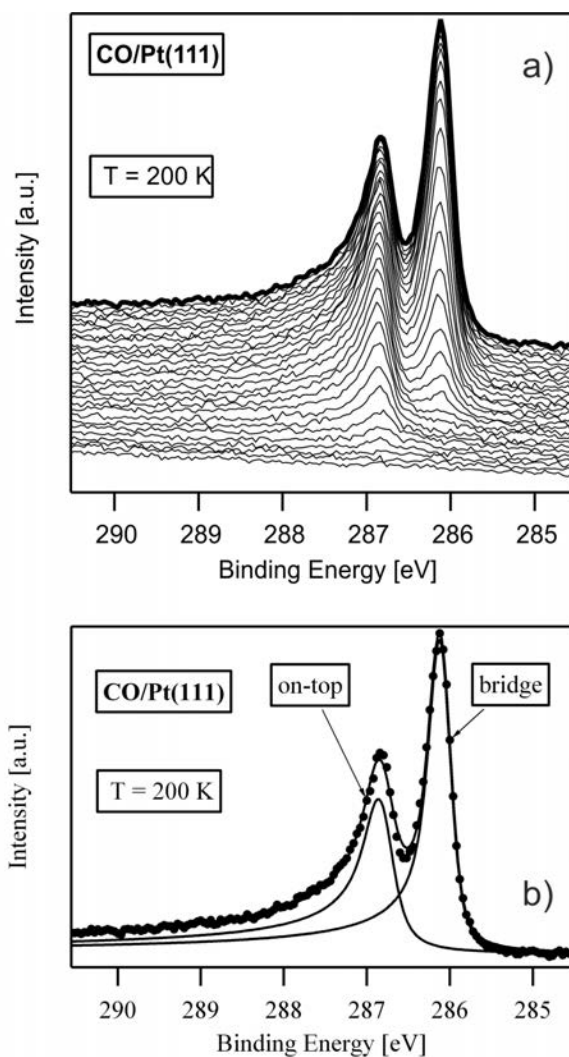


**Figure 4.29:** a) C 1s spectra of the adsorption of CO at 200 K on Pt(111) according to<sup>46</sup> ( $p_{CO}=1.7 \cdot 10^{-9}$  mbar, every spectrum took 4.8 s, 60 s between each spectrum ); b) Fit of the saturated C 1s spectrum, corresponding to the  $c(4 \times 2)$  superstructure of CO on Pt(111) (0.5 ML). Taken from [45,54]

In Figure 4.30a C 1s spectra measured under equilibrium conditions (i.e. with the molecular beam on) are shown, and Figure 4.30b depicts the corre-

sponding equilibrium coverages vs. temperature. The data in the temperature range from 375 to 450 K were taken from ref.<sup>45</sup> and the data from 460 to 500 K, were obtained within this thesis. Overall, a strong temperature dependence of the equilibrium coverage is observed; the spectra for higher temperatures in Figure 4.30a show that the population of the bridge adsorption site selectively decreases and at 500 K only the more stable top site is populated.

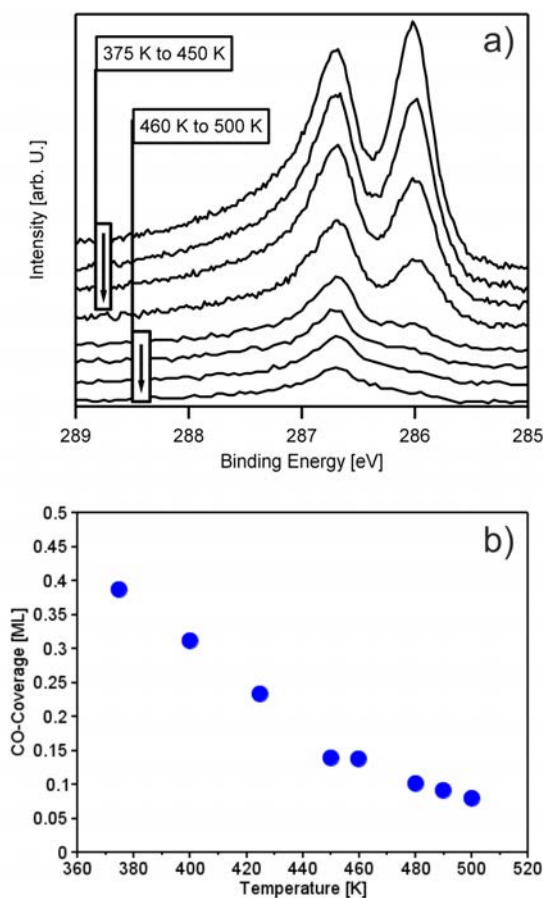


**Figure 4.30:** a) C 1s spectra taken at the given temperatures between 375 to 500 K at a CO pressure of  $2 \cdot 10^{-6}$  mbar. Data partly taken from [46]. b) Coverage of CO on Pt(111) at different temperatures ( $p_{CO}=2 \cdot 10^{-6}$  mbar).

Next, the time-dependent adsorption and desorption behavior at temperatures from 460 to 500 K is discussed and compared to previous data for lower temperatures taken from Ref.<sup>44</sup>. The measurements between 460 and 500 K were performed using the new approach. A typical data set measured at  $T = 460$  K and  $p = 2 \cdot 10^{-6}$  mbar is shown in Figure 4.31a with the chan-

neutron set to the binding energy of the on top site (286.8 eV) and in Figure 4.31b for the bridge site (286.1). The lower signal for the latter is due to its lower occupation (see Figure 4.29). Figure 4.31c shows the sum of the two signals as grey data, which reflect the total CO coverage. The data has been measured with 500  $\mu\text{s}$  per data point. As the characteristic time scales of the experiment are much slower, we can sum up 10 successive data points and thereby obtain a better signal to noise ratio, without a loss of information. The resulting curve (black data) then corresponds to data measured with 5 ms per data point. This signal will be used for the following analysis.

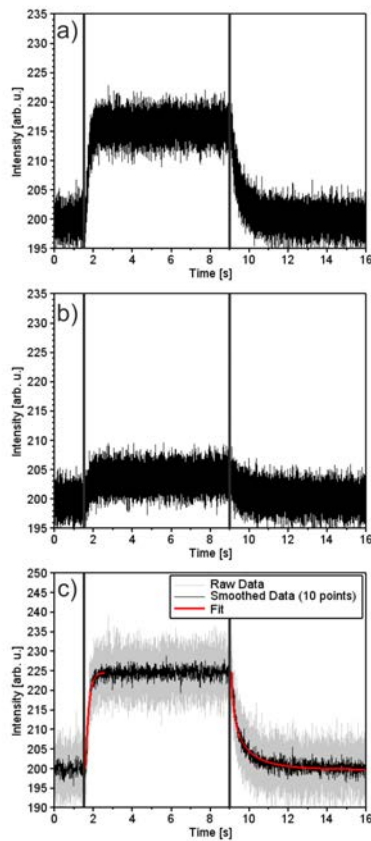


**Figure 4.31:** a) A complete measurement with a dwell time of 500  $\mu\text{s}$  and 100 times repeated on the binding energy of the top position and b) on the bridge energy position. c) Light Grey curve shows both channels from a) and b) added and scaled similar to<sup>46</sup>. Lightest grey gives a time resolution of 500 microseconds. The darker grey gives 5 ms of time resolution. Black bars show the opening and closing of the molecular beam shutter. ( $\Theta_{\text{tot}} = 0.14 \text{ ML}$ ,  $T = 460 \text{ K}$ ,  $p_{\text{CO}} = 2 \cdot 10^{-6} \text{ mbar}$ )

In Figure 4.32 and 4.33, the isothermal adsorption behavior (obtained from the data after switching on the CO beam) at temperatures between 460 and 490 K is shown, and the isothermal desorption behavior (obtained after switching off the CO beam) of CO on Pt(111) at temperatures between 375 and 500 K; the denoted coverages represent total coverages. The data up to 450 K was measured with the standard swept approach, with 3-4 s per spectrum (cf, Figure 4.30a). At higher pressures and/or temperatures, this type of swept mode measurements were not possible, due to the much faster characteristic time scales. This becomes evident from the adsorption measurements at  $2 \cdot 10^{-6}$  mbar, where the equilibrium coverage is reached already after 0.3-0.4 s (see Figure 4.32) or from the desorption measurement at 500 K, where more than 90% of the adsorbed molecules have desorbed within the first second (Figure 4.33b). The data above 450 K at pressures of  $2 \cdot 10^{-6}$  mbar thus have been derived from measurements using our new approach, i.e. from experiments like that shown in Figure 4.31. Note that the higher pressure compared to the adsorption at 200 K was also necessary to achieve a higher equilibrium surface coverage. The denoted coverages again are the total coverages; they are derived by adding the signals for the on top peak (at 286.8 eV) and the bridge peak (at 286.1 eV), obtained from two independent experiments. We want to point out, that the former experiments were done with a higher photon flux (by 17%), but as we show further below all experiments are in line with each other, so that we can exclude significant light-induced side effects.

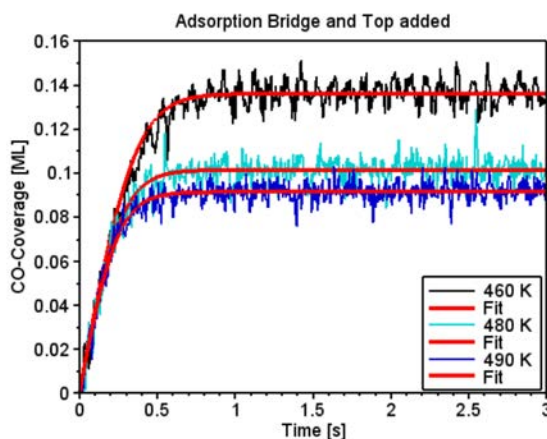


**Figure 4.32:** Total coverage during the adsorption of CO on the Pt(111) surface at different temperatures.  $p_{\text{CO}} = 2 \cdot 10^{-6}$  mbar.

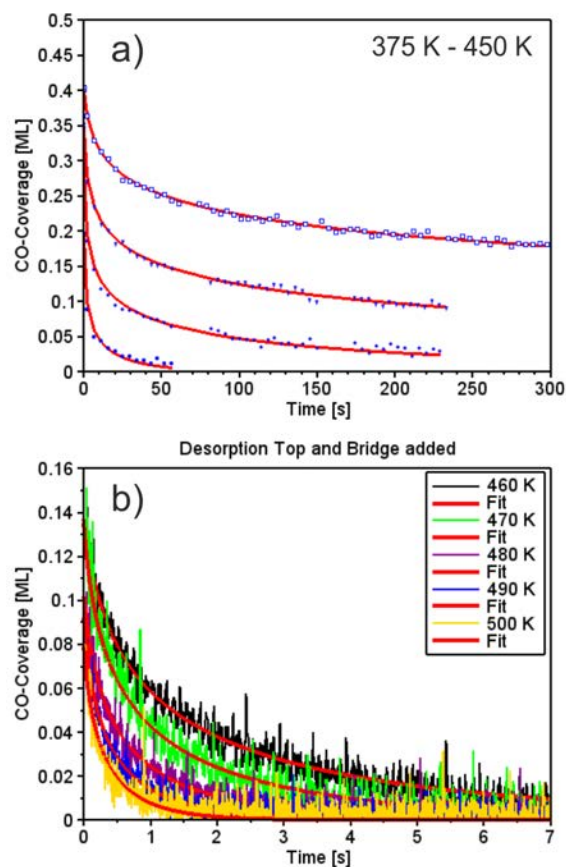


**Figure 4.33:** Desorption of CO from the Pt(111) surface for different temperatures. The conventional method is shown in a) (data taken from<sup>46</sup>). In b) the faster method is shown.  $p_{CO}=2 \cdot 10^{-6}$  mbar.

These data demonstrate that with the new approach it is indeed possible to extend the accessible timescale for in situ adsorption and desorption experiments considerably, i.e., by a factor of 50 - 100 for the here presented data. In the next step a simple analysis of both the existing data at the lower temperatures and pressures (Figure 4.33a) and the here obtained data (Figure 4.32 and 4.33b) with the new approach is performed to check for consistency.

Before doing that, a simple model to describe adsorption and desorption of CO on Pt(111) is introduced. Since the adsorption energy difference between the on top site and the bridge site is very small (40-90 meV, depending on the model<sup>46,54</sup>), site exchange between these two sites is in equilibrium. Considering that the adsorption energy,  $E_a$ , is much higher (e.g. 1.43 eV according to Ref.<sup>54</sup>) than this difference, one can treat the adsorption and

desorption behavior at elevated temperatures, as studied here, by using an average adsorption energy (and also prefactor), as well as sticking coefficient<sup>45,54</sup>. This certainly is a major simplification, but it allows us to check the data sets obtained under different conditions for consistency. Within this approach, the measured coverage change,  $\dot{\Theta}$ , can be described by coupled differential equations with a term for adsorption,  $\dot{\Theta}_{ad}$ , and desorption,  $\dot{\Theta}_{des}$ <sup>45,105</sup>.

$$\dot{\Theta} = \dot{\Theta}_{ad} - \dot{\Theta}_{des} = j \cdot S(\Theta, T) - D \cdot \Theta \quad (4.5)$$

$j$  is the molecule flux,  $S(\Theta, T)$  is the coverage-dependent sticking coefficient and  $D$  the desorption constant. Strictly speaking,  $S(\Theta, T)$  depends on the fractional coverages of bridge sites and on top sites. However, since at a given temperature, the fractional coverages are precisely determined by the equilibrium between the two sites, the total coverage,  $\Theta$ , can be used without loss of information. Adsorption is commonly described with the Kisliuk model, which considers direct chemisorption on the bare surface and precursor-mediated adsorption on adsorbate-covered regions<sup>106</sup>:

$$S(\Theta, T) = S_0 \left( 1 + K(T) \cdot \frac{\Theta}{\Theta_{max} - \Theta} \right)^{-1} \quad (4.6)$$

Here,  $S_0$  is the initial sticking coefficient, and the Kisliuk parameter,  $K$ , describes the ratio of the desorption and chemisorption rates from the physisorbed precursor<sup>106</sup>. The desorption constant can be expressed with<sup>107</sup>:

$$D = D_0(T) \cdot \exp\left(-\frac{E_a(\Theta)}{k_B T}\right) \quad (4.7)$$

$D_0(T)$  is the preexponential factor and  $k_B$  the Boltzmann constant. It has been shown by Kinne et al., that the adsorption energy  $E_a$  linearly decreases with coverage<sup>54</sup>:

$$E_a(\Theta) = E_0 + E_1 \cdot \Theta \quad (4.8)$$

Based on these considerations, the desorption behavior can be modeled, with the fit parameters  $E_0$ ,  $E_1$  and  $D_0$ , and the adsorption behavior with  $j \cdot S_0$ ,  $K$ .

For the fitting the desorption behavior in Figure 4.32 and 4.33b, we constrained the value for the adsorption energy  $E_0$  to be 1.43 eV and the

coverage dependent term  $E_1$  to be -0.65 eV, i.e. to the values obtained by Kinne et al. for the low temperature data (375 - 450 K). Using these values, we obtain a consistent fit to the complete data set, i.e. also the data measured with the new approach for higher temperatures, the prefactor  $D_0$  is in the range of  $1 \cdot 10^{14.8 \pm 0.3} \text{ s}^{-1}$ . The fit results are indicated as red lines in the Figures. The derived prefactor compares very well to the value of  $2 \cdot 10^{15 \pm 1} \text{ s}^{-1}$  determined by Kinne et al. for the much smaller temperature range from 375 to 450 K<sup>45</sup>. The good agreement over the large temperature range is strong evidence for the reliability of the data obtained by the new approach and also shows that the intermolecular interaction ( $E_2$ ) is not temperature dependent, at least in the simple model used here.

To describe the adsorption behavior, Equation 4.5 was fitted with the constraint of a temperature independent value for  $j \cdot S_0$ , which is justified considering the small temperature interval from 460 to 490 K; for  $E_0$  and  $E_1$  the values determined above (1.43 and 0.65 eV) were used and  $D_0$  was allowed to vary within the above denoted error bars. The Kisliuk parameters were determined as a function of temperature from former experiments<sup>45</sup>, yielding values of 0.80, 0.84 and 0.87 for the 460, 480 and 490 K, respectively. The corresponding fit results, shown as red lines in Figure 4.32, are in excellent agreement with the experimental data.

Finally, the potential and limits of our new approach has to be addressed. The data in Figure 4.31a and b has been collected with a time resolution (dwell time) of 500  $\mu\text{s}$ . From this experiment, the smallest reasonable time resolution, i.e. dwell time, can be interpolated (cf. table 4.1). The count rate in this experiment is  $\sim 400.000 \text{ cps}$  ( $\sim 200 \text{ cts/channel}$  in 500  $\mu\text{s}$ ), but with a higher photon flux or lower energy resolution count rates of up to 5 Mcps are possible when using channeltrons (nonlinearity  $< 5\%$ ; total deadtime incl. electronics: 70 ns). With a reasonable number of counts per time step, which we propose to be 100 cts/channel (with the signal to be 10%) and by an increase of the total measuring time by a factor of 2 (200 instead of 100 repetitions, yielding a total time for a complete experiment of 4000 s), a factor of  $\sim 25$  in time resolution can be gained. Thus from technical side, a time resolution of  $\sim 20 \mu\text{s}$  appears feasible. Please note that if the signal is stronger (e.g. for metal adsorbates due to the much higher photoionization cross sections), even lower times might be possible.

cps	$\Delta t$ [ $\mu\text{s}$ ]	cts	rpt	$\Sigma\text{cts}$
400.000	500	200	100	20.000
400.000	10	4	100	400
5.000.000	10	50	100	5.000
5.000.000	10	50	400	20.000

**Table 4.1:** Different scenarios for enhancing the count rate and the intensity to improve the time resolution. cps : counts per second,  $\Delta t$  : time resolution, cts : counts, rpt : repetitions,  $\Sigma\text{cts}$  : resulting counts per second

## 4.7.2 Simulation

During the work on this new method the question of the influence of the perturbation caused by the adsorption came up. In this section the ideas to answer these questions are discussed. From perturbation theory it is known that a system that is disturbed tries to compensate this perturbation as quickly as possible. If the perturbation is sufficiently small the characteristic time of the perturbation and the time for the subsequent relaxation have to be the same.

Interestingly the desorption takes longer than the adsorption and the question is now at which temperature the disturbance is small enough so that both times are equivalent. For this a simulation was made with all the parameters obtained from the previous analysis only raising the temperature. The corresponding coverage was taken from an exponential fit of the dependency of the coverage and the temperature in Figure 4.30b. The resulting adsorption and desorption lines are presented in Figure 4.34. From this data the difference of the area below the adsorption and the desorption is plotted against the temperature and is presented in Figure 4.35. At 750 K no difference between these two areas is visible. This shows that at 750 K and higher the disturbance is so small that the system shows an ideal behavior in view of perturbation theory.

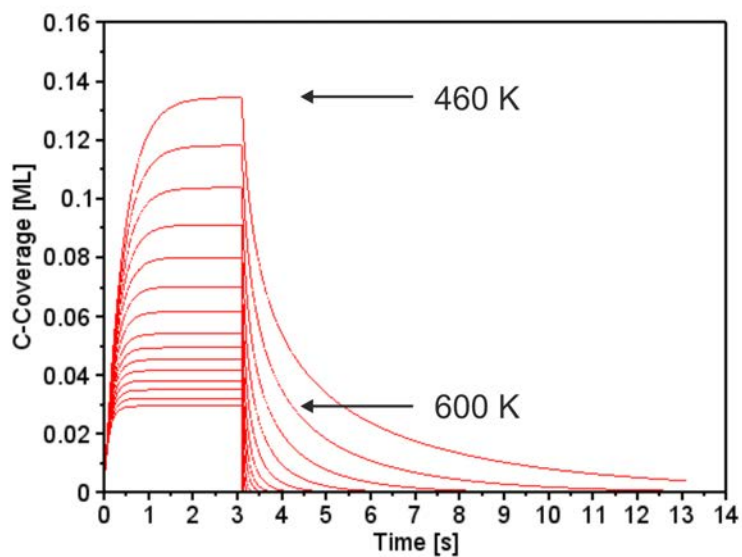


**Figure 4.34:** Simulated adsorption and desorption curves for different temperatures from 460 to 600 K

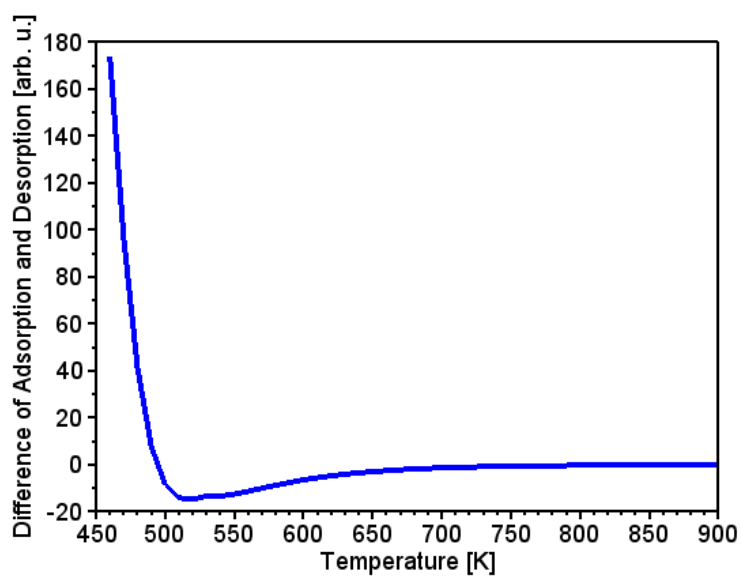


**Figure 4.35:** Difference in area beneath the adsorption and desorption part from figure 4.34

## 4.8 Conclusion

### 4.8.1 CO Oxidation on nickel oxide

The growth of nickel oxide supported by Pd(100) were studied in situ by HR-XPS and a clear difference between the first and second layer was found. Films of different thickness, reaching from 0.5 up to 6 ML, were studied towards the interaction with CO, leading to the insight that this reaction is thickness dependent in the way that thicker films are not reactive. For the 1 ML and 2 ML thick nickel oxide films, a kinetic analysis is presented with respective models showing that the activation energy for the 2 ML thick film is less than for the 1 ML thick film. Furthermore, the 2 ML thick films were reoxidized and afterwards reduced again. It was not possible to completely reduce these films again due to the change in the film structure. The reoxidized nickel formed clusters.

### 4.8.2 CO Adsorption and Desorption at higher temperatures

A new approach for ultrafast XPS to investigate surface processes is presented. It is based on a conventional XPS setup with a channeltron-based electron energy analyzer and uses a modified signal processing unit, allowing for measurements in the  $\mu\text{s}$  regime. First measurements with an time resolution of 500  $\mu\text{s}$  allow to study the adsorption and desorption of CO on a Pt(111) surface at significantly higher temperatures and significantly higher pressures than were previously possible, i.e., up to 500 K and  $2 \times 10^{-6}$  mbar. By comparing results obtained below 450 K by using the conventional XPS detection mode, i.e., the classical swept mode, to the results above 450 K obtained with our new approach, i.e. ultrafast measurements at a fixed energy, the reliability of this new technique was demonstrated. From a detailed analysis of the desorption data it is shown that the simple assumption of a linear decrease of the adsorption energy with coverage is leads to consistent results for the temperature range from 375 to 500 K. From a critical evaluation of the experimental parameters and boundary conditions, it can be extrapolated that under favorable condition (i.e. high photoionization cross section of the investigated core levels and high photon flux) a time resolution of 20  $\mu\text{s}$  or below seems feasible.

# Chapter 5

## H<sub>2</sub>O

### 5.1 H<sub>2</sub>O on Pd(100)

Adsorbing water on the clean Pd (100) surface was already discussed in literature<sup>51,108–113</sup>. It was shown that water adsorbs molecularly with a layer-by-layer growth on the (100)<sup>108</sup> and (111)<sup>51</sup> surfaces. DFT calculations support the results from these previous experiments adding the fact that the reaction barrier for water dissociation on the Pd surface is 1.12 eV. Due to this high barrier it is more likely that water desorbs than that it dissociates. On the Pd(111) surface, water stays intact to a desorption temperature of 163 K; on the oxygen precovered surface the desorption temperature is increased to 177 K but the preadsorbed oxygen partly reacts at 155 K to a mixed H<sub>2</sub>O/OH overlayer<sup>51</sup>. This mixed H<sub>2</sub>O/OH overlayer is also found on the oxygen precovered Pd(100) surface. Stuve et al studied the dependency of the amount of hydroxide to oxygen, revealing a decrease of hydroxide at higher oxygen coverages (>0.2 ML) due to blocking of the reaction sites by oxygen atoms<sup>108</sup>.

#### 5.1.1 Adsorption

During the adsorption of water on the surface at 120 K in the O 1s region a broad peak becomes visible at 532.8 eV that shifts to 534.0 eV at 4.2 L (see Figure 5.1). A close examination of the spectra shows three contributions. For the clean surface, the Pd 3p<sub>5/2</sub> peak with a binding energy of 532 eV (orange line) is shown in Figure 5.1. After the exposure of 0.4 L, a peak at 532.8 eV rises. The peaks shift 1.2 eV to higher binding energies during

adsorption. As it is known that water forms multilayers<sup>51</sup> the binding energy of 534.0 eV is considered as the binding energy of water multilayers. Because of the large full width at half maximum no statement solely from the spectra is made and a deconvolution of the spectra is necessary.

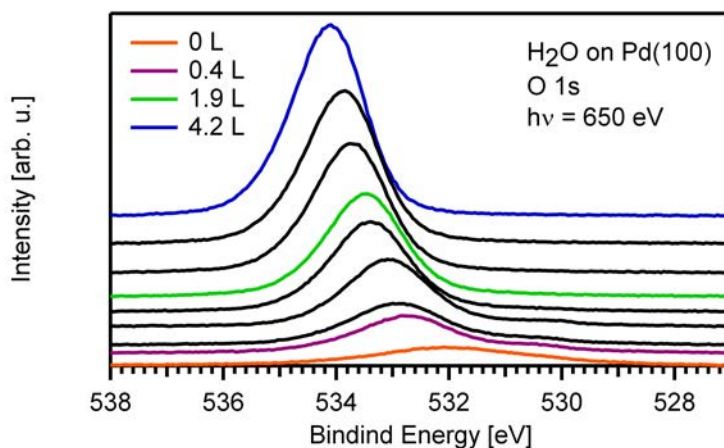


**Figure 5.1:** Spectra of the adsorption of the adsorption of water on Pd(100)

An example for this deconvolution is shown in Figure 5.2. The Pd 3p<sub>3/2</sub> peak is visible at the binding energy of 531.9 eV (grey curve). In addition, a small peak due to hydroxide is observed at 530.2 eV (green). The bright blue line describes the water monolayer at 532.4 eV and the dark blue line the water multilayer with a peak at 533.5 eV. At higher coverages the water multilayer peak shifts by 500 meV to 534.0 eV.

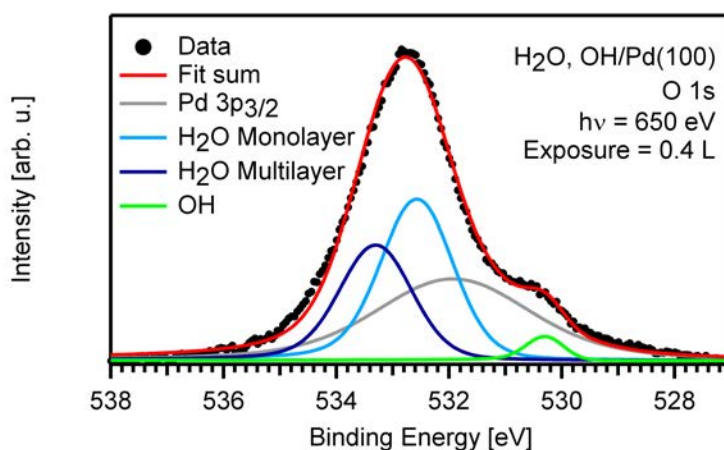


**Figure 5.2:** Spectrum and fit of water adsorbed on Pd(100)

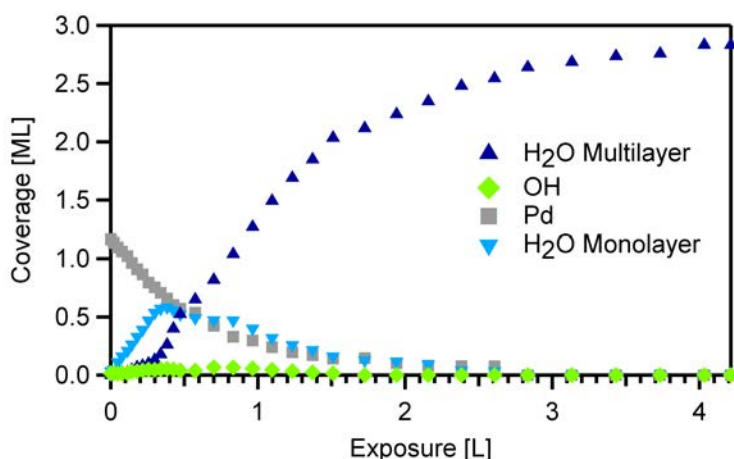


**Figure 5.3:** Quantitative analysis of the adsorption of water on Pd(100). Guides to the eye added to underline the layer by layer growth at 120 K.

The quantitative analysis of the XP spectra in Figure 5.1 is presented in Figure 5.3. Initially, only the water monolayer adsorbs up to an exposure of 0.3 L; it saturates at 0.6 ML. After this, the multilayer adsorbs and at 4 L it is the only visible species. A close look to the Figure 5.3 shows that directly after saturation of the first layer the second layer starts to grow. This means that the first layer is closed completely before the next layers adsorb. From  $\sim 0.5$  L on, all other signals are damped by the multilayers.

The Pd 3d spectra before and after water adsorption are presented in Figure 5.4. Before water adsorption, three peaks are visible: The peak at 335.1 eV is assigned to the bulk peak<sup>51</sup>. The other two peaks at 334.6 and 335.6 eV describe atoms in the topmost layers. The peak at 334.6 eV is due to atoms in the top most layer while the peak at 335.6 eV stems from the atoms in the second layer<sup>51</sup>. After the adsorption of water the peak at 334.6 eV is gone, in line with the proposed model. A peak at 335.6 eV is still visible, but by comparison to other adsorption experiments it is not assigned to the second layer atoms. This becomes clear by a comparison to the adsorption of acetylene on Pd (100) (Section 6.1), because in this experiment the second surface peak vanishes while another peak with nearly the same parameters rises exactly at the same binding energy. Here a similar behavior is probable, which would mean that the interaction of water with palladium leads to a peak at 335.6 eV.

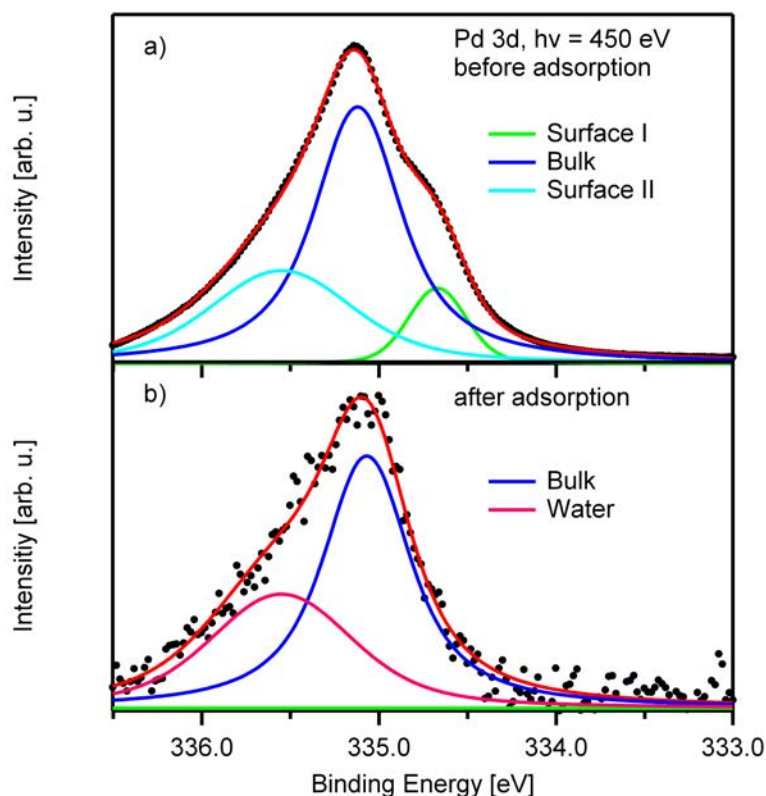


**Figure 5.4:** Pd 3d signal a) before and b) after adsorption of 4 L water on Pd(100)

### 5.1.2 Reaction

The desorption temperature of water from a clean Pd (100) surface was determined by Stuve et al<sup>108</sup> with TPD experiments to 160 K. At 120 K only the multilayer peak at 534.0 eV is visible in the O 1s spectra and above 170 K only the overlaying Pd 3p<sub>3/2</sub> peak at 532 eV appears. This shows that the desorption temperature of the monolayer (532.8 eV) and the multilayer is nearly the same, because otherwise a monolayer peak has to show up as mentioned by Gladys et al<sup>51</sup>. The quantitative analysis is presented in Figure 5.5 and confirms the finding of the similar desorption temperature of the multi- and monolayer. The previously observed small hydroxide signal is not found after the desorption of water, which could mean that the hydroxide is only a local and temporal dissociation of water to hydrogen and hydroxide due to the intense synchrotron radiation. Please note that the amount of beam damage was reduced by shifting the sample during both the adsorption and reaction experiments.

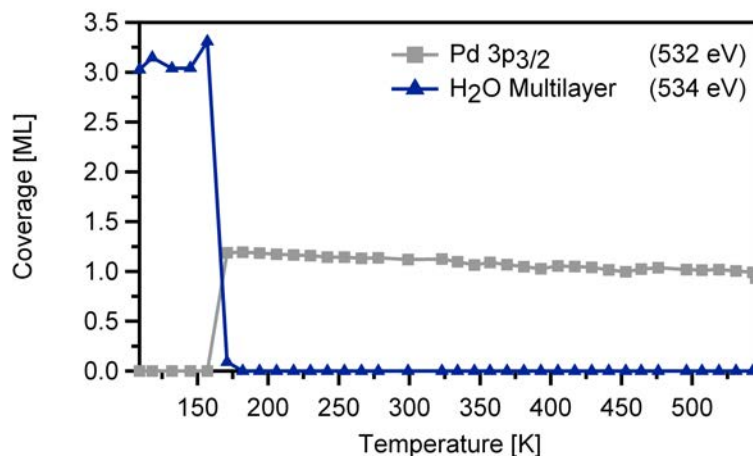


**Figure 5.5:** Quantitative analysis of the desorption of water from Pd(100)

## 5.2 H<sub>2</sub>O on O/Pd(100)

### 5.2.1 Adsorption

The adsorption of water on a surface precovered with 0.25 ML oxygen is discussed in this section. Note that the adsorbed layer contains 0.18 ML O and 0.06 ML OH. The corresponding density plot is depicted in Figure 5.6 a), in b) one representative spectrum with the respective fits is shown. From the density plot two main features are recognizable, the first one at a binding energy 530 eV and the second and bigger one at 532 eV. The latter shifts to higher energies with exposure. The deconvolution of the spectra reveals a binding energy position of the oxygen peak of the preadsorbed oxygen at 529.5 eV and the hydroxide peak at 530.3 eV. The water monolayer is measured at a binding energy of 532.3 eV and the multilayer shows up at 533.0 eV whereas the palladium peak is located at 532 eV. These values are similar to the measurements of water on oxygen precovered Pd(111)<sup>51</sup>.

The quantitative analysis of this adsorption experiment is shown in Figure 5.7. Oxygen and hydroxide stays constant at 0.18 ML and 0.07 ML respectively over the whole adsorption experiment. Interestingly, the saturation of the water monolayer is 0.76 ML after 0.7 L. This result is in contrast to the adsorption on a clean surface where only 0.6 ML form the monolayer. Another difference is the start of the growth of the multilayer which occurs at an exposure, when the monolayer still increases significantly. A reason for

this could be Stranski-Kastranov growth. The formation of 3D islands would also correspond with the slow decrease of the O and OH signals.

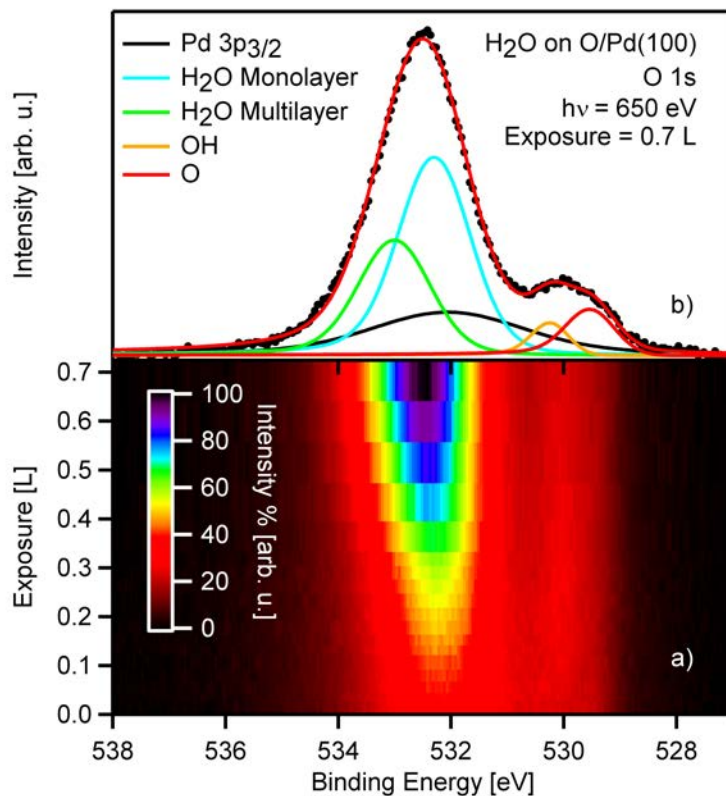


**Figure 5.6:** Adsorption of H<sub>2</sub>O on O/Pd a) density plot b) selected spectrum with fitted peaks

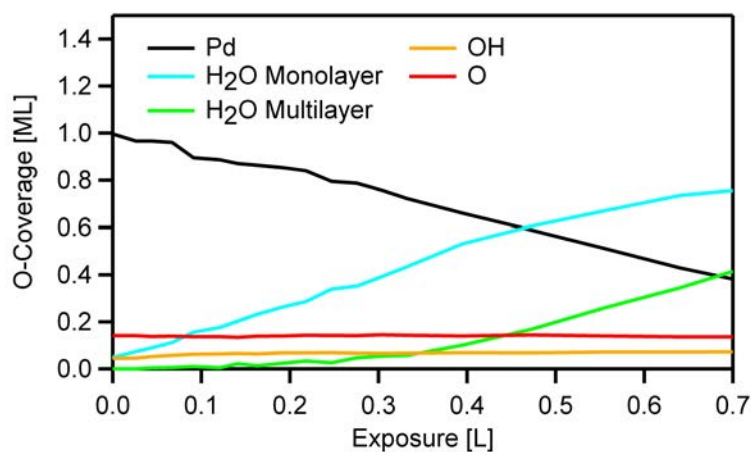


**Figure 5.7:** Quantitative analysis of the adsorption of water on oxygen precov-ered Pd(100)

### 5.2.2 Reaction

The density plot and one representative spectrum of the reaction of adsorbed H<sub>2</sub>O on oxygen precovered Pd(100) surface is shown in Figure 5.8. Here the color coded density plot reveals a massive loss in the intensity of the signal at 533 eV at the temperature of 160 K. As mentioned above this signal consists mainly of the multilayer of water and its loss is due to desorption. This desorption temperature was also found on the O/Pd(111) system<sup>51</sup>. An additional feature at the binding energy of 530.3 eV is formed, which is identified as hydroxide<sup>51</sup>. This feature decreases in intensity up to a temperature of 270 K till it is gone and only the palladium peak at 532 eV and the oxygen at 529.5 eV remains visible. The single spectrum presented in Figure 5.8 shows the same deconvoluted parts as discussed in the previous section.

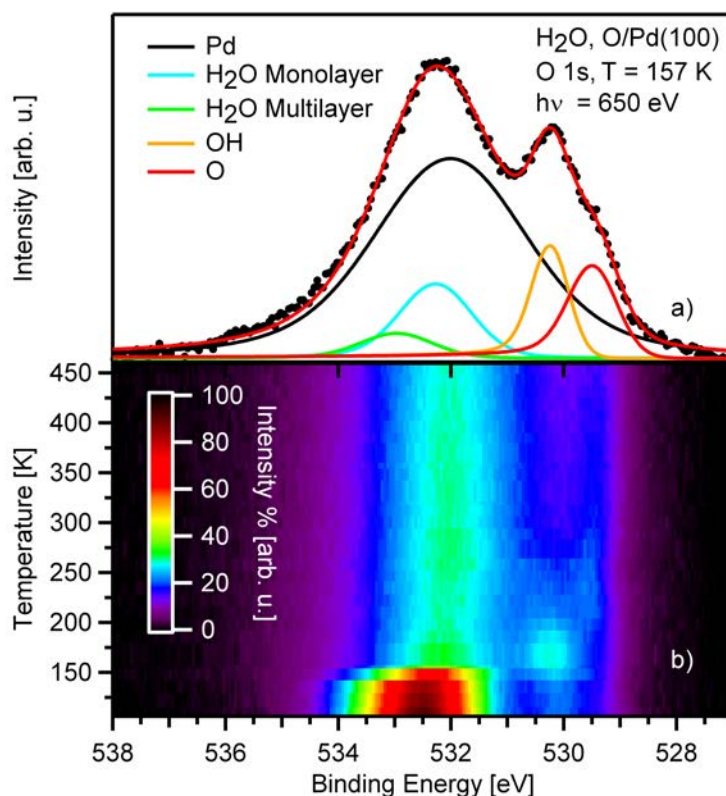


**Figure 5.8:** Reaction of water on O/Pd(100) in the O 1s. The oxygen precoverage is 0.25 ML oxygen and partially hydroxide.

The quantitative analysis (cf. Figure 5.9) of this experiment reveals that at first the multilayer desorbs at 150 K and the monolayer of water at 160 K, which is in good agreement with literature<sup>51,108</sup>. At 160 K, an increase in

hydroxide is found. Water dissociates to OH and hydrogen, because the amount of oxygen stays constant at 0.18 ML over the whole experiment, while the hydroxide amount rises to a maximum (0.14 ML) at 180 K and then gets less and less till 270 K where it is not visible any more. A model is proposed in Figure 5.10 for the formation of hydroxide on the O/Pd(100) surface, which is based on calculations<sup>112</sup>. Here, the water adsorbs on the surface next to an oxygen atom at low temperatures forming a hydrogen bond. At higher temperatures this bond is transformed to two hydroxide molecules on the surface. Stuve et al<sup>108</sup> proposed a recombination of these hydroxide molecules to water which desorbs immediately. From the here presented data this model can be confirmed.

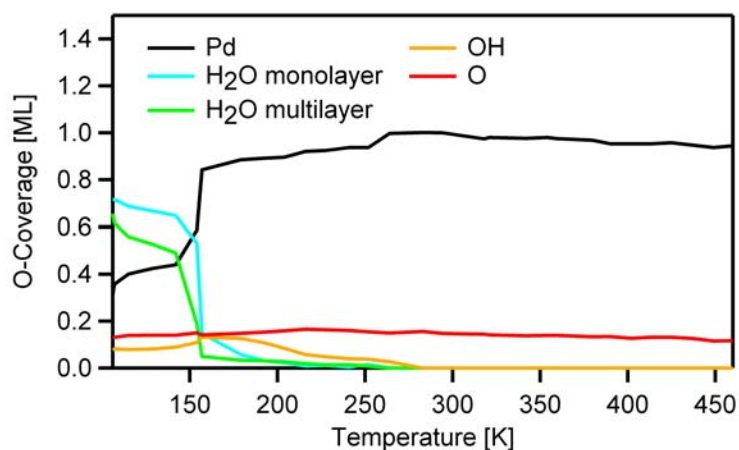


**Figure 5.9:** Quantitative analysis of the reaction of H<sub>2</sub>O on O/Pd(100)

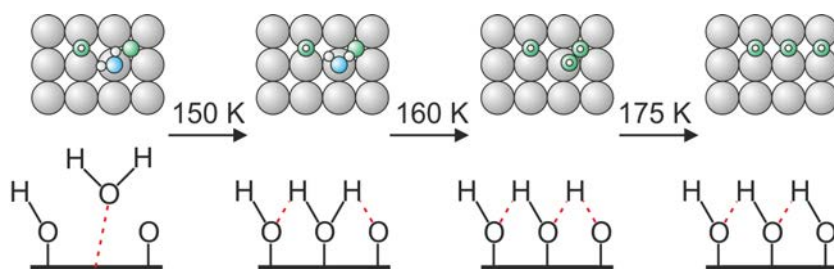


**Figure 5.10:** Reaction scheme H<sub>2</sub>O on O/Pd(100). Large Gray: Pd; Small Gray: Hydrogen; Green and Blue is oxygen, green for hydroxide and oxygen and blue for water. According to [108].

## 5.3 H<sub>2</sub>O on NiO/Pd(100)

Water adsorption and reaction was also studied on nickel oxide by experiments<sup>114,115</sup> and by calculations<sup>116,117</sup>. Reissner and Schulze investigated the adsorption of water multilayers and observed a phase transition of the multilayer at 143 K from an amorphous phase to an ordered phase. They found that water adsorbs molecularly on a perfect NiO(100) surface. On reactive sites like kinks and steps, however, water dissociates. In agreement with these results, Simpson et al<sup>116</sup> described the adsorption and dissociation of water on NiO(100) and MgO(100). On both surfaces water dissociates only on the steps. By EELS Cappus et al<sup>118</sup> showed that water dissociates to OH on NiO only on the steps. Yu et al<sup>117</sup> studied the adsorption configuration of water on NiO by DFT and came to the conclusion that water mainly binds to the nickel atoms. From these studies it becomes obvious that the product of water dissociation, OH, is a very important intermediate that is always present due to the existence of steps and kinks; here several studies have been done<sup>118,119</sup>, e.g. by Hoppe et al<sup>119</sup>, who studied different nickel hydroxides by XPS.

For the following discussions one has to mention that all the adsorption experiments were performed at 150 K to inhibit the adsorption of a water multilayer and to form crystalline ice which is formed at an temperature higher than 143 K<sup>114,115</sup>.

### 5.3.1 1 ML

#### 5.3.1.1 Adsorption

The XP spectra of the adsorption of water on 1 ML nickel oxide at 150 K are shown in Figure 5.11, where two representative spectra and the density plot are depicted. The first spectrum shows the O 1s spectrum of a clean 1 ML thick nickel oxide film. Two contributions are visible, the oxygen from the oxide film (529.2 eV) and the Pd 3p peak at 532.2 eV. The binding energy of the oxygen film is similar to the binding energy of oxygen on pristine palladium indicating a strong interaction with palladium. The fit of this spectrum reveals a third contribution which is located at 530.0 eV and is identified as hydroxide due to a comparison of the spectrum in Section 4.2. During the adsorption of H<sub>2</sub>O, a new peak at 532.6 eV evolves, and the

hydroxide peak shifts to a binding energy of 530.5 eV. A shift depending on the coverage is very common for molecules on metal substrates, but the value of 500 meV is considered as too high. It is proposed that the shift originates from the formation of a different adsorption site for OH.

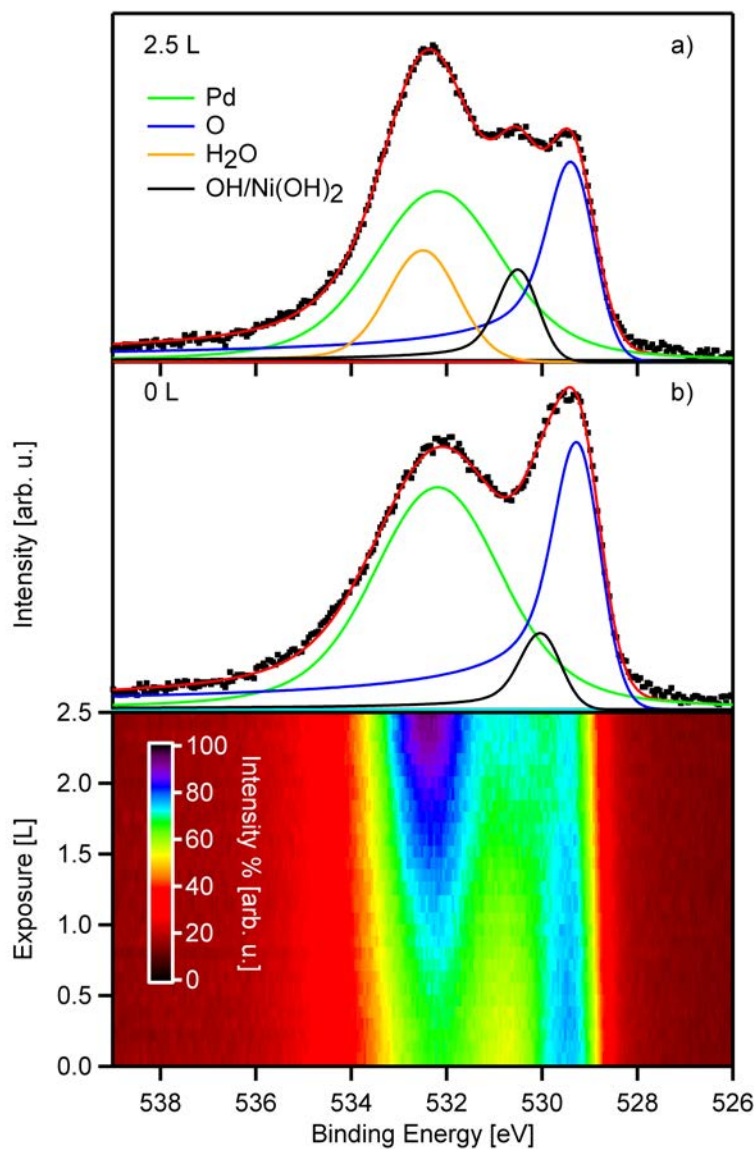


**Figure 5.11:** Adsorption of water on a 1 ML thick NiO film on Pd(100). a) and b) at the depicted exposures and c) color coded density plot

The quantitative analysis (see Figure 5.12) reveals that the oxygen amount before the adsorption experiment is 0.5 ML which is expected for the first layer of nickel oxide (wetting layer). The monolayer of water is saturated at 0.25 ML. As mentioned above, the monolayer of NiO on Pd(100) has a

stoichiometry of Ni<sub>3</sub>O<sub>4</sub> which leads to a Ni-coverage of 0.375 ML (and a "coverage" of nickel vacancies of 0.125 ML). Interestingly, the hydroxide amount is 0.1 ML. This fits very well to the nominally 0.125 ML of nickel vacancies, possibly binding to the Pd atoms underneath. After the adsorption of water, the amount of OH rises to 0.16 ML. This could be now additional hydroxide on the nickel because Yu et al<sup>117</sup> found out that on nickel oxide water adsorbs mainly on the nickel and the additional hydroxide is probably related to dissociated water. Coming back now to the shift of the hydroxide peak, it is explained by the changed adsorption site. In the beginning hydroxide adsorbs on palladium in the nickel vacancies giving a similar signal than OH on palladium. At higher exposures the OH from dissociated water adsorbs on nickel sites on the nickel oxide film. OH on nickel has a binding energy of 531.0 eV<sup>120</sup>. The here measured peak at 530.5 eV is a superposition of the 530.0 eV of OH on Pd and 531.0 eV from OH on Ni.

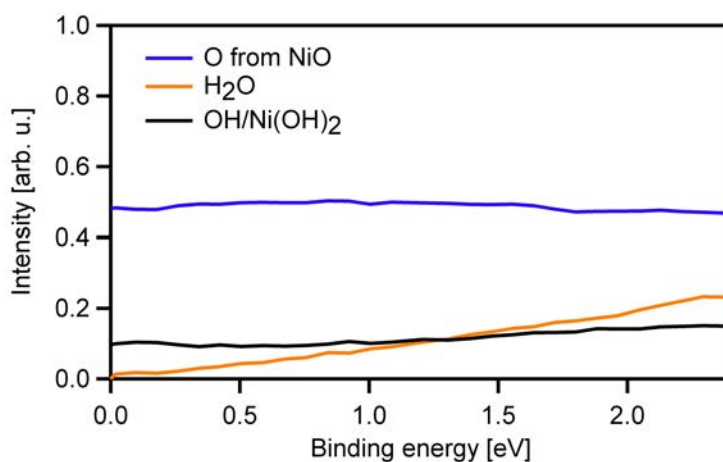


**Figure 5.12:** Quantitative analysis of the H<sub>2</sub>O adsorption on 1 ML thick NiO/Pd(100)

### 5.3.1.2 Reaction

The XP spectra of the reaction of water with a 1 ML thick nickel oxide layer are shown in Figure 5.13. Here, also a density plot with representative spectra is presented. From the density plot, it becomes obvious that only desorption takes place. The spectrum at the beginning of the heating ramp shows the same peaks as described during the adsorption and at the end of the heating ramp the spectrum looks like no water was adsorbed on the nickel oxide before. The last spectrum shows still a hydroxide peak, but

this is not surprising because the nickel hydroxide reacts to nickel oxide only above a temperature of 450 K (cf section 4.5.3), which is not reached in this experiment. The quantitative analysis is presented in 5.14.

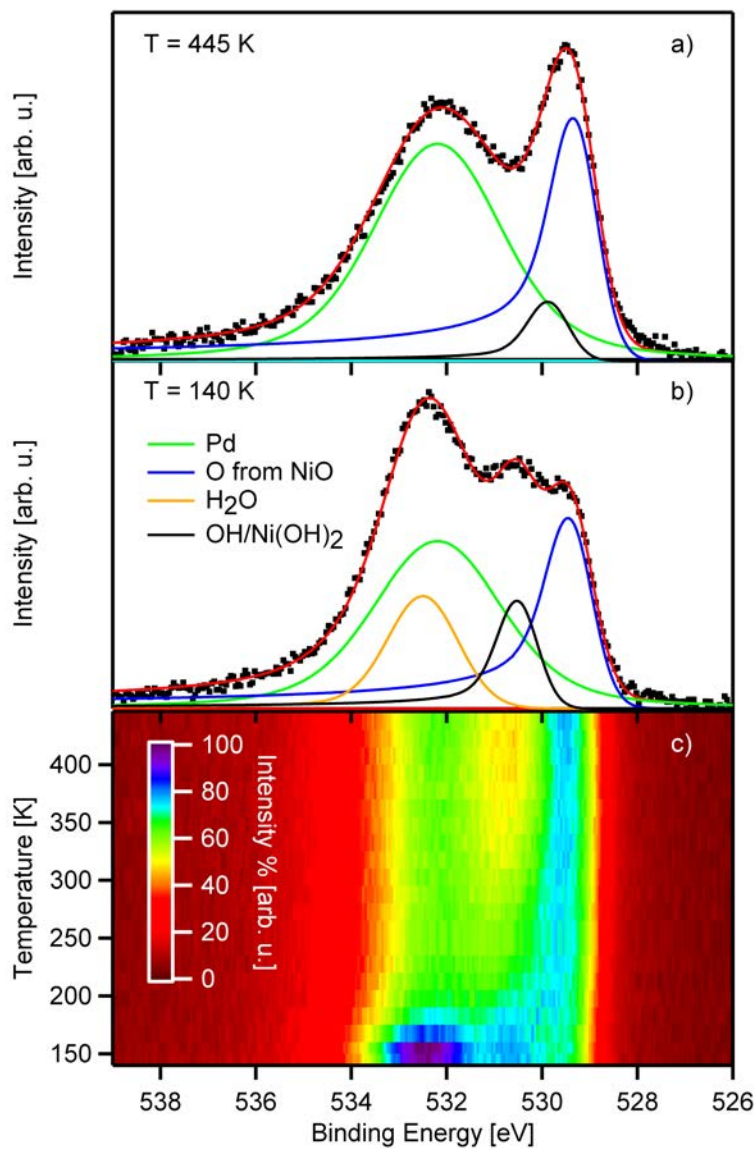


**Figure 5.13:** XPS spectra of the reaction of water adsorbed on the nickel oxide wetting layer on Pd(100); respective spectra a) before and b) after the temperature evolution and c) the density plot

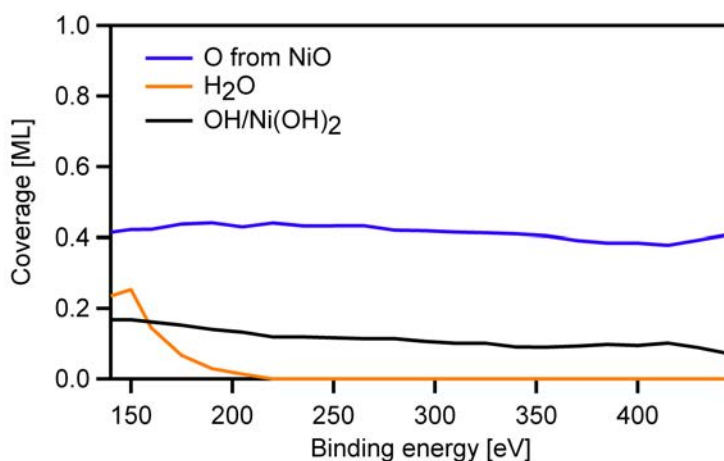


**Figure 5.14:** Quantitative analysis of the reaction of water adsorbed on the nickel oxide wetting layer on Pd(100)

### 5.3.2 2 ML

#### 5.3.2.1 Adsorption

The adsorption experiment of H<sub>2</sub>O at 150 K on a 2 ML nickel oxide film is depicted in Figure 5.15 as a density plot. At low exposures (0 L) two contributions are visible. The first is found at an energy of 529.7 eV while the other is located at 532 eV. These peaks belong to the oxygen of the nickel oxide and the Pd 3p peak of the substrate, respectively. As soon as water is adsorbed (1 L) on the nickel oxide, a shift of the oxygen peak by 0.3 eV to a lower binding energy occurs. This shift is interpreted as the effect of the water on the oxygen from the nickel oxide film and is modeled by an additional peak called O\*. At 531.3 eV a Ni(OH)<sub>2</sub> peak arises, which is also identified by literature<sup>120,121</sup>. The hydroxide peak also shifts by 0.5 eV to a lower binding energy. The reason for this could either be the change of the adsorption site due to the effect of adsorbing water or to an effect similar to the shift in the binding energy of the oxygen atoms mentioned above. The water peak grows at 532.6 eV.

The quantitative analysis shown in Figure 5.16 reflects the behavior described before. At first the oxygen from the nickel oxide film (1 ML) decreases due to damping and a change to O\*, which saturates at 1 ML. The water saturates at an coverage of 1 ML. Both the water and the O\*-species have a similar growth behavior suggesting a correlation of the amount of water

and the formation of the O<sup>\*</sup>-species. The Ni(OH)<sub>2</sub>-Species adsorbs to a saturation coverage to 0.4 ML at 2.0 L.

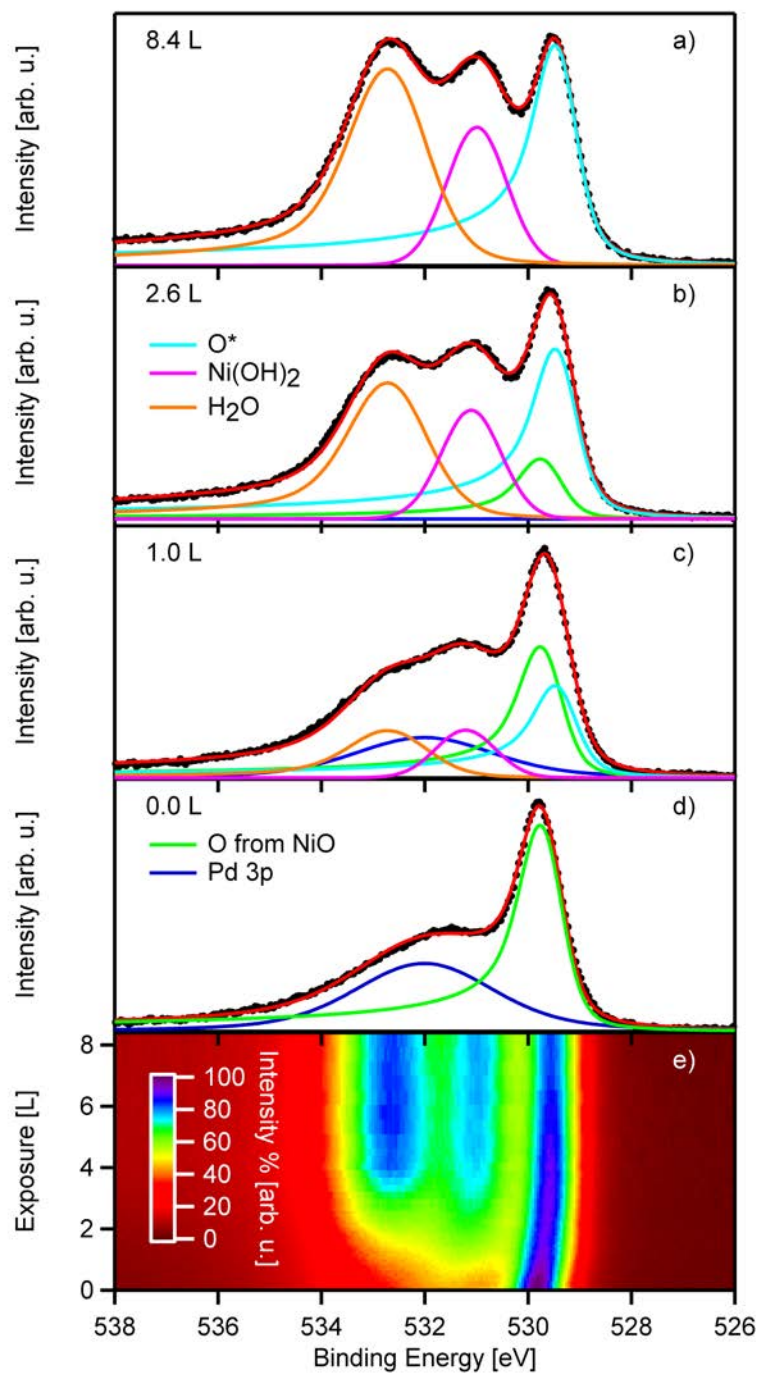
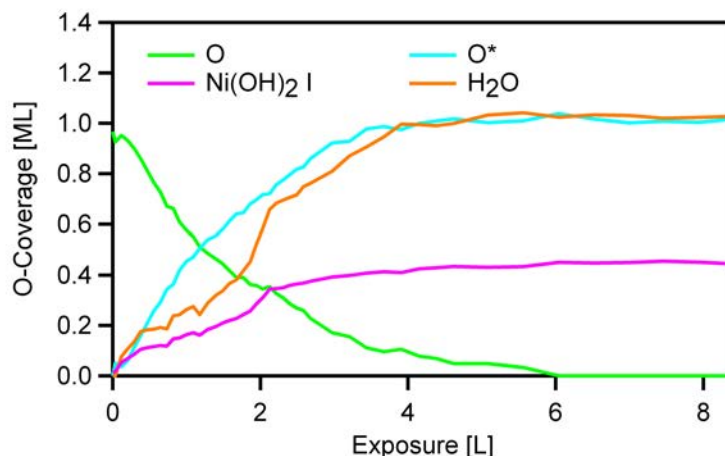


Figure 5.15: Adsorption of water on 2ML NiO at 150 K.



**Figure 5.16:** Quantitative analysis of the adsorption of water on the 2ML NiO

### 5.3.2.2 Reaction

After the adsorption of water on 2 ML thick nickel oxide film the system is heated and analyzed by XPS in situ. The density plot and representative spectra are shown in Figure 5.17. In the density plot no reaction altering the nickel oxide film is seen, confirmed by the analysis of the spectra. At 150 K, the spectrum looks like the last spectrum of the adsorption with three species visible. The first species is O\* at 529.4 eV, the second is Ni(OH)<sub>2</sub> at 531.0 eV and the last one is the water at 532.6 eV. By heating the crystal all these species desorb/disappear at different temperatures generating a result similar to a pristine nickel oxide film at 500 K (not shown). This is better recognizable in the quantitative analysis which is presented in Figure 5.18.

At first the water starts to desorb at a temperature of 160 K. As soon as the water disappears also the Ni(OH)<sub>2</sub> shifts in binding energy. This is the reversed process observed in the adsorption above where additional OH adsorption leads to a different binding energy. Now the OH desorbs probably as recombined water and the binding energy shifts back. At 180 K, the O\*-species decreases while the oxygen from the nickel oxide film rises again. And at 370 K no water is found and the last traces of the hydroxide are gone at 470 K. A minor change in the oxygen amount can be attributed to a healing of the nickel oxide film.

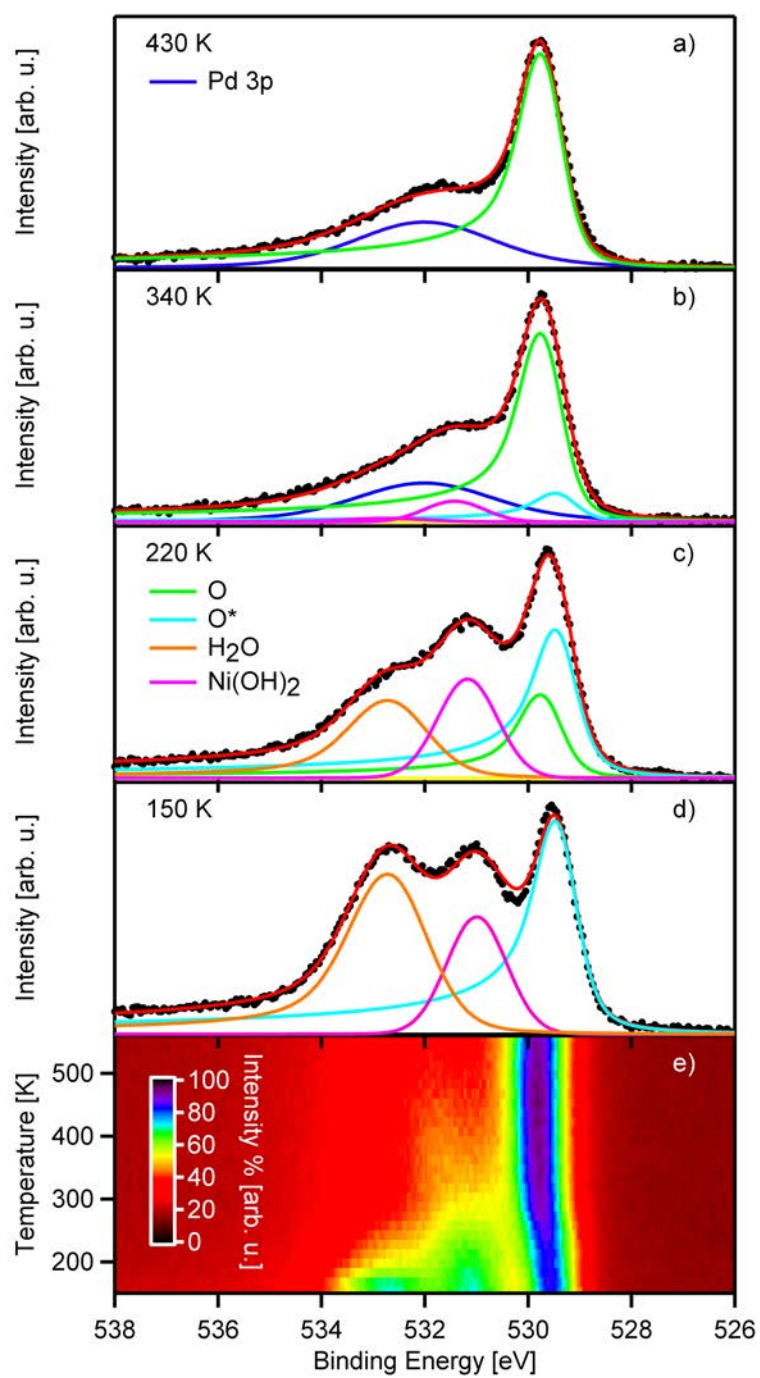


**Figure 5.17:** Representative spectra and density plot of the reaction of 1 ML water on a 2 ML NiO film on Pd(100)

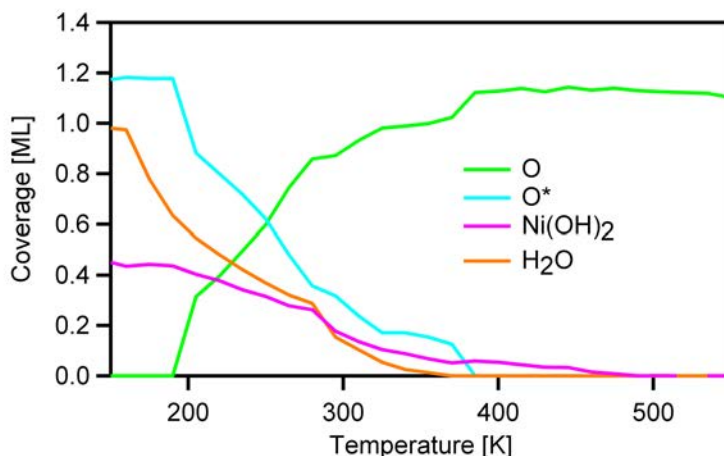


**Figure 5.18:** Quantitative analysis of the reaction of 1 ML water on a 2 ML NiO film on Pd(100)

### 5.3.3 6 ML

#### 5.3.3.1 Adsorption

The adsorption of H<sub>2</sub>O on a 6 ML - bulk like - nickel oxide film is depicted in Figure 5.19. Here the density plot shows a sharp feature at 529.7 eV and an evolving broad feature 531.3 eV. The sharp feature is oxygen from nickel oxide and the small broad feature in the beginning (0 L) is hydroxide (531.3 eV) adsorbed from the residual gas in the chamber during the deposition. At 0.6 L three new peaks evolve: the first at the binding energy of 529.4 which is identified as O\* as mentioned before. The next one is at the binding energy of 531.0 eV and is labeled as hydroxide as described above and the last is measured at 533.1 eV which is identified as water. All three peaks shift to a lower binding energy with higher exposure as seen before.

The quantitative analysis shown in Figure 5.20 is similar to the water adsorption on 2 ML thick nickel oxide film, besides the shift of the water and OH contributions at higher exposures (2.6 L). In the quantitative analysis the amount of oxygen is found to be 4 ML where it should be only 3 ML in a perfectly grown nickel oxide film with a 1:1 ratio between nickel and oxygen and a film thickness of 6 ML. This discrepancy is attributed to the higher roughness and therefore higher number of oxygen terminated steps and kinks of the nickel oxide film<sup>31</sup>. First the 4 ML of the clean nickel oxide film decrease to 1 ML while O\* grows to 2 ML. The initial coverage of Ni(OH)<sub>2</sub> is 0.9 ML and after growth it saturates at an exposure of 1 L at a

coverage of 1.8 ML. At 0.2 L water starts to adsorb with saturation at 0.9 L and coverage of 1.8 ML. As soon as this saturation coverage is reached the amount of water declines by 0.2 ML while the water peak shifts to a lower binding energy ( $\sim 0.4$  eV). The water amount stays constant at 1.6 ML. An explanation for this behavior could be a reordering in the ice film.

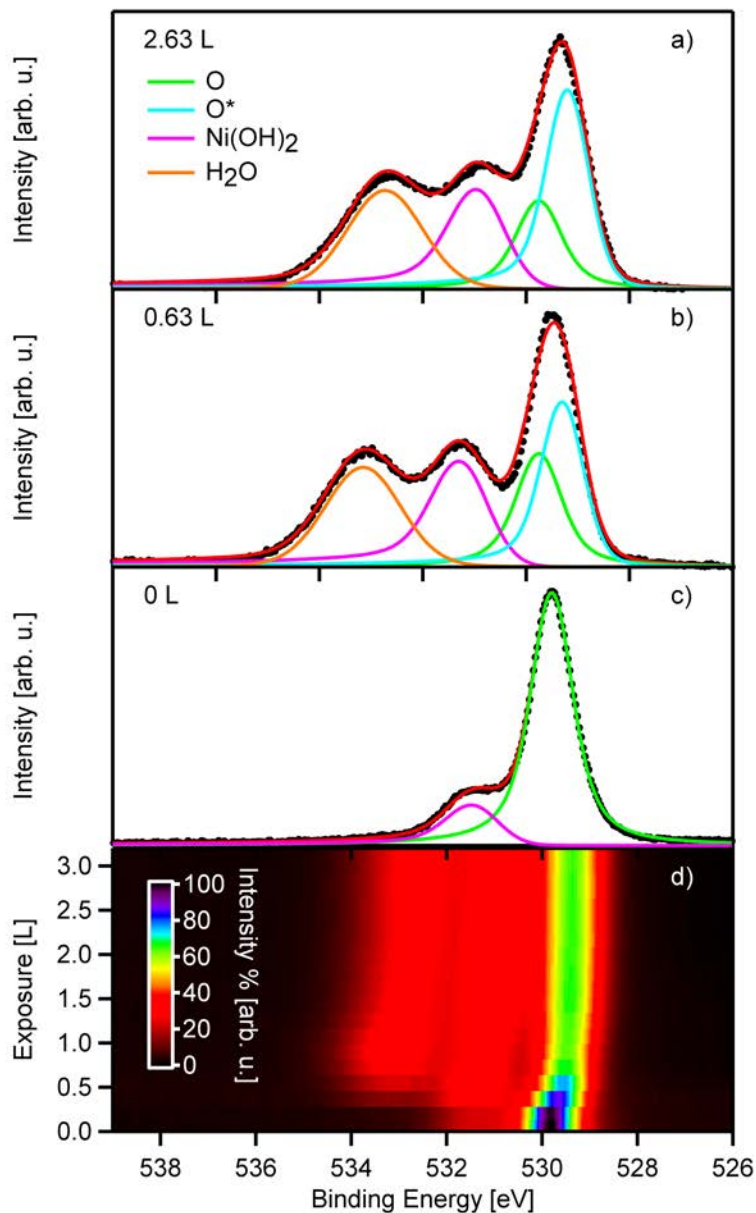


**Figure 5.19:** Representative spectra and density plot of the adsorption of H<sub>2</sub>O on 6ML NiO

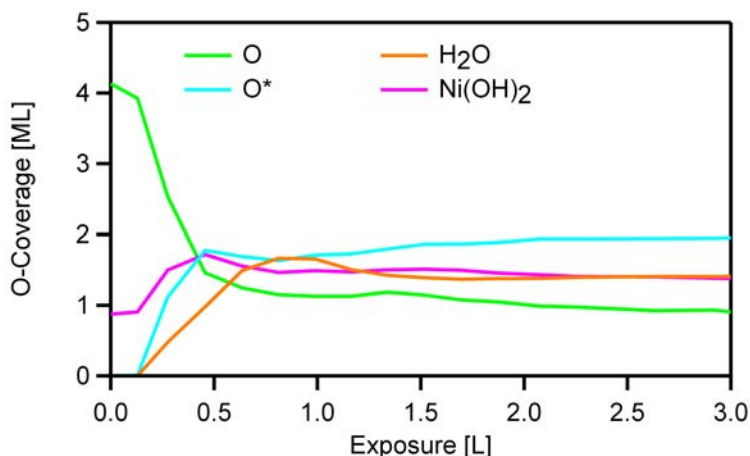


**Figure 5.20:** Quantitative analysis of the adsorption of H<sub>2</sub>O on 6ML NiO

### 5.3.3.2 Reaction

The reaction of water on this nickel oxide film is presented in Figure 5.21. From the density plot three distinct peaks are recognizable. The first at 529.4 eV, the second at 531 eV and the last at 533 eV. These three peaks were identified as O\*, Ni(OH)<sub>2</sub> and H<sub>2</sub>O respectively as shown in the previous section. In the following the thermal evolution is discussed together with the quantitative analysis shown in Figure 5.22. Interestingly, the amount of O\* increased by 0.3 ML while the amount of water decreased by 1.3 ML between the adsorption and thermal evolution experiment. The Ni(OH)<sub>2</sub> species introduced in the last section was found in the beginning at an binding energy of 531.0 eV. This binding energy is lower than the energy at the end of the adsorption experiment. Together with the lower water amount and the higher O\* concentration, a time dependent reordering of the ice film is assumed.

At 150 K the water starts to desorb and is visible up to a temperature of 340 K. This is already known from the thermal evolution of the adsorbed water on the 2 ML thick nickel oxide film. Normally, this indicates a desorption accompanied by the transformation of the film and therefore several different not exactly distinguishable reaction pathways.

At the complete decline of water and O\* a massive jump of the pure oxygen intensity is visible. This can be explained by a completely changed film with a roughened or even clustered film integrating more oxygen than

used prior to the growth of the film. A 7 % higher palladium bulk signal supports the finding of the change of the nickel oxide film.

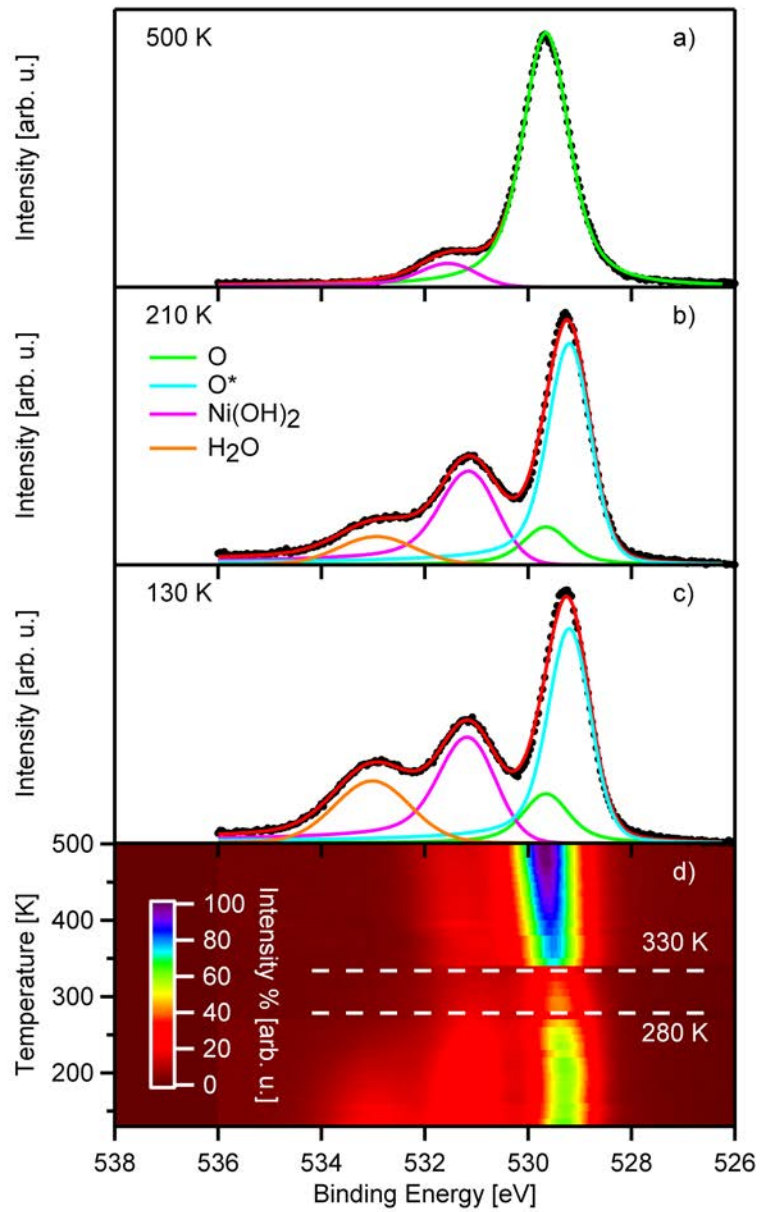


**Figure 5.21:** a) Density plot and respective Spectra b)-d) of the thermal evolution of water on 6 ML NiO/Pd(100)

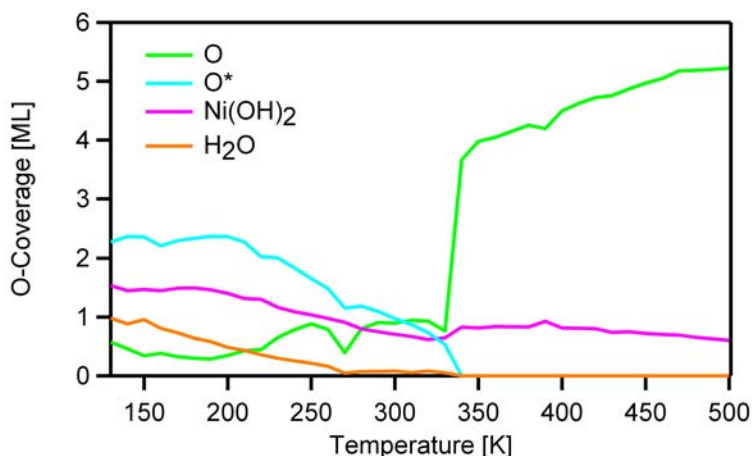


**Figure 5.22:** Quantitative analysis of the thermal evolution of water adsorbed on 6 ML NiO/Pd(100)

## 5.4 Conclusion

In this chapter, the adsorption and reaction of water on clean, oxygen pre-covered palladium and on thin nickeloxide films supported by palladium was shown and discussed. On the clean palladium, water adsorbs molecularly and closes the first layer before the multilayer adsorbs. The monolayer saturates at an coverage of 0.6 ML. The desorption temperature for the monolayer and the multilayer is nearly the same with 160 K. For the oxygen precovered palladium, a Stranski-Kastranov growth was found during the adsorption. The saturation coverage is 0.76 ML and therefore higher than on the clean surface. Water desorbs also at 160 K with a small rise in the hydroxide amount, which is addressed to the partial dissociation of water. A model introduced by Stuve et al and confirmed here describes the adsorption of water below 160 K with a state with water coadsorbed on the palladium with oxygen atoms. The hydrogen atoms of the water molecule are bound via hydrogen bridge linkages to other hydroxide or oxygen atoms. At 180 K, the water has desorbed or is partially dissociated. The dissociated parts formed additional hydroxide with the formerly hydrogen bridge bond molecules. The adsorption and reaction of water was also studied on differently thick NiO surfaces, namely 1 ML, 2 ML and 6 ML. On the wetting layer H<sub>2</sub>O saturates after an exposure of 2.3 L at a coverage of 0.25 ML and at 160 K it starts to desorb without changing the nickel oxide film. At a 2 ML thick nickel oxide film the

saturation coverage of water is 1 ML while the oxygen peak shifts by 0.5 eV to a lower binding energy. Also a Ni(OH)<sub>2</sub> species appear. With the thermal evolution the water starts to desorb over a wide temperature range, while the hydroxide also disappears resulting in a clean 2 ML thick nickel oxide film. The saturation coverage of a 6 ML film was found to be 1.6 ML while the desorption of water also starts at 160 K. Here the film was altered because at the end more oxygen is visible than in the beginning of the adsorption leading to the assumption that the roughness has increased.

# Chapter 6

## C<sub>2</sub>H<sub>2</sub>

### 6.1 C<sub>2</sub>H<sub>2</sub> on Pd(100)

The adsorption and reaction of acetylene on single metal surfaces is a well studied subject<sup>122</sup> as it provides a starting point for addressing more complex systems. In former studies, e.g., acetylene was found to form benzene on (111) surfaces of some metals at higher temperatures<sup>123–125</sup>, whereas this was observed on (100) surfaces to a much lesser extent<sup>126,127</sup>. Furthermore, no ordered acetylene superstructures were observed on metal (100) surfaces<sup>128</sup>; interestingly, on the polar NaCl(100) surface an ordered structure was reported<sup>129</sup>. On Pd(100), the adsorption geometry of acetylene was experimentally determined as the fourfold hollow site, with the two carbon atoms sitting off center at on top sites, as schematically shown in Figure 6.1<sup>130</sup>. The molecule adsorbs di- $\sigma$ /di- $\pi$  bonded: thereby, the  $\pi$ -interaction occurs to those two Pd atoms of the fourfold hollow site, which are not involved in the di- $\sigma$  bonds<sup>130</sup>, see Fig. 6.2. In vibrational spectroscopy, a strong band at 1209 cm<sup>-1</sup> is identified as the C-C stretching mode, which is strongly softened relative to a value of 1974 cm<sup>-1</sup> for the gas phase molecule. These results are similar to the findings on Cu(100), where the same adsorption site and molecule orientation were determined theoretically<sup>131</sup> as well as experimentally<sup>132–135</sup>, also revealing a strong  $\pi$ -Cu interaction. The reaction pathways upon heating strongly depend on the substrate: On Ni(100), at increased temperatures acetylene subsequently dehydrogenates to CCH, CH, and pure carbon<sup>136</sup>. On the other hand, on Fe(100) the dehydrogenation and hydrogenation process leads to CCH<sub>3</sub><sup>137</sup>. In a study addressing the reactivity

of thin Pd films on Mo(100) the dehydrogenation rate was found to depend on the film thickness<sup>138</sup>. On Pd(100), decomposition of acetylene to CCH is proposed from vibrational spectroscopy; the formed CCH species exhibits a rather high thermal stability, up to temperatures of about 650 K.<sup>126,127</sup>

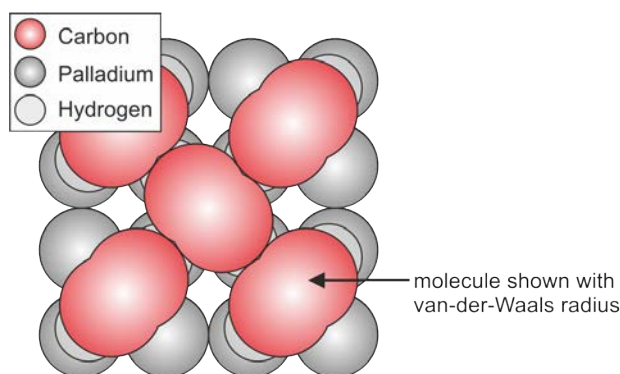


**Figure 6.1:** Sketch of a closed packed acetylene on Pd(100). Here the van-der-Waals radius of the molecules is shown.

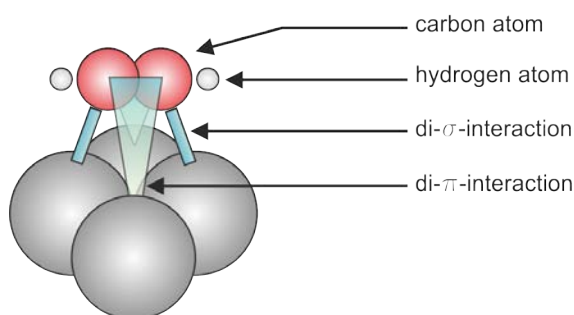


**Figure 6.2:** Adsorption site and bonding model according to<sup>130</sup>. Here the atom radius of the molecule atoms is shown.

Based on the XPS measurements in the C 1s and the Pd 3d<sub>5/2</sub> regions, a simple model of the adsorption that allows simulating the adsorption behavior on the clean surface is presented. The thermal evolution of acetylene is monitored in situ with XPS, in a continuous manner. Since XPS probes the species adsorbed on the surface, these data are complementary to those obtained by TPD<sup>127,139,140</sup>, where the desorbing species is probed in the gas phase.

### 6.1.1 Adsorption

First the adsorption of acetylene on a clean Pd(100) surface at 130 K is investigated. The corresponding C 1s spectra in Figure 6.3 show a single peak

at the binding energy of 283.30 eV, with a shoulder at 0.36 eV higher binding energy. Peak fitting shows that both rise together with a constant ratio of 0.17 and with a constant binding energy difference. From this behavior, two contributions are assigned to one C<sub>2</sub>H<sub>2</sub> species with a symmetric adsorption site (i.e. equivalent carbon atoms) on the Pd(100) surface. For an exemplary analysis of the spectra see Figure 6.4. The constant intensity ratio, denoted as S-factor, is typical for high resolution XP spectra of adsorbed small hydrocarbons on metal surfaces<sup>42</sup>. It is due to the excitation of the C-H vibrations in the final state ion in the course of the photoemission process. The main peak at 283.30 eV is the adiabatic peak and the shoulder at 283.66 eV is due to the vibrationally excited final state. Please note that with our resolution we can only identify these two contributions; higher vibrational states and also other vibrations such as the C-C vibrations contribute to the asymmetry of the fit functions<sup>141</sup>. Our results confirm the adsorption of acetylene at one symmetric adsorption site on Pd(100), as has been proposed earlier in Ref. [130]. The quantitative analysis (see Figure 6.5) yields a coverage of 0.68 ML of carbon atoms. This corresponds to 0.34 ML of acetylene molecules (C<sub>2</sub>H<sub>2</sub>) at 130 K.

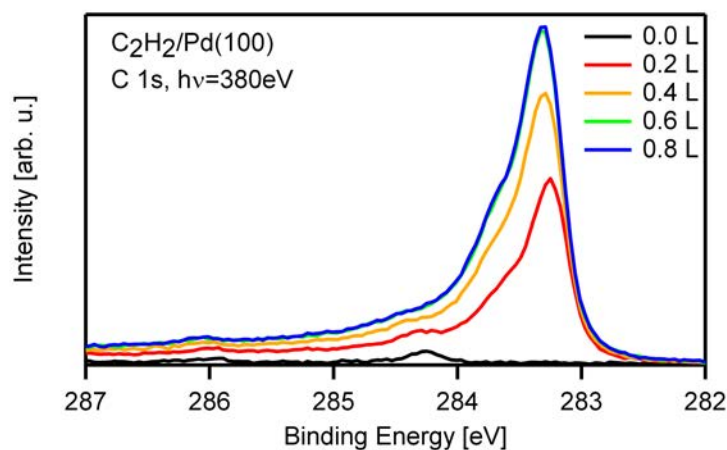


**Figure 6.3:** Spectra of the adsorption of C<sub>2</sub>H<sub>2</sub> on Pd(100)

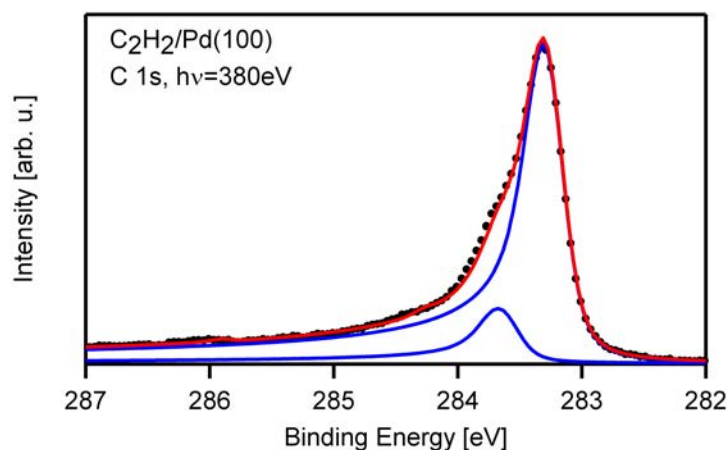


**Figure 6.4:** Exemplary fit of the C 1s spectrum with a saturated layer

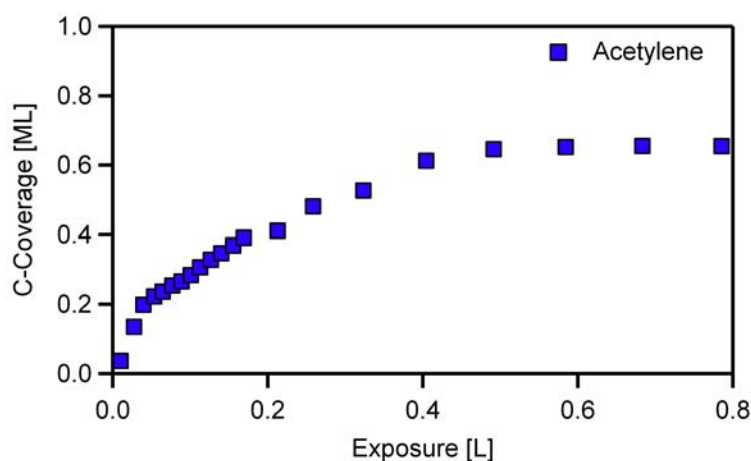


**Figure 6.5:** Quantitative analysis of the adsorption of C<sub>2</sub>H<sub>2</sub>

The adsorption of acetylene was also monitored by recording the Pd 3d<sub>5/2</sub> core level; selected spectra are shown in Figure 6.6. On the clean surface, we find two contributions, the palladium bulk signal at 335.0 eV and the surface components<sup>51</sup> at 334.6 and 335.6 eV (see Section 5.1). This core level shift results from the different coordination and thus electronic structure of the Pd surface layer as compared to the bulk<sup>38</sup>. Upon increasing the acetylene coverage we find that the surface contribution vanishes and the Pd bulk contribution decreases due to damping by the adsorbate. Simultaneously, the subsequent evolution of two new C<sub>2</sub>H<sub>2</sub>-induced contributions at 335.5 and 336.0 eV is observed. The quantitative analysis of the surface component and the acetylene-induced components of the Pd 3d<sub>5/2</sub> signal during adsorption

is presented in Figure 6.7 (the Pd bulk contribution is not shown for the sake of clarity). In the analysis, we find the continuous decrease of the surface contribution to zero at 0.55 L. At low exposures, a C<sub>2</sub>H<sub>2</sub>-induced Pd 3d<sub>5/2</sub> signal at 335.5 eV increases to a maximum at 0.4 L, and thereafter slightly decreases towards higher exposures. The second C<sub>2</sub>H<sub>2</sub>-induced Pd 3d<sub>5/2</sub> signal at 336.0 eV rises slower and only saturates when the maximum coverage of acetylene is reached. An example of the fitting procedure of the spectra is shown in Figure 6.8.

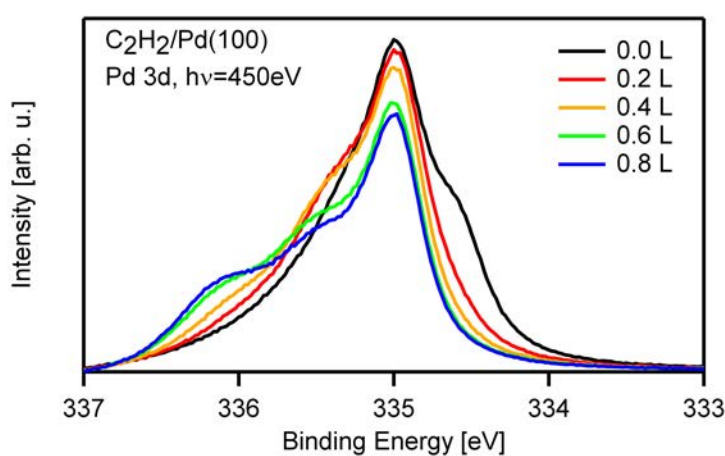


**Figure 6.6:** Pd 3d<sub>5/2</sub> spectra of the adsorption of acetylene on Pd(100)

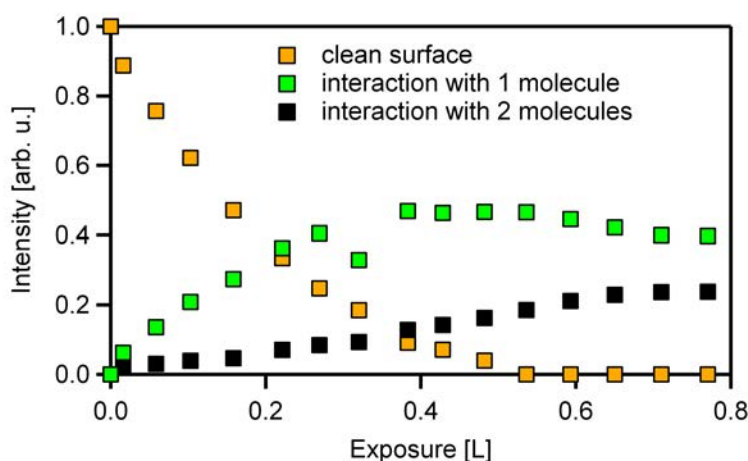


**Figure 6.7:** Quantitative analysis of the adsorption of acetylene in the Pd 3d<sub>5/2</sub> core level.

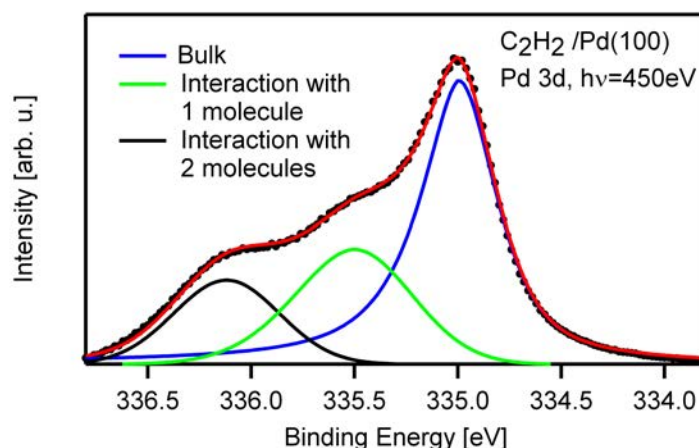


**Figure 6.8:** Exemplary fit of a Pd 3d<sub>5/2</sub> peak following<sup>51</sup>

To explain this behavior, a fourfold hollow adsorption site of acetylene is considered. The first C<sub>2</sub>H<sub>2</sub>-induced Pd peak is assigned to the four Pd surface atoms interacting with one acetylene molecule (either by a C- $\sigma$  or by a  $\pi$ -interaction (see Figure 6.2)<sup>130</sup>. The second C<sub>2</sub>H<sub>2</sub>-induced Pd peak found at higher coverages is then related to Pd atoms that are in contact with two acetylene molecules, again via a  $\sigma$ - or a  $\pi$ -bond. A similar explanation was proposed for the surface core level shift induced by CO on Pd(100) in Ref.<sup>53</sup>; there, in the  $p(4\sqrt{2} \times \sqrt{2})R45^\circ$  superstructure, also an additional high binding energy Pd peak was found due to Pd atoms in contact with two CO molecules<sup>53</sup>. Within this interpretation the quantitative data in Figure 6.7 indicate that on the clean surface, acetylene initially adsorbs as individual molecules with comparably large intermolecular distances, such that only one Pd surface atom is in contact with one acetylene molecule. Acetylene molecules that adsorb closer together, such that an increasing number of Pd surface atoms is in contact with two molecules, lead to the second Pd 3d<sub>5/2</sub> contribution.

If the coverage of the surface peak in the Pd 3d<sub>5/2</sub> region is plotted against the coverage of the molecules, it should give the number of covered surface atoms just by calculating the slope of the decrease<sup>142,143</sup>. The results are presented in Figure 6.9. It turns out that the fit of the first two points gives indeed the expected slope of -4, but the analysis is certainly not convincing. If the whole coverage range is taken into account a slope of -3 is found. The interpretation of this result is the consequence of island growth already at low coverages.

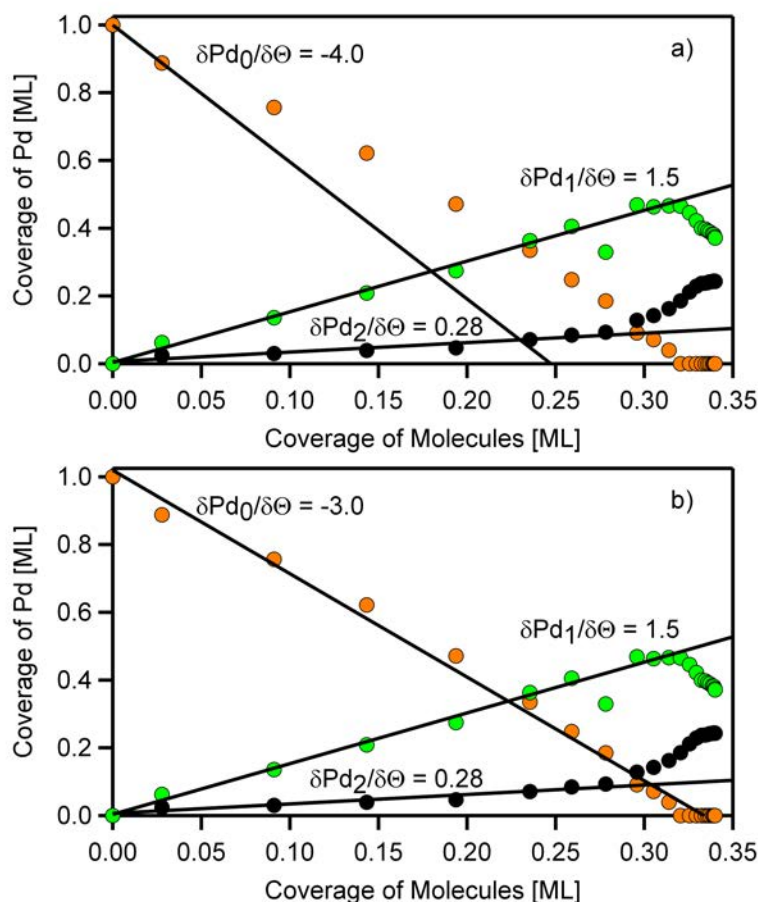


**Figure 6.9:** Analysis of the change in clean substrate surface atoms following<sup>142,143</sup>

### 6.1.2 Simulation

In the following, a simple model to simulate the uptake behavior in Figure 6.7 is proposed; it is based on the fourfold site and the flat adsorption geometry known from literature<sup>130</sup>. From their van-der-Waals dimensions, a closely packed ordered layer with a p(2x2) unit cell and a saturation coverage of 1 ML carbon (0.5 ML acetylene molecules) appears possible, see Figure 6.1. Under the condition of this study, however, only 0.68 ML of carbon coverage is reached, which is attributed to a limited mobility at 130 K; indeed, for acetylene adsorption at room temperature a saturation coverage of 0.95 ML was reported by Vattuone et al.<sup>144</sup>. In the here presented simulation, a statistical adsorption process is assumed with limited diffusion on the bare surface and on the adsorbate covered areas (details are provided in the attachments). The results of the simulation are shown in Figure 6.10b. Comparison to the

experimental data of the Pd 3d<sub>5/2</sub> data in Figure 6.10a shows very good qualitative agreement considering the simplicity of the model. The main difference between the experiment and this simulation is the complete decline of the surface species in the experimental analysis. This occurs possibly due to the lack of diffusion of acetylene after chemisorption in the simulation, but also minor uncertainties in the fitting of the experimental data.

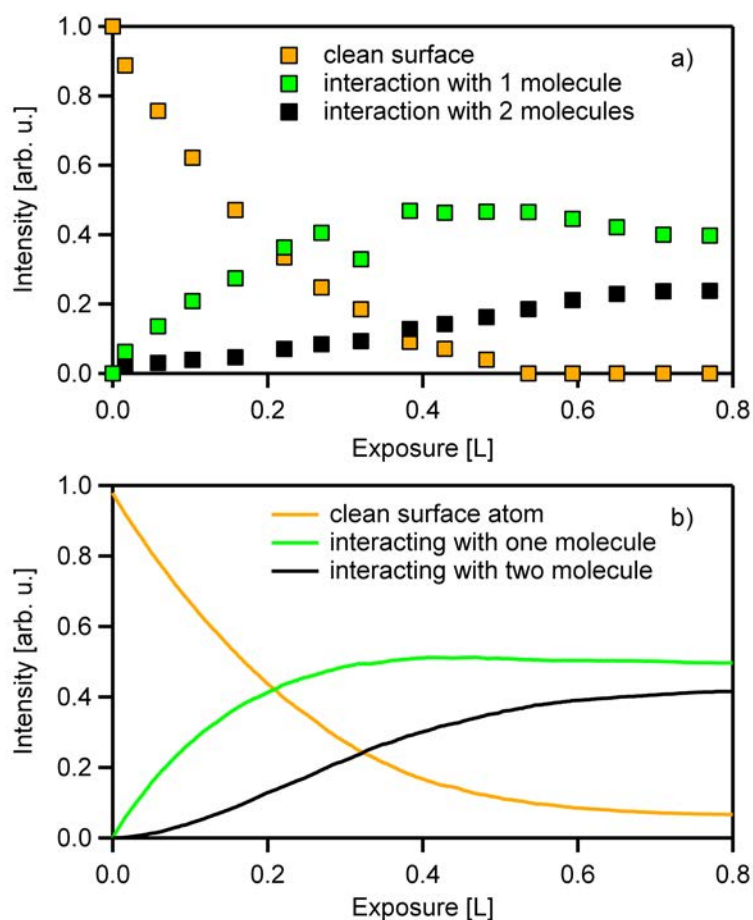


**Figure 6.10:** a) Experimental and b) simulated coverages and interactions of C<sub>2</sub>H<sub>2</sub> adsorption on the Pd(100) surface

In Figure 6.11 the surface arrangement of the acetylene molecules is depicted, showing the formation of (2x2) small islands on the surface, which are separated by domain boundaries, where Pd atoms that are coordinated to only one molecule or in few cases also to no molecule. In these regions, due to steric reasons, it is not possible to adsorb more acetylene. Interestingly, the simulated pattern shows no long range order and is consistent with LEED, where no superstructure was observed. Adsorption at a higher temperature

would result in a longer diffusion length and therefore in a higher mobility and higher coverage. The higher temperature and the induced higher mobility can be modeled by a larger diffusion length of the molecules on the substrate and on the molecules - the preadsorbed state. This is depicted in Figure 6.12. Here the coverage is plotted in dependency of the distances the molecules can travel. For higher traveling distances the coverage increases. Interestingly, the diffusion length on the substrate has a higher influence on the saturation coverage than the diffusion distance in the precursor state, i. e. on the chemisorbed acetylene molecules.

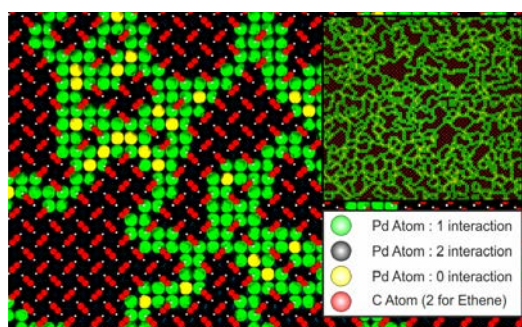


**Figure 6.11:** Simulated coverage of the adsorption of acetylene on Pd(100)

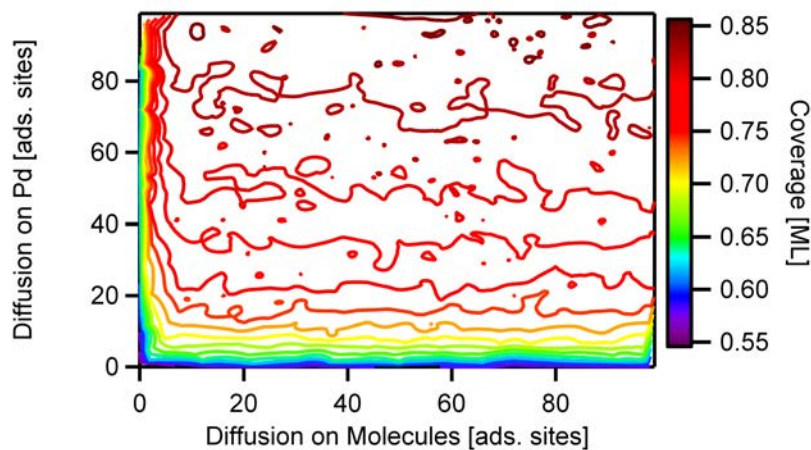


**Figure 6.12:** Dependency of the coverage to temperature and diffusion lengths shown in a contour plot. The different saturation coverages are depicted in color-coded contour lines. The simulation program was started with different maximum diffusion lengths for the preadsorbed ("Diffusion on Molecules") and chemical adsorbed state ("Diffusion on Pd"). The sample size is 1000 experiments with randomly chosen diffusion lengths. The contour lines are smoothed afterwards.

### 6.1.3 Reaction

As the next step, the thermal evolution of the adsorbed acetylene layer upon heating to 600 K was investigated. Figures 6.13 a-c show C 1s spectra at selected temperatures along with the corresponding fits, Figure 6.13d the complete data set in a color-coded density plot, and Figure 6.14 the quantitative analysis. At low temperatures (150 K, Figure 6.13c) the C 1s peaks of C<sub>2</sub>H<sub>2</sub> already known from the adsorption experiment in Figure 6.3 are found. At 250 K, a small shift of the peaks to lower binding energies by 20 meV is observed. In the same temperature region also slight changes in the 3d<sub>5/2</sub> region are observed (not shown), with a small increase of the contribution from Pd atoms in contact with one acetylene molecule. These small changes can not be attributed to a reaction of the acetylene molecules on the surface, but rather to a local rearrangement and/or minor change of the interaction with the substrate.

At about 370 K, a new peak starts to grow, at the expense of the acetylene peak, and reaches its maximum at 420 K (see Figure 6.13c). Its binding energy is 283.76 eV, with a vibrational satellite at 284.12 eV and a S-factor of 0.09, as expected for one H atom bond to two carbon atoms. This species is assigned to CCH, according to vibrational spectroscopy studies in literature<sup>126,136</sup>. Please note that due to the overlap with acetylene peaks a clear distinction from e.g. CCH<sub>3</sub> based on the satellite intensity is difficult from the XP spectra alone. Starting at ~390 K, two additional contributions start to grow at 284.22 and 284.58 eV; we identify them as the completely dehydrogenated product carbon on different adsorption sites. This assignment is based on the binding energies<sup>145,146</sup> and the temperature stability of the species. From the quantitative analysis of the thermal evolution in Figure 6.14 it is obvious that acetylene (blue curve) mostly dehydrogenates up to temperatures of 600 K, with some CCH species left in accordance to literature<sup>126,127</sup>.

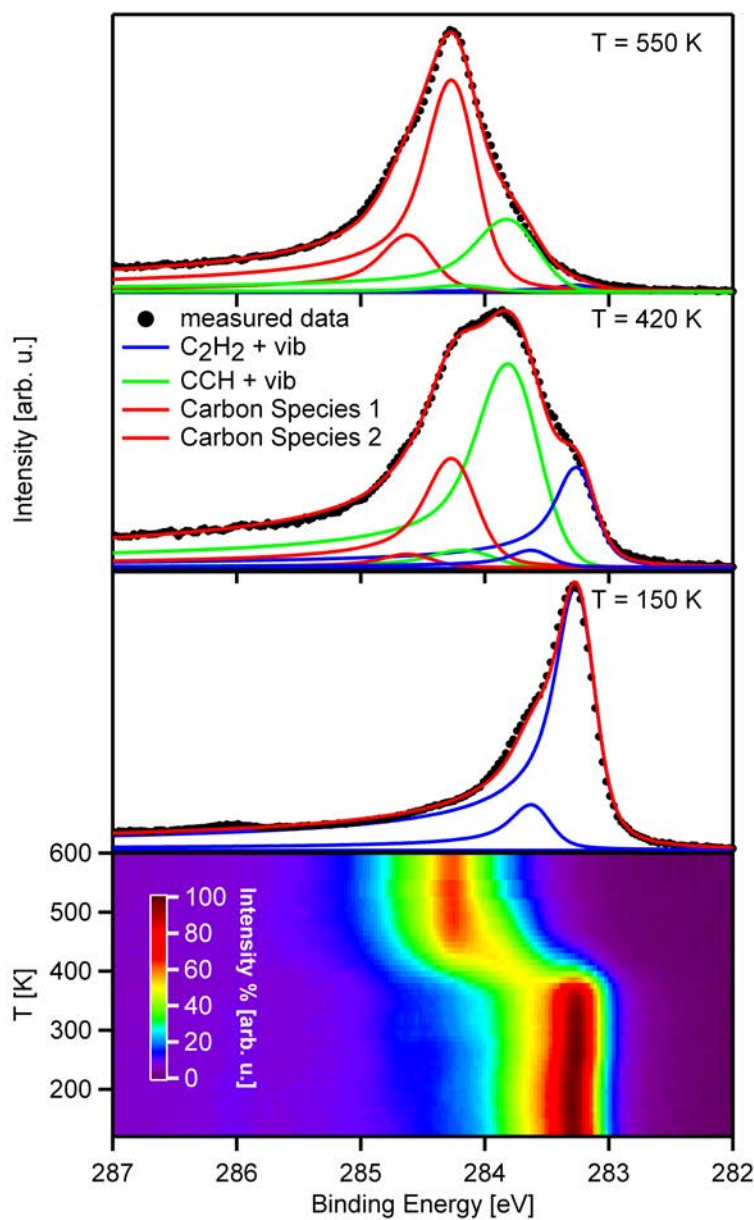


**Figure 6.13:** Representative fits and density plot of the thermal evolution of acetylene adsorbed on Pd(100)

The quantitative analysis in Figure 6.14 shows the data fitted with one acetylene species (blue curve). From this fit it is evident that up to  $\sim 350$  K the total amount of carbon on the surface remains unchanged. This result is in contrast to observations in a temperature programmed desorption studied, where a small acetylene peak is reported below room temperature (180 - 220 K, using a heating rate of 25 K/s<sup>127,139</sup>). The origin of this discrepancy is not clear. It could either be due to the fact that in the TPD spectra

some contribution from the sample holder was detected or that the XPS signals of the two species below and above 200 K display slightly different photoelectron diffraction (PED) effects, which cancel by coincidence. With the transformation from acetylene to the CCH species and the formation of the completely dehydrogenated product around 390 K a slow decrease of the total amount of carbon set in, which is either due to a change of the photoelectron diffraction behavior or to diffusion of carbon into the bulk of the Pd crystal; the latter has also been reported in [127,139].

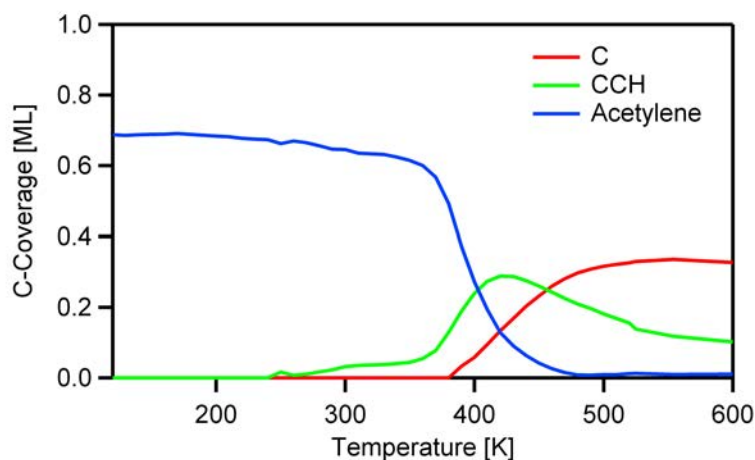


**Figure 6.14:** Quantitative analysis of the reaction of acetylene on Pd(100) in the C 1s region

In Figure 6.15 the reaction of acetylene on Pd(100) monitored in the Pd 3d<sub>5/2</sub> is shown. Here it gets obvious that a minor change in the adsorption state of the molecule can be seen around 250 K. The respective quantitative analysis is depicted in Figure 6.16.

This change in the Pd 3d<sub>5/2</sub> is also reflected in the C 1s by the occurrence of 20 meV shift in the binding energy (see above). This shift is in the magnitude of the binding energy resolution and therefore highly speculative. For the sake of completeness an alternative fit with a second acetylene species is shown in Figure 6.17 and its quantitative analysis in 6.18. The reason for this shift in the binding energy and the different acetylene species could be a rearrangement of the molecules on the surface.

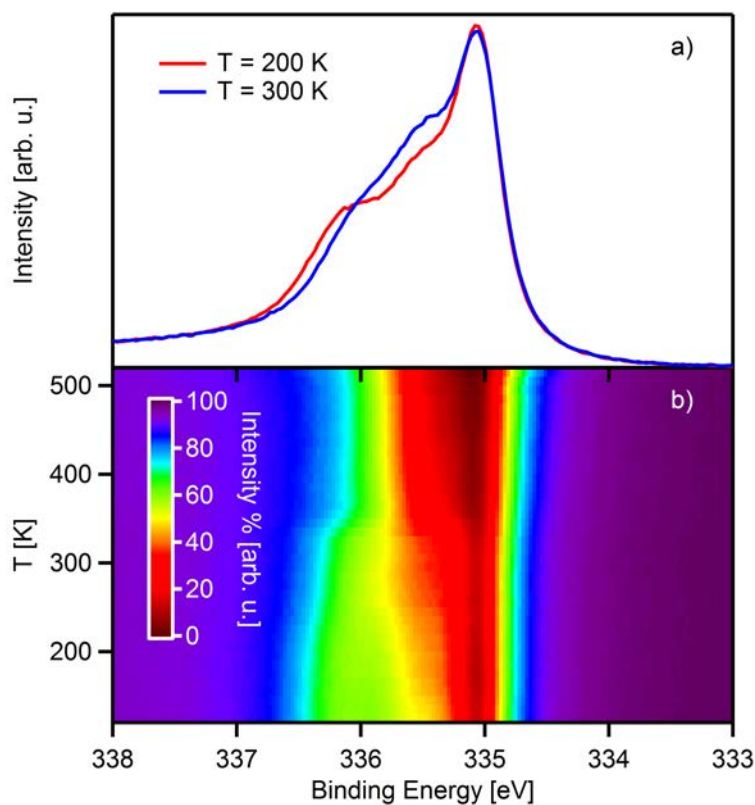


**Figure 6.15:** a) Spectra and b) density plot of the reaction experiment monitored in the Pd 3d region

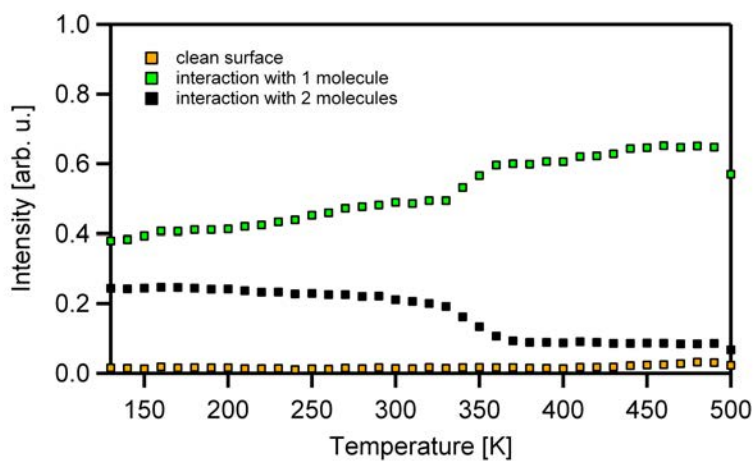


**Figure 6.16:** Quantitative analysis of the reaction experiment of C<sub>2</sub>H<sub>2</sub> in the Pd 3d region

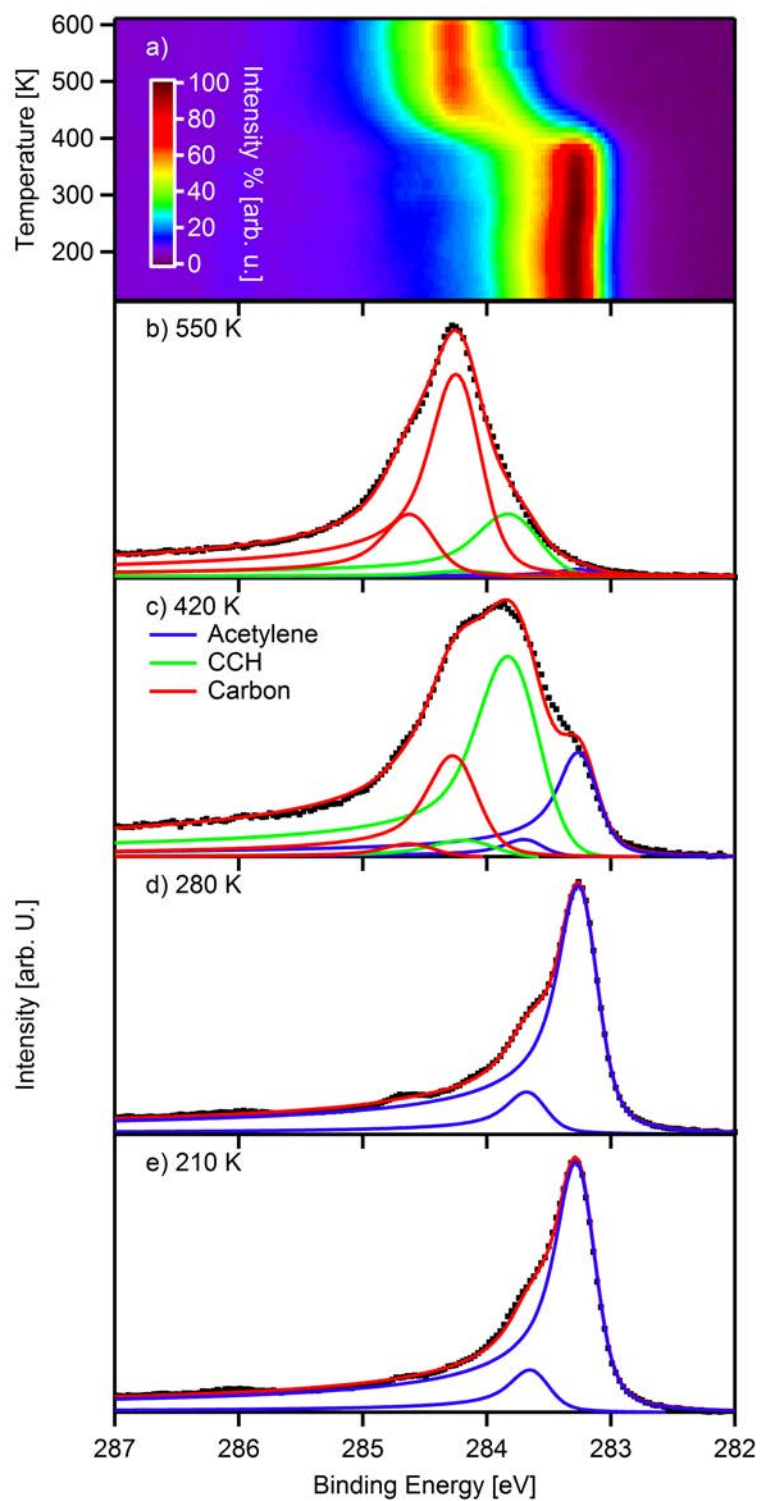
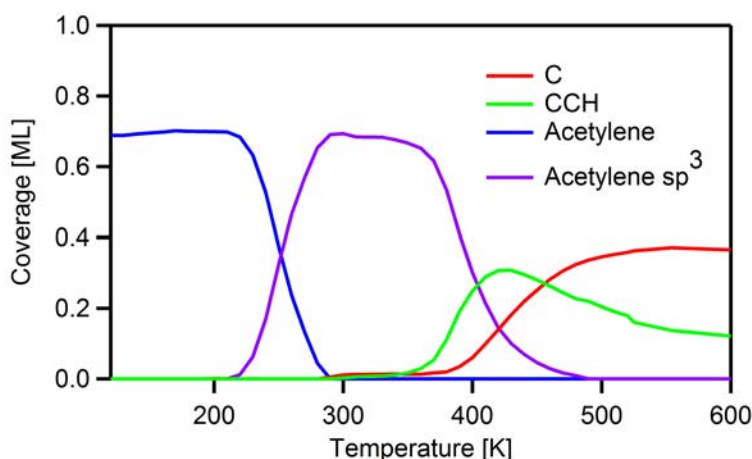


Figure 6.17: Alternative fit of the reaction of acetylene on Pd(100)



**Figure 6.18:** Quantitative analysis of the reaction of acetylene on Pd(100)

## 6.2 C<sub>2</sub>H<sub>2</sub> on O/Pd(100)

### 6.2.1 Adsorption

In this section the influence of preadsorbed oxygen on the adsorption and reaction behavior of acetylene is addressed. In Figure 6.19a and b, selected spectra of acetylene adsorption on Pd(100) precovered with 0.25 ML oxygen are shown. The spectrum at low exposures (Figure 6.19: 0.4 L) shows a peak at 283.16 eV with a vibrational splitting, indicative of molecular adsorption. The vibrational splitting of 0.36 eV and the S-factor of 0.17 are identical to the values on the clean surface. The peaks are broader than on clean Pd(100) (cf. Figure 6.3), which is attributed to a less well-defined adsorption geometry in the coadsorption case and to lateral interactions with the coadsorbed oxygen. At higher exposures (Figure 6.19: 1.0 L), a weak additional contribution is observed at 283.70 eV, indicating the formation of CCH with a maximum coverage of 0.03 ML. This shows that on the oxygen-precovered surface C<sub>2</sub>H<sub>2</sub> partly dehydrogenates already at low temperatures. From the corresponding O 1s spectra (see figure 6.20), the formation of a hydroxyl species, i.e. C<sub>2</sub>H<sub>2</sub> reacts to CCH + OH is deduced.

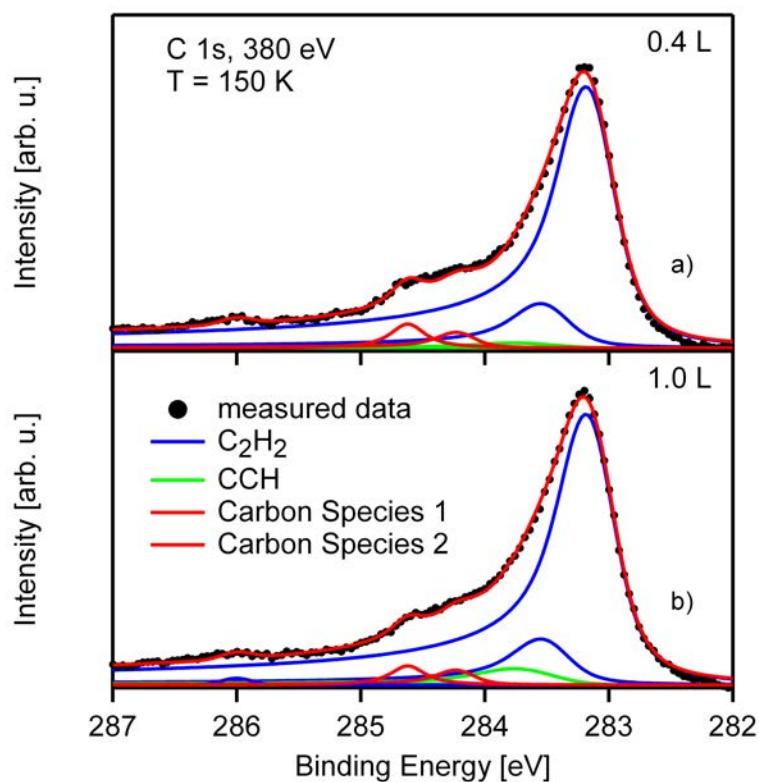


**Figure 6.19:** Spectra of acetylene adsorption on O/Pd(100)

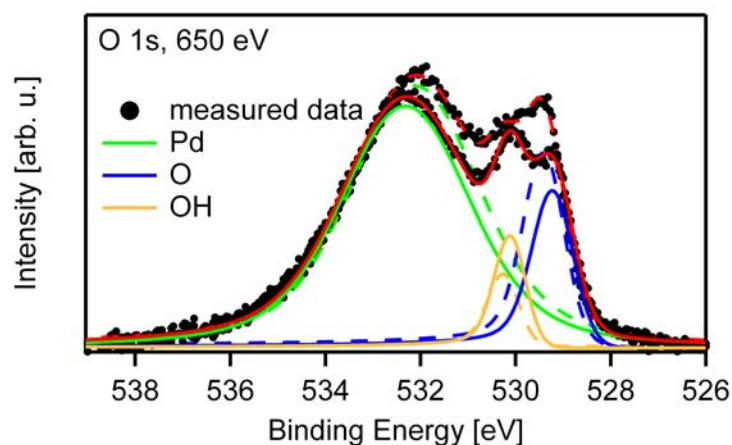


**Figure 6.20:** O 1s region before and after the adsorption of acetylene on O/Pd(100)

From the quantitative analysis of the C 1s spectra in Figure 6.21, the carbon coverage is determined to 0.40 ML carbon, i.e. 0.20 ML C<sub>2</sub>H<sub>2</sub> plus CCH. This value is lower than on the clean surface, due to the blocking

of adsorption sites with oxygen. Both, oxygen (0.25 ML) and acetylene are adsorbing on hollow sites giving an overall coverage of adsorbed carbon and oxygen atoms of 0.65 ML which corresponds very well to the acetylene saturation coverage on the clean surface (see Section 6.1).

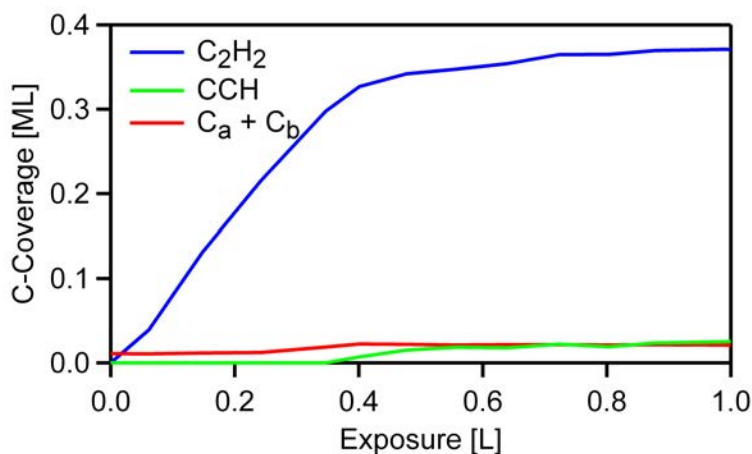


**Figure 6.21:** Quantitative analysis of acetylene adsorption on O/Pd(100)

### 6.2.2 Reaction

Finally, the thermal evolution of the coadsorbed acetylene and oxygen layer is discussed. In Figure 6.22a-c, spectra at selected temperatures are displayed, Figure 6.22d shows the complete data set in a color-coded density plot, and in Figure 6.23 the quantitative analysis is presented. At low temperatures, the situation corresponds to the end of the adsorption experiment in Figure 6.19. While the reaction overall proceeds similar to that on the clean Pd(100) surface, a strong difference is found in the temperature dependence: The reaction to the intermediate CCH at 283.67 eV starts already at the very beginning of the TP XPS experiment, i.e. at low temperatures, and yields a maximum CCH coverage at 280 K; on the clean surface the maximum was only reached at 410 K. Also the onset of the formation of surface carbon species (284.17 and 284.62 eV) is shifted to lower temperatures by 180 K (from 390 to 210 K). Furthermore, we also find small amounts (< 0.01 ML) of CO at bridge positions (286.0 eV)<sup>53</sup>. Above 250 K, the total amount of carbon strongly decreases upon heating, from 0.40 ML before to 0.15 ML after the reaction (see Figure 6e). This is attributed to the reaction of oxygen with carbon to carbon monoxide and carbon dioxide. The decrease

in carbon coverage of 0.25 ML fits very well to the amount of available oxygen, which could imply exclusive CO formation. However, as the CO signal does not increase, we conclude that at least part of the CO is oxidized to volatile CO<sub>2</sub> and it is also necessary to the desorption of acetylene or other carbon-containing species, to account for the carbon loss. Furthermore, oxygen can also recombine with hydrogen to form hydroxyl and upon heating subsequently water, which desorbs from Pd(100) at 180 K<sup>147</sup>.

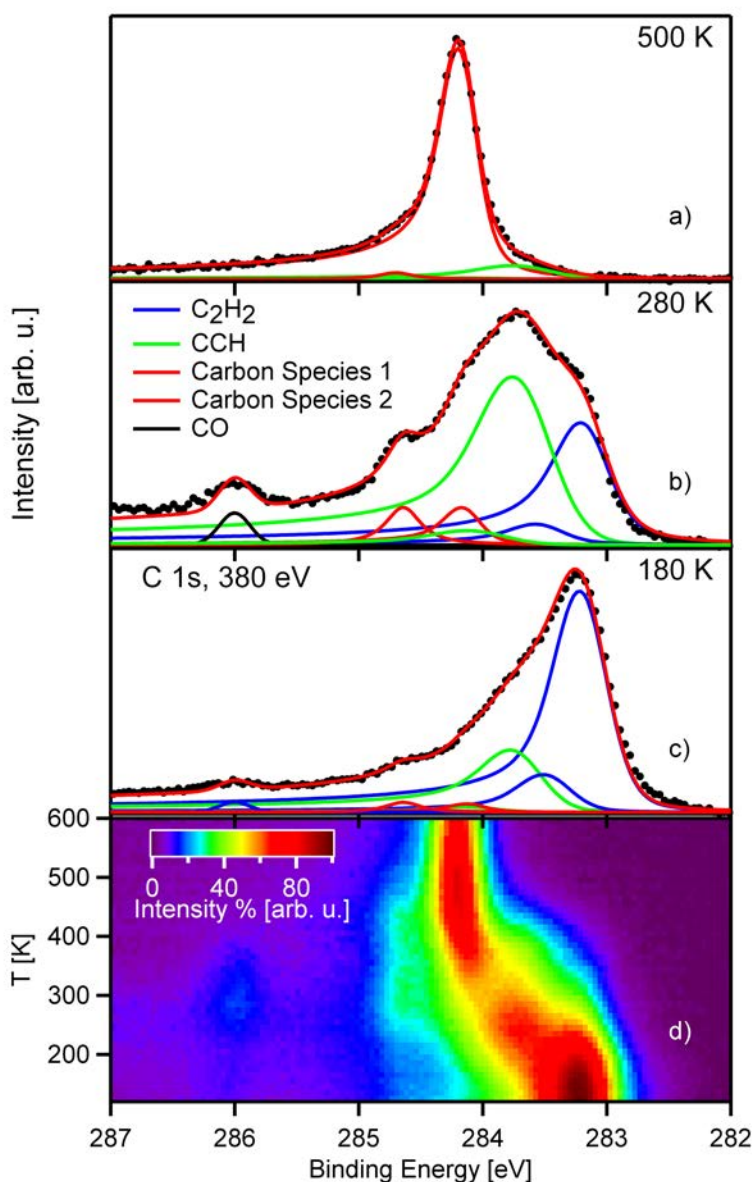


**Figure 6.22:** Spectra and density plot of the thermal evolution of acetylene on O/Pd(100) a) 500 K b) 280 K c) 180 K d) density plot

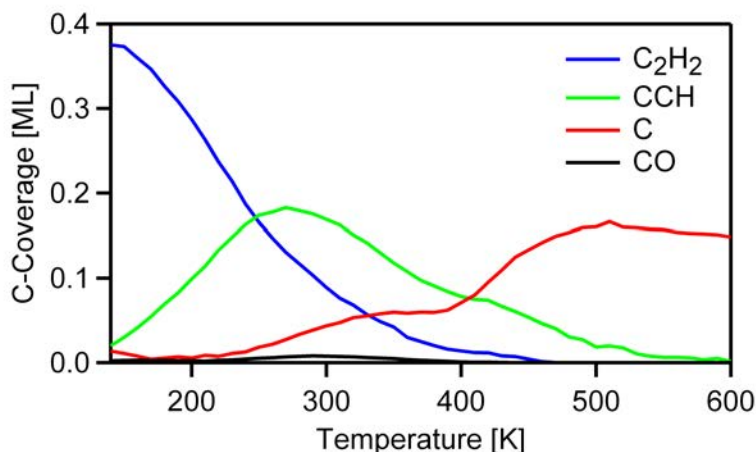


**Figure 6.23:** Quantitative analysis of the thermal evolution of acetylene on O/Pd(100)

To conclude this section, the coadsorption experiment demonstrated that the dehydrogenation of acetylene on Pd(100) is shifted 200 K to lower temperatures by preadsorbed oxygen. This is attributed to the strong affinity of oxygen to hydrogen, corresponding to a basic site on the surface.

### 6.3 C<sub>2</sub>H<sub>2</sub> on NiO/Pd(100)

In addition to the PhD thesis of Lorenz<sup>120</sup> several articles<sup>148,149</sup> have been published about oxygen precovered Ni(111) surfaces interacting with C<sub>2</sub>H<sub>2</sub>. The topmost layer in an ideal (111) nickel oxide surface is either oxygen or nickel, leading to a electrostatic charge of the layer. Normally the charge compensation in a nickel oxide bulk crystal in the [111] direction involves the next layer, which is oppositely charged. A complete charge compensation can never be achieved, because at least one half of a layer is always missing in this electrostatic model and therefore surface reconstructions are observed. These reconstructions add further complexity. Additionally, an oxygen covered surface is not an oxide surface, because the oxygen interacts different if it is integrated or adsorbed. From this point of view it is hard to compare the adsorbed acetylene on an oxygen precovered surface with the adsorption behavior on a nickel oxide. A closer system could be the adsorption of acetylene on MgO. Especially, in this case as it is reported that MgO growth and structure is very similar to the one of nickel oxide supported on palladium (100), besides, that on the latter a wetting layer exists<sup>35,73,150</sup>. However, on

MgO a (2x2) superstructure was found with the acetylene molecules centered on top of the magnesium atoms in the film<sup>151</sup>.

### 6.3.1 NiO film: 1 ML

#### 6.3.1.1 Adsorption

This part describes the adsorption and reaction of acetylene on 1 ML nickel oxide. As previously discussed, this system is not simply a NiO layer on a substrate, but this nickel oxide layer has a Ni<sub>3</sub>O<sub>4</sub> stoichiometry with regular nickel vacancies<sup>33</sup>. During adsorption of acetylene on this system one broad peak arises which can be deconvoluted in two parts, C<sub>2</sub>H<sub>2</sub> on the Ni<sub>3</sub>O<sub>4</sub> (283.3 eV) and on the palladium substrate (282.9 eV). Also another peak at 285.0 eV is revealed at higher exposures by the deconvolution. This is another acetylene species adsorbed on NiO. Please also refer to the section about the adsorption experiment on the 2 ML thick nickel oxide layer. The quantitative analysis shown in Figure 6.25 reveals an amount of 0.05 ML of acetylene on the palladium, while the amount of acetylene on the nickel oxide is 0.12 ML. These two acetylene signals on the nickel oxide do not belong to only one chemical species, as they appear at different coverages. Additionally, the relative coverage of the two contributions changes during adsorption, which would not be the case for one chemical species.

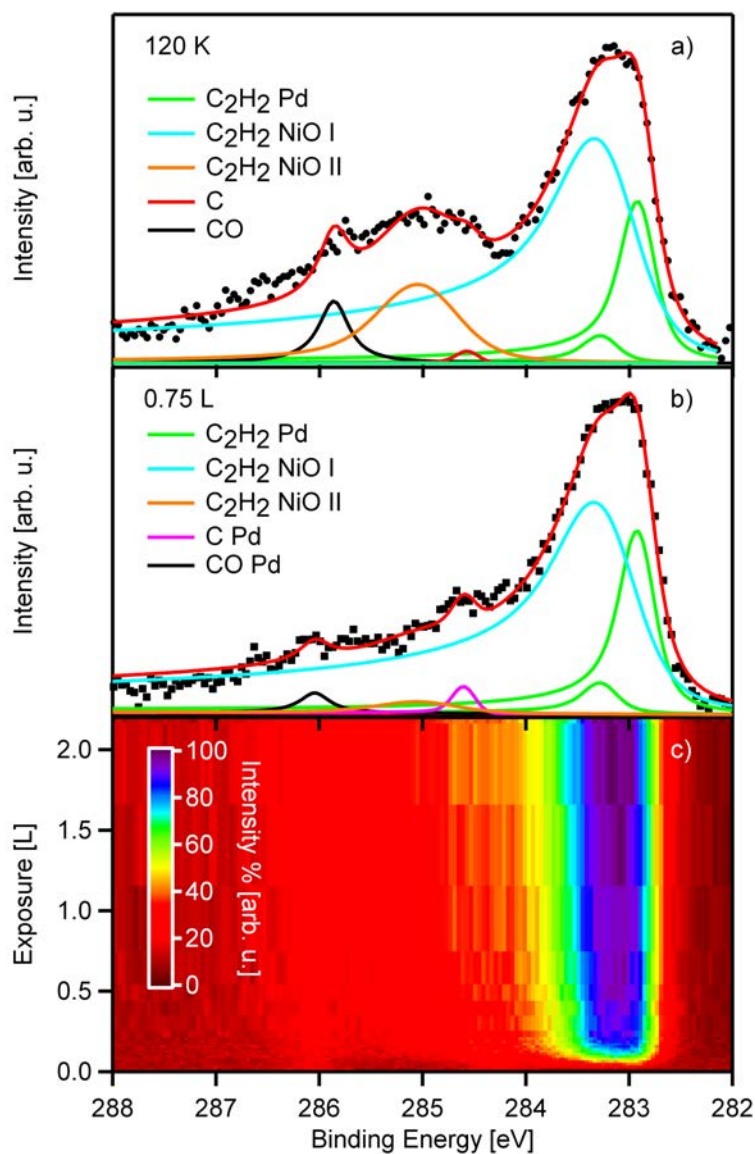


**Figure 6.24:** Spectra and density plot of the adsorption of acetylene on 1 ML NiO/Pd(100) at 120 K. Please note that the spectrum in a) is taken after the adsorption and before the reaction experiment. b) is taken directly after the adsorption, ~5 Minutes are gone between a) and b).

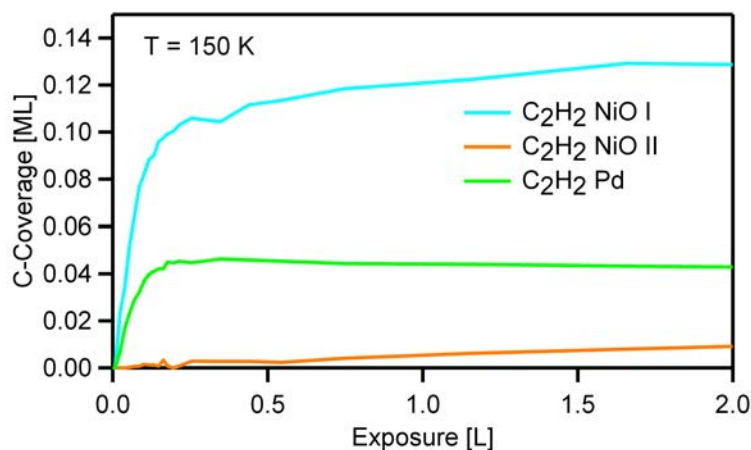


**Figure 6.25:** Quantitative analysis of the adsorption of acetylene on 1 ML NiO/Pd(100)

### 6.3.1.2 Reaction

The spectra with the deconvoluted peaks and a density plot of the reaction acetylene on nickel oxide are shown in Figures 6.26 and 6.27. At first, the acetylene species at 285.0 eV vanishes till 220 K. Afterwards, the C<sub>2</sub>H<sub>2</sub> species on palladium at 282.9 eV decreases and the second species on nickel oxide at 283.5 eV decreases in intensity till 300 K. A broad peak is visible at a binding energy of 283.7 eV up to a temperature of 400 K, which is assumed to be the decay product of the acetylene. A sharp peak becomes visible with a binding energy of 284.2 eV at a temperature of 360 K and at 470 K it becomes obvious that this new species is carbon due to its sharp peaks and the thermal stability. The reaction of acetylene on the 1 ML thick nickel oxide film completely reduces the film to metallic nickel.

The quantitative analysis is presented in Figure 6.28. Here it is shown that at a temperature of 120 K three species are on the surface, C<sub>2</sub>H<sub>2</sub> on Pd and two species of acetylene on the NiO. At 160 K the decay of acetylene starts and two new signals become visible. They have a maximum coverage of 0.04 and 0.07 ML at 300 K. Starting at 250 K carbon is formed with a maximum coverage of 0.05 ML. All decay products are named CCH<sub>x</sub> because no information about the chemical state can be obtained from the deconvolution. Nevertheless, from the previous experiments on the clean and oxygen precovered palladium surfaces it is suggested that the major reactions are

dehydrogenation reactions of the molecule. From the amounts found during the reaction it is concluded that acetylene partially desorbs.

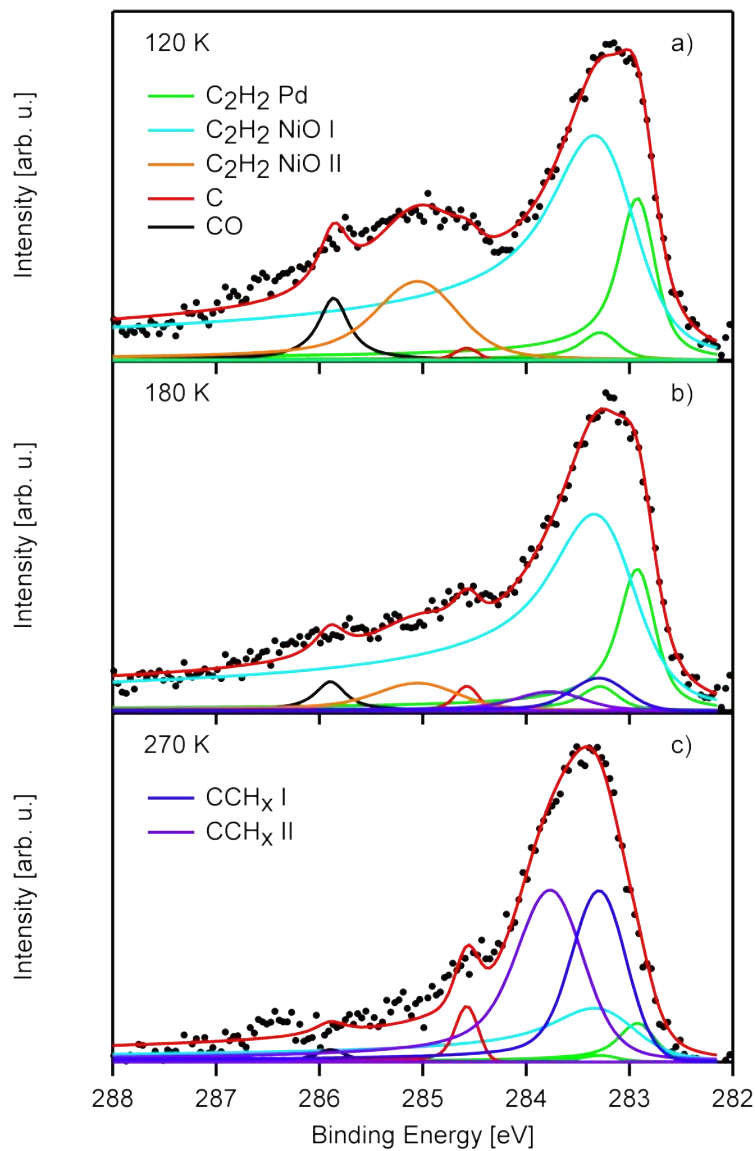


**Figure 6.26:** Spectra up to a temperature of 350 K of the reaction of C<sub>2</sub>H<sub>2</sub> on 1 ML NiO/Pd(100)

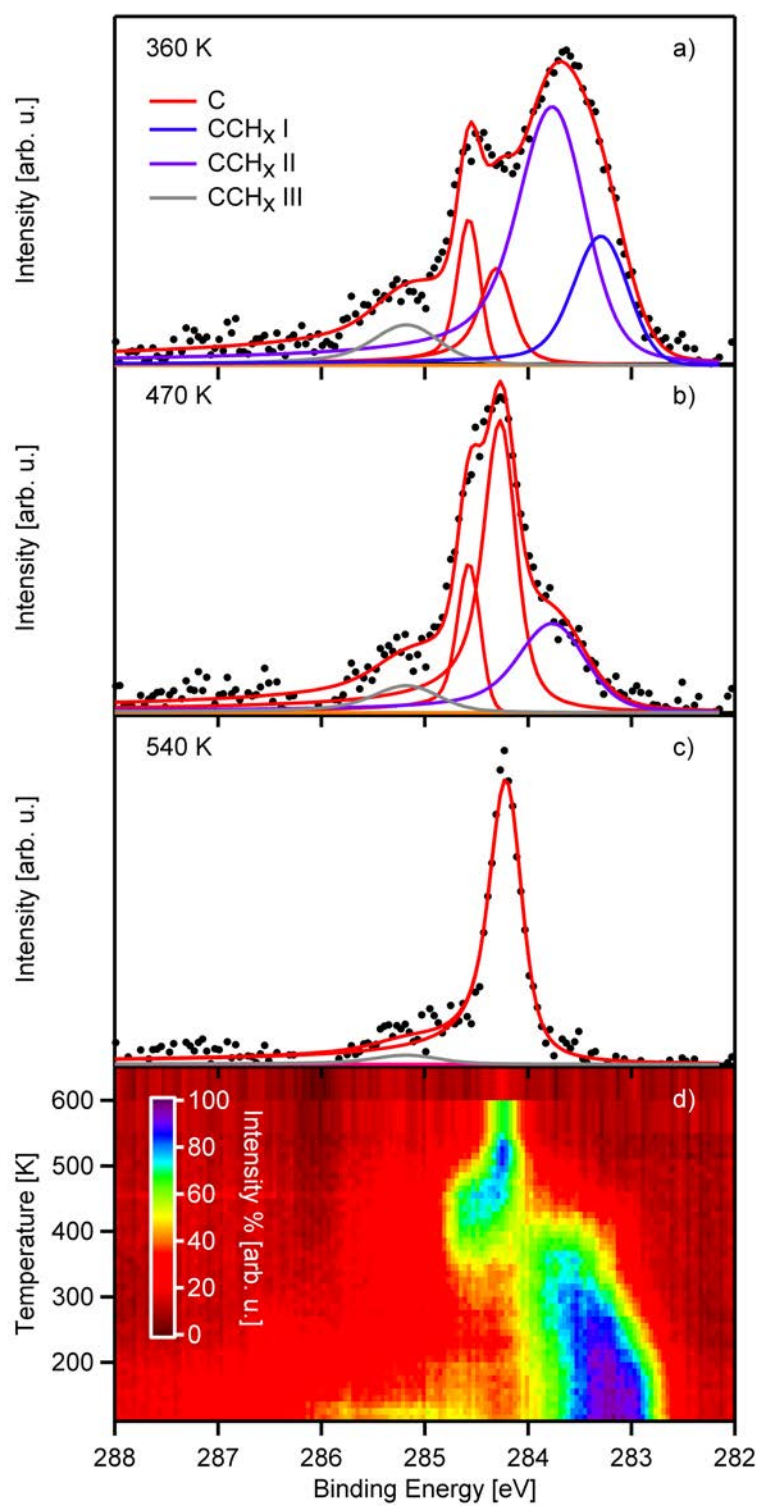


**Figure 6.27:** Spectra higher than a temperature of 350 K of the reaction of C<sub>2</sub>H<sub>2</sub> on 1 ML NiO/Pd(100)

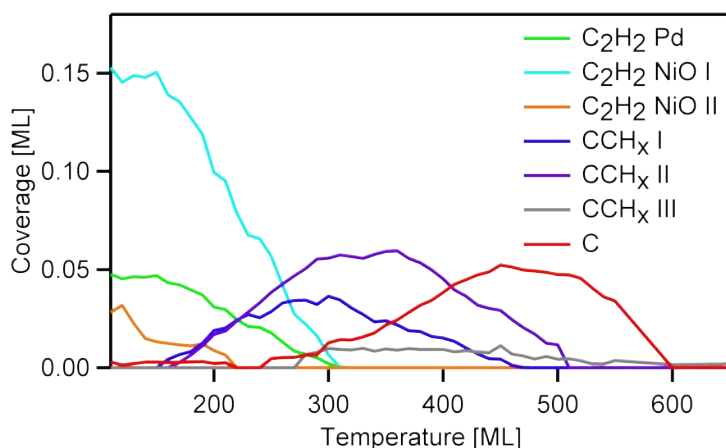


**Figure 6.28:** Quantitative analysis of the reaction of acetylene on 1 ML NiO/Pd(100)

## 6.3.2 NiO film: 2 ML

### 6.3.2.1 Adsorption

During the exposure of acetylene on 2 ML thick NiO film at 120 K two features are recognized. The first feature has a binding energy of 283.3 eV while the second species is found at 285.0 eV (cf. Figure 6.29). The FWHM of the acetylene peaks is higher than for peaks on the clean sample due to a not clear distinct adsorption site of the C<sub>2</sub>H<sub>2</sub>, which was also found in earlier studies on NiO<sup>120</sup>.

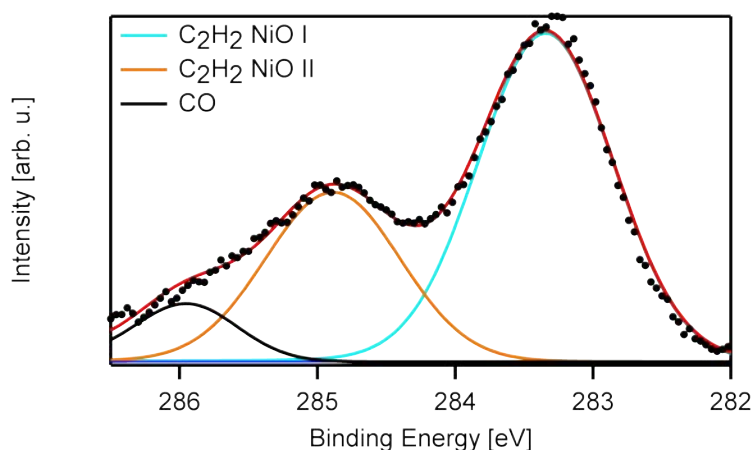


**Figure 6.29:** Spectrum and fit of the adsorption of acetylene on a 2 ML thick NiO film after an exposure of 7.3 L of acetylene.

The quantitative analysis reveals that the first species adsorbs up to an exposure of 5 L and then saturates with a coverage of 0.17 ML. The second peak saturates already at  $\sim 1$  L at a coverage of 0.09 ML. (cf. Figure 6.30) So the overall saturation coverage is 0.26 ML, which is roughly the same amount than on the 1 ML thick nickel oxide film ( $\sim 0.22$  ML). In contrast to the thinner film the amount of the second acetylene species on the nickel oxide is higher. This suggest that this species is acetylene on the stoichiometric NiO while the first species is C<sub>2</sub>H<sub>2</sub> adsorbed on a chemical different site. As CO does not adsorb on a closed nickel oxide layer at these low temperatures, it is assumed from the small CO-peak that the film is not completely closed and only traces of CO which does not interfere with the later reaction experiments are adsorbed.

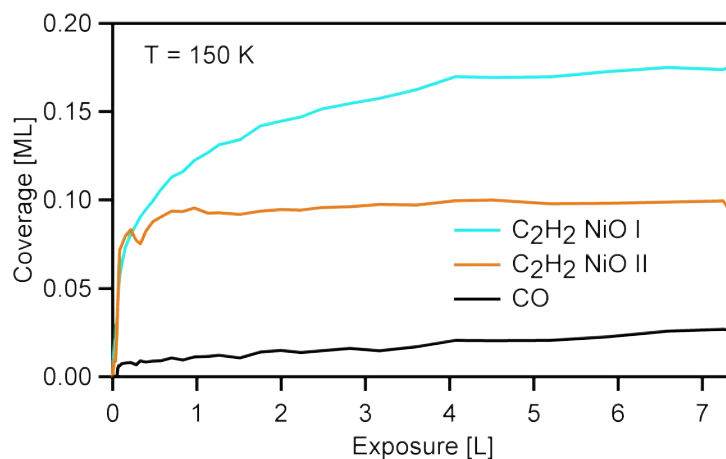


**Figure 6.30:** Quantitative analysis of the adsorption of acetylene on 2 ML thick NiO film

### 6.3.2.2 Reaction

In Figure 6.31 the quantitative analysis of the reaction of the previously adsorbed acetylene is presented. Till 180 K parts of both species, 0.09 ML for the first species and 0.02 ML for the second species, decline very fast, leading to the assumption that these molecules desorb, because no other species arise. From this temperature on, the remaining 0.08 ML of the first species at 283.3 eV decrease constantly till 280 K. The amount of second species is constant till 230 K and afterwards it decreases completely. Two new species at 283.4 and 284.7 eV, identified as not further specified carbon species on pure nickel, arise. The identification is due to the fact that the

2 ML thick film gets reduced during the reaction and at 500 K nothing is left in the C 1s region, everything has reacted with oxygen either to water or carbon dioxide. Remaining oxygen ( $\sim 80\%$  ML = 0.8 ML) is still visible in the O 1s region after the experiment was finished.

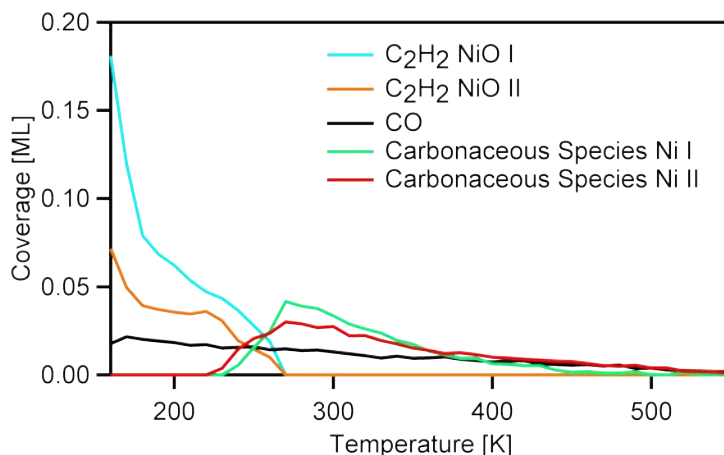


**Figure 6.31:** Quantitative analysis of the reaction of acetylene on 2 ML thick NiO film

### 6.3.3 NiO film: 6 ML

#### 6.3.3.1 Adsorption

As mentioned before, the six monolayer film has nearly bulk-like NiO structure and stoichiometry. This means the ratio between the nickel and the oxide is one to one and the crystal lattice is a fcc crystal. The amount of facets and edges is relatively high<sup>31</sup>. When acetylene adsorbs at 120 K on this surface, two peaks are visible in the C 1s region. The first has a binding energy of 283.8 eV while the other is located at 285.8 eV (cf. Figure 6.32). The peaks are rather broad compared to prior experiments on the clean Pd(100) surface. This broadening is explained by the higher disorder of the surface and the adsorption of acetylene in no distinct adsorption site. Nevertheless, two different peaks are clearly visible. By the deconvolution (see Figure 6.32 a and b) of this adsorption experiment it becomes clear that two peaks are not sufficient to describe the behavior and a third peak at 285.1 eV is added. It is assumed that this third peak belongs to a third unspecified acetylene species because uncovered palladium in the corresponding amount can be excluded.

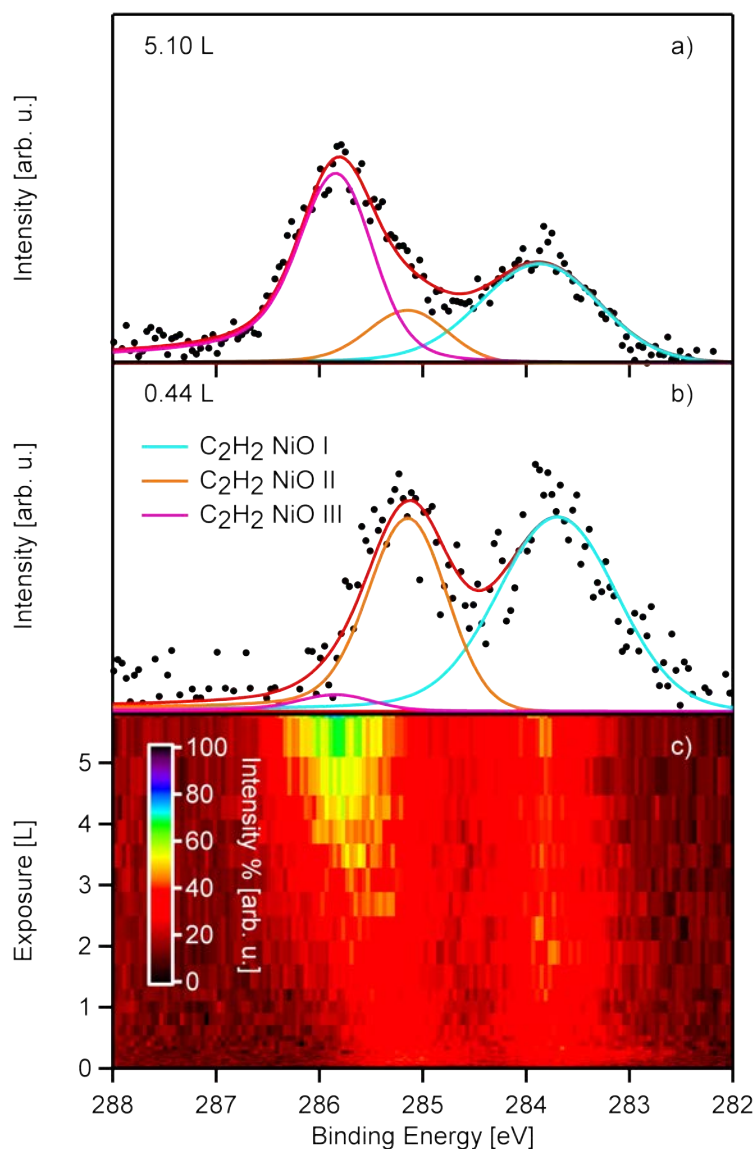


**Figure 6.32:** Spectra a) and b) and densityplot c) of the adsorption of acetylene on 6 ML NiO

The quantitative analysis (cf. Figure 6.33) reveals an overall coverage of 0.08 ML of acetylene. Both peaks of acetylene on NiO rise nearly simultaneously to an exposure of 0.2 L. Afterwards the third species starts to grow and it seems that this species is in a very different chemical surrounding due to its almost linear growth. Please note that the coverage on the NiO film is very low compared to Ni, Pd and the adsorption on the wetting layer.

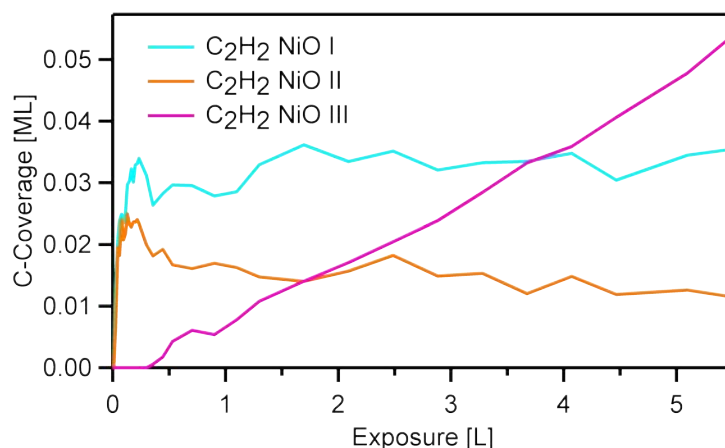


**Figure 6.33:** Quantitative analysis of the adsorption of acetylene on 6 ML NiO

### 6.3.3.2 Reaction

From a temperature of 140 K on, the two visible signals decrease to a temperature of 230 K, at which the peak at 286.0 eV binding energy vanishes. At 280 K no signal can be found anymore in the C 1s region. A deconvolution is necessary to gain more insight into the reaction behavior of the acetylene on the 6 ML NiO film. The respective fits were done in agreement with the adsorption experiment discussed above (see Figure 6.34). This means that in the beginning three species are recognizable; the first species at 283.8 eV, the second species at 285.1 eV and the third species at 285.8 eV. The quantitative analysis is presented in Figure 6.35. Here it can be seen that from 140 K all three species decrease at the same rate till 230 K. At this temperature, the second species has almost vanished and the first species has decreased by 50%, from 0.04 to 0.02 ML, and it is completely gone at 280 K. The third species desorbs at 230 K instantly. The slow decrease of all three species in the beginning of the reaction experiment and the rather large temperature range in which the desorption takes place for the first and second species indicates that not a single reaction step has to be taken for the molecule to desorb but several indistinguishable processes induced by reconstructions of the surface. From the knowledge of the fast desorption of the third species one could speculate that this species adsorbs on rather distinct adsorption sites, for example on steps, while the first and second species adsorb on reactive spots like kinks and dislocations.

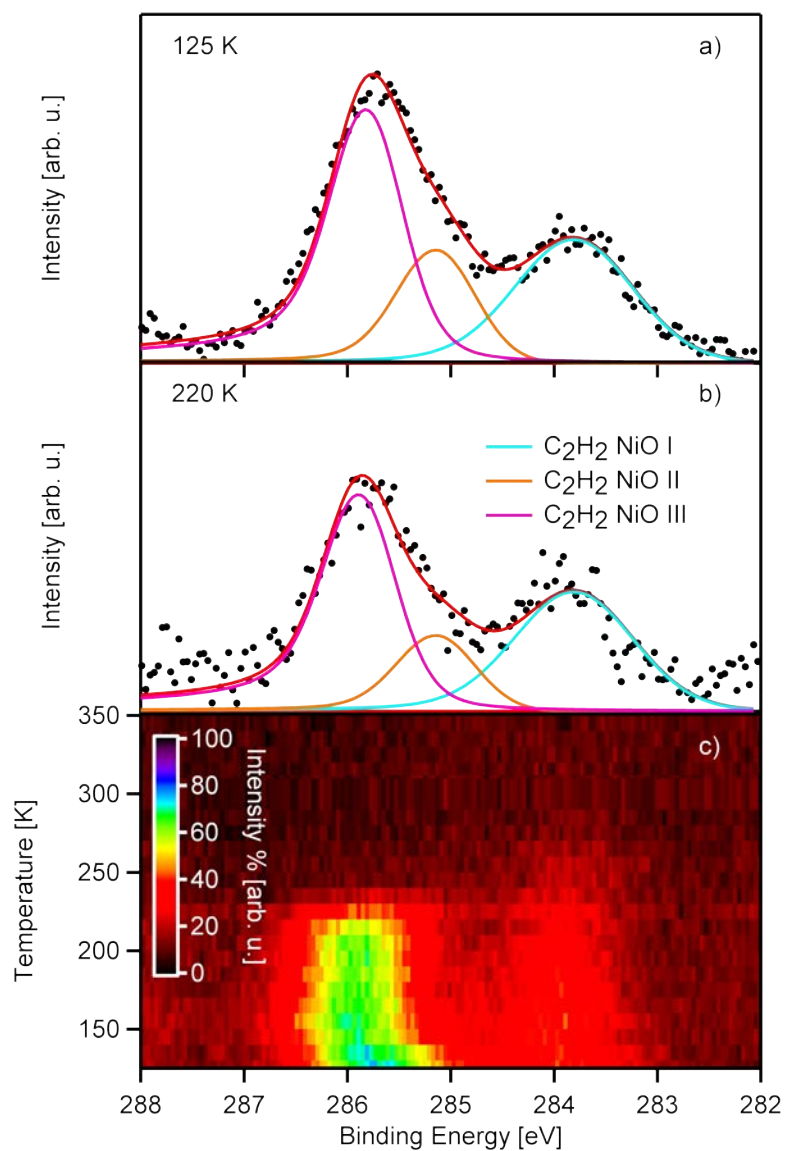


**Figure 6.34:** Spectra and density plot of the reaction of C<sub>2</sub>H<sub>2</sub> on 6 ML NiO/Pd(100)

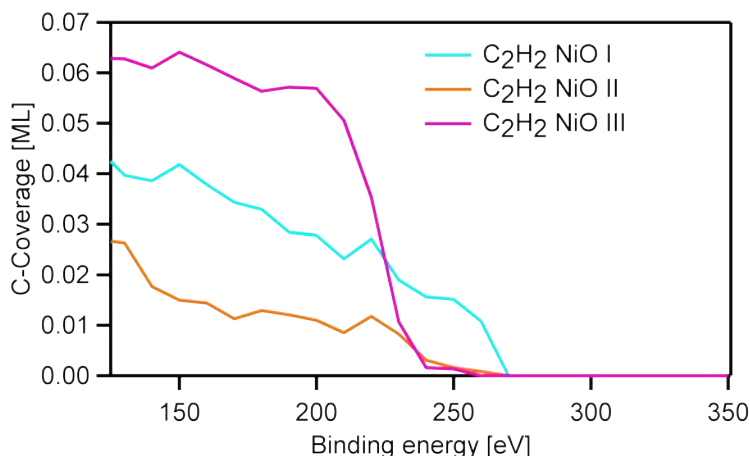


**Figure 6.35:** Quantitative analysis of the reaction of acetylene on 6 ML NiO/Pd(100)

## 6.4 Conclusion

The adsorption and reaction of acetylene on clean Pd(100) was revisited and the behavior on oxygen-precovered Pd(100) was investigated using fast in situ x-ray photoelectron spectroscopy, by recording of the C 1s and Pd 3d<sub>5/2</sub> regions. On the clean surface, the adsorption of a single molecular species in a fourfold hollow site is found. The data are consistent with the previously proposed di- $\sigma$ /di- $\pi$  bonded adsorption geometry, with the  $\pi$ -interaction occurring to those two Pd atoms of the fourfold hollow site, which are not involved in the di- $\sigma$  bonds. From the characteristic changes of the Pd 3d<sub>5/2</sub> spectra, it is deduced that at low coverage acetylene molecules adsorb at larger intermolecular distances, such that Pd surface atoms are in contact to only one molecule. At higher coverages an increasing number of Pd surface atoms are in contact to 2 molecules. The observed behavior is quantitatively explained by a simple statistical adsorption model. Upon heating, a small shift in the C 1s spectra around 200 K indicates changes in the arrangements of the acetylene molecules on the surface. Around 390 K, dehydrogenation to a CCH species and also a completely dehydrogenated species occurs. On the oxygen-precovered surface, overall the same reaction behavior is observed. The main difference is that acetylene dehydrogenation already starts upon adsorption at 130 K and the maximum CCH population and the onset for complete dehydrogenation are shifted to lower temperatures by 200 K, indi-

cating a drastically enhanced reactivity towards dehydrogenation of acetylene followed by oxidation. The adsorption and reaction of acetylene on the different thick nickel oxide layers, namely 1, 2 and 6 ML, show an increasing reactivity with decreasing film thickness. The nickel oxide monolayer, C<sub>2</sub>H<sub>2</sub> starts to dehydrogenate around a temperature of 200 K, comparable to the oxygen precovered palladium. On the 2 ML thick nickel oxide film the main part of the acetylene desorbs while the minority also dehydrogenates at 250 K. In contrast to the prior films the adsorbed C<sub>2</sub>H<sub>2</sub> completely desorbs, instead of reacting at 6 ML thick nickel oxide film.

# Chapter 7

## C<sub>2</sub>H<sub>4</sub>

### 7.1 C<sub>2</sub>H<sub>4</sub> on Pd(100)

Ethylene on transition metal crystal surfaces has been studied on Pd(111)<sup>126,152</sup>, Pd(110)<sup>23</sup> and also on Pd(100)<sup>153–155</sup>. In these former studies, it was proposed by vibrational spectroscopy that ethylene adsorbs molecularly in the temperature range between 80 and 150 K, either as *di*– $\sigma$ -species or  $\pi$ -species. Both species are present on the surface, with the *di*– $\sigma$ -species being the more stable one<sup>153</sup>. The adsorption site for both species is determined by coadsorption experiments (see section 7.2 and 7.3.1). For the reaction a decay to CH and CCH<sub>3</sub> was found at a temperature of 280 K<sup>153</sup> with EELS measurements. Both species occur at the same temperature. One has to note that EELS is not a quantitative technique and therefore one species could be a minor product of the reaction on reactive sites.

#### 7.1.1 Adsorption

If ethylene is dosed at a pressure of  $6.7 \times 10^{-9}$  mbar, at a sample temperature of 150 K a peak with two shoulders is observed (cf. Figure 7.1). This profile is considered as an overlap of the above mentioned *di*– $\sigma$ - and  $\pi$ -species with its vibrational splitting. Minor amounts of CO and carbidic carbon were also found. But these impurities are assumed to have no effect on the discussed experiments.

The deconvolution of the spectrum (see Figure 7.1b) shows the two contributions from the two species (283.2 and 283.6 eV). Each species has its vibrational satellite at a 0.36 eV higher binding energy. The peak of the vi-

brational splitting of the species at lower binding energy has nearly the same binding energy than the adiabatic peak of the species at the higher binding energy. The assignment of the species was based on the thermal evolution of the system as di- $\sigma$ -ethylene is the thermally more stable species<sup>153</sup>, see below. The peak with the lower binding energy is the  $di-\sigma$ -species and the one with the higher binding energy is the  $\pi$ -species. The S-factor for both species is 0.34, which leads to the conclusion, that two hydrogens are bound to one carbon atom. The sharp peaks result from distinctive adsorption sites and due to the vibrational splitting molecular adsorption is assumed. Looking at the evolution of the peaks at higher coverages a small shift to higher binding energy ( $\sim 0.2$  eV) is visible, which is attributed to the intermolecular interactions.

The quantitative analysis of the adsorption, shown in Figure 7.2, results in a total carbon saturation coverage of 0.24 ML. The  $di-\sigma$ -species saturates at 0.6 L (0.06 ML) and the  $\pi$ -species at 1.0 L (0.18 ML). Both species appear from the start on, but the growth rate differs, with  $\pi$ -species growing faster (see Figure 7.2).

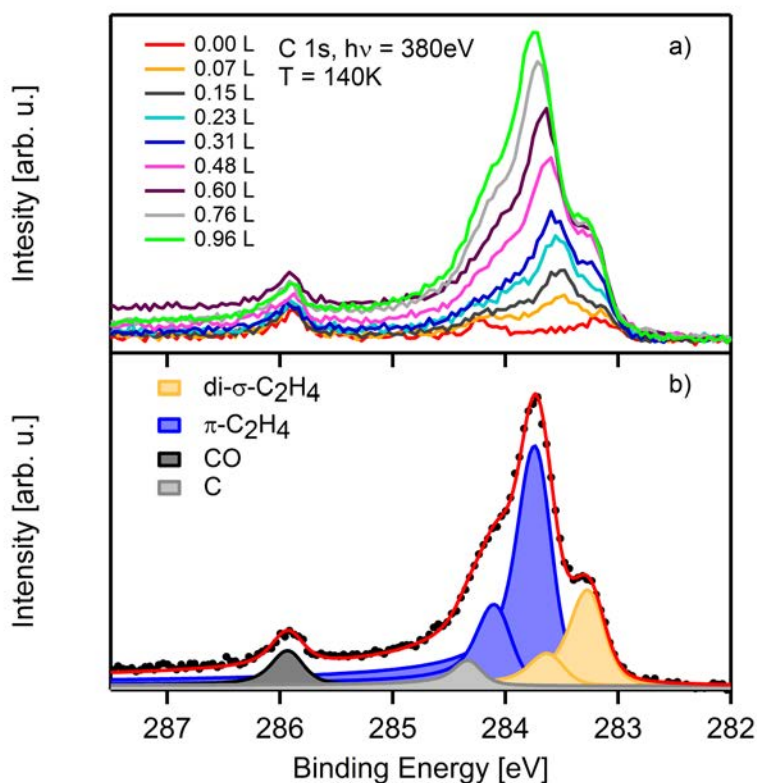


**Figure 7.1:** Spectra of the adsorption of C<sub>2</sub>H<sub>4</sub> on Pd(100)

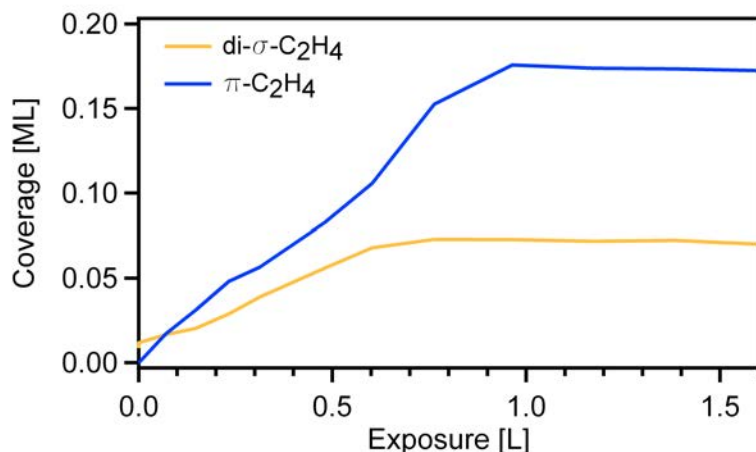


**Figure 7.2:** Quantitative analysis of the adsorption of C<sub>2</sub>H<sub>4</sub> on Pd(100)

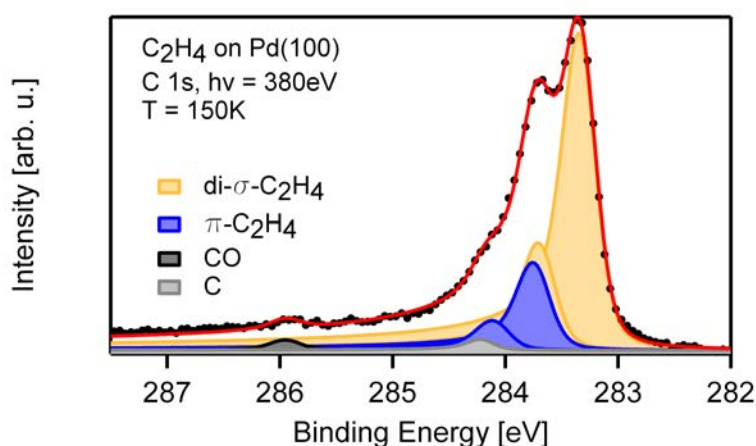


**Figure 7.3:** Higher pressure ( $2.1 \times 10^{-6}$  mbar) adsorption experiments of C<sub>2</sub>H<sub>4</sub> on Pd(100) at 150 K. In comparison to the adsorption at  $6.7 \times 10^{-9}$  mbar the amount of the *di* –  $\sigma$ -species is increased by a factor of four.

Till now, the adsorption at low pressure was discussed and in the following the pressure dependency of the adsorption is shown by experiments at higher adsorption pressure (up to  $2.1 \times 10^{-6}$  mbar) resulting in a higher total coverage. A time resolved picture was impossible and therefore only the final spectrum is presented in Figure 7.3. The different carbon coverages depending on the ethylene pressure on the sample are shown in Figure 7.4. This pressure dependency becomes obvious by comparison of the coverages achieved with high ( $2.1 \times 10^{-6}$  mbar, 0.46 ML) and low ( $6.7 \times 10^{-9}$  mbar, 0.24 ML) pressures. Another interesting aspect is the pressure-dependent coverage of the two species. This data supports that each species has its own

signal and the two species differ in the adsorption site and the binding to the surface. Interestingly this suggests that the two carbon atoms of each species has the same chemical environment, this means both carbon atoms of one molecule have to sit either on top, bridge or hollow sites.

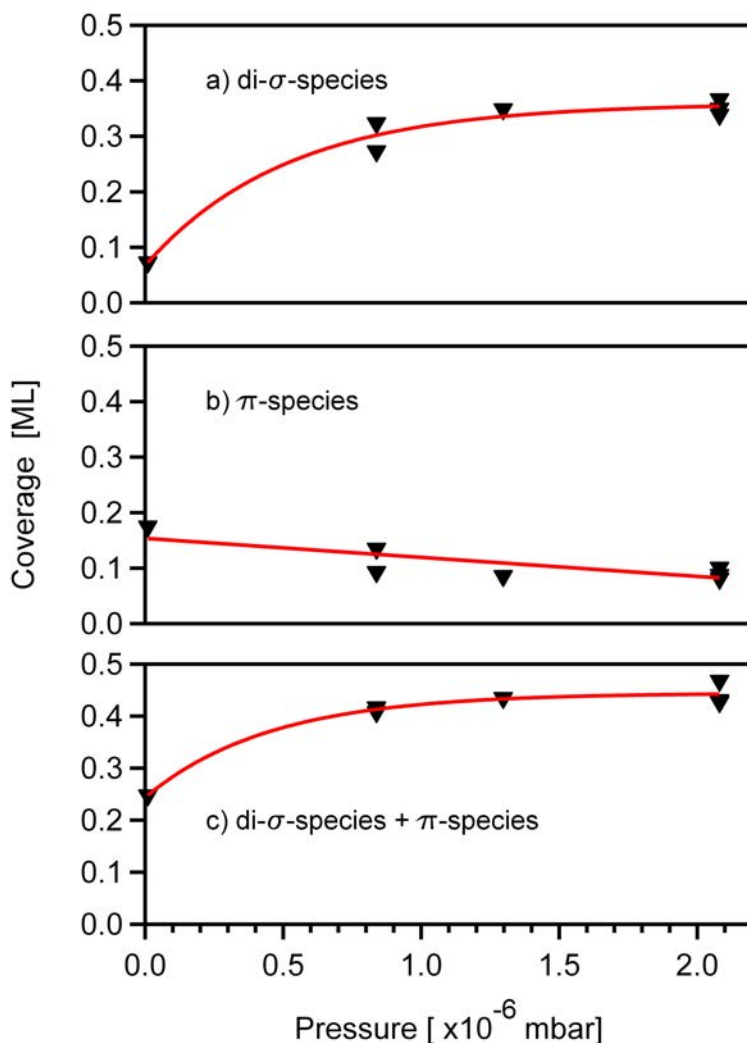


**Figure 7.4:** Pressure dependency of the adsorption of C<sub>2</sub>H<sub>4</sub>; a) di- $\sigma$ -ethylene b)  $\pi$ -ethylene c) total carbon coverage of both species

The saturation coverage in literature is known as 0.74 ML of carbon<sup>153</sup>. The reason for the discrepancy is the higher adsorption temperature in the here presented experiments. In these experiments, the adsorption temperature was 140 K in contrast to literature where the temperature was 80 K. The difference in coverage is mainly in the amount of the  $\pi$ -species which starts to desorb at a temperature of 100 K and takes place over a temper-

ature range of 100 K to 300 K. Interestingly, the  $\pi$ -species is the majority species at low pressures whereas the di- $\sigma$ -species is the majority species at high pressures. An explanation for this is that the adsorbing molecule has to overcome an energy barrier to become a di- $\sigma$ -species. This energy barrier might exist due to lateral interactions.

### 7.1.2 Reaction

After the adsorption of ethylene the system was heated and every 10 K a spectrum was measured. A color-coded density plot is presented in Figure 7.5. In the experiment, the intensity of the  $\pi$ -species (283.6 eV) decreases up to a temperature of 280 K. Then the di- $\sigma$ -species also decreases and a new species with the binding energy of 283.1 eV is formed. At 400 K this species reacts to a single sharp peak at 284.1 eV.

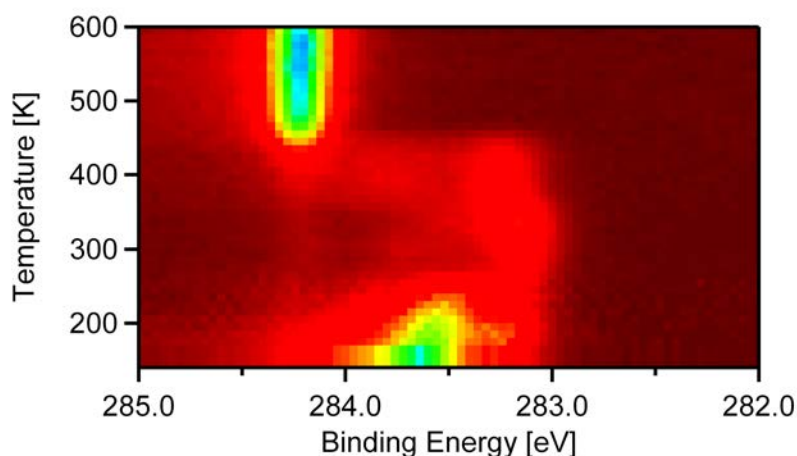


**Figure 7.5:** Density plot of the reaction of C<sub>2</sub>H<sub>4</sub> on Pd(100)

The fit of the above mentioned contributions reveals more insight into the reaction of ethylene on Pd(100) (cf. Figure 7.6). The first spectrum is fitted like the adsorption experiment in section 7.1.1. Two peaks are recognizable, for each the di- $\sigma$ -species and the  $\pi$ -species with a binding energy of 283.2 eV and 283.6 eV respectively. Both species have a vibrational satellite with a S-Factor of 0.34 as they are both ethylene on different adsorption sites. Also, for both species the distance in the binding energy of the adiabatic and the vibrational splitting peak is 0.36 eV. At higher temperatures the intensity of the  $\pi$ -species decreases till 290 K, where it is gone. In contrast, the amount of the di- $\sigma$ -species stays constant at 0.06 ML (cf. Figure 7.7) till 200 K.

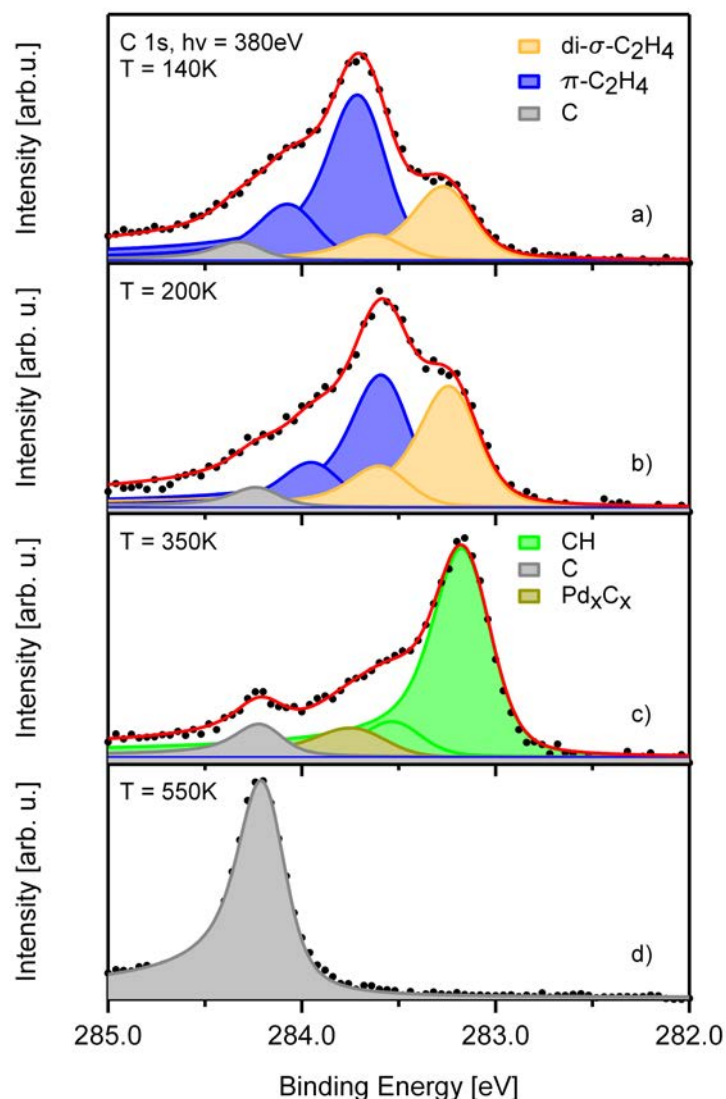


**Figure 7.6:** Representative spectra and fits of the reaction of C<sub>2</sub>H<sub>4</sub> on Pd(100) a) 140 K b) 200 K c) 350 K and d) 550 K

Above 200 K the di- $\sigma$ -signal also decays and two new species rise. For the first one the binding energy is 283.7 eV and the S-Factor is 0.26 in an energy distance of 360 meV. So the species is identified as HCCH<sub>2</sub>, which is mentioned by Stuve et al<sup>153</sup>. The other species (283.2 eV) is the majority species (0.05 ML) and is identified by its S-factor of 0.17 ( $\Delta E = 360\text{meV}$ ) as CH which was also seen before<sup>153</sup>. In comparison to the acetylene experiments ethylene reacts to CH and not to CCH. A third reaction species arise at 340 K which cannot be identified because of its low intensity. It is assumed, that this is an undefined mixture of Pd<sub>x</sub>C<sub>x</sub>. At 550 K, 0.1 ML pure

carbon is measured at 284.1 eV. No vibrational splitting is visible and therefore the identification as pure carbon seems reasonable. The discrepancy of the amount of pure carbon and the amount of the di- $\sigma$ -species is attributed to photoelectron diffraction<sup>136</sup>. Interestingly, the amount of the reaction products is the same amount as of the di- $\sigma$ -species leading to the assumption the  $\pi$ -species desorbs while in comparison the di- $\sigma$ -species is reacting.

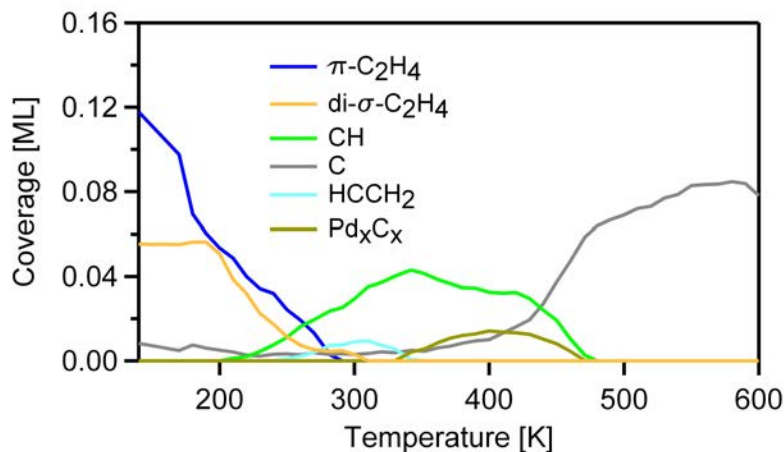


**Figure 7.7:** Qualitative analysis of the reaction of  $C_2H_4$  on Pd(100)

## 7.2 Coadsorption with CO

For identification of the adsorption site, it is helpful to exclude certain adsorption sites by coadsorption with this molecule. In this section, the coadsorption with carbon monoxide is studied because CO adsorbs on the bridge sites<sup>53</sup>. After the saturation of ethylene at  $7.0 \times 10^{-7}$  mbar, CO was dosed at the same pressure. The adsorption process of ethylene cannot be followed in situ as discussed in the previous section, due to the relatively high pressure; however the adsorption of CO and the replacement of ethylene with CO could be monitored regularly. Due to the relatively high pressure, the amount of the di- $\sigma$ -species is higher than that of the  $\pi$ -species (cf. Figure 7.8 top). This phenomenon was discussed in the previous section. After the adsorption of carbon monoxide, the di- $\sigma$ -species is reduced more than the  $\pi$ -species (cf. Figure 7.8 bottom). This suggests that CO adsorbs on the same sites than di- $\sigma$ -ethylene. In the following this is discussed in detail and an adsorption model is presented.

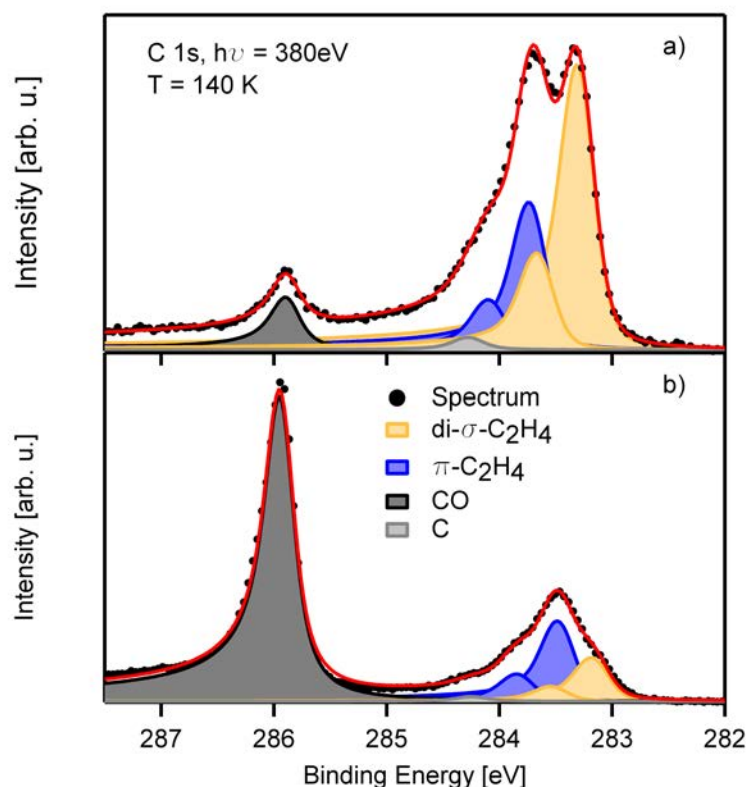


**Figure 7.8:** Representative spectra of the coadsorption of C<sub>2</sub>H<sub>4</sub> and CO

The fits were done with the same parameters as in the adsorption and reaction experiments (cf. sec. 7.1.1); representative spectra are shown in Figure 7.8. The quantitative analysis is presented in Figure 7.9. Up to 0.5 L CO a rearrangement takes place evidenced by the amount of the di- $\sigma$ -species that decreases from 0.27 ML to 0.13 ML while the  $\pi$ -species increases from 0.13 ML to 0.20 ML. An explanation of this behavior could be that the CO rearranges the di- $\sigma$ -species and some molecules change their adsorption site to the one of the  $\pi$ -species, while another part desorb. After this rearrangement, the amounts of both species decrease in the same way. This is due to the adsorption of CO that displaces C<sub>2</sub>H<sub>4</sub> from the surface.

From literature it is known that CO adsorbs only on bridge sites<sup>53</sup>. So the former discussed behavior of displacing the di- $\sigma$ -species suggests that both CO and di- $\sigma$ -ethylene adsorb on the same site, the bridge site. A model is depicted in Figure 7.10 and assigns the di- $\sigma$ -ethylene to the bridge site because of the direct identification due to the coadsorption experiment and the  $\pi$ -species to the hollow site. The reason for the proposed adsorption site of the  $\pi$ -ethylene is given by the preadsorbed oxygen experiment discussed

in section 7.3.1. This assignment is nevertheless speculative due to the fact that only the coadsorption experiments are used to identify the adsorption site under the condition that the coadsorbed molecule, here CO, behaves the same way than on the pristine palladium surface. The model here has its drawbacks because the maximum coverage obtained experimentally is 0.4 ML of CO but normally below 160 K the maximum coverage is 0.75 ML. The distinct adsorption site of di- $\sigma$ -ethylene is not clear besides two facts: the species is displaced by CO and both  $\sigma$ -bonds have to be of the same character. Nevertheless the model gives a possible adsorption sites of ethylene.

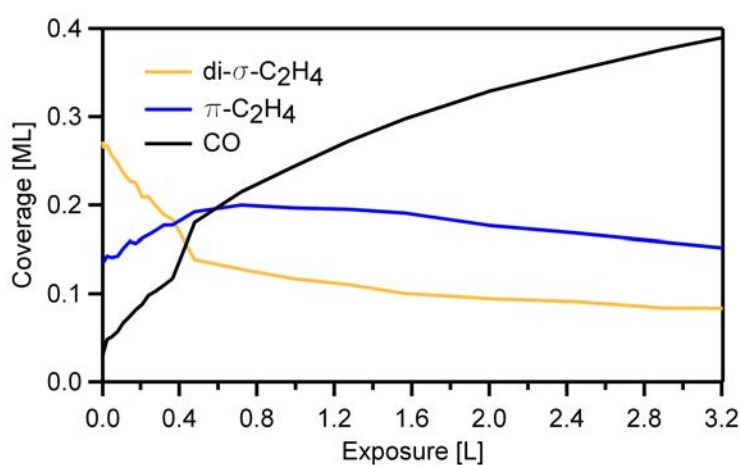


**Figure 7.9:** Quantitative analysis of the co adsorption of CO and ethylene

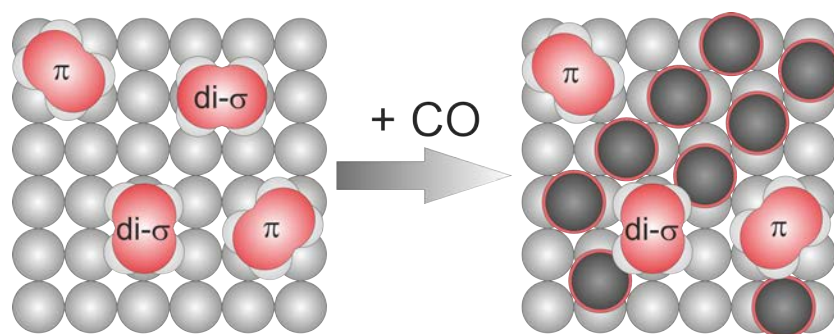


**Figure 7.10:** Model scheme of the coadsorption of CO with C<sub>2</sub>H<sub>4</sub>. CO: black with red rings, Palladium: grey, Carbon: red, Hydrogen: light grey

## 7.3 Coadsorption with O

### 7.3.1 Adsorption

In this experiment, the coadsorption of oxygen and ethylene was studied. The first step was to adsorb 0.25 ML of oxygen. The corresponding spectra in the O 1s region are depicted in Figure 7.11a, showing no significant change in hydroxide concentration as seen in the adsorption of acetylene on O/Pd(100). Now ethylene was dosed onto the oxygen covered Pd substrate and meanwhile the C 1s core region was observed (cf. figure 7.12a).

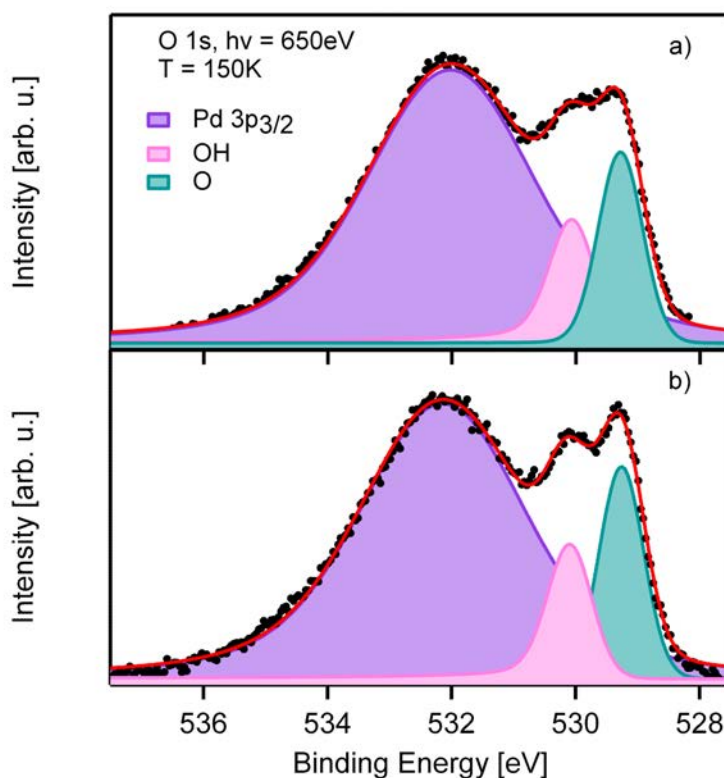


**Figure 7.11:** Oxygen coverage before (a) and after (b) the adsorption experiment

In contrast to the former adsorption experiment without preadsorbed oxygen there is only one peak. This peak is broader and no fine structure is visible. So it is not possible to tell if ethylene adsorbs molecularly on the surface from this experiment, but other experiments have shown this fact<sup>153,154,156,157</sup>. This broad single peak is fitted with only one component of 283.7 eV (cf. figure 7.12b). This binding energy suggests that it is the  $\pi$ -species. The higher width is associated to the interaction of ethylene and

the dissociated oxygen. The quantitative analysis gives a saturation coverage of 0.24 ML (cf. figure 7.13). From this result one can assume that the here adsorbed species is indeed the  $\pi$ -species. From the steric point of view (cf. fig. 7.14) only the 4-fold hollow site is available.

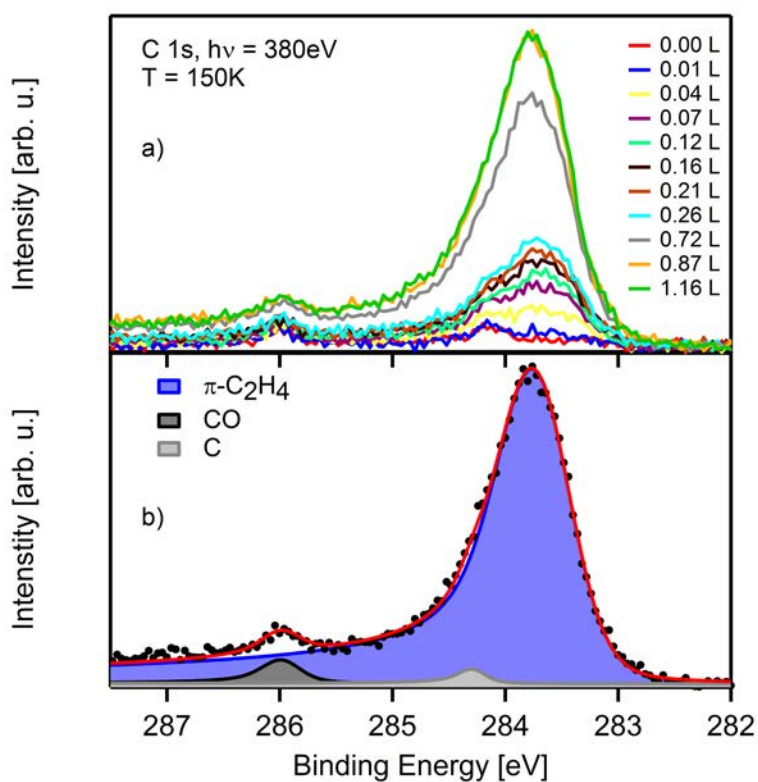


**Figure 7.12:** Spectra (a) and fit (b) of the adsorption of ethylene on O/Pd(100)

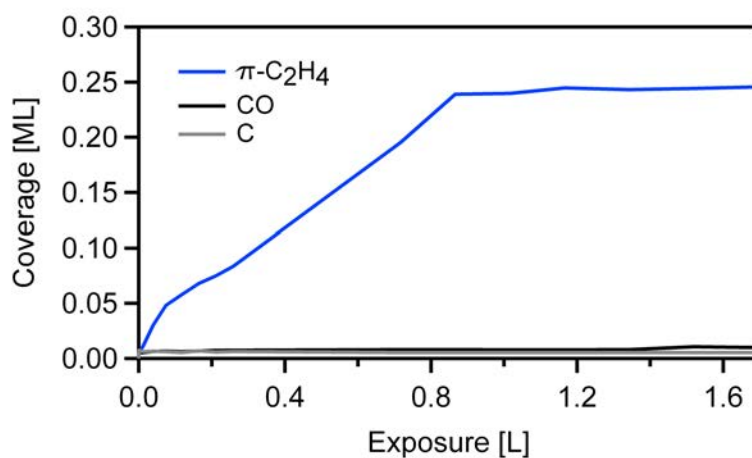


**Figure 7.13:** Quantitative analysis of the adsorption of ethylene on O/Pd(100)

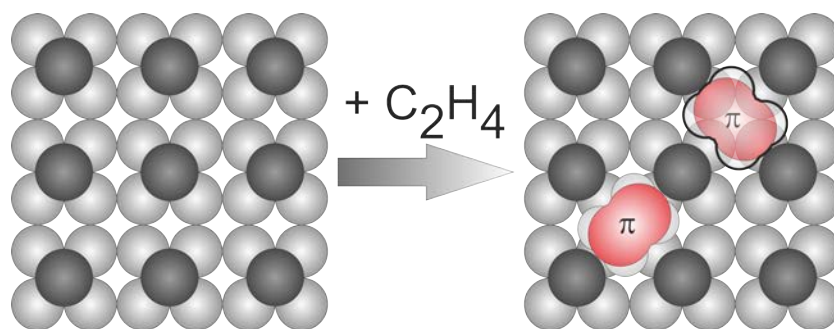


**Figure 7.14:** Model of the adsorption site of ethylene on an oxygen precovered Pd(100) substrate. Light gray: palladium, dark gray oxygen, red: carbon atoms in of the ethylene molecule

### 7.3.2 Reaction

After the adsorption experiment the system was continually heated from 160 K to 600 K. Interestingly, the C 1s peak vanishes without any reaction (cf. fig. 7.15). This behavior was also seen before<sup>153,156</sup>. In contrast to the reaction of acetylene on oxygen precovered Pd(100) surface, the reactivity is not enhanced.

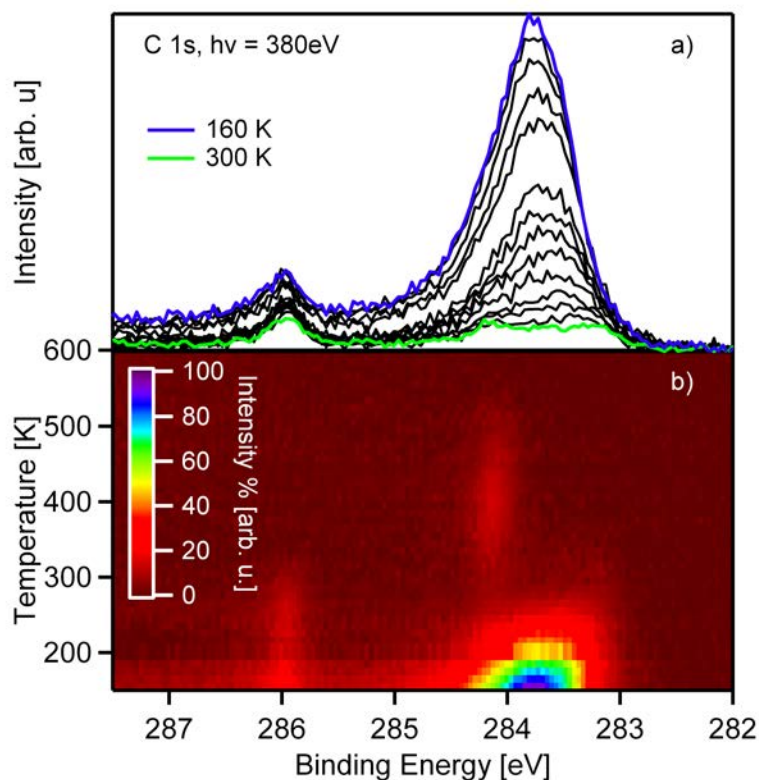


**Figure 7.15:** Spectra and density plot of the reaction of ethylene on O/Pd(100)

The missing reaction of  $C_2H_4$  on O/Pd(100) points to a weak bonding to the substrate, resulting in a situation where it is energetically preferable to desorb than to react for the molecule. This is also a strong hint that the ethylene only adsorbs as the  $\pi$ -species. Another reason for the absence of a reaction could be the missing of adsorption sites for decomposition products.

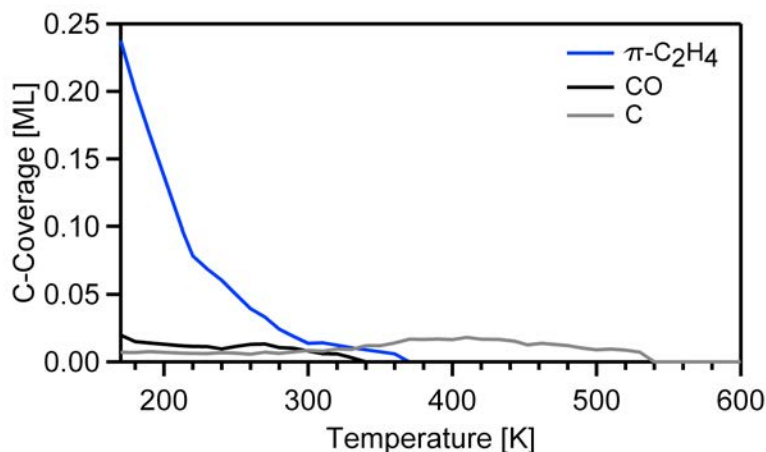


**Figure 7.16:** Quantitative analysis of the reaction of ethylene on O/Pd(100)

## 7.4 Conclusion

The study of  $C_2H_4$  has shown that two species, di- $\sigma$ - and  $\pi$ -species adsorbs at 150 K on the clean palladium surface. The more stable di- $\sigma$ -species reacts at 200 K to  $HCCH_2$  while the other species desorbs over several different channels from 100 K. In this context, the influence of the pressure during the adsorption was studied, revealing that the di- $\sigma$ -species becomes the majority adsorbed species at higher pressures up to  $2 \times 10^{-6}$  mbar. From the coadsorption experiments with CO and O, it can be suggested that the adsorption sites for the  $\pi$ -species is the on-top site while the di- $\sigma$ -species adsorbs on the bridge site. On an oxygen precovered surface no reaction takes place and the molecule only desorbs.



# Chapter 8

## $C_6H_6$

### 8.1 $C_6H_6$ on Pd(100)

The adsorption of benzene was studied on several different (100) metal surfaces including Cu<sup>158</sup>, Ni<sup>159 160–162</sup>, Au<sup>163</sup> and on stepped Pt surfaces with (100) steps<sup>164</sup>. This selection of different surfaces includes transition metals from relatively high to low reactivity. On Ni(100) a diffraction pattern with a c(4x4) supercell was found leading to the statement that eight nickel atoms are interacting with one benzene molecule<sup>160</sup>. Later studies have shown that the molecular plane is parallel to the surface. A closer look to the bond character revealed that a delocalized mixture of  $\pi$  and  $\sigma$  orbitals is responsible for the chemisorption of the molecule to the Ni(100) surface<sup>162</sup>. On Cu(110), this strong interaction was not found, leading to the assumption that no reaction takes place upon heating and the molecule desorbs intact at elevated temperatures<sup>162</sup>. On Cu(100) the adsorption of the benzene molecule was found on the 4-fold hollow site. Two energetically nearly equal positions were found by calculations: the first with two carbon atoms located on the bridge site and four carbon atoms sitting on the ontop site. The other configuration is rotated by 15° around the surface normal<sup>163</sup>, such that all six carbon atoms have the same "adsorption site". On gold the hollow site is the preferred adsorption site, like copper and nickel. On the stepped platinum surfaces with (100) steps no adsorption of benzene was found at 300 K.

### 8.1.1 Adsorption

Benzene was dosed at 200 K on a clean Pd(100) crystal. The spectrum of an adsorbed benzene (C<sub>6</sub>H<sub>6</sub>) molecule has a main signal at 284.09 eV with a vibrational peak at a 0.37 eV higher binding energy, shown in Figure 8.2. The ratio between the vibrational and the adiabatic peak is 0.17 (S-Factor), which leads to the conclusion that one hydrogen atom is bound to one carbon atom, i.e. benzene adsorbs molecularly. At higher coverages, the main peak shifts to a binding energy of 284.2 eV. The quantitative analysis is shown in Figure 8.2b. The saturation coverage is 0.8 ML C atoms, i.e. 1.4 ML benzene.

A diffraction pattern was not observed by LEED, which means that there is no long range ordering of the molecules on the surface. From literature two configurations are known: one with carbon atoms in different chemical surroundings and one with all carbon atoms at the same adsorption site (cf. Figure 8.1)<sup>163</sup>. From the absence of two signals one can conclude that benzene adsorbs in the later configuration.

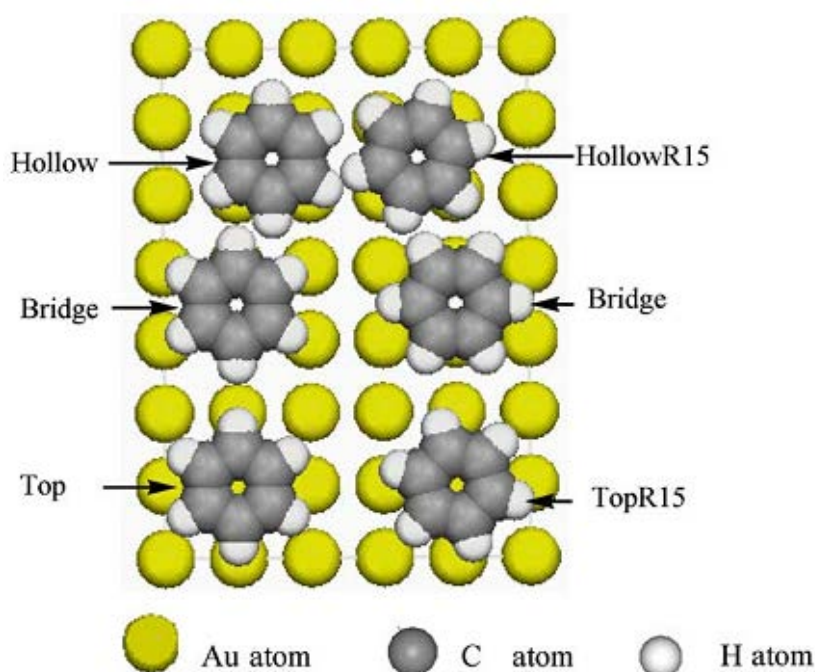


**Figure 8.1:** Possible adsorption sites of a benzene on Au(100) taken from [163]. The geometries labeled with R15 are rotated by 15°.

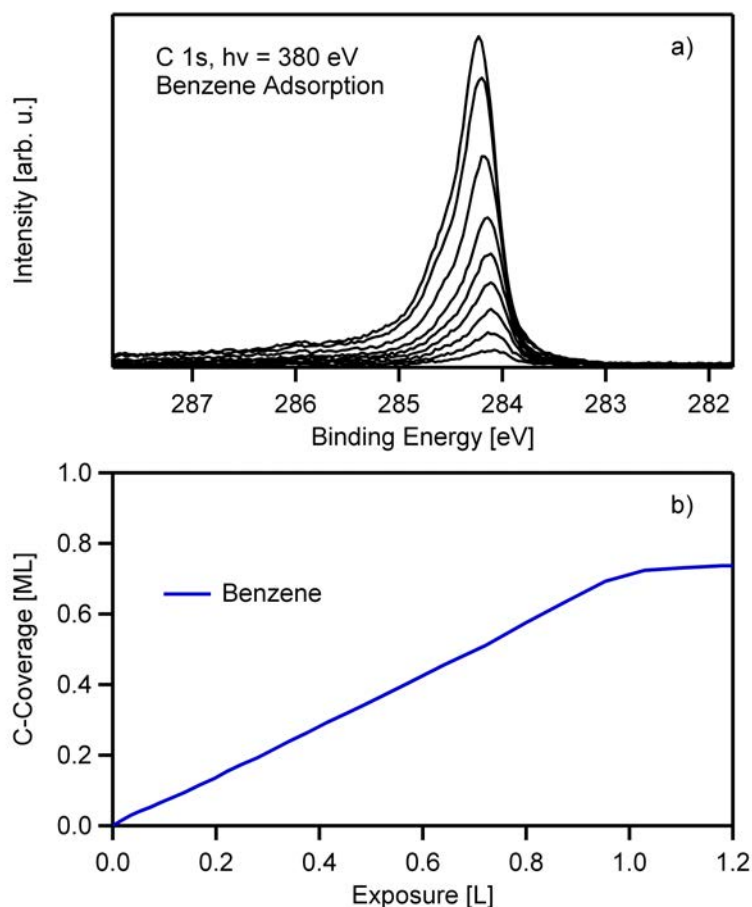


**Figure 8.2:** Spectra (a) and quantitative analysis (b) of benzene adsorption on Pd(100) at 200 K

The adsorption was also followed in the Pd 3d region to obtain additional insight. In Figure 8.3, representative spectra are presented: The bulk peak is observed at a binding energy of 335.0 eV, while the two surface contributions are located at 334.5 and 335.5 eV. The fit results are in agreement with Gladys et al.<sup>51</sup>. At higher exposures, the surface peaks disappear, while a shoulder on the higher binding energy side evolves, which can be fitted with two contributions (335.4 eV and 336.0 eV). These peaks were formerly introduced and attributed to the interaction with one and two carbon molecules<sup>53,165</sup>.

According to the analysis of Baraldi et al.<sup>91,143</sup>, the concentration of the surface atoms depends on the surface atoms interacting with the adsorbed molecules. This analysis is presented in figure 8.4. Here a fit is presented with a slope of -4 leading to the assumption that 4 surface atoms are "cov-

ered” by one benzene molecule (the error bar is  $\pm 1$  surface atom). This value seems not unreasonable, because literature mentions that the benzene molecule adsorbs parallel to the surface on a hollow adsorption site<sup>158,159,163</sup> and thereby ”covers” four surface atoms from a steric point of view. However, only one source reports from the interaction of one molecule with eight surface atoms on Ni(100)<sup>160</sup>, but this is an ordered layer which is not given here.

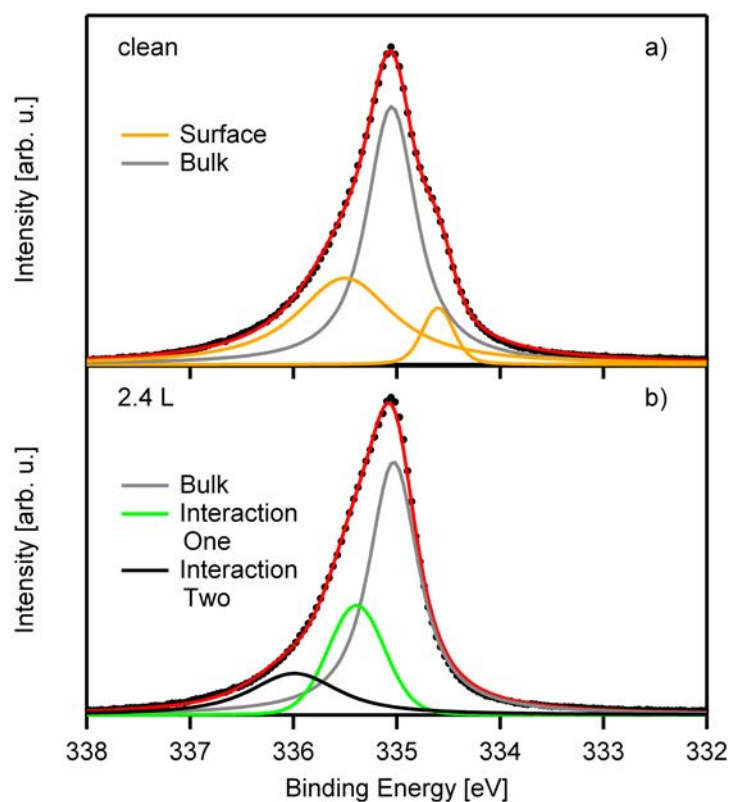


**Figure 8.3:** Spectra of the Pd 3d<sub>5/2</sub> peak before (a) and after (b) the adsorption of benzene

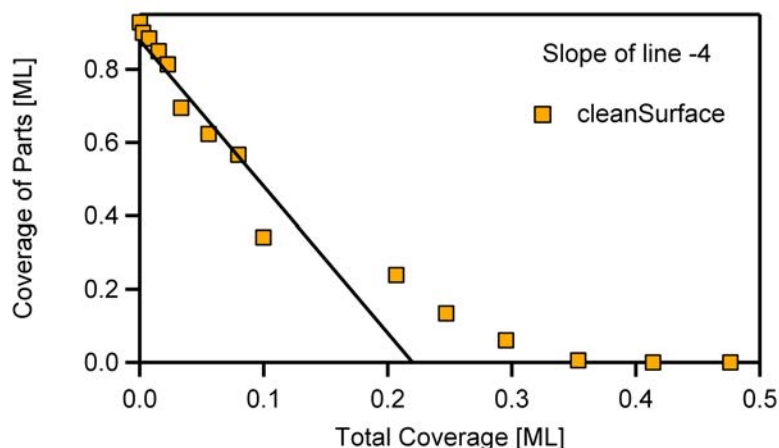


**Figure 8.4:** Analysis of the reduction of the surface atoms depending on the adsorbed coverage

### 8.1.2 Reaction

To study the reactivity of benzene on Pd(100), the sample is heated to 700 K and every 10 K a spectrum is taken. In Figure 8.5a a color-coded density plot is presented. Here it becomes obvious that the benzene signal (284.2 eV) is stable up to a temperature of  $\sim 450$  K. A small peak on the lower binding energy side appears (283.6 eV), slowly increases with temperature and reaches a maximum at  $\sim 520$  K, and then vanishes at higher temperatures. Above  $\sim 480$  K a much smaller and narrower peak at 284.2 eV is observable up to 700 K. The identification of the peak at 283.6 eV is not straight forward because the intensity is very low and the overlap with other species is too high, so that the S-Factor cannot be determined. From its binding energy it can be guessed that this is a dissociation product, which is similar to the reaction path of C<sub>2</sub>H<sub>2</sub> or C<sub>2</sub>H<sub>4</sub>, CH or CCH<sub>3</sub> (see Section 6.1 and 7.1). The narrow peak at a temperature above 500 K is attributed to carbon. The quantitative analysis (cf. Figure 8.5) shows a complete picture of the reaction behavior of benzene. From the amount of pure carbon (0.38 ML) at 550 K one can conclude that benzene partly desorbs.

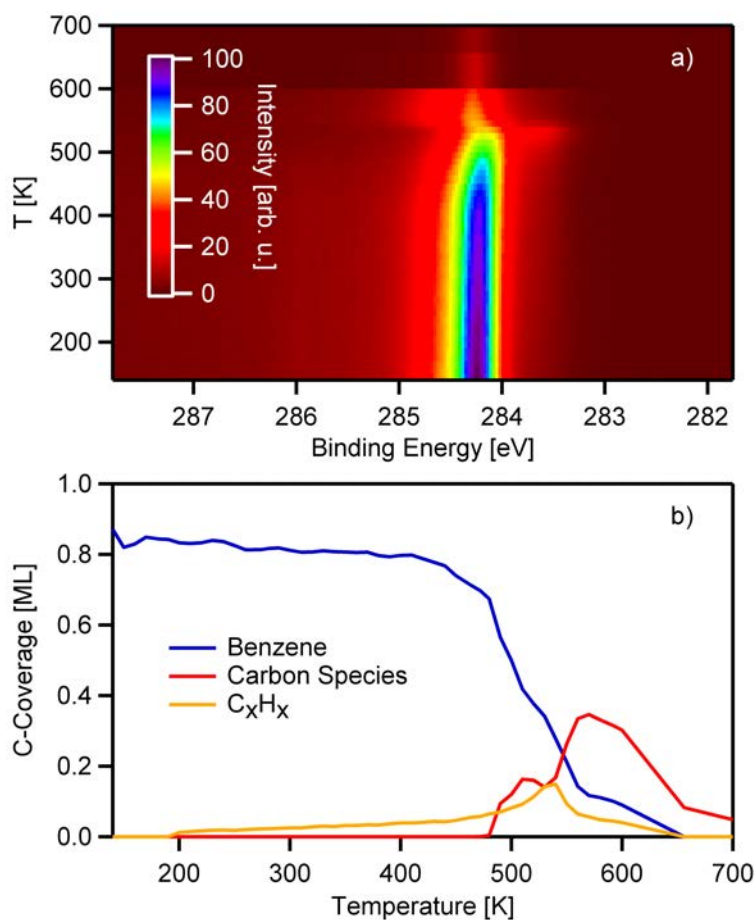


**Figure 8.5:** Density plot (a) and quantitative analysis (b) of the reaction of C<sub>6</sub>H<sub>6</sub> on Pd(100)

## 8.2 C<sub>6</sub>H<sub>6</sub> on O/Pd(100)

### 8.2.1 Adsorption

The observation of the adsorption of benzene on the oxygen-precovered palladium surface at 200 K in the C 1s region reveals one peak as for on the clean substrate at a binding energy of 284.0 eV (cf. Figure 8.6). Again a peak regarding the vibrational splitting is necessary to deconvolute this spectrum. This peak is located at a binding energy of 284.4 eV and has an S-factor of 0.17. This means that benzene adsorbs molecularly due to the fact that there is only one peak with a vibrational peak for a CH-bond. Also, minor amounts of CH (283.3 eV) are visible. The minor carbon impurity at 284.2 eV was already adsorbed on the surface before the experiment started.

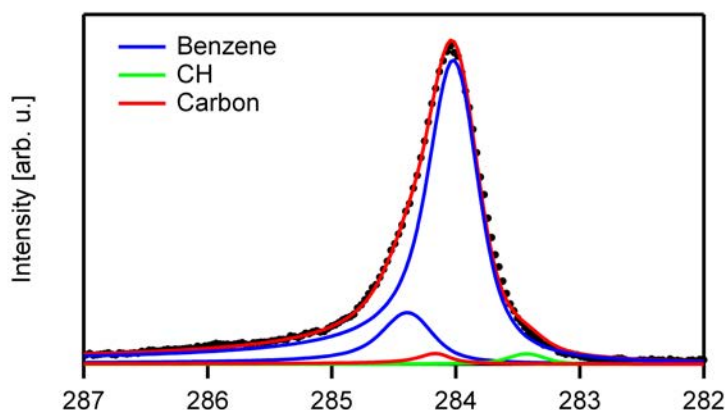


**Figure 8.6:** Fitted spectrum of the adsorption of benzene on O/Pd(100)

The quantitative analysis in Figure 8.7 reveals that the adsorption saturates at a carbon coverage of 0.6 ML, which corresponds to a coverage of 0.1 ML benzene.

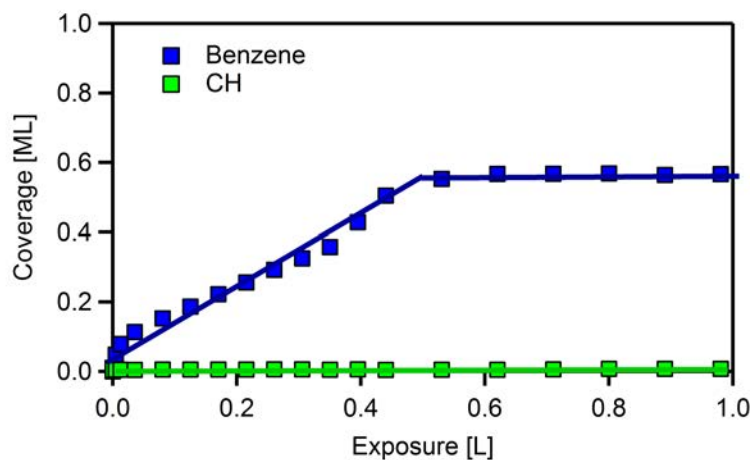


**Figure 8.7:** Quantitative analysis of the adsorption of benzene on O/Pd(100)

### 8.2.2 Reaction

In this section, the reaction of C<sub>6</sub>H<sub>6</sub>/O/Pd(100) is discussed. In Figure 8.8, the density plot is shown. The characteristic shift of the benzene peak is observed at 50 K lower temperatures than on clean Pd(100). This first impression is confirmed by the quantitative analysis in Figure 8.9. The spectrum at 125 K corresponds to the last spectrum in the uptake series at 120 K (taken at an other spot on the surface to minimize beam damage). The single

peak (284.0 eV), with its vibrational splitting at a 0.40 eV higher binding energy and a S-factor of 0.17, is assigned to molecularly adsorbed benzene. Around 300 K, the intensity drops by 40%, and at 500 K a further decrease in intensity takes place. At 480 K another species arises on the lower binding energy side and finally a new peak at 284.1 eV starts to grow. Selected fits obtained from the spectra are shown in Figure 8.8.

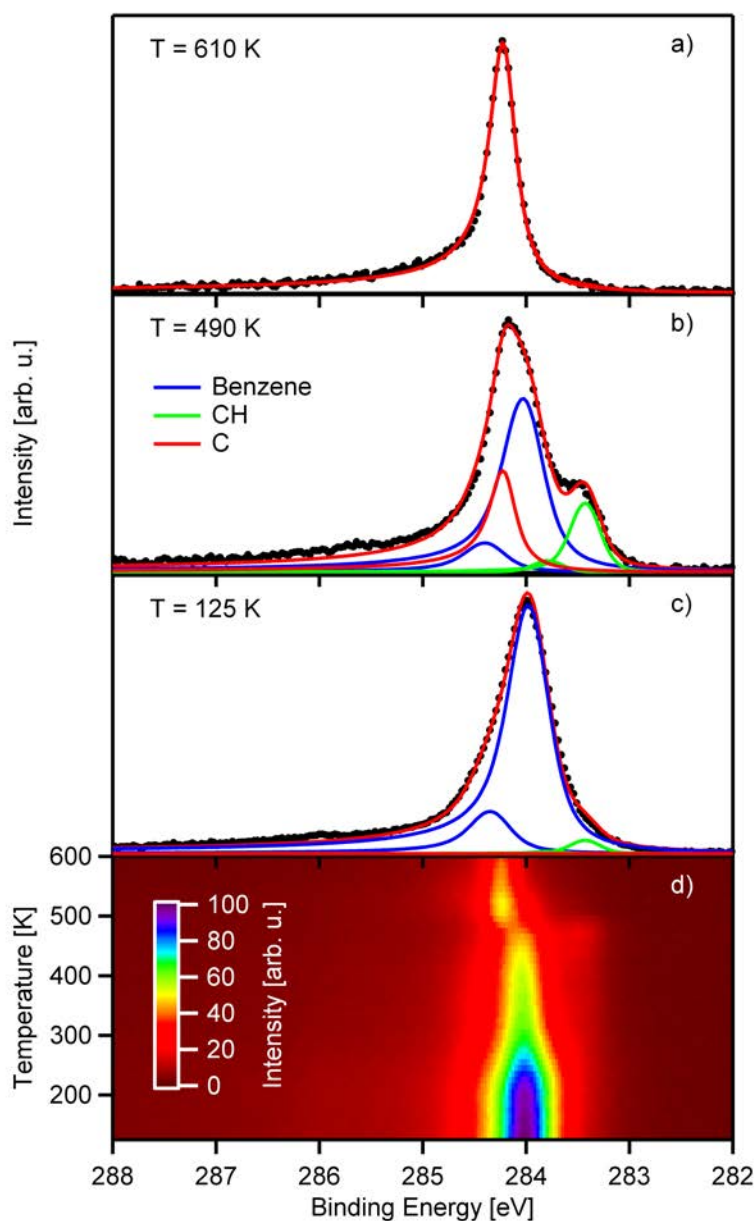


**Figure 8.8:** Spectra and density plot of the reaction of benzene on O/Pd(100). Spectra at a) 610 K b) 490 K c) 125 K and d) density plot.

From these fits and the corresponding quantitative analysis (cf. Figure 8.9) it gets obvious that at low temperatures benzene adsorbs molecularly on the oxygen-covered surface. The loss in benzene coverage of 0.25 ML at 280 K is caused by desorption. From the beginning of the experiment, a small amount (0.03 ML) of CH is recognizable. This species starts to grow at 450 K, and above 480 K it dehydrogenates completely. At 480 K, the parts of benzene, which did not desorb up to now, start to dehydrogenate to carbon. In comparison to the reaction on the clean surface the temperature for complete dehydrogenation is shifted by 50 K to lower temperatures, from 530 to 480 K. Additionally, a dehydrogenated product is formed in a lower amount, probably forming CO, CO<sub>2</sub> or H<sub>2</sub>O and desorbing instantly. The rising peak around 480 K at an binding energy of 283.7 eV is identified as CH due to its binding energy and the later species at 284.01 eV as carbon, due to the temperature stability.

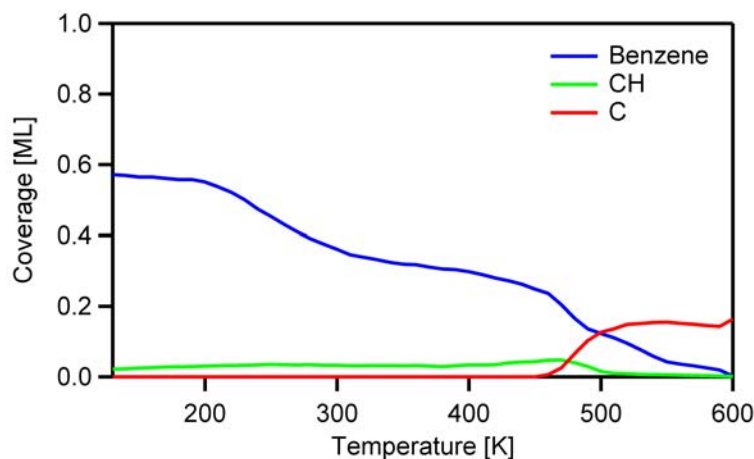


**Figure 8.9:** Quantitative analysis of the reaction of benzene on O/Pd(100)

## 8.3 Conclusion

In this chapter, the adsorption and reaction of benzene on different surfaces, namely clean Pd(100) and oxygen precovered Pd(100), were studied. The adsorption of benzene on the clean palladium surface saturates at a coverage of 0.8 ML. Benzene adsorbs molecularly, which is identified by its vibrational splitting. The analysis of the Pd 3d spectra reveal that one benzene molecule interacts with four surface atoms when adsorbing. The thermal evolution of the system shows that parts of the C<sub>6</sub>H<sub>6</sub> desorbs while other parts dehy-

drogenate at 500 K. The adsorption of benzene on an oxygen-precovered palladium surface leads to a saturation coverage of 0.6 ML and the reaction looks similar to the one on the clean surface, besides the fact that 0.2 ML already desorb at a temperature of 250 K.

Additionally, benzene was dosed on differently thick nickel oxide films and the succeeding reactions at elevated temperatures were observed, but not shown in this part due to uncertainties in the analysis. These uncertainties are caused by the lack of information besides XPS, i.e. adsorption sites and reaction products. An important role plays the quality and reproducibility of the nickel oxide film, which is in this work high but in the case of benzene on nickel oxide so many questions and problems arise that minor changes in the mentioned film properties can have a large effect, and therefore complicate the hole analysis. Nevertheless, the data and the corresponding analysis is shown in the attachments in Section 12.1.

# Chapter 9

## TEB

### 9.1 TEB on Pd(100)

To investigate a more complex system triethyleboran was chosen because it is used in organic chemistry as an initiator for radical reactions at low temperatures<sup>166</sup> and additionally it can be used to produce boron-doped graphene, so called B-graphene<sup>167</sup>. This makes it interesting to look at the reaction in UHV at low temperatures. The molecule itself is composed of three ethyl groups bound to the boron atom. The  $BC_3$  core is planar and therefore assumed to adsorb parallel to the surface like the previously studied molecules like benzene and acetylene.

#### 9.1.1 Adsorption and Reaction from 180 K

The adsorption of TEB on Pd(100) was followed by recording B 1s and C 1s levels. In the following, the experiments in the B 1s level are shown and discussed and subsequently the experiments in the C 1s level.

##### 9.1.1.1 Adsorption

During the adsorption at 180 K two peaks are visible in the B 1s region, one at 187.9 eV and the other one at 189.1 eV (cf. Figure 9.1). First, the peak at 187.9 eV grows and saturates at 0.2 L. The second peak at 189.1 eV is evolving at higher exposures and saturates after 0.6 L. From the higher FWHM of the second peak in comparison to the first peak it is concluded that the adsorption site is less defined. The peak-shift of the peak at 189.1 eV is much bigger (0.2 eV) for higher exposures than for the peak at 187.9 eV,

which is only 40 meV. In the following, the second species is called the loosely bound species (187.9 eV) and the first (189.2 eV) is called the strongly bound one, due to the reaction experiment shown later. In section 9.1.2 it will be shown that the loosely bound species is not a multilayer.

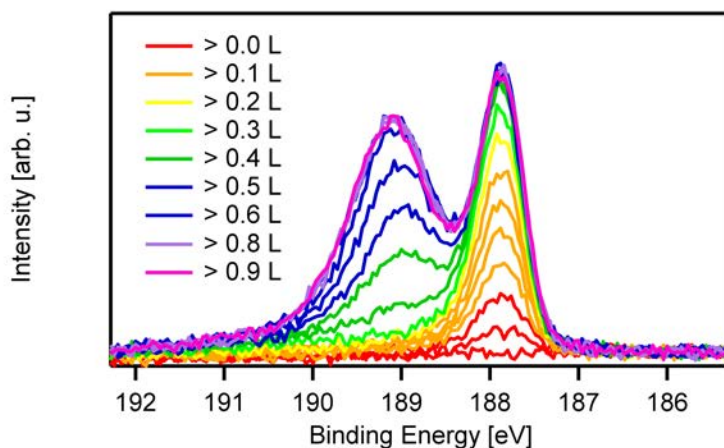


**Figure 9.1:** Spectra of the adsorption of TEB on Pd(100) at 180 K. The exposure of TEB is color coded

In the quantitative analysis of the B 1s core level at 180 K, both peaks are fitted with one single peak, respectively. At saturation, the amount of the strongly bound species is 0.05 ML boron and for the loosely bound one 0.1 ML boron. This amount was calculated from the carbon amount in TEB which has a ratio 1:6 for boron:carbon. In Figure 9.2, a representative fit of a spectrum and the complete quantitative analysis is shown.

After the discussion of the adsorption experiment of TEB monitored in the B 1s corelevel, the experiments in the C 1s region are presented. From the B 1s it is known that after 0.2 L the signal of the loosely bound species rises, while the signal of the strongly bound species stagnates. So up to 0.2 L the complete signal is assigned to the strongly bound species. At higher exposures all new intensity is assigned to loosely bound species. To model this behavior the spectrum at 0.2 L is subtracted from the later ones to gain the signal of the loosely bound species solely (shown in Figure 9.3 b).

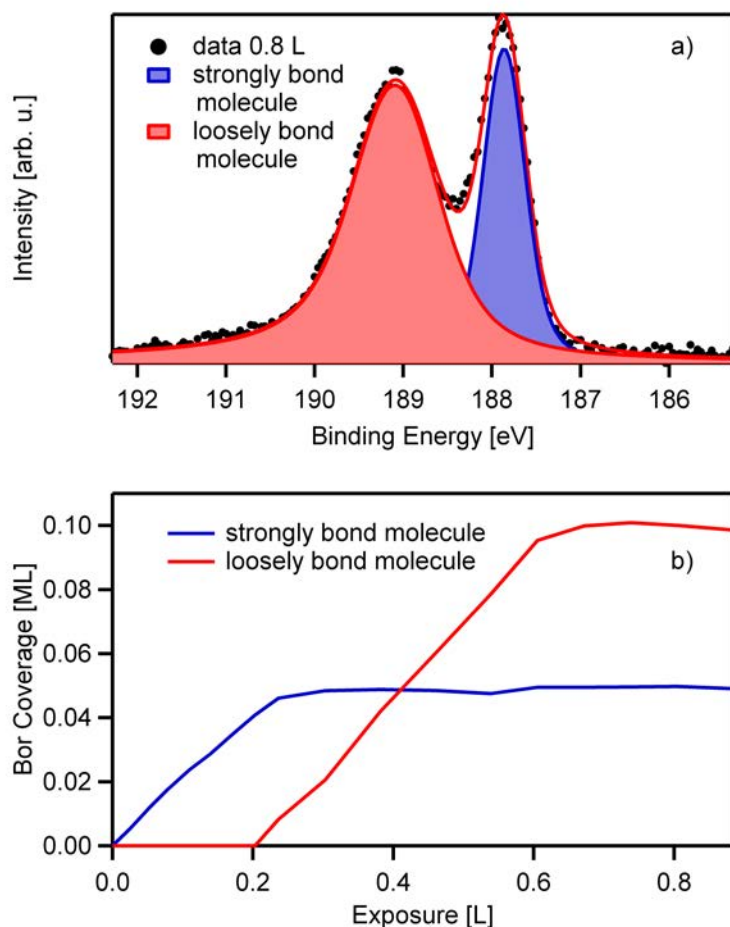


**Figure 9.2:** Fitted spectrum (a) and quantitative analysis (b)

The first visible species at 0.2 L gives a broad signal with two distinctive main peaks at the binding energy of 283.3 and 283.6 eV. Also a shoulder at 283.9 eV is visible. This structure is used as the TEB spectral fingerprint in the following. In TEB two chemical different species of carbon can be distinguished. The first is the methylene group ( $\text{CH}_2$ ) next to the boron atom at a binding energy of 283.3 eV. The second is the methyl group ( $\text{CH}_3$ ) at 283.6 eV. To fit the TEB fingerprint with these two carbon groups two more peaks are necessary resulting from the vibrational splitting with an S-Factor of 0.51 for methyl (283.98 eV) and 0.34 for methylene (283.68 eV). The result of the fit is presented in Figure 9.4d. The methyl group has a higher binding energy as the methylene part due to its bond to the boron atom. The area ratio of both groups is 0.54. This is in contrast to the expected 1:1 ratio; the reason for this discrepancy is unknown, but photoelectron diffractions effects are likely to contribute<sup>98</sup>. Nevertheless, the ratio is constant during

adsorption. Combined with the results from the B 1s core level it is suggested that TEB adsorbs molecularly.

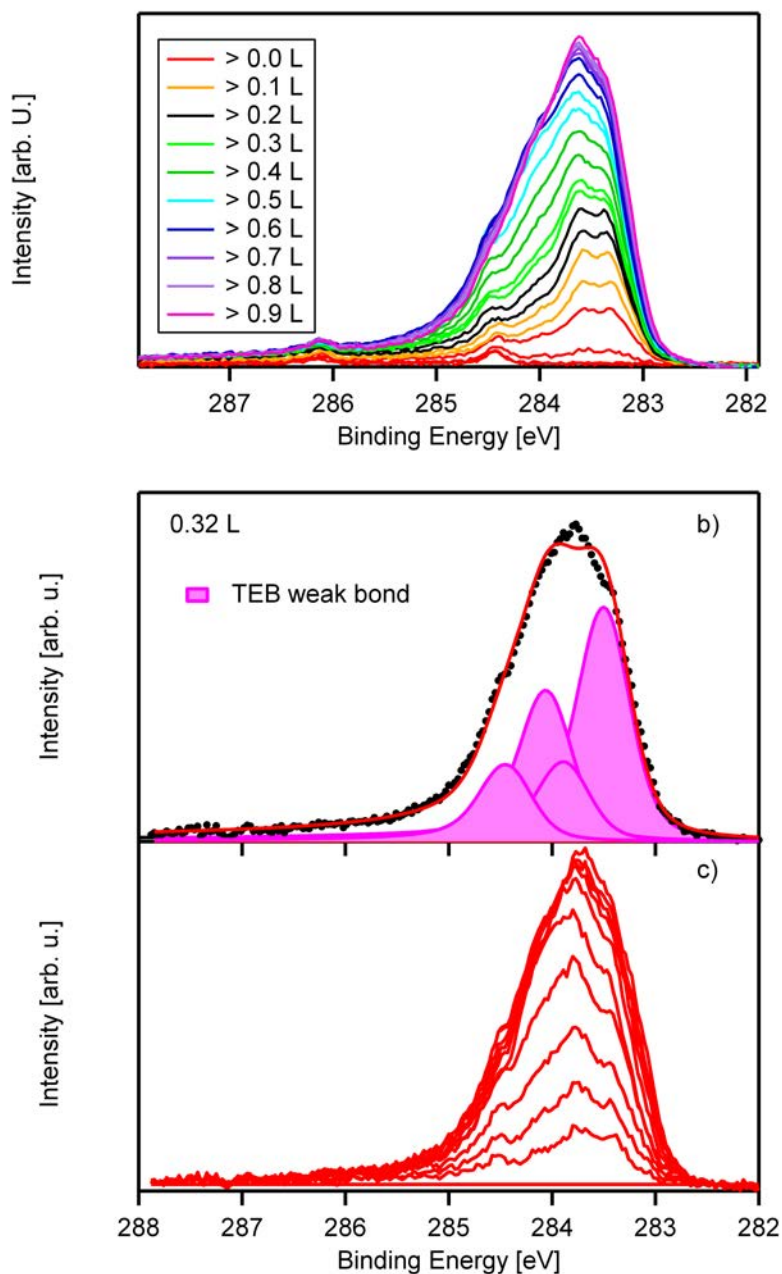


**Figure 9.3:** a) measured spectra of the adsorption of TEB in the C 1s region at 180 K b) spectrum of 0.9 L with subtracted spectrum of 0.2 L with respective fits c) spectra of the adsorption of the loosely bound species after the subtraction of the spectrum in b with a higher exposure than 0.2 L

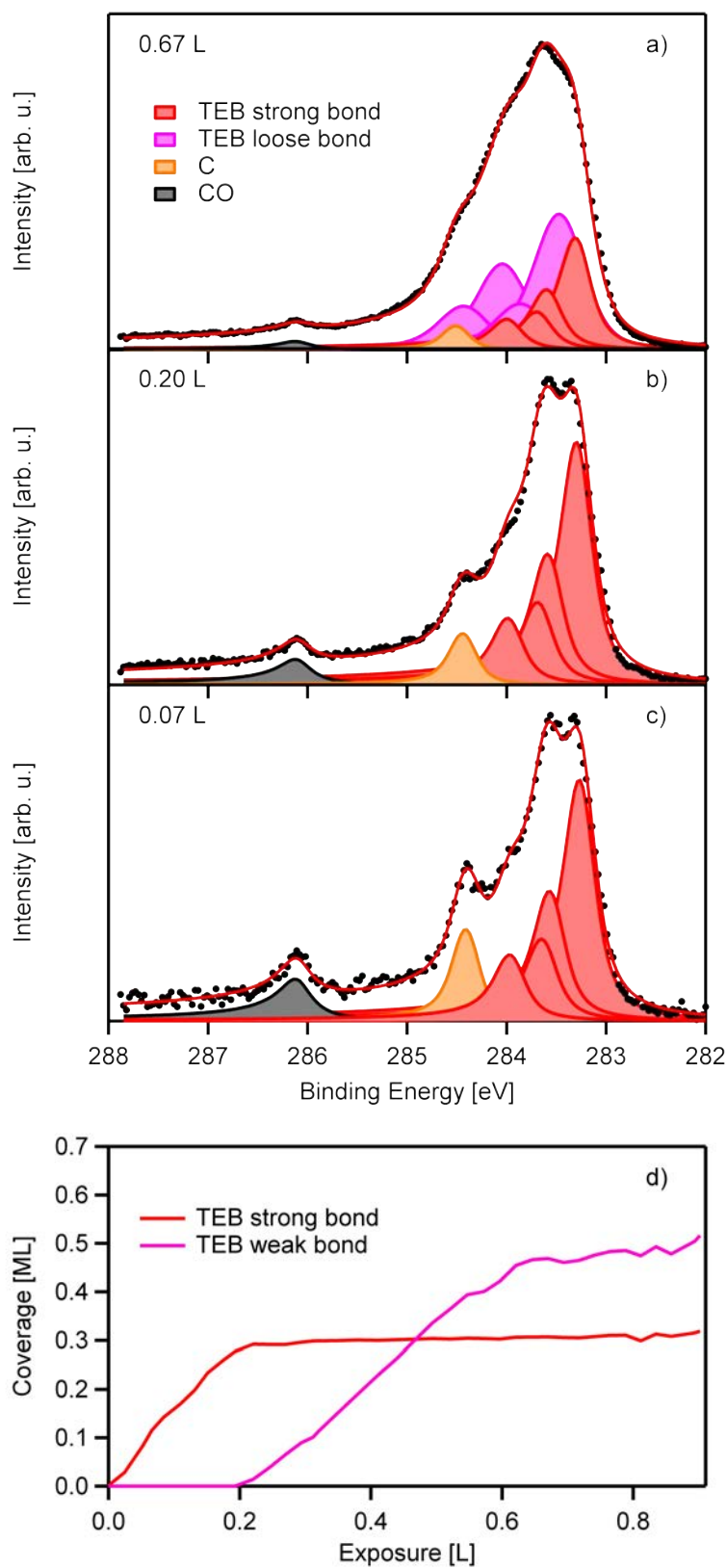


**Figure 9.4:** a), b) and c) representative spectra and fits d) quantitative analysis of TEB adsorption on Pd(100) at 180 K

For an exposure of more than 0.2 L TEB the clear double peak structure becomes broader and only one peak is visible. This is consistent with the results in B 1s region where a second species is growing after 0.2 L of TEB. From the subtraction of the spectrum of 0.2 L from all later spectra a set of new spectra is available and shown in Figure 9.3 b. The quantitative analysis of those spectra is similar to the spectra discussed above. The signal consists of a main peak at the binding energy of 283.7 eV with a shoulder on the lower binding energy side (283.3 eV) and on the higher binding energy side (284.2 eV). In the analysis it becomes clear that this signal can be modeled again by one methyl group (S-Factor 0.51;  $\Delta E = 390$  meV) and a methylene group (S-Factor 0.34;  $\Delta E = 390$  meV). In contrast to the strongly bond species the height ratio is now 0.65 and therefore a bit closer to the theoretical ratio. Furthermore, the signal is, as in the B 1s spectra, much broader. Also a higher binding energy distance between the methylene and the methyl group ( $\Delta E = 570$  meV) is observable, which points to a weaker binding between the molecule and the substrate. The discrepancy in the methyl-methylene-ratio is unclear but cannot be caused solely by photoelectron diffraction as stated above, but is closer to the expected value of one [120]. The different binding of the adsorbate can cause a different environment for photoelectron diffraction and could explain the discrepancy in the ratio of the two TEB species.

In summary, for the adsorption of TEB on Pd(100) two species are observed on the surface. One below an exposure of 0.2 L and the other above this exposure, while the height of the first one keeps constant. The differences in the adsorption site, one distinctive and the other not very well defined, induce a different photoelectron diffraction and a different FWHM of the signal and therefore a slightly different peak shape.

#### 9.1.1.2 Reaction

By heating the system to 600 K, several reaction products are distinguishable. At 180 K, the already known spectrum from the adsorption with a peak at 283.6 eV is visible, which represents the fingerprint of the strongly and weakly bond TEB. At 240 K, a decrease in intensity occurs. Regarding the binding energy it becomes obvious that the weakly bond TEB has desorbed because the clear double peak structure of the strongly bond species appears. At 280 K, the remaining TEB dissociates and a new peak at 283.4 eV rises. At 410

K the next reaction step takes place and an intermediate at an energy of 284.0 eV is visible. This intermediate disappears and at 470 K a single sharp peak is found (cf. Figure 9.5).

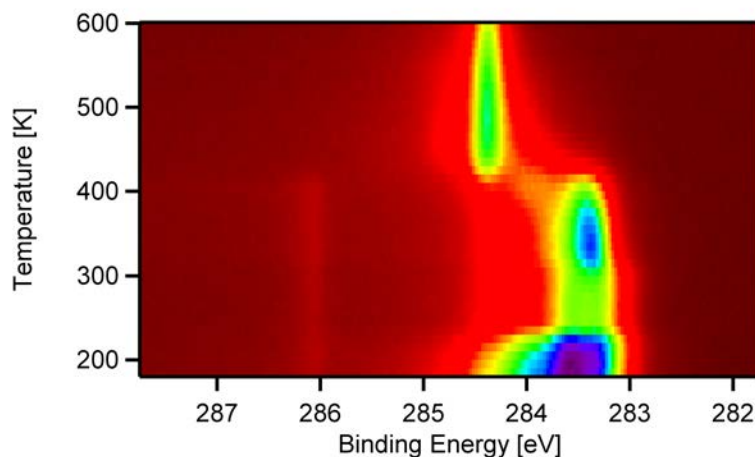


**Figure 9.5:** Color coded density plot of the reaction of TEB on Pd(100) in the C 1s region

The deconvolution of the spectra (cf. Figure 9.6) leads to the quantitative analysis (cf. Fig. 9.7), which reveals more insight of the processes on the surface and is discussed in the following. At 190 K, the known fingerprints of the strong and weakly bound TEB are fitted with the same parameters as before, the binding energy of the strongly bound methylene group is 283.3 eV and the methyl group comes to 283.6 eV. The S-factor of the vibrational splitting for the methylene is 0.34 and the binding energy difference 0.36 eV. The methyl has an energy distance of 0.42 eV and an S-factor of 0.51. The intensity of the weakly bound TEB-signal declines and is not visible anymore at a temperature of 250 K. Also during desorption a rearrangement process take place resulting in a 0.1 ML higher coverage of the strongly bound species. This rearrangement was hindered by the lower temperatures during the adsorption. It is known for boron coordinated in a carbon matrix, namely boron doped graphene on nickel, that the boron adsorbs on highly coordinated sites<sup>167</sup>. But due to the lack of structure information, statements about the adsorption site are impossible to make.

At a temperature of 300 K, a reaction of the strongly bound TEB-species to a new species is visible, which is at an binding energy of 283.3 eV in the C 1s region. In an energy distance of 0.37 eV a shoulder occurs, i.e. has the typical binding energy difference of a vibrational splitting. On the basis of

the S-Factor of 0.34 one can conclude that this species is  $C_2H_4$ . This means that the TEB molecule dissociates to boron and ethylene.

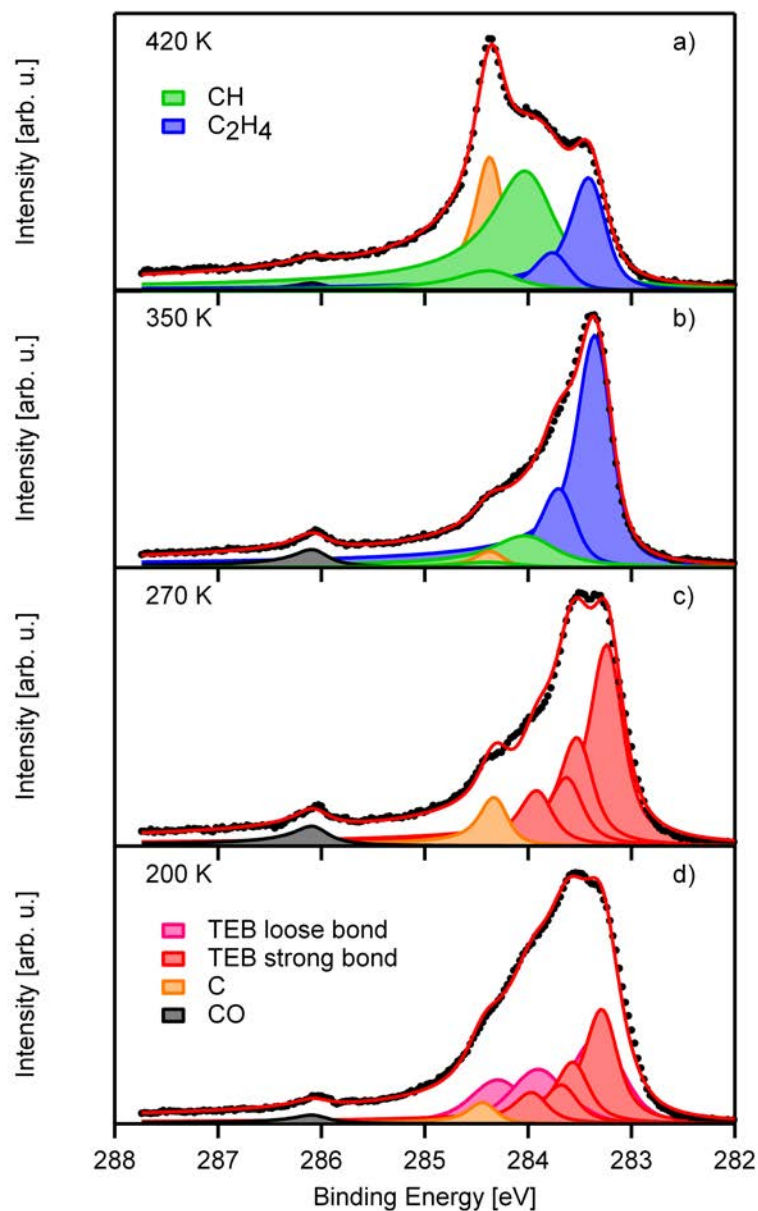


**Figure 9.6:** Spectra of the reaction of TEB on Pd(100) in the C 1s region

Starting at 300 K an additional species (283.9 eV) is observed, with maximum coverage around 420 K. It is identified as CH by the literature<sup>153</sup> and also by its vibrational splitting ( $\Delta E = 350$  meV, S-Factor: 0.17). Please note that the identification of this species is not easy due to the overlap with other contributions. Nevertheless with the literature sources<sup>153–155</sup> and the

fits the assumption of CH on the surface is reasonable. From  $\sim 400$  K on, an additional species arises. This single sharp peak is identified as carbon, the typical decay product of hydrocarbons on palladium. The identification is due to the lack of a shoulder resulting from a vibrational splitting. At even higher temperatures the carbon diffuses into the bulk. Figure 9.7 shows that aside from the desorption of the weakly bound species no desorption of hydrocarbons takes place because there is no decrease in the overall carbon coverage.

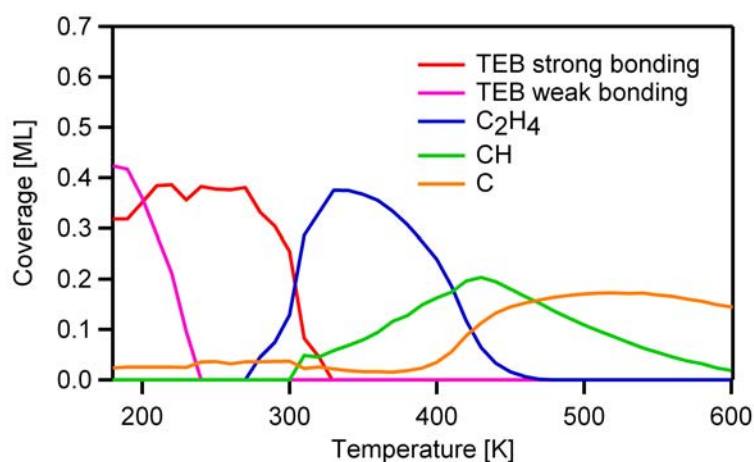


**Figure 9.7:** Quantitative analysis of the spectra in the C 1s region

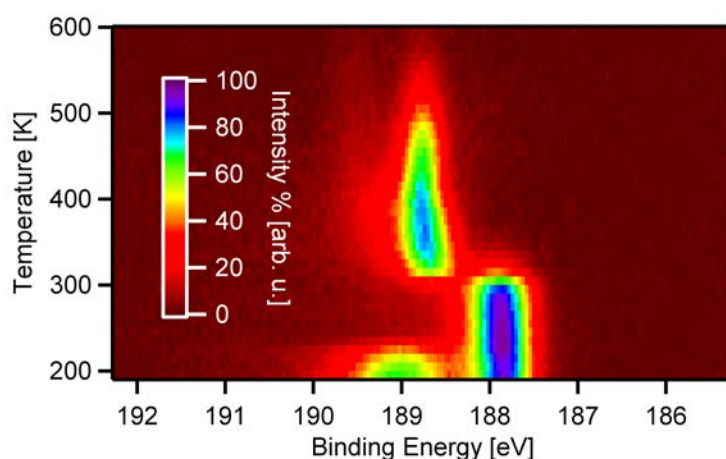


**Figure 9.8:** Color coded density plot of the reaction of TEB on Pd(100) in the B 1s region

In the following, the B 1s region is discussed for the completion of the understanding of the reaction (cf. Figure 9.8 and 9.9). At the beginning

of the experiment (180 to 240 K) the decline of the peak at 189.1 eV takes place. The quantitative analysis (cf. Figure 9.10) shows the rearrangement of the weakly bond species. At 300 K, strongly bond TEB molecules dissociate and pure boron is found at the binding energy of 188.7 eV. The sum of both species stays constant, which means that no desorption of boron happens. Smaller changes in the peak are attributed to creation of PdB or PdC species, but these species are hard to model because of their small amount and are not discussed in this context.

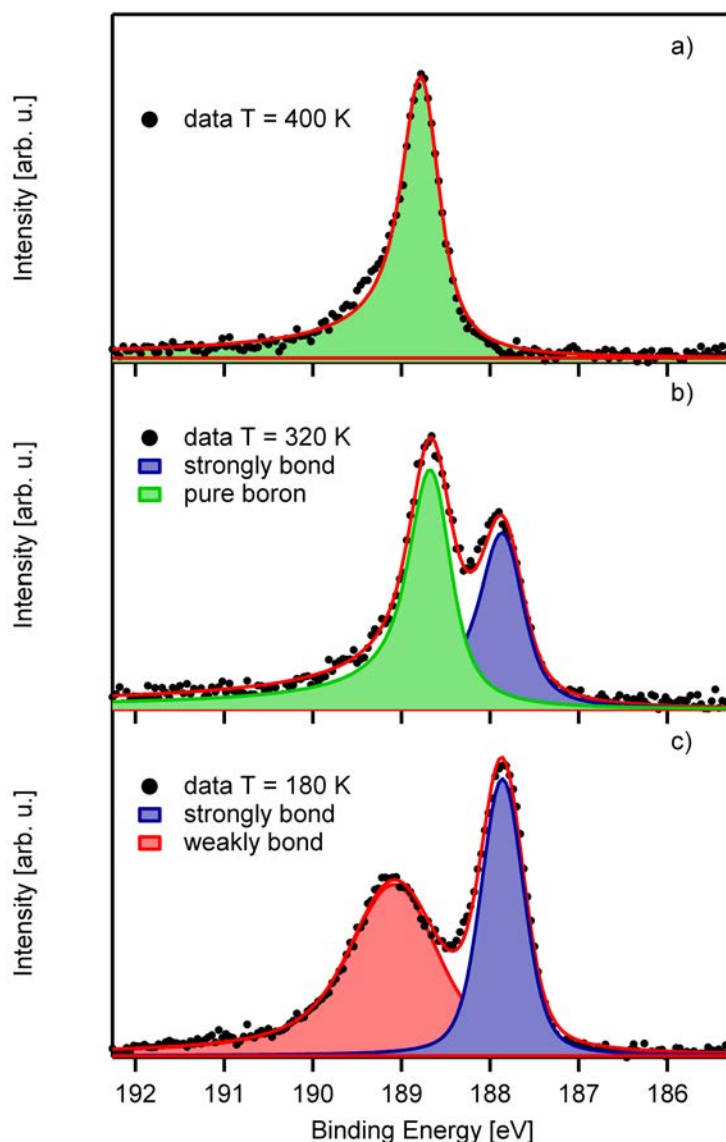


**Figure 9.9:** Selected spectra and fits in the TEB reaction in the B 1s region

The strong decrease in the intensities above 450 K is due to the diffusion of the boron into the substrate. The conclusion of this behavior is that the TEB dissociates after the first decay reaction (300 K) and boron does not take part in any other reaction later on the surface. The results in the B 1s region (cf. Figure 9.8 and 9.9) show clearly that the weakly bond species desorbs till 240 K.

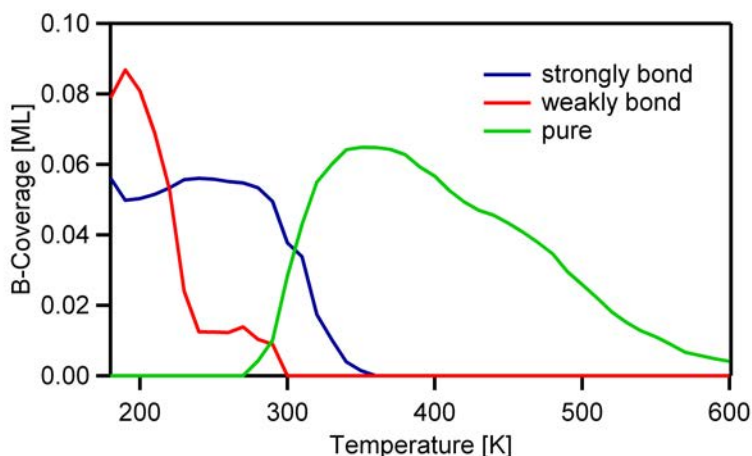


**Figure 9.10:** Quantitative analysis of the reaction of TEB on the Pd(100) in the B 1s region

Concluding the adsorption and reaction experiments the complete picture looks like this:

Up to an exposure of 0.2 L TEB adsorbs solely with a strong bonding to the surface at 180 K. After this exposure, additional adsorption yielding a weakly bond TEB occurs. Therefore at saturation two species coexist on the surface, a strongly bound and a weakly bound species. This is the starting situation for the reaction. Here the weakly bond species desorbs nearly completely till 240 K, and a small amount rearranges to the strongly bound species. This species dissociates to ethylene and boron at 300 K. After this reaction boron does not take part in any other reaction and diffuses into the bulk at higher temperatures. The maximum coverage of ethylene is around 340 K. Ethylene starts to dehydrogenate to CH at 300 K and the maximum coverage of CH is found at 420 K. At 400 K the CH decays to pure carbon which diffuses into the bulk at higher temperatures.

### 9.1.2 Adsorption at 120 K

This section shortly discusses the formation of multilayers in the TEB Pd(100) system.

First, the B 1s region is discussed. In Figure 9.11 an exemplary fit is shown that reveals that three different boron species adsorb on the surface at 120 K. Two of them are known from the adsorption experiments at 180 K, namely the strongly and weakly bound TEB at 187.6 and 188.9 eV respectively. The third species is found at a higher binding energy of 189.7 eV. This last peak shifts with increasing exposure. The density plot of this experiment is shown in Figure 9.12.

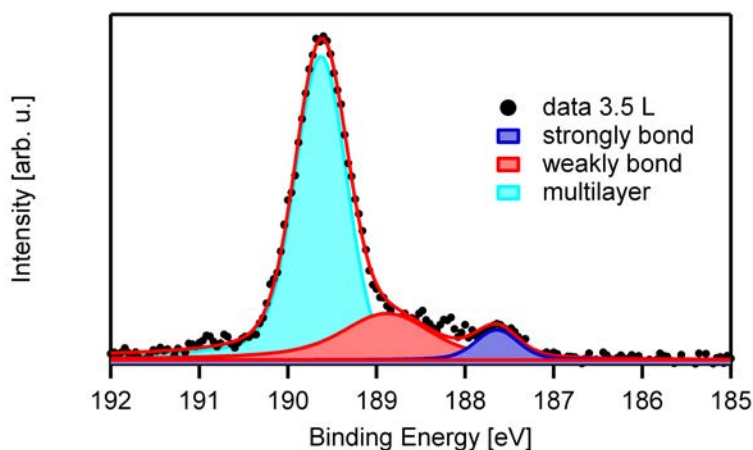


**Figure 9.11:** Spectrum with fit of the adsorption of TEB on Pd(100) at 120 K

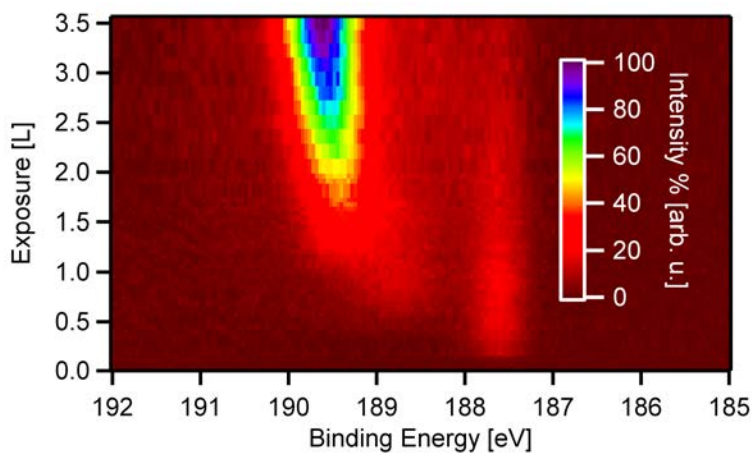


**Figure 9.12:** Density plot of the adsorption of TEB on Pd(100) at 120 K

The quantitative analysis (cf. Figure 9.13) of the adsorption experiment in the B 1s region reveals that at first the strongly bound species is growing, as soon as these sites are completely filled (0.04 ML of B) the weakly bound TEB species starts to grow. With the saturation of this species (0.09 ML of B) another species, namely the multilayer grows. This multilayer does not saturate but damps the other two species, which is typical for a multilayer.

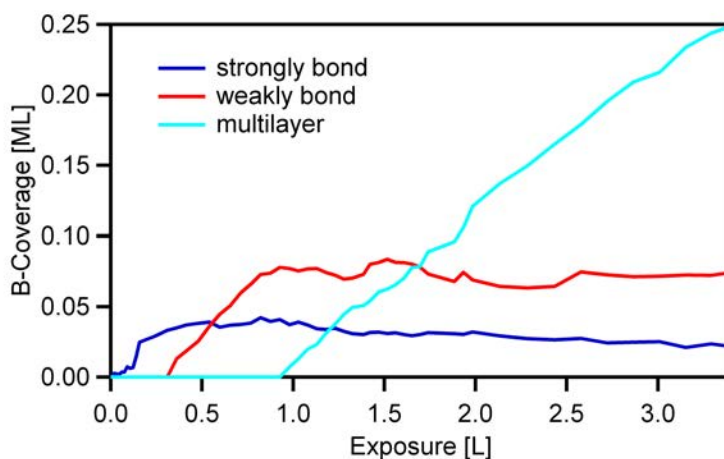


**Figure 9.13:** Quantitative analysis of the adsorption of TEB on Pd(100) in the B 1s region

The experiment was repeated in the C 1s core level and representative spectra are shown in Figure 9.14. Note that this was one of the first experiments performed with TEB and in contrast to the other experiments observed significant contamination were found. The already known group of peaks for the strongly and weakly bound species starts to grow and after an exposure of 0.4 L the multilayer occurs (cf. Figure 9.15). The multilayer is fitted with only one very broad peak, shifting from 283.7 to 284.4 eV with higher exposures. Another peak at 282.7 eV comes from a decay product of the TEB, probably generated by the synchrotron light. The binding energy of this decay product is comparable to  $C_2H_4$ . A quantitative analysis is shown in Figure 9.15. Please note that the peaks of the  $C_2H_5$  groups are not varied above 1 L, as a clear fit is not possible. Additionally the experiment and the occurrence of the several TEB species in the C 1s and the B 1s levels is different. This difference is due to the large amount of contamination (CO and several C species) on the surface. The lower TEB amount is also caused by the contamination.

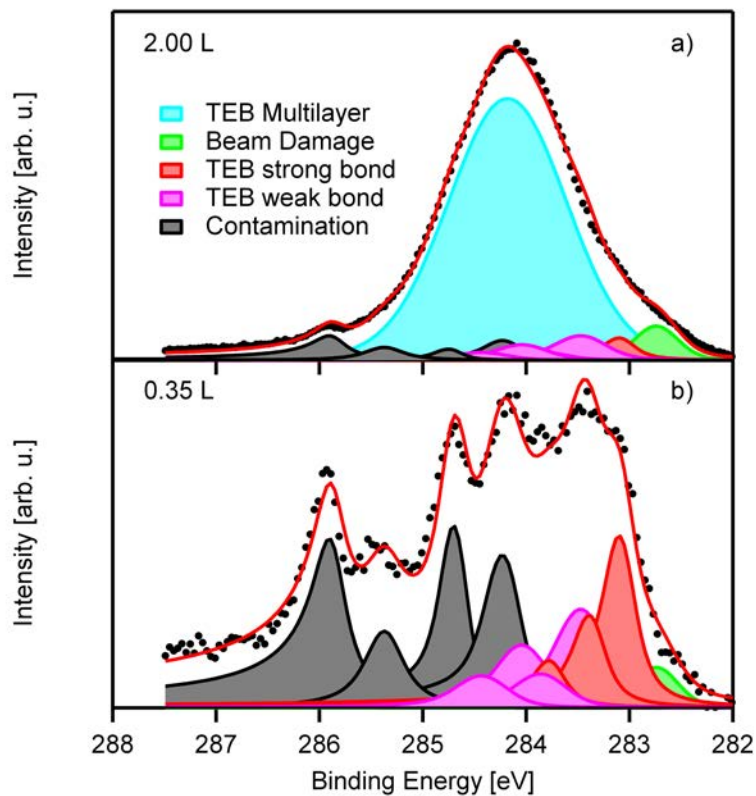


**Figure 9.14:** Representative spectra and fits of the TEB adsorption on Pd(100) at 120 K; a) 2.0 L b) 0.35 L

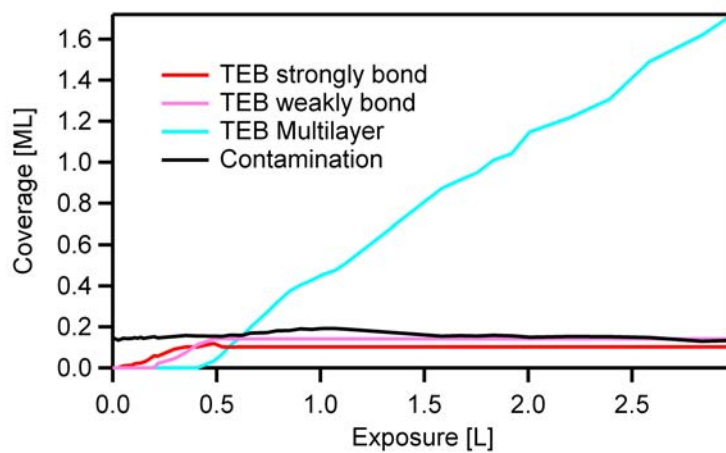


**Figure 9.15:** Quantitative analysis of the TEB adsorption on Pd(100) at 120 K

### 9.1.3 Adsorption and Reaction from 300 K

In section 9.1.1.1 the adsorption at 180 K and the successive reaction upon heating was studied. In this part the adsorption of TEB at 300 K is discussed. From the previous sections it is known that TEB already undergoes decomposition at this temperature. The experiment allows to populate reaction products. In the following, the C 1s region is discussed and afterwards the B 1s region.

#### 9.1.3.1 Adsorption

The analysis of the spectra in the C 1s region reveals a main contribution at a binding energy of 283.3 eV with a shoulder at 360 meV higher binding energy (cf. Figure 9.16). During the adsorption experiment the ratio between the main peak and the shoulder, which gives the S-Factor, stays constant at 0.34. This results in the identification of this species as ethylene. Two additional peaks are necessary to fit the spectrum (cf. Figure 9.17); identified as CH (283.9 eV) and its shoulder with a S-Factor of 0.17 for the first vibrational splitting ( $\Delta E = 350\text{meV}$ ). With these results the adsorption is in line with the reaction of TEB in the C 1s region shown in section 9.1.1.1. At higher exposures above 0.25 L the strongly bound TEB occurs in accordance to the later shown B 1s spectra. This effect can be explained that not only the right temperature but also enough space on the surface is necessary for the dissociation of TEB, which is not given at this time of the experiment, resulting in the adsorption of TEB.

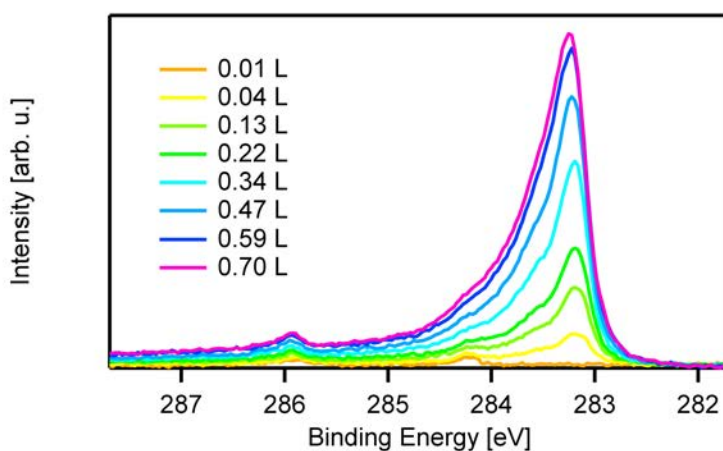


**Figure 9.16:** Spectra of the adsorption of TEB on Pd(100)

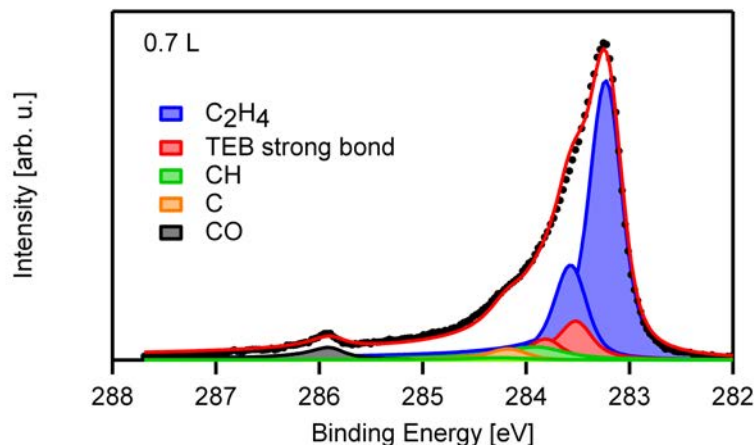


**Figure 9.17:** Representative fit of the adsorption of TEB at 300 K on Pd(100)

The quantitative analysis is presented in Figure 9.18. Here the saturation coverage of  $C_2H_4$  is 0.43 ML while CH has a coverage of 0.03 ML. The TEB saturation coverage is 0.12 ML. A comparison of the carbon amounts between the 180 K and 300 K adsorption reveals that equal coverages are achieved.

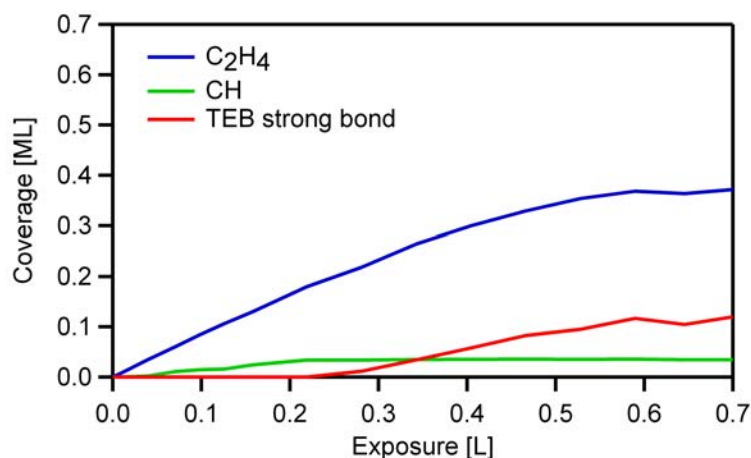


**Figure 9.18:** Quantitative analysis of the adsorption of TEB on Pd(100) at 300 K

In the following the results from the B 1s core level are discussed. A density plot is shown in Figure 9.19 and the according spectra in Figure 9.20. Up to an exposure of 0.2 L a single peak at 188.8 eV grows. This was identified as pure boron according to the reaction experiments in the previous chapter (see section 9.1.1.2). Above 0.5 L a second peak appears at a binding energy of 187.8 eV, which is assigned to the strongly bound

TEB species found during adsorption at 180 K. The fits and the quantitative analysis are shown in Figure 9.21 and 9.22 respectively.

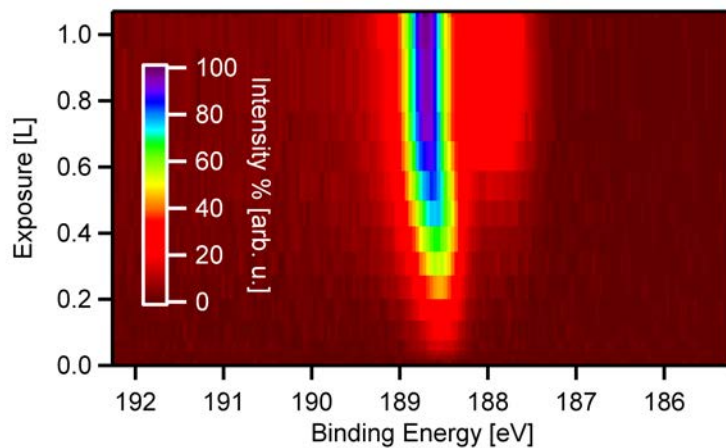


**Figure 9.19:** Density plot of the adsorption of TEB on Pd(100) at 300 K.

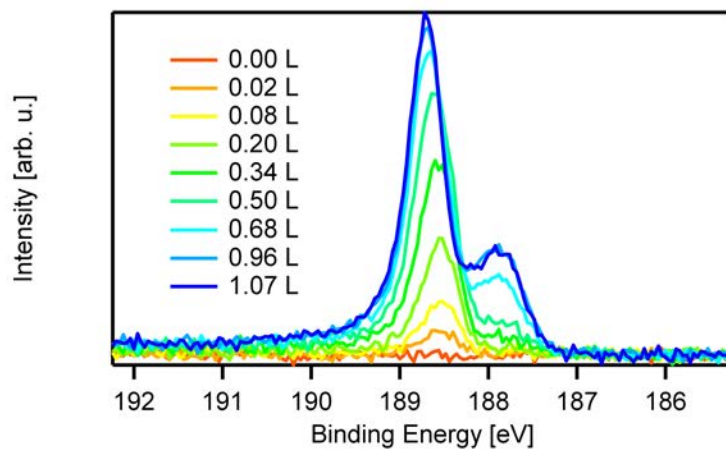


**Figure 9.20:** Spectra of the adsorption of TEB on Pd(100) in the B 1s region at 300 K.

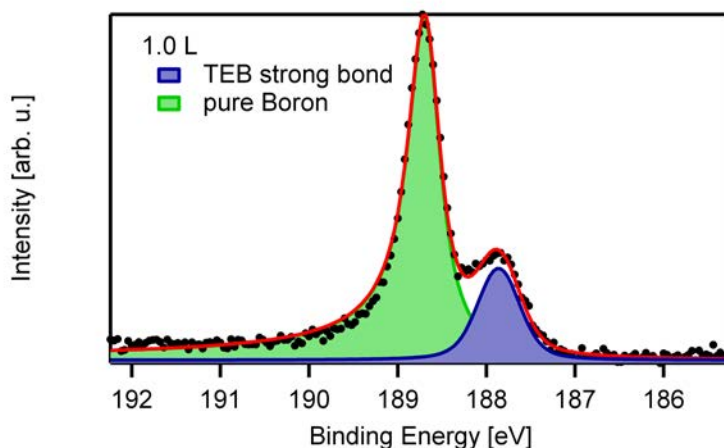


**Figure 9.21:** Representative fit of the TEB adsorption on Pd(100) at 300 K in the B 1s region.

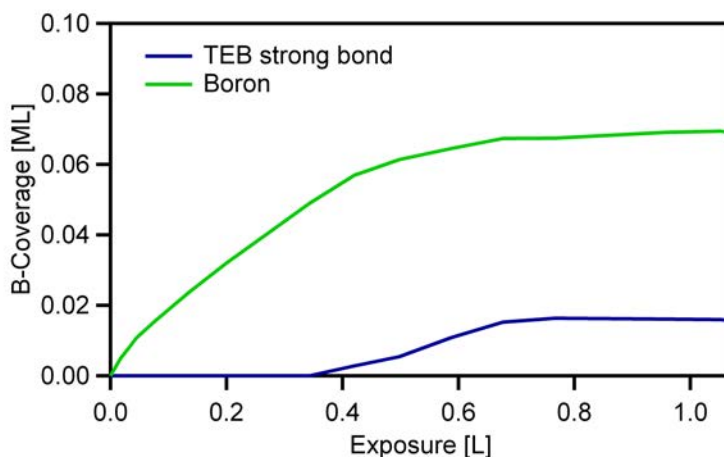


**Figure 9.22:** Quantitative analysis of the boron region from the adsorption experiment at 300 K.

### 9.1.3.2 Reaction

In this section, the thermally induced reactions for TEB adsorbed at room temperature are studied. The C 1s spectra are shown in a color-coded density plot in Figure 9.23. The  $C_2H_4$  peak (283.3 eV), which was identified in the previous section stays at a constant height until 400 K. Now an intermediate (283.9 eV) occurs with a maximum coverage (0.35 ML) at 420 K. This was also previously identified as CH. At the last step the CH dehydrogenates completely and pure carbon appears, which diffuses into the bulk at higher temperatures. The fits are shown in Figure 9.24 and confirm the identification

of ethylene (283.3 eV; vib. splitting  $\Delta E = 360\text{meV}$ ,  $S = 0.34$ ), CH (283.9 eV; vib. splitting  $\Delta E = 350\text{meV}$ ,  $S = 0.17$ ) and carbon (284.3 eV; no vib. splitting) due to the S-Factor and the binding energies. Thus the reaction proceeds in the same way as for TEB adsorbed at 180 K. The fits of these spectra were done with the same parameters as in the previous sections. Selected spectra and the quantitative analysis are shown in Figure 9.24 and 9.25

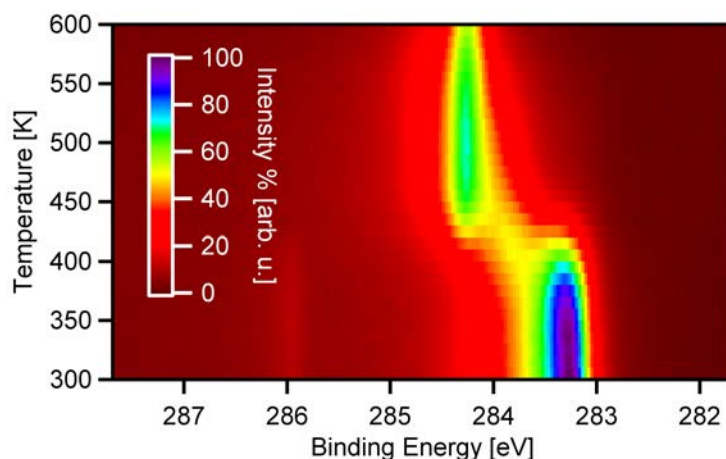


**Figure 9.23:** Density plot of the reaction of TEB on Pd(100) adsorbed at room temperature in the C 1s region

The spectra of the B 1s region are shown in the color-coded density plot (cf. Figure 9.26). In the temperature range between 300 and 360 K the intensity of the boron species with the binding energy (187.7 eV) disappears. The peak for pure boron with a binding energy of 188.8 eV also gets constantly smaller. At temperatures of 420 K this peak changes in width before it vanishes due to diffusion of the boron into the bulk. The change in width could have different reasons; on the one hand it could mean that boroncarbides or palladium boron composites form on the other hand it could also mean a minor rearrangement in the adsorption site happens. None of these possibilities can be ruled out due to the method of investigation. The quantitative analysis is shown in Figure 9.27.

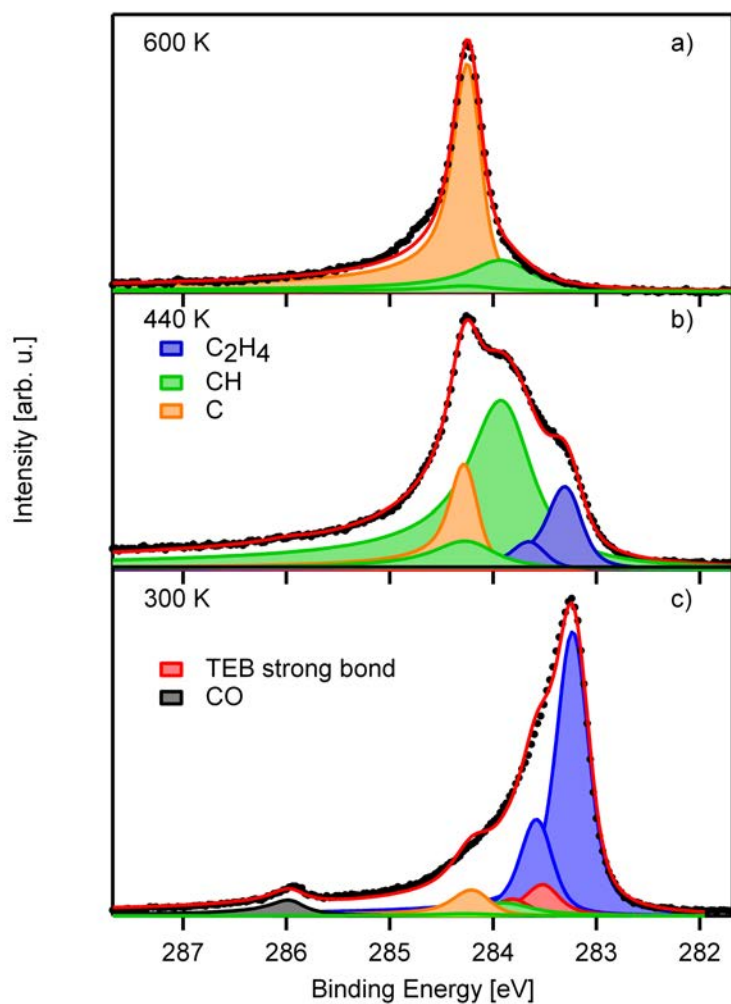


**Figure 9.24:** Selected spectra of the reaction of TEB adsorbed on Pd(100) at RT

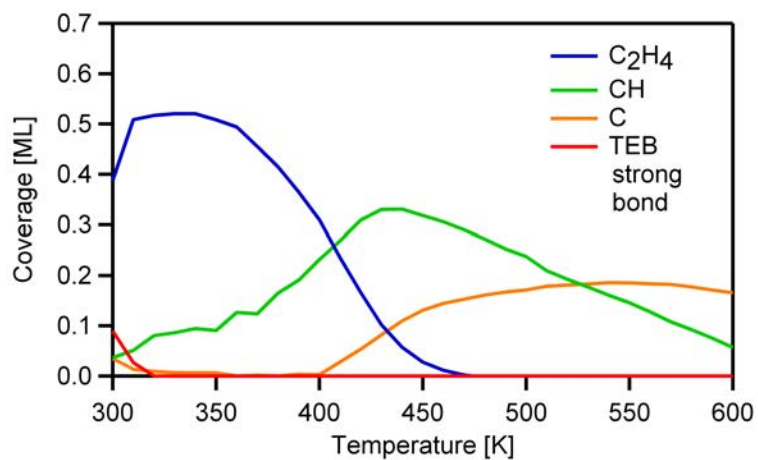


**Figure 9.25:** Quantitative analysis of the reaction of TEB adsorbed on Pd(100) at RT

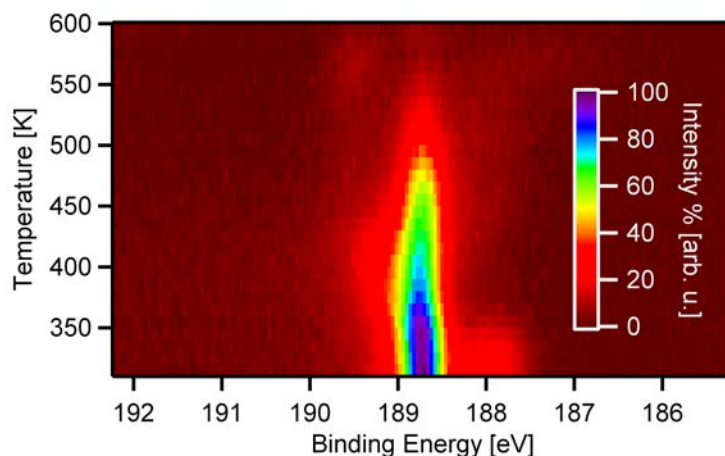


**Figure 9.26:** Density plot of the B 1s region of the reaction of TEB adsorbed on Pd(100) at 300 K

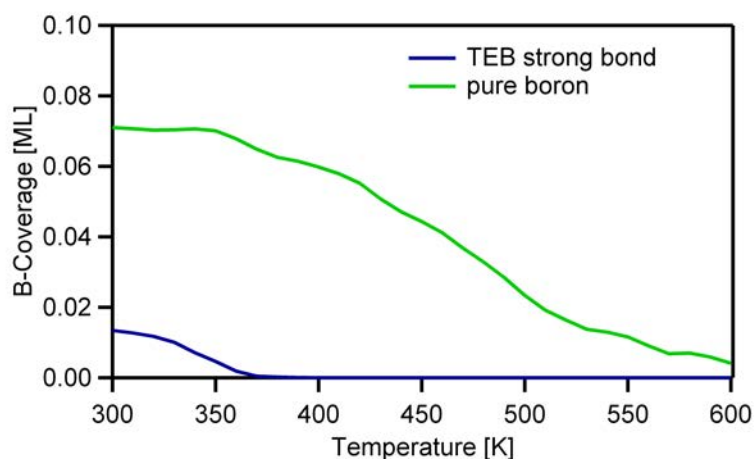


**Figure 9.27:** Quantitative analysis of the reaction of TEB adsorbed on Pd(100) at 300 K

## 9.2 Conclusion

In this chapter the adsorption and the thermal stability of Triethyleborane (TEB) was studied. The experiments were performed in the C 1s and B 1s regions and revealed that TEB adsorbs at 180 K with two different surface species. One species is a strongly bound species while the other is a weaker bound species. These different bonding situations were identified by the thermal evolution in both examined core levels. The study of the reaction revealed that the first step of the TEB reaction on palladium is the dissoci-

ation of the strongly bound TEB to ethylene and boron. The weakly bound species desorbs. The further reaction of ethylene on this boron-covered surface is not changed and the dehydrogenation to CH and then carbon is similar to the one the boron free surface.

# Chapter 10

## Summary

Basic research often uses model systems in order to simplify the complex situation of real applications. In the case of heterogeneous catalysis, a surface approach is used to obtain a fundamental understanding of relevant elementary reactions steps in a well-defined and clean environment. However, this approach leads to "gaps" between the conditions of the model experiments and the real application, and one has to ask, to which extent results can be directly compared. One of these gaps is the complexity of industrially used catalysts in comparison to the simplified model systems used in surface science. This thesis aims at studying model systems with an increased degree of complexity, i.e., studying the adsorption and reaction of small molecules on different surfaces, from clean and oxygen precovered Pd(100) surfaces to nickel oxide films with different thicknesses supported by Pd(100) metal crystal. In this context, also the growth of nickel oxide films on Pd(100) was investigated and a clear difference between the first and the second layer were found. The investigations were mainly performed with in situ high resolution XPS using synchrotron radiation at the synchrotron radiation facility BESSY II at the Helmholtzzentrum in Berlin (HZB). In addition to these investigations, methodological developments were performed, leading to an enhancement of the time resolution of XPS by a factor of  $\sim 2000$ , i.e. from 1 s down to 500  $\mu\text{s}$  per spectrum.

The oxidation of carbon monoxide on NiO films was found to strongly depend on the thickness of the films. Thicker, bulk-like films do not react under ultra high vacuum conditions up to a temperature of 600 K. For the monolayer and for the two layer thick film, a kinetic analysis was performed and a first order reaction behavior was found. On the 2 ML thick film the

model had to be extended with another first order process describing the diffusion of the oxygen to the reactive sites. Both films were completely reduced. This complete reduction was not possible when the 2 ML film was reoxidized because a structural change in the film led to cluster formation.

The adsorption of water on the clean Pd(100) surface revealed a layer-by-layer growth, with the monolayer saturating at 0.6 ML. The thermal evolution shows that water desorbs at 160 K. For the oxygen-precovered surface, a slightly higher saturation coverage of 0.76 ML is found, but the desorption temperature does not change. On the nickel oxide films different saturation coverages of 0.25 ML, 1.0 ML and 1.6 ML are found for 1 ML, 2 ML and 6 ML thick nickel oxide respectively. Also several hydroxide species are observed. From the 2 ML thick film upwards a shift of the oxygen peak by 0.5 eV is visible. No reaction of the water was found on the nickel oxide films, and H<sub>2</sub>O was found to desorb at a temperature of 160 K, as on the clean palladium surface.

The adsorption and reaction of C<sub>2</sub>H<sub>2</sub> on clean Pd(100) was revisited. Here the C 1s and Pd 3d<sub>5/2</sub> regions were recorded and a single molecular species was found adsorbing on a fourfold hollow site, with a saturation coverage of 0.68 ML. From the changes in the Pd 3d<sub>5/2</sub> spectra, a model was deduced in which the palladium surface atoms interact either with one adsorbate molecule at low coverages, or with two acetylene molecules at higher coverages. From this data, a statistical simulation was made, which reproduced the observed behavior in an excellent way allowing a deeper insight. Upon heating, acetylene reacted on clean Pd(100) by dehydrogenation to CCH at 390 K, and subsequently to carbon. The adsorption of C<sub>2</sub>H<sub>2</sub> on an oxygen-precovered Pd(100) surface results in a slightly lower saturation coverage of 0.4 ML. The temperature for dehydrogenation is lowered by ~200 K to 190 K, but the reaction-pathway is similar as on the clean surface. On the 1 ML thick nickel oxide film, the reaction is comparable to the reaction on the oxygen-precovered surface. In contrast, on the two layer thick film most of the adsorbed acetylene desorbs molecularly, with only the minority of the molecules dehydrogenating at 250 K. For 6 ML NiO, the bulk-like nickel oxide is unreactive.

The study of C<sub>2</sub>H<sub>4</sub> shows that two species, di- $\sigma$ - and  $\pi$ -species, adsorb at 150 K on the clean Pd(100) surface. The more stable di- $\sigma$ -species reacts at 200 K to HCCH<sub>2</sub> while the other species desorbs over several different

channels from 100 K on. In this context, the influence of the pressure on the coverage during the adsorption was studied, revealing that the di- $\sigma$ -species becomes the majority adsorbed species at higher pressures up to  $2 \times 10^{-6}$  mbar, while it is the minority at lower pressures of  $3 \times 10^{-9}$  mbar. From the coadsorption experiments with CO and O it is suggested that the adsorption sites for the  $\pi$ -species is the on-top site while the di- $\sigma$ -species adsorbs on the bridge site. On an oxygen-precovered surface no reaction takes place and the molecule only desorbs molecularly.

The saturation coverage of benzene on a clean Pd(100) surface is found to be 0.8 ML. The XPS measurements show a single peak with a clear vibrational splitting, which suggests molecular adsorption. The analysis of the Pd  $3d_{5/2}$  levels indicates that atoms are in contact with one benzene molecule, confirmed the recently proposed four surface four fold hollow site<sup>158,163</sup>. The majority of the adsorbed molecules desorb at a temperature of 500 K, while the minority dehydrogenates yielding carbon on the surface. A similar adsorption and reaction behavior is observed for the oxygen-precovered surface with the difference that only 0.6 ML adsorb on the surface, which is explained by the blocking of adsorption sites by oxygen. The reaction temperatures are also similar besides that one third of the benzene desorbs already at a temperature of 250 K.

The adsorption and the thermal stability of triethyleboran (TEB) were studied. These experiments were performed in the C 1s and B 1s regions and revealed that TEB adsorbs at 180 K as two different surface species, a strongly bound species and a weaker bound species. These different bonding situations were identified from the thermal evolution of both core levels. Upon heating, the first step of the TEB reaction on Pd(100) is the dissociation of the strongly bound TEB to ethylene and atomic boron, while the weakly bound species desorbs. The further reaction of ethylene on this boron-covered surface and the dehydrogenation to CH and C is similar as found for pure ethylene on the clean Pd(100) surface.

Last but not least a new approach for the reduction of the time resolution in XPS measurements is presented, allowing measurements in the  $\mu$ s time domain. First measurements with a time resolution of 500  $\mu$ s were performed to study the adsorption and desorption of CO at elevated temperatures up to 500 K. The reliability of this new approach was shown by the comparison of data obtained with the conventional setup at temperatures below 450 K

leading to consistent results for the experiments from 375 to 500 K. From a critical evaluation of the experimental parameters and boundary conditions, it was extrapolated that under favorable condition a time resolution of 20  $\mu\text{s}$  or below seems feasible.

# Chapter 11

## Zusammenfassung

Im Gegensatz zu technischen Anwendungen arbeitet die Grundlagenforschung, hier speziell die Oberflächenwissenschaft, mit sogenannten Modellsystemen. Diese sind in Bezug auf die Rahmenbedingungen (z.B. Umgebungsdruck) als auch die Anzahl gleichzeitig eingesetzter Materialien stark vereinfacht. Dies führt zu sogenannten "Gaps", sprich Lücken, zwischen technischer Anwendung und Forschung, sowohl im Verständnis als auch in der Methodik. Im Rahmen dieser Arbeit wurde an der Verringerung dieser "Wissenslücke" mittels unterschiedlich komplexer Oberflächen und der Adsorption und Reaktion von kleinen Molekülen auf diesen gearbeitet. Die Komplexität der Oberfläche in dieser Arbeit wird dabei von der simplen Pd(100)-Oberfläche über die mit Sauerstoff vorbedeckte Pd(100) Oberflächen bis hin zu nanostrukturierten Nickeloxidoberflächen auf Pd(100) erhöht. Als Messmethode kam die hochaufgelöste Photoelektronenspektroskopie zum Einsatz. Die Experimente wurden am Synchrotron BESSY II im Helmholtzzentrum in Berlin durchgeführt. Im Folgenden werden die Ergebnisse der einzelnen Adsorptions- und Reaktionsexperimente verschiedener Moleküle auf den eben angesprochenen Oberflächen zusammengefasst.

Als erstes wurde das Wachstum der Nickeloxidfilme auf Pd(100) mittels XPS charakterisiert und ein klarer Unterschied der elektronischen Struktur der ersten Lage, dem "Wetting Layer", und der zweiten Lage gefunden. Anschließend wurde auf unterschiedlich dicken Nickeloxidfilmen versucht, CO zu oxidieren. Hierbei stellte sich heraus, dass NiO(100) Filme mit Schichtdicken von  $\sim 6$  ML, die schon einem Festkörper ähnlich sind, nicht mehr reaktiv sind. Für den "Wetting Layer" und die zwei Monolagen dicke Schicht wurden dann reaktionskinetische Untersuchungen durchgeführt; diese ergaben, dass beide

Filme komplett reduziert werden können und der Reaktionsmechanismus der ersten Reaktionsordnung folgt. Für die zwei Lagen dicke Schicht musste das Modell mit einem weiteren Prozess erster Ordnung erweitert werden um die Sauerstoffdiffusion zu beschreiben. Wird diese zwei Lagen dicke Schicht reoxidiert, kann sie im Anschluss nicht mehr komplett reduziert werden, da strukturelle Änderungen auftreten, die zur Clusterbildung führen.

Bei der Adsorption von Wasser auf sauberem Pd(100) hat sich herausgestellt, dass die Sättigungsbedeckung 0,6 ML für die erste Lage beträgt und der Wasserfilm Lage für Lage wächst. Ab einer Temperatur von 160 K hingegen desorbieren sowohl Mono- als auch Multilage. Für die mit Sauerstoff vorbedeckte Oberfläche wird eine leicht höhere Bedeckung von 0,76 ML für die erste Lage erreicht, wohingegen die ersten Lagen auf den 1, 2 und 6 ML dicken Nickeloxidfilmen jeweils 0,25, 1,0 und 1,6 ML betragen. Bei dickeren Filmen ( $\geq 2$  ML) ist außerdem eine Verschiebung der O 1s Bindungsenergie des Sauerstoffs des Nickeloxids um 0,5 eV hin zu niedrigeren Bindungsenergien zu beobachten; diese wird mit einem der Oberflächenrumpfniveaueschiebung ähnlichen Phänomen, induziert durch die Wassermoleküle, erklärt. Abgesehen von den elektronischen Änderungen während der Adsorption kann keine Reaktion zwischen Wasser und NiO(100) bei höheren Temperaturen beobachtet werden und die Desorptionstemperatur beträgt auch hier 160 K.

Die Acetylenadsorption und die folgende Reaktion auf Pd(100) wurden nochmals untersucht, um offene Fragen zu klären. Bei den XPS Messungen wurde nicht nur das Molekül über das C 1s Niveau betrachtet, sondern auch die elektronische Wechselwirkung im Pd  $3d_{5/2}$ . Es konnte der in der Literatur gefundene vierfach koordinierte Adsorptionsplatz bestätigt werden, ebenso wie die assoziative Adsorption von  $C_2H_2$ . Die Sättigungsbedeckung beträgt 0,68 ML. Aus den Änderungen des Signals des Pd  $3d_{5/2}$  wurde ein statistisches Modell abgeleitet, welches die Adsorptionsdaten exzellent reproduziert und tiefe Einsichten in den Adsorptionsmechanismus bietet. Die thermische Evolution hat ergeben, dass Acetylen ab 390 K zuerst zu CCH dehydrogeniert und anschließend bei höheren Temperaturen zu reinem Kohlenstoff reagiert. Auf einer Sauerstoff vorbedeckten Oberfläche adsorbieren lediglich 0,4 ML Acetylen und die Dehydrogenierung beginnt schon bei 190 K, also 200 K niedriger als auf der einen Oberfläche, wobei der Reaktionsverlauf unverändert ist. Auf dem Nickeloxid "Wetting Layer" verläuft die Reaktion

ähnlich wie bei der Sauerstoff-vorbedeckten Pd(100)-Oberfläche, während der 6 ML dicke Nickeloxidfilm unreaktiv ist.

Die Studien über die Adsorption von  $C_2H_4$  auf Pd(100) bei 150 K zeigen zwei Spezies auf der Oberfläche, nämlich eine di- $\sigma$ - und eine  $\pi$ -Spezies. Die stabilere di- $\sigma$ -Spezies reagiert bei 200 K zu HCCH<sub>2</sub>, während die andere über unterschiedliche Reaktionskanäle ab 100 K desorbiert. In diesem Rahmen wurde auch der Zusammenhang zwischen dem Druck und der Bedeckung untersucht und dabei festgestellt, dass bei höherem Druck die di- $\sigma$ -Spezies die vorherrschende Spezies bildet. Aus Experimenten an koadsorbierten Molekülen, hier CO und O, kann angenommen werden, dass die di- $\sigma$ -Spezies auf Bridge-Plätzen und die  $\pi$ -Spezies auf den On-Top-Plätzen adsorbiert.

Die Sättigungsbedeckung von Benzol auf einer sauberen Pd(100)-Oberfläche beträgt 0,8 ML Kohlenstoffbedeckung. In der Literatur wurde als Adsorptionsplatz der vierfach-koordinierte Platz als energetisch günstigster Platz beschrieben. Im C 1s Rumpfniveau erkennt man bei der Adsorption nur eine einzige Spezies mit einer Vibrationsanregung, was auf einen spezifischen Adsorptionsplatz und assoziative Adsorption schließen lässt. Aus der Analyse der Adsorption im Pd 3d<sub>5/2</sub>-Niveau kann man schließen, dass vier Oberflächenatome mit einem Benzolmolekül interagieren. All diese Ergebnisse bestätigen die Annahme, dass Benzol auf einem vierfach-koordinierten Adsorptionsplatz bindet. Ein Teil des Benzols desorbiert bis 500 K, während der restliche Anteil zu Kohlenstoff dehydrogeniert. Für die Sauerstoff-vorbedeckte Oberfläche findet man eine niedrigere Kohlenstoffbedeckung von 0,6 ML, welche mit der Blockierung von Adsorptionsplätzen mit Sauerstoff erklärt werden kann. Die Reaktionstemperaturen sind ähnlich denen der sauberen Pd(100)-Oberfläche, abgesehen von einer Desorption von einem Drittel des Benzols bei 250 K.

Als nächstes wurde die Adsorption und Reaktion von Triethylboran (TEB) auf Pd(100) erforscht. Diese Experimente wurden sowohl am B 1s und C 1s Rumpfniveau durchgeführt. Sie ergaben, dass bei einer Temperatur von 180 K zwei Spezies aufwachsen, wobei eine stärker als die andere gebunden ist. Dieser Unterschied in der Bindungsstärke wurde anhand der thermischen Evolution identifiziert. Weiterhin hat die Untersuchung von TEB bei höheren Temperaturen ergeben, dass die stärker gebunden Spezies zu Ethylen und Bor zerfällt, während die schwächer gebunden Spezies desorbiert. Die weitere Reaktion des Ethylen wird durch das anwesende Bor

nicht gestört und es dehydrogeniert zu CH und C wie vorher schon auf dem sauberen Pd(100) gezeigt.

Als ein besonderer Aspekt in dieser Arbeit wurde erfolgreich die signifikante Maximierung der Zeitauflösung von XP Messungen um einen Faktor  $\sim 2000$  umgesetzt. Ein Aufbau und anschließende Messungen von XPS im  $\mu\text{s}$  Zeitregime werden hier präsentiert. Die ersten Messungen wurden mit einer Zeitauflösung von  $500 \mu\text{s}$  durchgeführt um die CO Oxidation auf Pt(111) bei Temperaturen bis zu  $500 \text{ K}$  zu beobachten. Die Zuverlässigkeit dieses Ansatzes wurde durch einen Vergleich mit früheren, herkömmlich gemessenen Daten erreicht und führte zu konsistenten Ergebnissen in einem Temperaturbereich von  $375$  bis  $500 \text{ K}$ . Nach eingehender Betrachtung der Rahmenparameter und Randbedingungen kann als untere Grenze der Zeitauflösung mit diesem Aufbau  $20 \mu\text{s}$  als machbar angesehen werden.

# Chapter 12

## Attachment

### 12.1 C<sub>6</sub>H<sub>6</sub> on NiO/Pd(100)

#### 12.1.1 NiO film: 1 ML

##### 12.1.1.1 Adsorption

The adsorption of benzene on a 1 ML thick nickel oxide layer at 140 K initially shows a single peak (cf. Figure 12.1) at 284.1 eV with a broad shoulder on the higher binding energy side. With increasing exposure, the peak broadens further and shifts slightly to higher binding energies. At 286.0 eV minor contaminations of carbon monoxide are formed.

The deconvolution of the spectra is presented in Figure 12.1 along with a waterfall plot of the adsorption experiment. From the figure, it gets obvious that two peaks are necessary to describe the measured spectrum at 0.46 L exposure. These two contributions are interpreted as different carbon species of the benzene molecule. The higher peak has a binding energy of 284.1 eV and the smaller one is found at a 0.6 eV higher binding energy. Both peaks shift by 0.1 eV to a higher binding energy with higher coverages and the ratio is constantly 0.56. At higher coverages, a second species appears which also consists of two peaks. The reason for necessity of two additional contributions becomes clear in the section about the adsorption of benzene on the 2 ML thick nickel oxide layer. One peak is at a binding energy of 284.4 eV while the second peak has a 0.21 eV higher binding energy. The ratio between these two contributions is again 2:1. A multilayer is found above an exposure of 2 L.

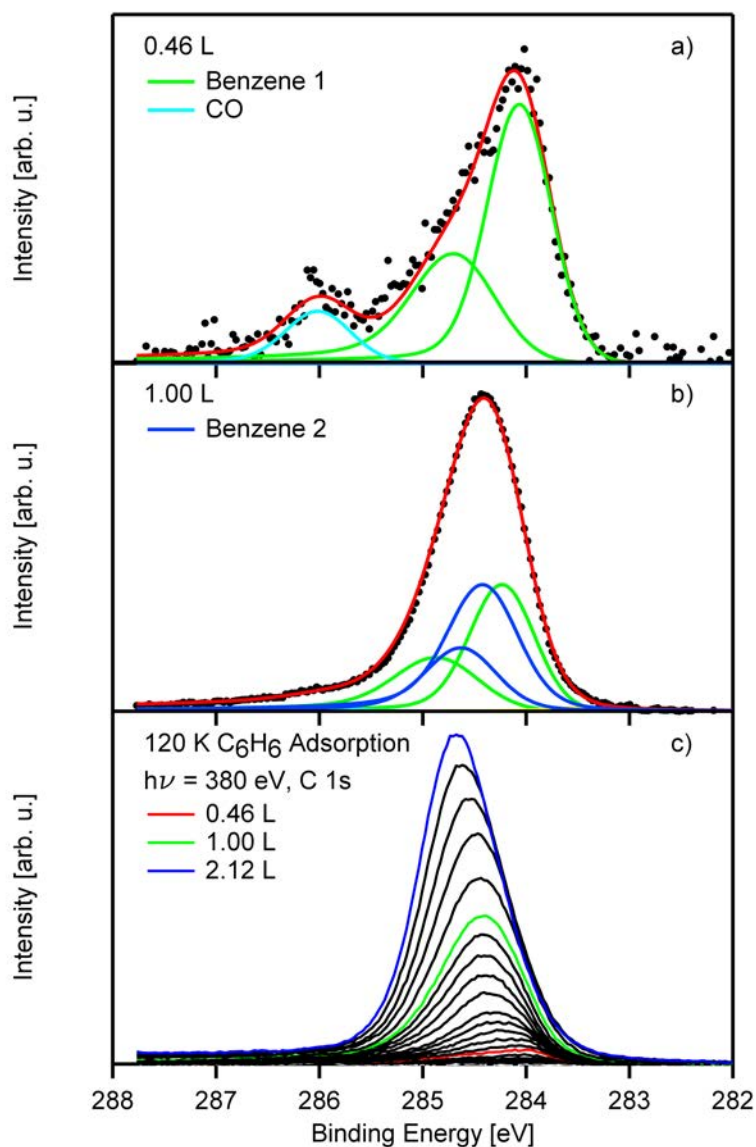


**Figure 12.1:** Spectra and waterfall plot of the adsorption of benzene on a 1 ML thick nickel oxide film.

In the following a possible model for the adsorption site is explained. First from the clean Pd(100) surface it is known that benzene adsorbs on the fourfold hollow site, and this is also assumed for the nickel oxide surface. Additionally two contributions for the signal of the first and second benzene species are found. In Figure 12.2 an explanation for a ratio of 0.5 between these two contributions is given, namely the adsorption of two carbon atoms on either oxygen and four carbon atoms on nickel (Possibility A) or vice versa (Possibility B). For the wetting layer, i. e. the first layer with a stoichiometry

of Ni<sub>3</sub>O<sub>4</sub>, the picture is slightly different. A ratio of 0.56 between the two peaks of this benzene species, the first benzene species, is found. This means that again two carbon species occur on the surface. Again two possibilities are depicted in Figure 12.2. Here the difference of 12% in the ratio by the ideal 2:1 ratio is explained by the different electronic structure of the nickel vacancy sites in comparison to the stoichiometrically NiO. The different electronic structure is assumed to be also responsible for the rather big distance in binding energy of 0.6 eV between the two contributions.

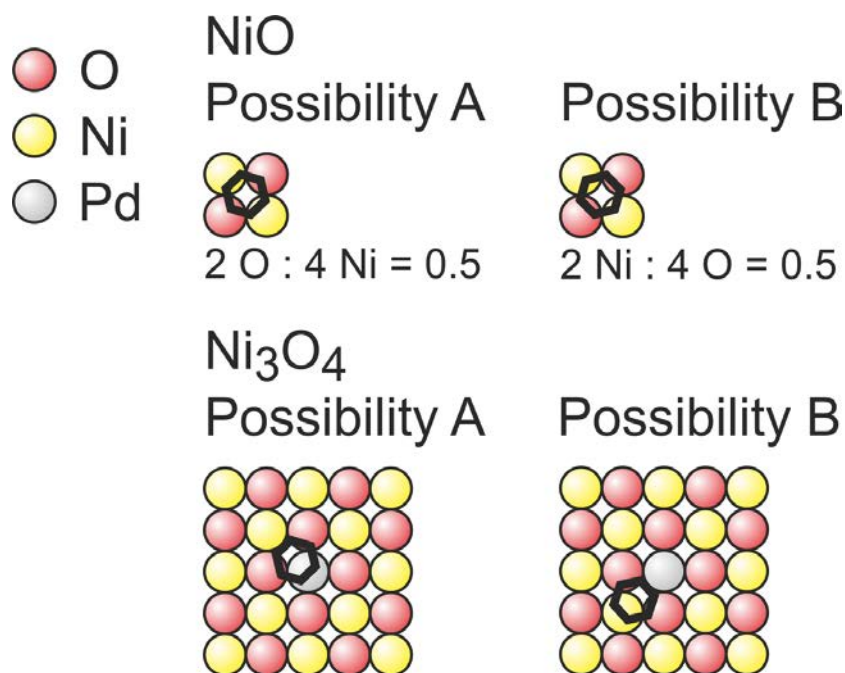


**Figure 12.2:** Model of the adsorption of benzene on nickel oxide (100) and the wetting layer with missing nickel vacancies. Here these vacancies are presented in gray as the underlying palladium. First the benzene molecule is set to the fourfold hollow site resulting to a ratio of 2:1 (0.5) for both possible orientations. For the Ni<sub>3</sub>O<sub>4</sub> also two possibilities can be found with a 2:1 ratio which comes close to the fitted 0.56 ratio.

In the quantitative analysis (cf. Figure 12.3) it is visible that the coverage raises very slowly to  $\sim 0.5$  L. This effect is attributed to a experimental difficulties due to the pumping. Before each adsorption experiment the nickel oxide film was prepared under an oxygen atmosphere. A residual amount of oxygen in the dosing system could have led to a substandard cleanliness of the benzene dosage. The oxygen does not alter the film nor does it react with benzene at these temperatures but it distorts the exposure axis till an

exposure of 0.5 L. The first benzene species grows and saturates at a coverage of 0.4 ML at 0.8 L. At 0.6 L the second benzene species rises and saturates at 1.2 ML. Finally, at 1.4 L the multilayer starts to grow. Minor amounts of a decay product are also found. It is assigned to CH due to the binding energy of 283.7 eV, as found in the ethylene studies. However, an exact assignment is not possible.

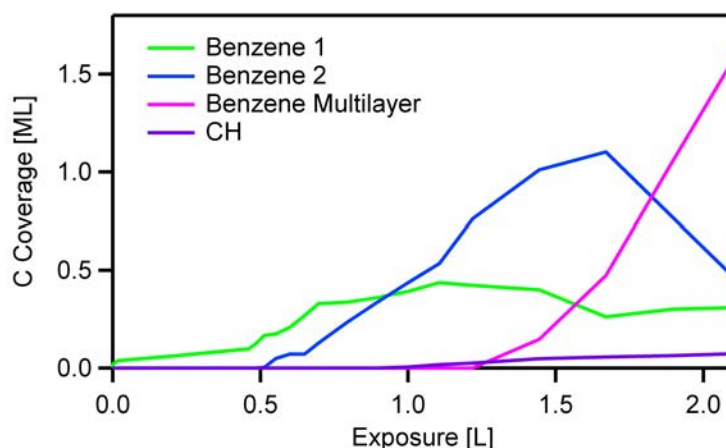


**Figure 12.3:** Quantitative analysis of the adsorption of benzene on a 1 ML thick nickel oxide film at 120 K

### 12.1.1.2 Reaction

In this section, the thermal evolution of benzene adsorbed on 1 ML NiO/Pd(100) is discussed. The complete experiment is shown in a color-coded density plot in Figure 12.4, along with additional representative spectra and respective fits. At temperatures below 200 K, a peak at 284.7 eV is visible. Starting at 130 K this peak undergoes a massive drop in intensity up to 200 K, and afterwards a shift in binding energy occurs by  $\sim -0.6$  eV. At 480 K, a broad peak rises at 285.5 eV and above 550 K the peak structure completely disappears. Due to the high FWHM of this peak it is necessary to deconvolute the different contributions by a numerical fit procedure. This is explained in the following.

Following the deconvolution procedure from the adsorption of benzene on this system four species are visible in the beginning: the first benzene species with two peaks at 284.2 and 284.8 eV and a constant ratio of 0.56, the second benzene species also with two peaks at 284.4 and 284.6 eV and a ratio of 0.5, the multilayer at 284.7 eV and an additional species, which

is tentatively assigned to CH for its binding energy (283.7 eV). At higher temperatures several minor decay products appear. It was not possible to identify these products in particular and therefore they are added up in the quantitative analysis (cf Figure 12.5).

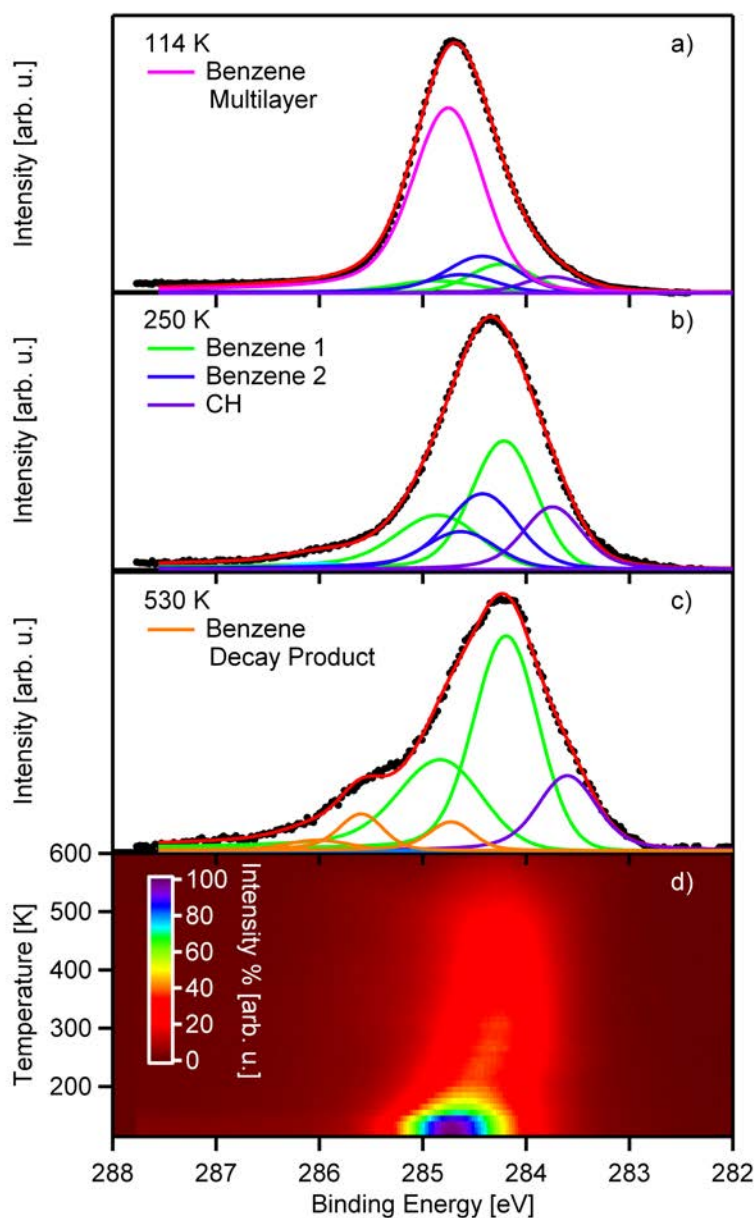


**Figure 12.4:** Spectra and density plot of the reaction of benzene on a 1 ML thick nickel oxide film

At 140 K, multilayers of benzene start to desorb and have completely vanished at 240 K (cf. Figure 12.5). The second benzene species (0.5 ML)

starts to decline partially while the amount of the first benzene species grows to a maximum amount of 0.7 ML at 310 K. After this it also desorbs, while minor amounts (0.1 ML) of a benzene decay product occurs at 480 K. At this temperature also the CH starts to vanish.

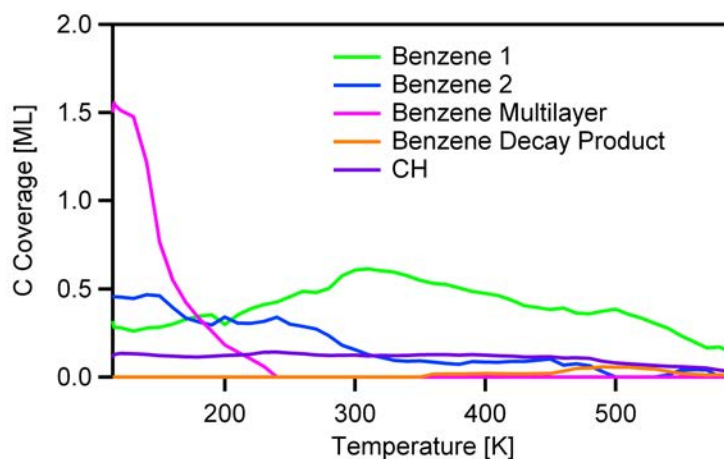


**Figure 12.5:** Quantitative analysis of the reaction of benzene on a 1 ML thick nickel oxide film

## 12.1.2 NiO film: 2 ML

### 12.1.2.1 Adsorption

The spectra of the adsorption of benzene on a 2 ML thick nickel oxide film show a big peak evolving at a binding energy of 284.5 eV. It shifts to 284.8 eV (cf. Figure 12.6 d) up to an exposure of 0.4 L. Interestingly the spectra shift back to 284.5 eV up to exposures of 1.1 L. When again additional  $C_6H_6$  is adsorbed the peak moves again to 284.8 eV. This unusual behavior is assigned to the subsequent population of the already discussed different benzene species 1 and 2 as well as the multilayer. The deconvolution of these spectra were also done with the fit procedure from the adsorption of the benzene on the 1 ML thick nickel oxide film leading to four species: the first benzene species with two peaks at a binding energy of 284.2 and 284.8 eV, the second benzene species also with two peaks at 284.7 and 284.9 eV, CH at 283.7 eV and the benzene multilayer at 284.5 eV. One has to note that all binding energies are shifted slightly to higher binding energies. This is explained by the different film characteristics of the second layer of the nickel oxide film compared to the wetting layer.

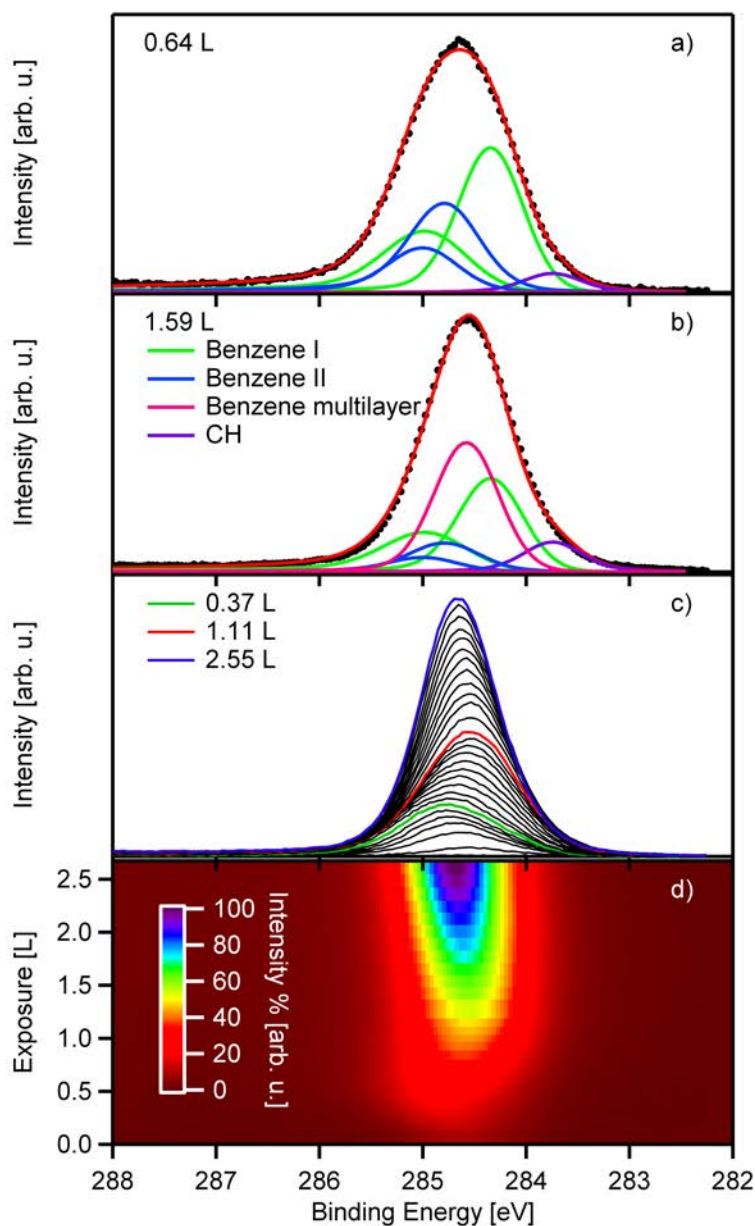


**Figure 12.6:** Spectra and density plot of the adsorption of benzene on a 2 ML thick nickel oxide film

The quantitative analysis is presented in Figure 12.6. Here it becomes visible that the second benzene species grows from the beginning on and saturates at an exposure of 0.3 L with a coverage of 0.4 ML. At this exposure the first benzene species starts to grow till a coverage of 0.9 ML. The saturation coverage of benzene with 1.2 ML for both species is reached after an exposure of 1.4 L. At 0.6 L the growth of the multilayer sets in. Interestingly the second benzene species starts to grow before the first species.

In the section above, it was assumed that the first species is the benzene adsorbed on the wetting layer and the second species is adsorbed on NiO. Within this assignment the adsorption site is not only on the wetting layer but also on the undercoordinated NiO. The missing damping of the first and second benzene species could be due to the growth of column-like structures covering only minor parts of the surface.

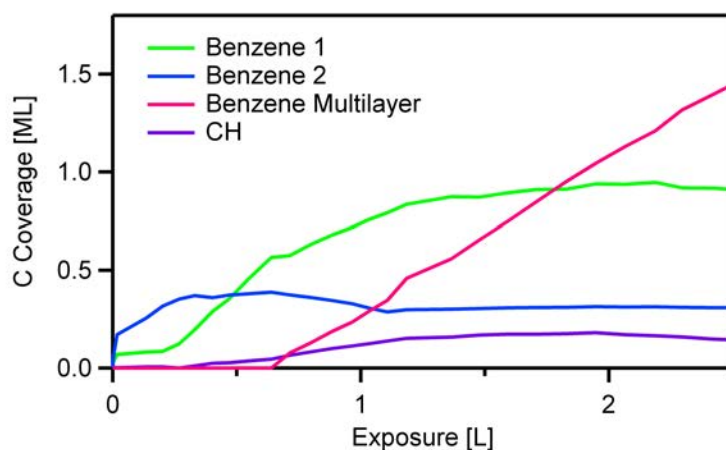


**Figure 12.7:** Quantitative analysis of the adsorption of benzene on a 2 ML thick nickel oxide film at 120 K

### 12.1.2.2 Reaction

The density plot of the reaction of benzene on 2 ML thick nickel oxide film is shown in Figure 12.8 d. At 200 K a drop in intensity occurs due to the desorption of the multilayer of benzene at 284.7 eV. Until 300 K, the remaining peak shifts to lower binding energy (284.3 eV). Above 300 K the peak shifts back to higher binding energy. The deconvolution was done with the four known species (benzene 1, benzene 2, benzene multilayer and CH). Additionally, a decay product (284.8 eV) is introduced to model the shift of the peak at 300 K.

The quantitative analysis is presented in Figure 12.9 and shows the start of the desorption of the multilayer at 140 K, while all other species stay constant in coverage. At 180 K, minor parts of the first benzene species desorb. The amount of the second benzene species decreases while the first benzene species increases. This indicates a change in the film following the argumentation that the first benzene species is benzene adsorbed on the

nonstoichiometric NiO. At 280 K, the first species decreases again and a decay product occurs at a binding energy of 284.7 eV.

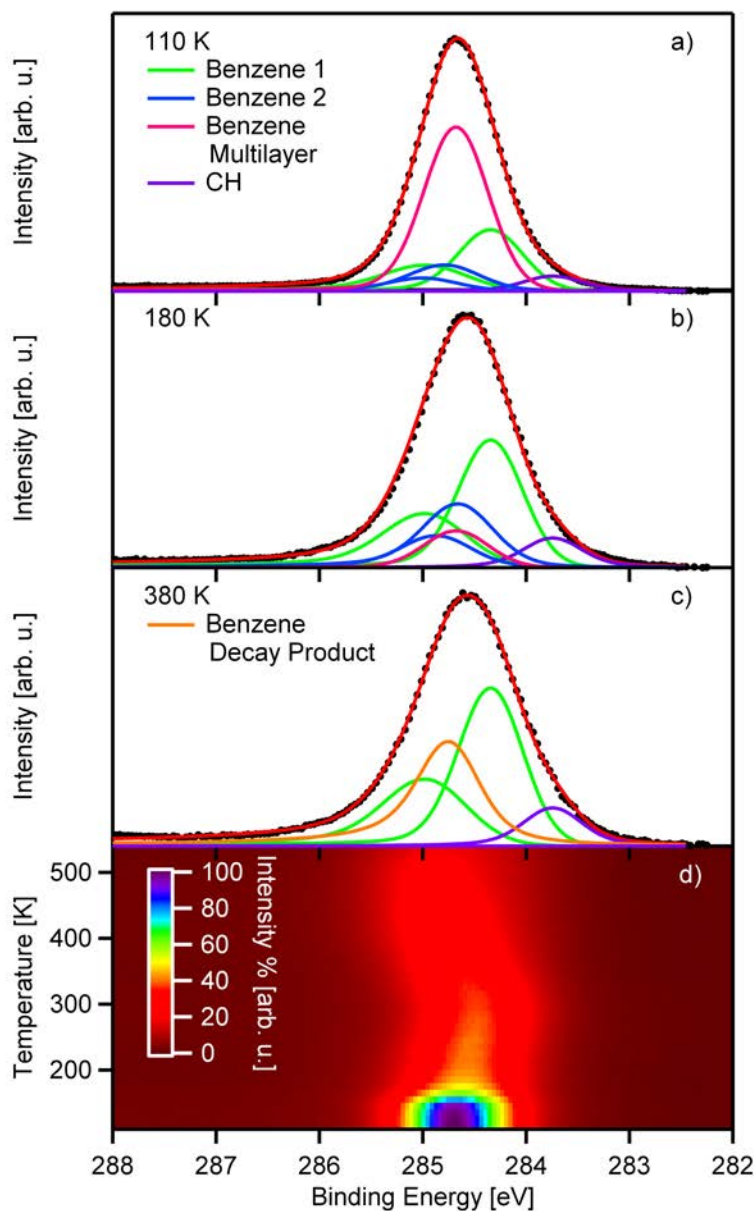


**Figure 12.8:** Spectra and density plot of the reaction of benzene on a 2 ML thick nickel oxide film

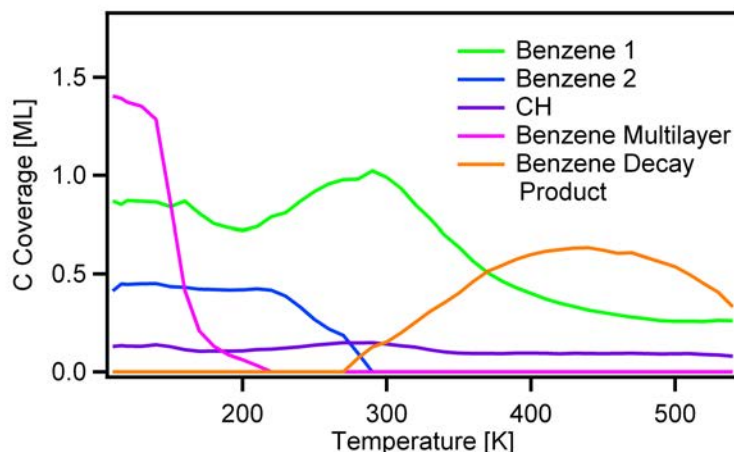


**Figure 12.9:** Quantitative analysis of the reaction of benzene on a 2 ML thick nickel oxide film

### 12.1.3 NiO film: 6 ML

#### 12.1.3.1 Adsorption

The corresponding spectra and the waterfall plot of the adsorption of benzene on six monolayer thick nickel oxide film is shown in Figure 12.10. During adsorption, a peak at 284.7 eV is rising till 0.3 L. From this point on, the intensity increases significantly. This is very unusual because it would mean a change in the sticking coefficient. It is more likely that the problems due to pumping in the dosing system are responsible for a distortion of the exposure values to a point where solely benzene is dosed ( $\sim 0.2$  L). This problem also occurred during the adsorption of benzene on the 1 ML thick nickel oxide film. Another explanation could be the dewetting of the layer. The deconvolution was done in an analogous way than before with four species, the two benzene species, a benzene multilayer and CH. Again, the identification of the CH is solely done by the binding energy (283.7 eV) of CH on Pd(100). The binding energy of the two contributions for the first benzene species is 284.3 and 284.9 eV, for the second benzene species 284.7 and 284.9 eV and for the multilayer 284.6 eV.

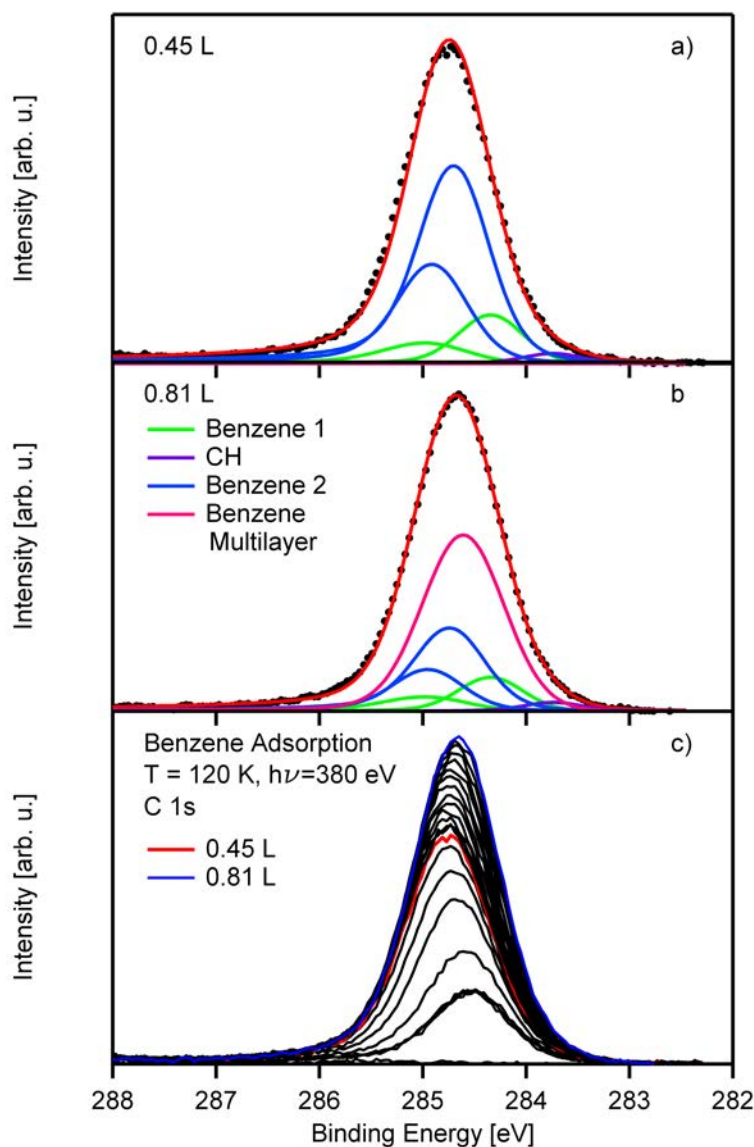


**Figure 12.10:** Spectra and density plot of the adsorption of benzene on a 6 ML thick nickel oxide film

The quantitative analysis depicted in Figure 12.11 shows that immediately both benzene species 1 and 2 show a coverage of 0.18 and 0.1 ML. This behavior cannot be explained easily. While the first benzene species keeps the 0.18 ML constant over the whole adsorption experiment the second benzene species starts to grow at 0.07 L and saturates at a coverage of 0.8 ML at an exposure of 0.5 L. As soon as the second benzene species saturates the multilayer starts to grow and damps the second benzene species.

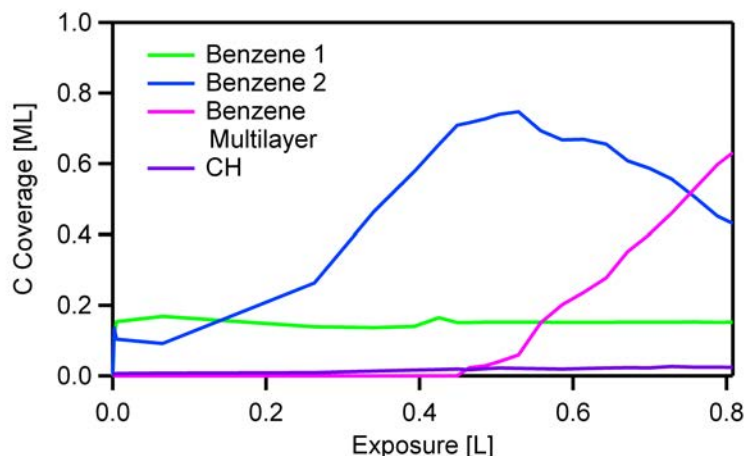


**Figure 12.11:** Quantitative analysis of the adsorption of benzene on a 6 ML thick nickel oxide film

### 12.1.3.2 Reaction

In this section the reaction of benzene with the rather unreactive six monolayer thick nickel oxide film on Pd(100) is discussed. Looking at the density plot of this experiment (cf. Figure 12.12) one will recognize that at low temperatures the main peak is at the binding energy of 284.8 eV. After a temperature rise to 180 K this peak loses a lot of intensity and a smaller peak at 284.3 eV remains. This peak shifts to higher binding energies during the heating process, the fact is similar to the reaction of benzene adsorbed on the 2 ML nickel oxide besides that the overall intensity is lower. The above mentioned four species appear again and additionally a benzene decay species is introduced like in the reaction of the benzene on the 2 ML nickel oxide layer.

In the following the quantitative analysis (cf. Figure 12.13) is discussed. The multilayer starts to decrease at a temperature of 140 K and has completely vanished at 180 K. The second benzene does not increase due to less damping which is caused by its desorption. At 220 K, the second benzene species is also vanished and the first benzene species starts to decrease. The decay product appears at 270 K.

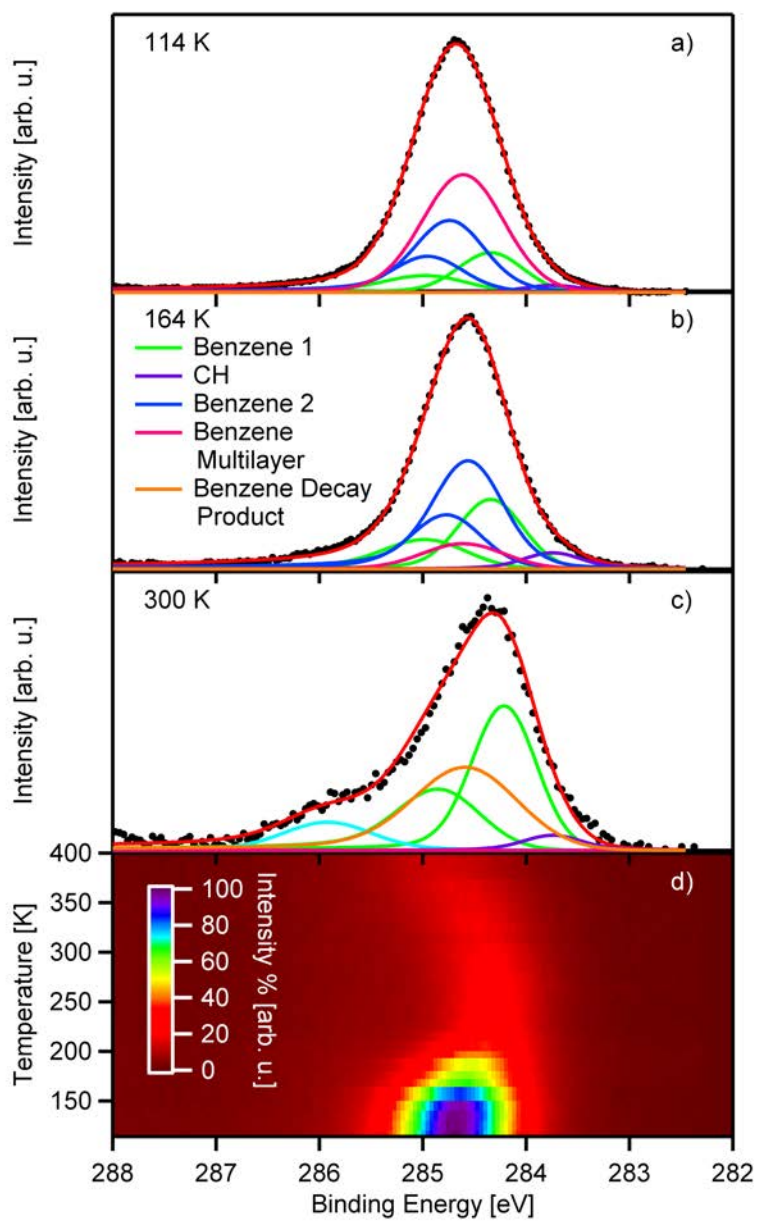


**Figure 12.12:** Spectra and density plot of the reaction of benzene on a 6 ML thick nickel oxide film

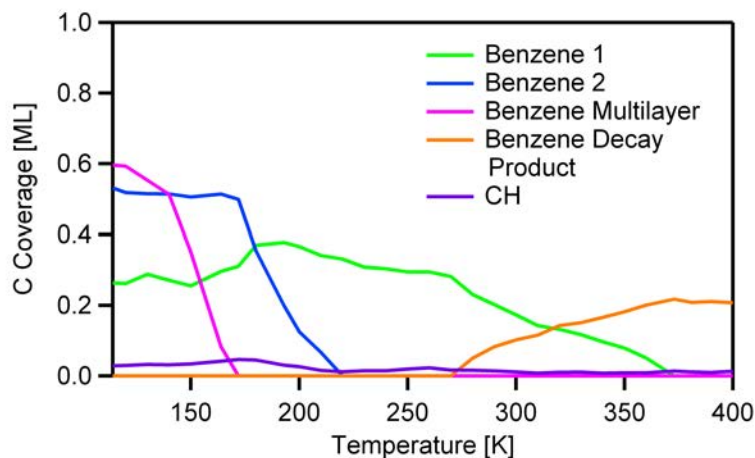


**Figure 12.13:** Quantitative analysis of the reaction of benzene on a 6 ML thick nickel oxide film

#### 12.1.4 Conclusion

For the 1 ML thick nickel oxide film, two species and a multilayer are found during the adsorption. The two adsorbing species have two contributions each, hinting to the fact that the carbon atoms from the benzene molecule adsorbed on nickel and oxygen have different signals respectively. The interpretation of these two species is that one species adsorbs on the undercoordinated nickel oxide while the second species adsorbs on the stoichiometric nickel oxide. The thermal evolution of this system showed that all benzene species desorb and only minor parts react to several different decay products. On the two monolayer thick nickel oxide film again two benzene species and the multilayer adsorb. In contrast to the reaction on the 1 ML thick film, benzene starts to react to only one decay product at the temperature of 280 K. A similar adsorption and reaction behavior is found for all oxide films.



## 12.2 Coverage Simulation



Figure 12.14: UML diagram of the simulation program for the C<sub>2</sub>H<sub>2</sub> coverage

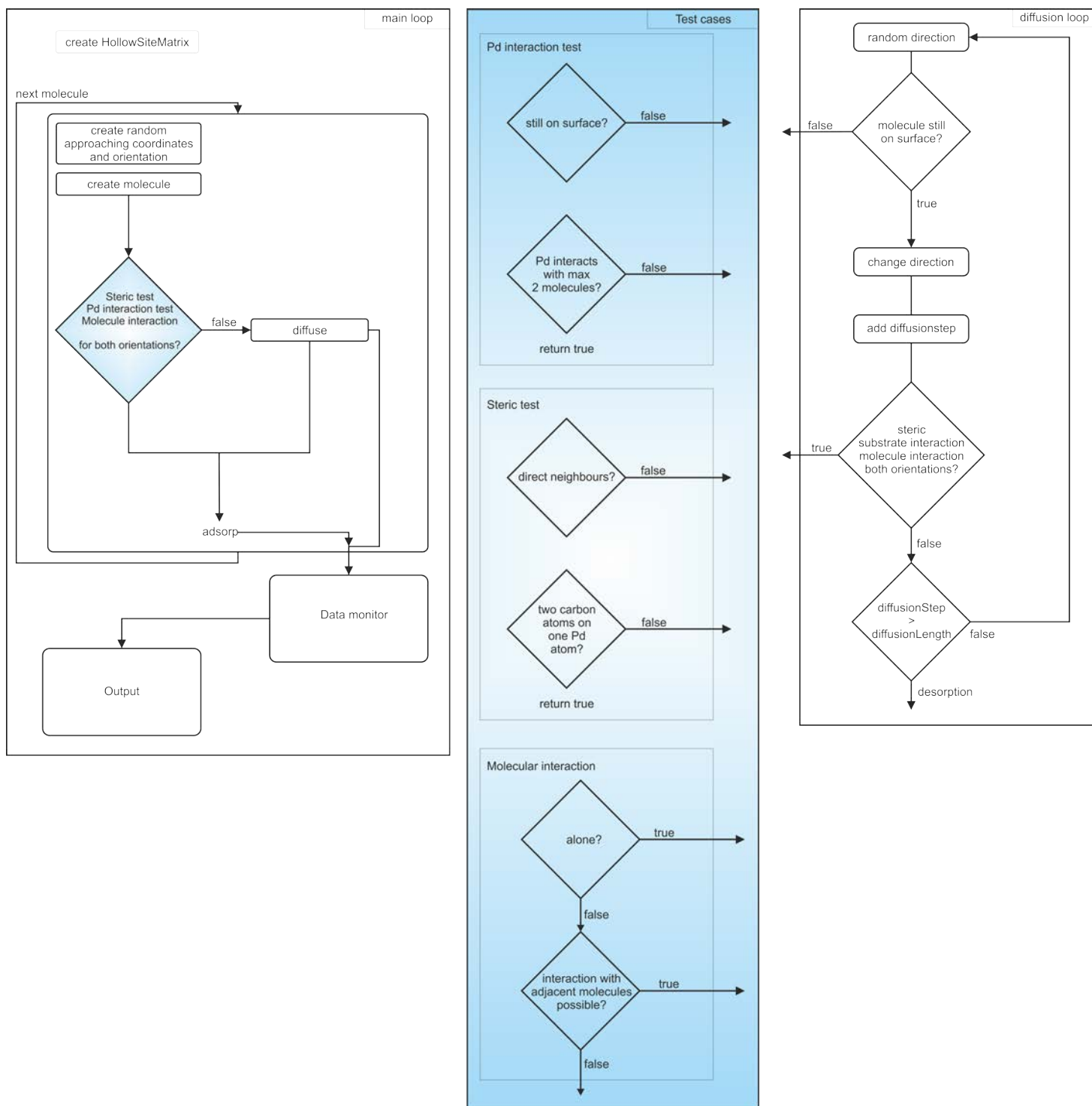


Figure 12.15: Flow chart of the simulation program

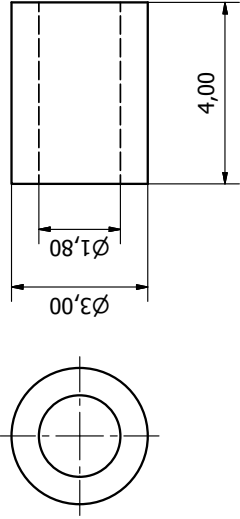
## 12.3 Transfer System Blueprints

PRODUCED BY AN AUTODESK EDUCATIONAL PRODUCT

PRODUCED BY AN AUTODESK EDUCATIONAL PRODUCT



PRODUCED BY AN AUTODESK EDUCATIONAL PRODUCT



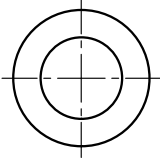
**4x aus Marcor anfertigen**

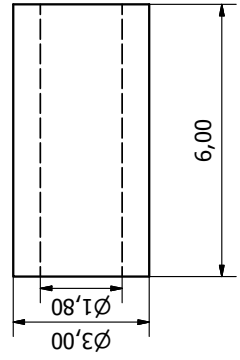
Designed by Oliver Höfert	Checked by PC II	Approved by Keramikhülse	Date 7/5/2010
		Edition Keramikhülse	Sheet: 1 / 1

PRODUCED BY AN AUTODESK EDUCATIONAL PRODUCT



PRODUCED BY AN AUTODESK EDUCATIONAL PRODUCT

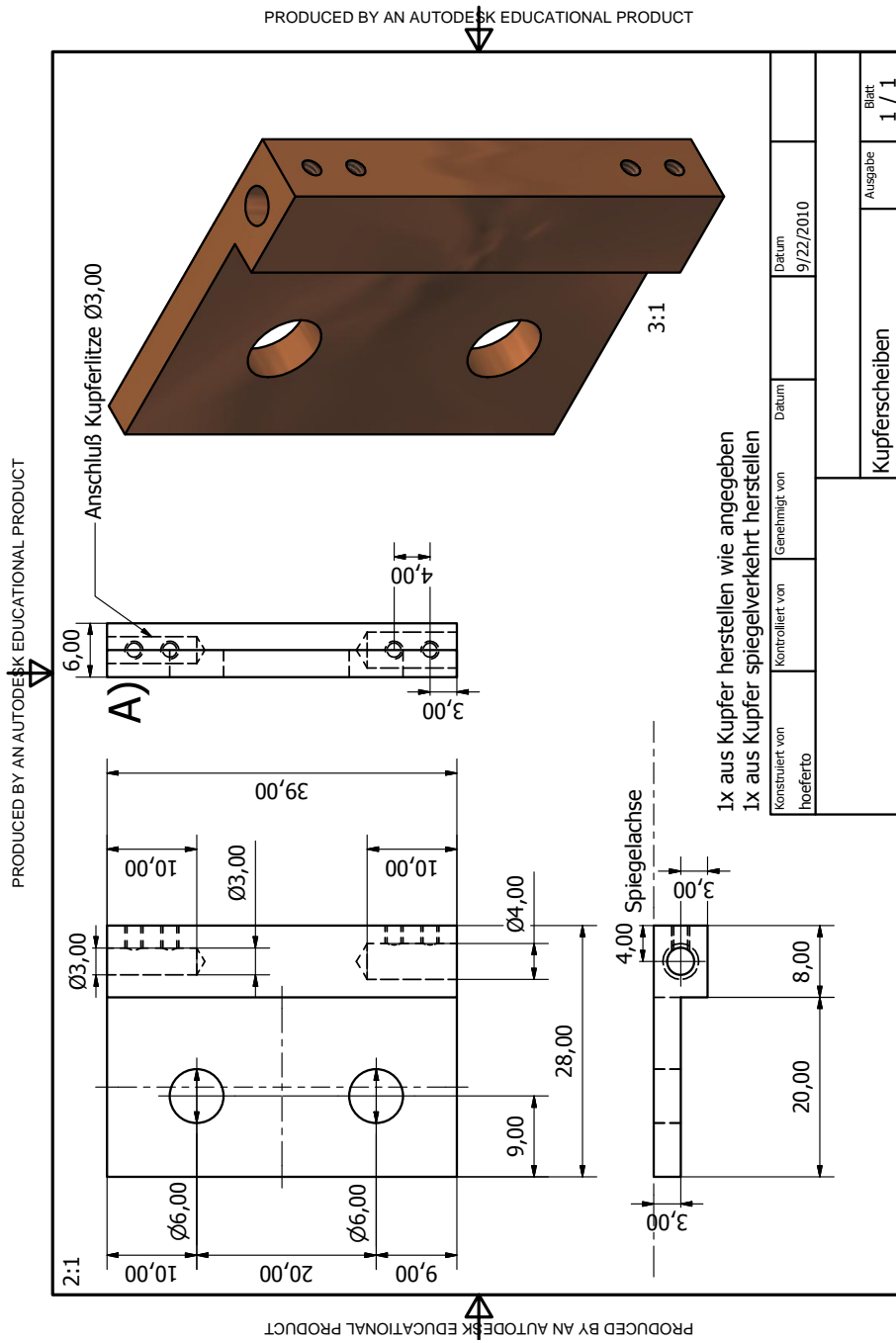


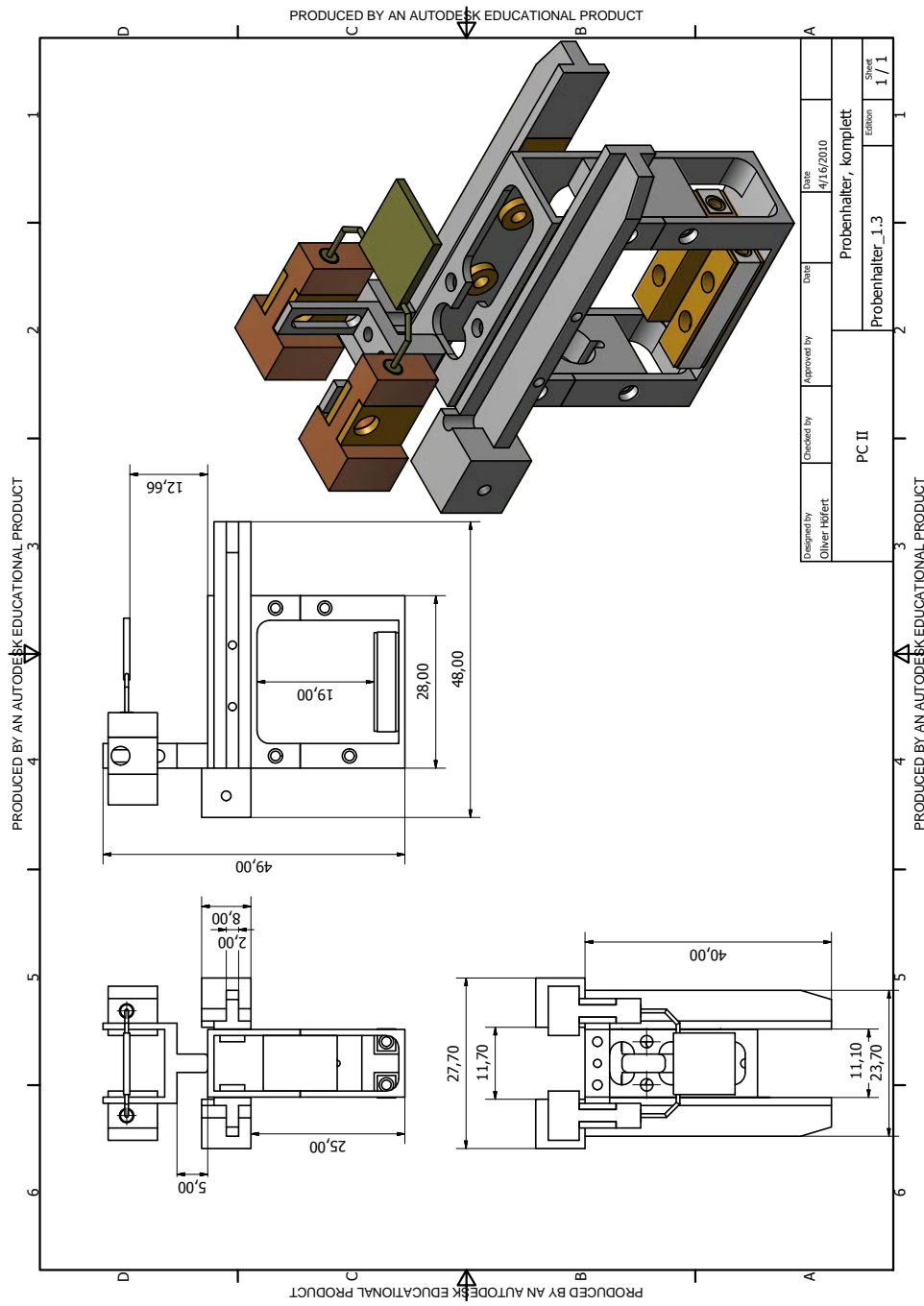


**4x aus Marcor anfertigen**

Designed by Oliver Höfert	Checked by	Approved by	Date	Date	Edition	Sheet
				7/5/2010	Keramikhülse 6mm	1 / 1
PC II					Keramikhülse 6mm	

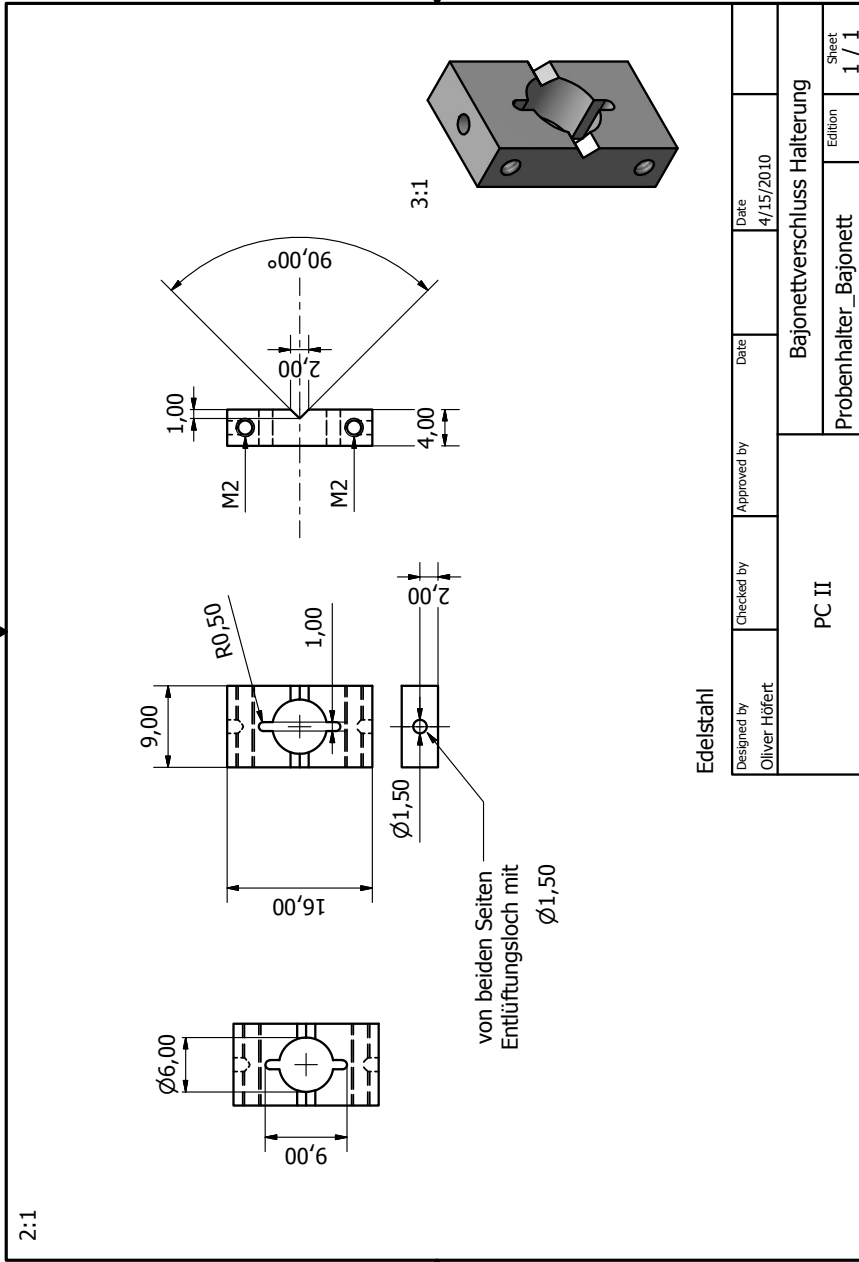
PRODUCED BY AN AUTODESK EDUCATIONAL PRODUCT





PRODUCED BY AN AUTODESK EDUCATIONAL PRODUCT

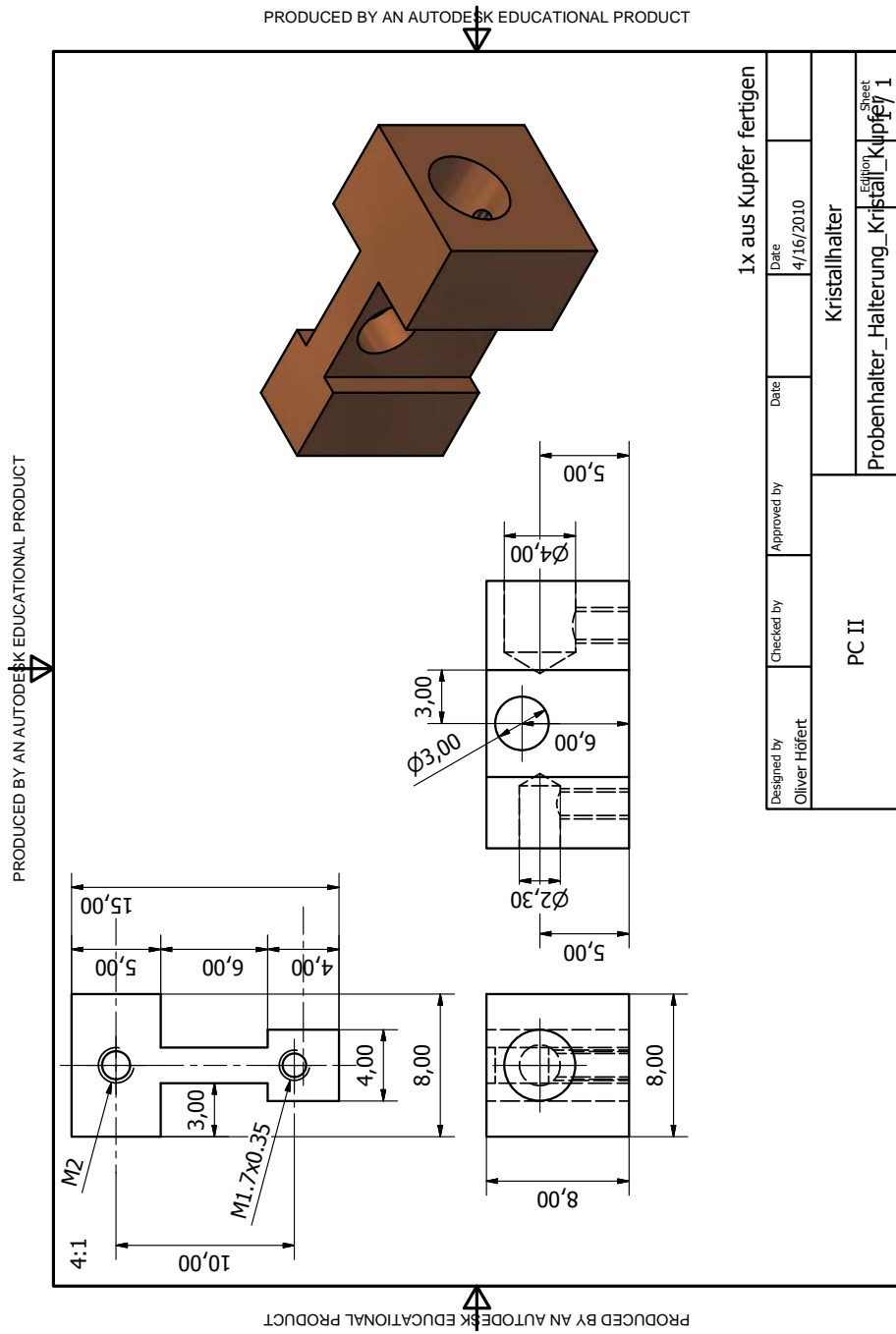
PRODUCED BY AN AUTODESK EDUCATIONAL PRODUCT



PRODUCED BY AN AUTODESK EDUCATIONAL PRODUCT

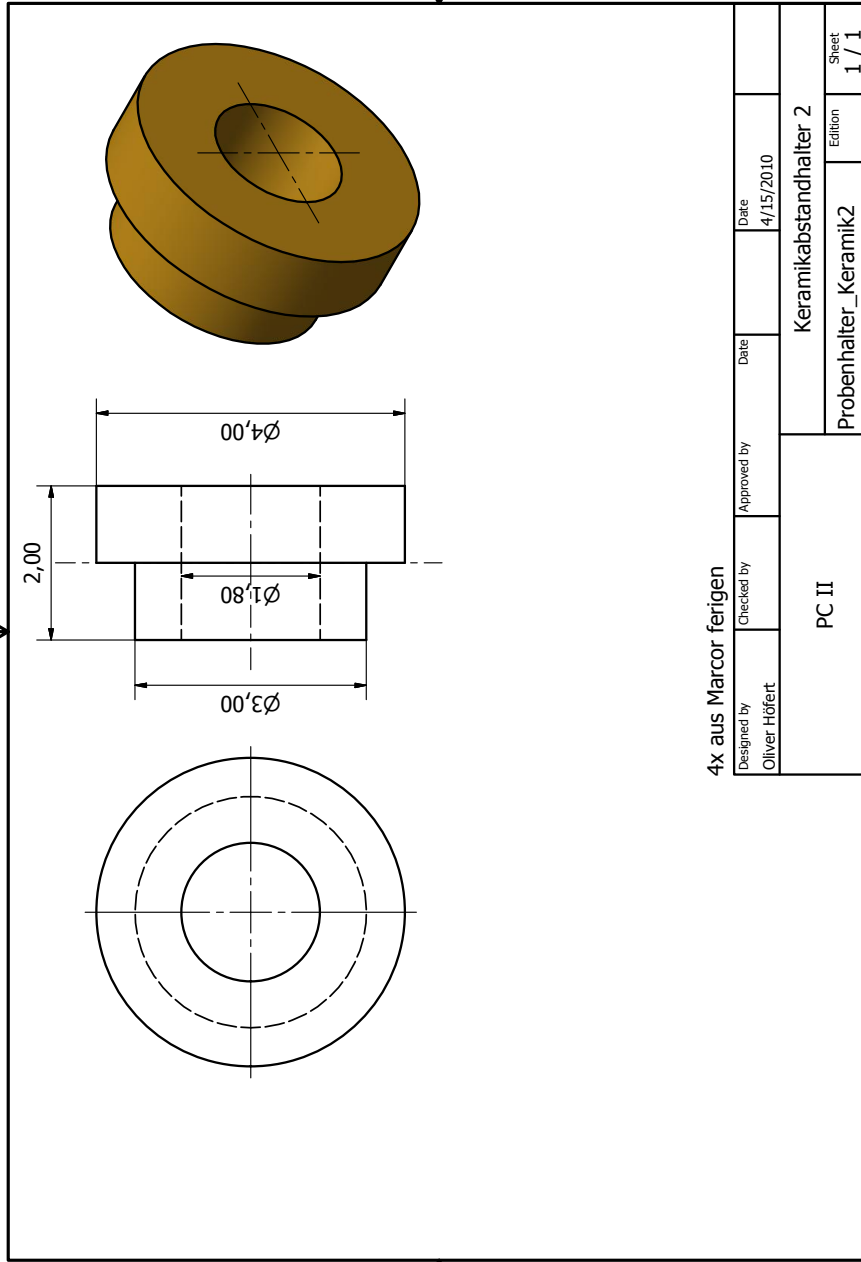
Designed by Oliver Höfert	Checked by	Approved by	Date 4/15/2010
PC II		Bajonettverschluss Halterung	
Edelstahl		Probenhalter_Bajonett	Sheet: 1 / 1

PRODUCED BY AN AUTODESK EDUCATIONAL PRODUCT



PRODUCED BY AN AUTODESK EDUCATIONAL PRODUCT

PRODUCED BY AN AUTODESK EDUCATIONAL PRODUCT

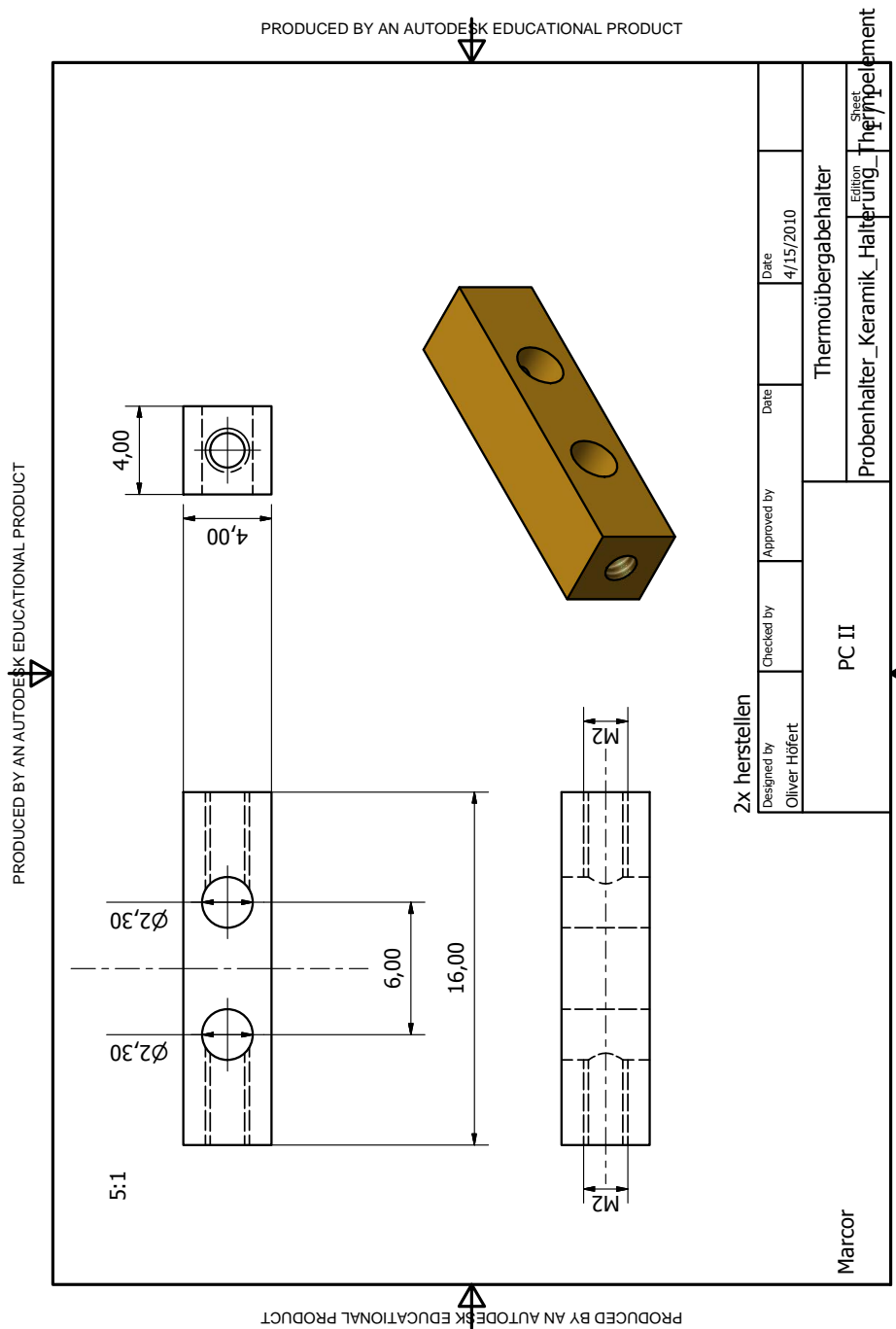


4x aus Marcor fertigen

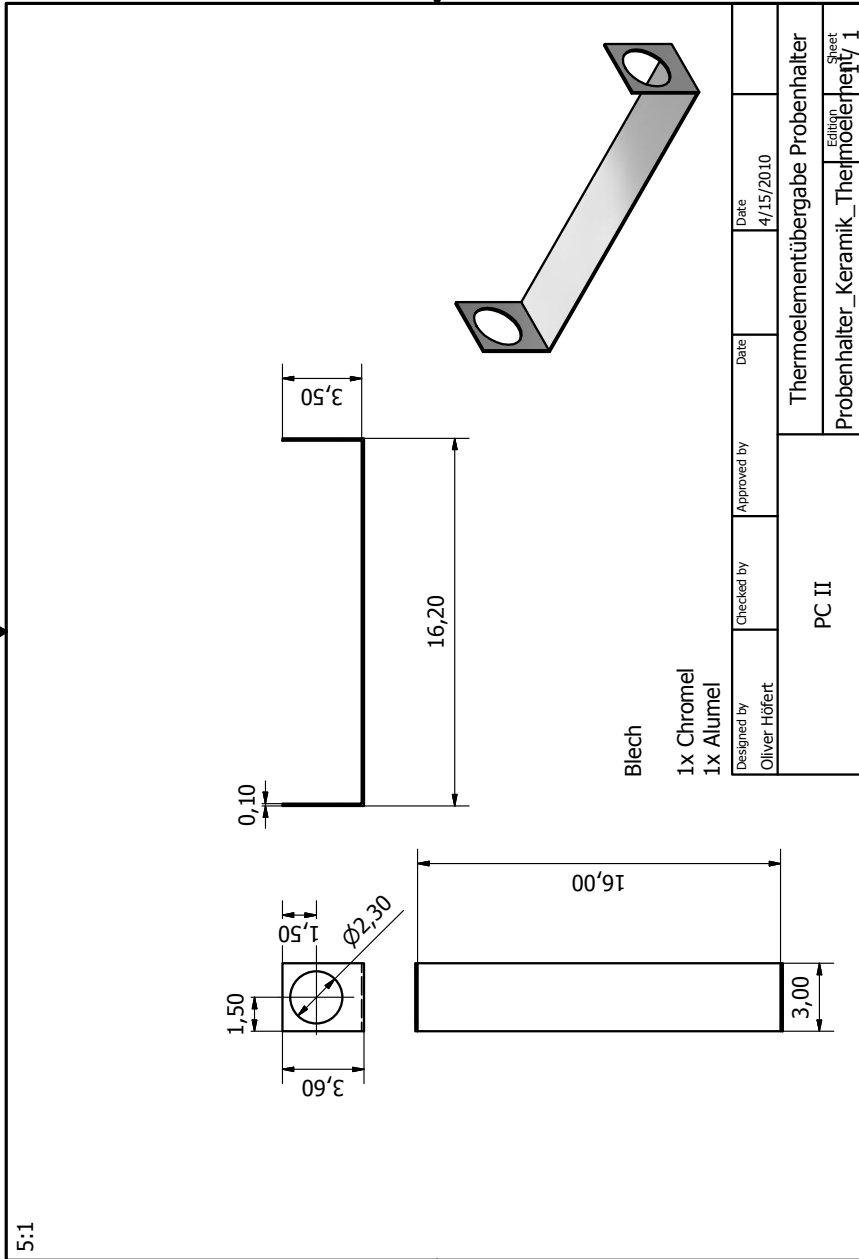
Designed by Oliver Höfert	Checked by	Approved by	Date 4/15/2010
PC II		Keramikaabstandhalter 2	
		Probenhalter_Keramik2	Sheet: 1 / 1

PRODUCED BY AN AUTODESK EDUCATIONAL PRODUCT

PRODUCED BY AN AUTODESK EDUCATIONAL PRODUCT

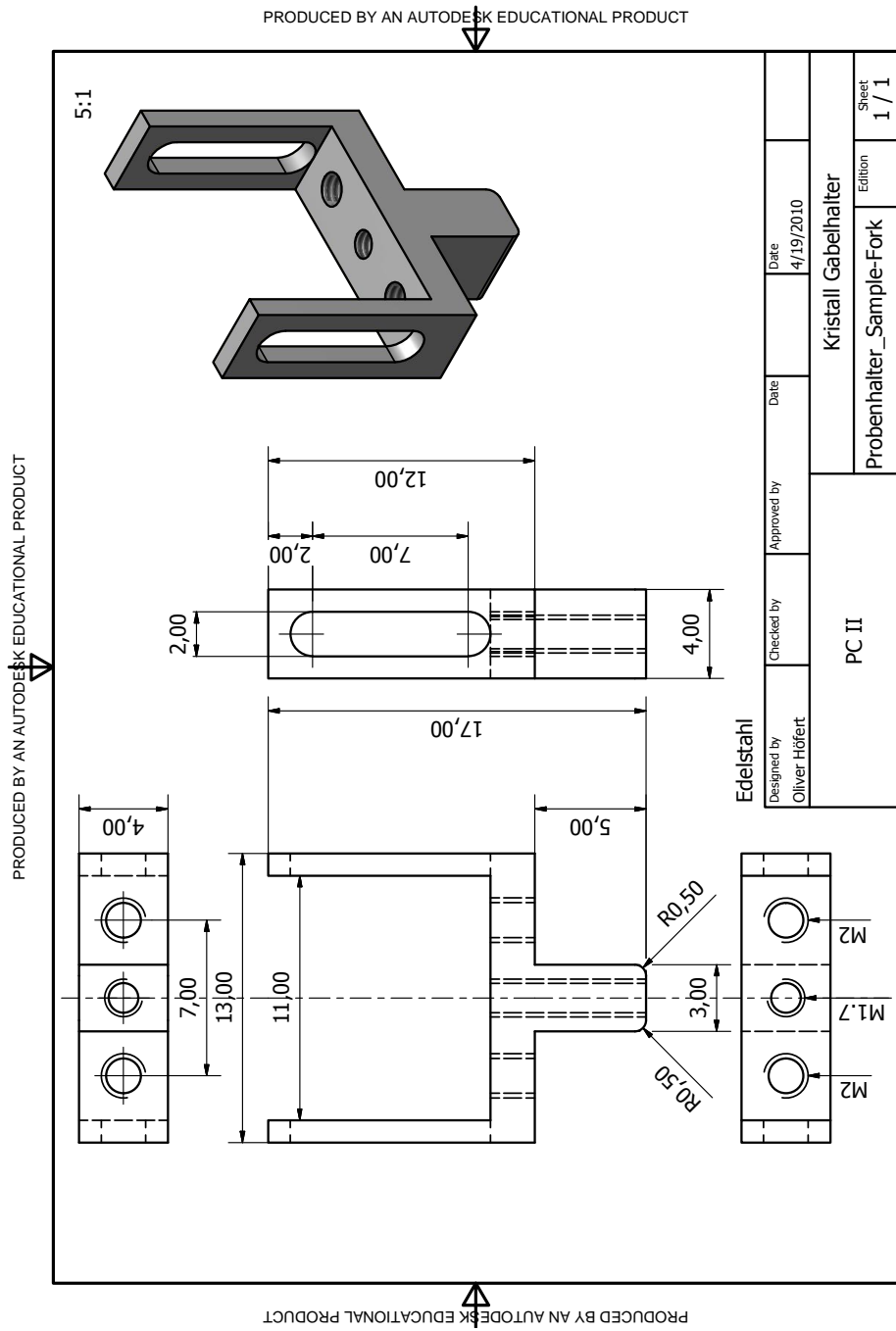


PRODUCED BY AN AUTODESK EDUCATIONAL PRODUCT

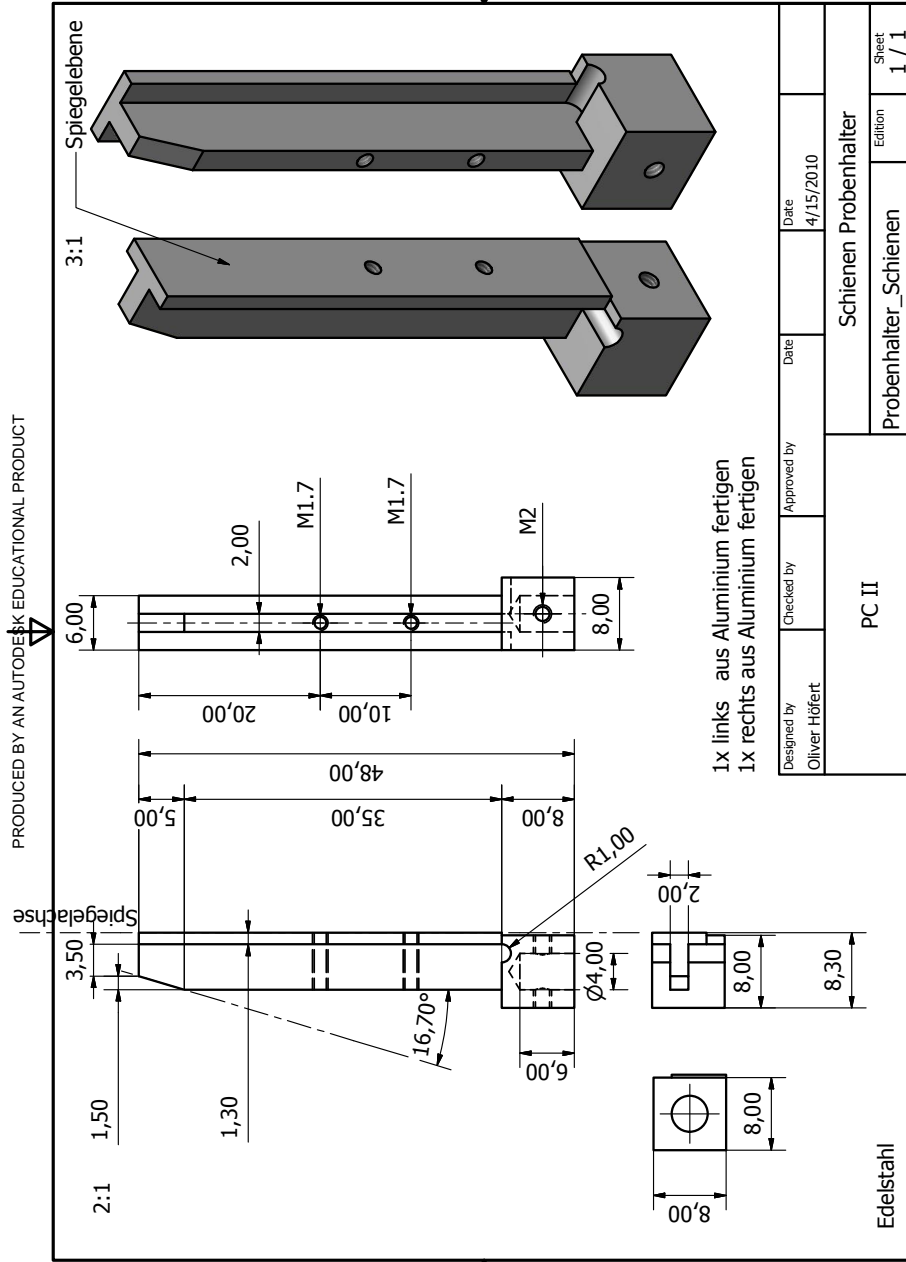


PRODUCED BY AN AUTODESK EDUCATIONAL PRODUCT

PRODUCED BY AN AUTODESK EDUCATIONAL PRODUCT



PRODUCED BY AN AUTODESK EDUCATIONAL PRODUCT



PRODUCED BY AN AUTODESK EDUCATIONAL PRODUCT

PRODUCED BY AN AUTODESK EDUCATIONAL PRODUCT

PRODUCED BY AN AUTODESK EDUCATIONAL PRODUCT

1x aus Edelstahl fertigen

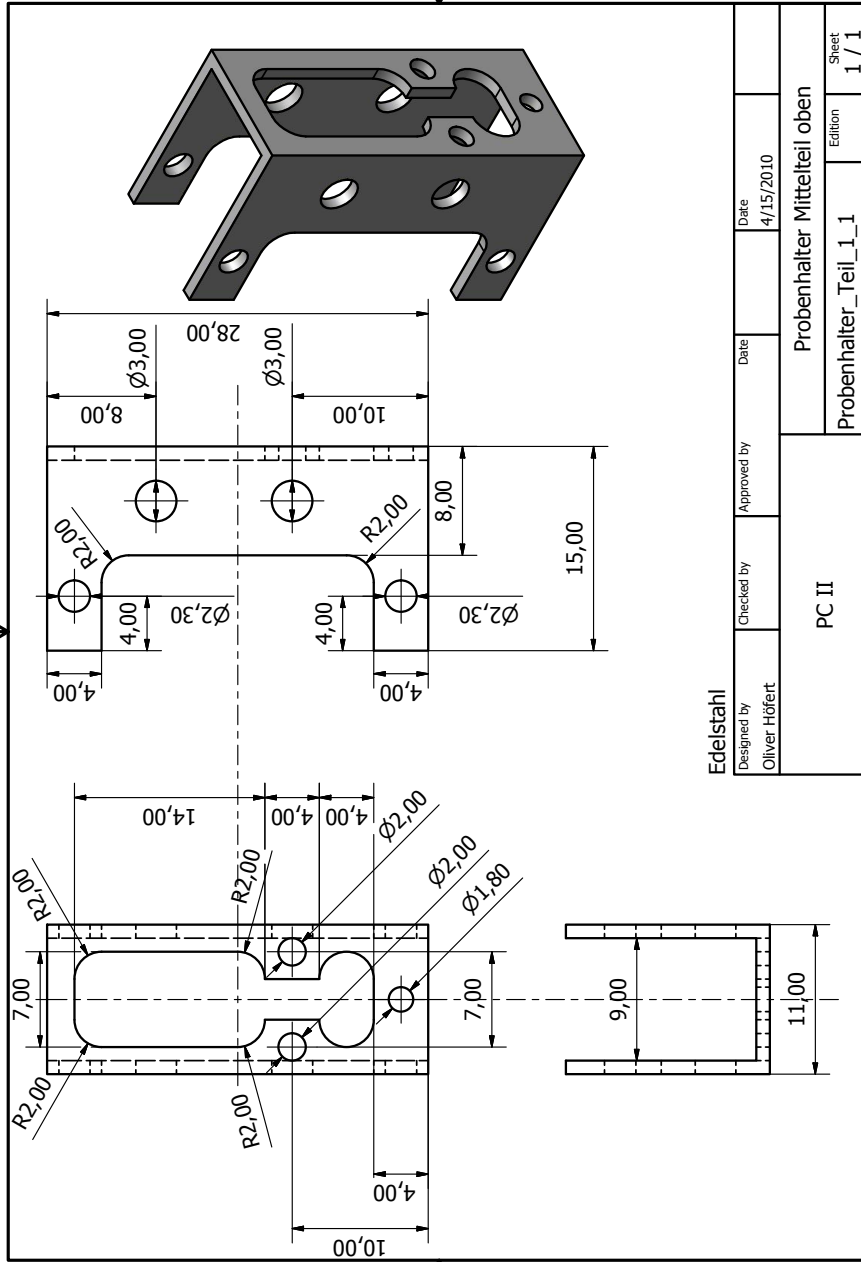
9,00  
4,00  
Ø1,50

12,00  
8,00  
M2  
M2  
4,00

5:1

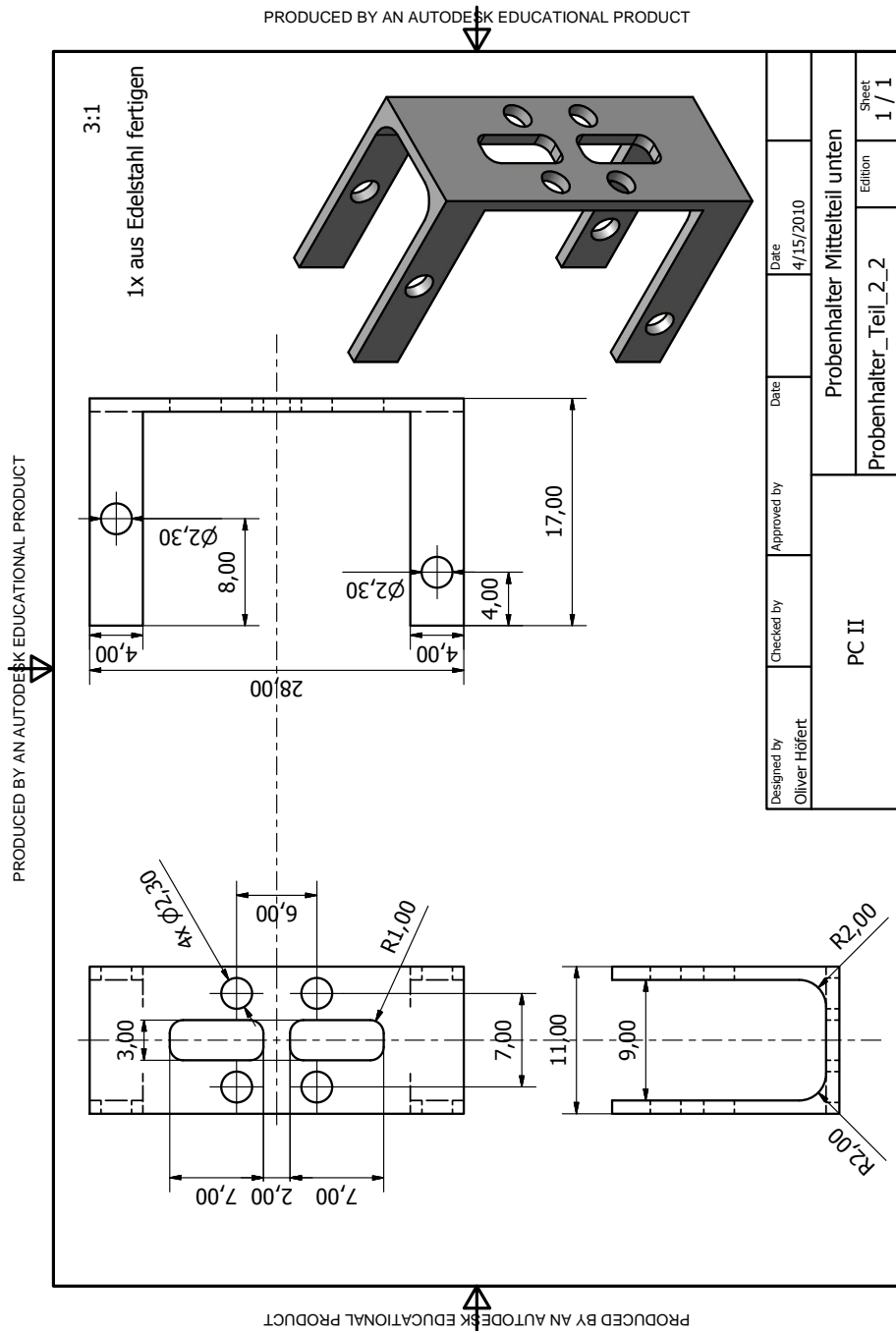
Designed by Oliver Höfert	Checked by	Approved by	Date 4/15/2010	
PC II			Stabilisierung Probenhalter	
			Edition Probenhalter_Stabilisierung_hinten	Sheet 1 / 1

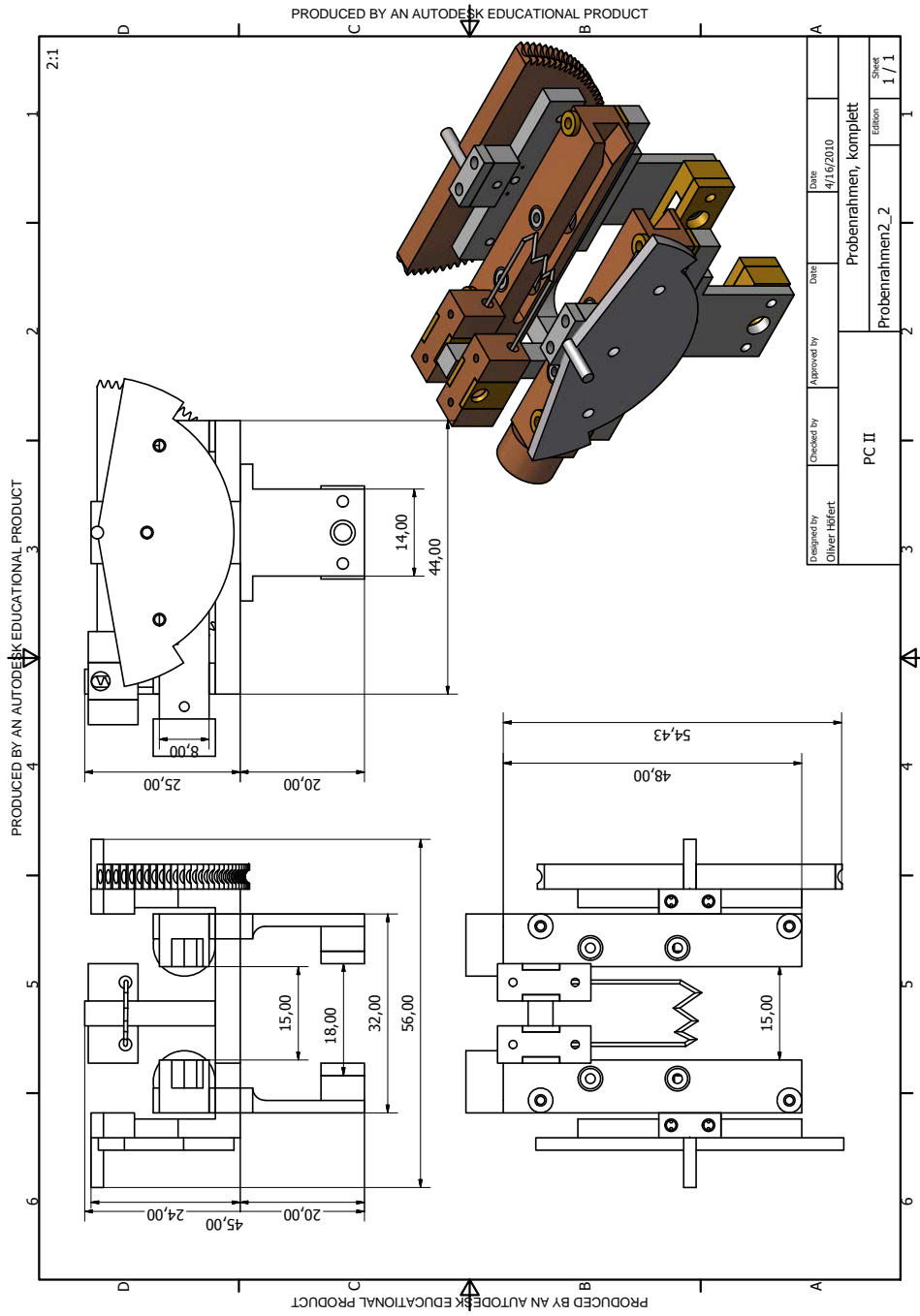
PRODUCED BY AN AUTODESK EDUCATIONAL PRODUCT

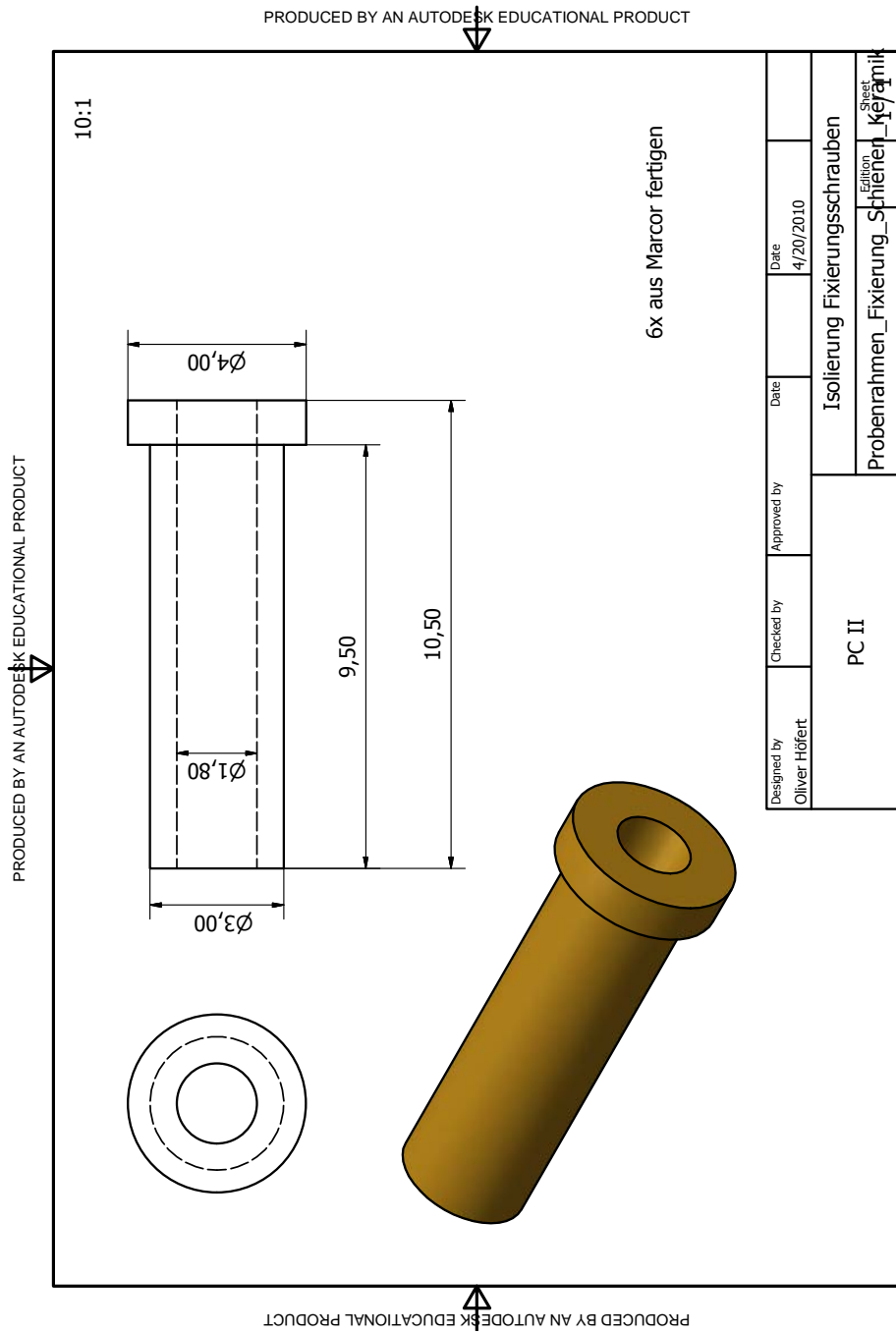


PRODUCED BY AN AUTODESK EDUCATIONAL PRODUCT

PRODUCED BY AN AUTODESK EDUCATIONAL PRODUCT

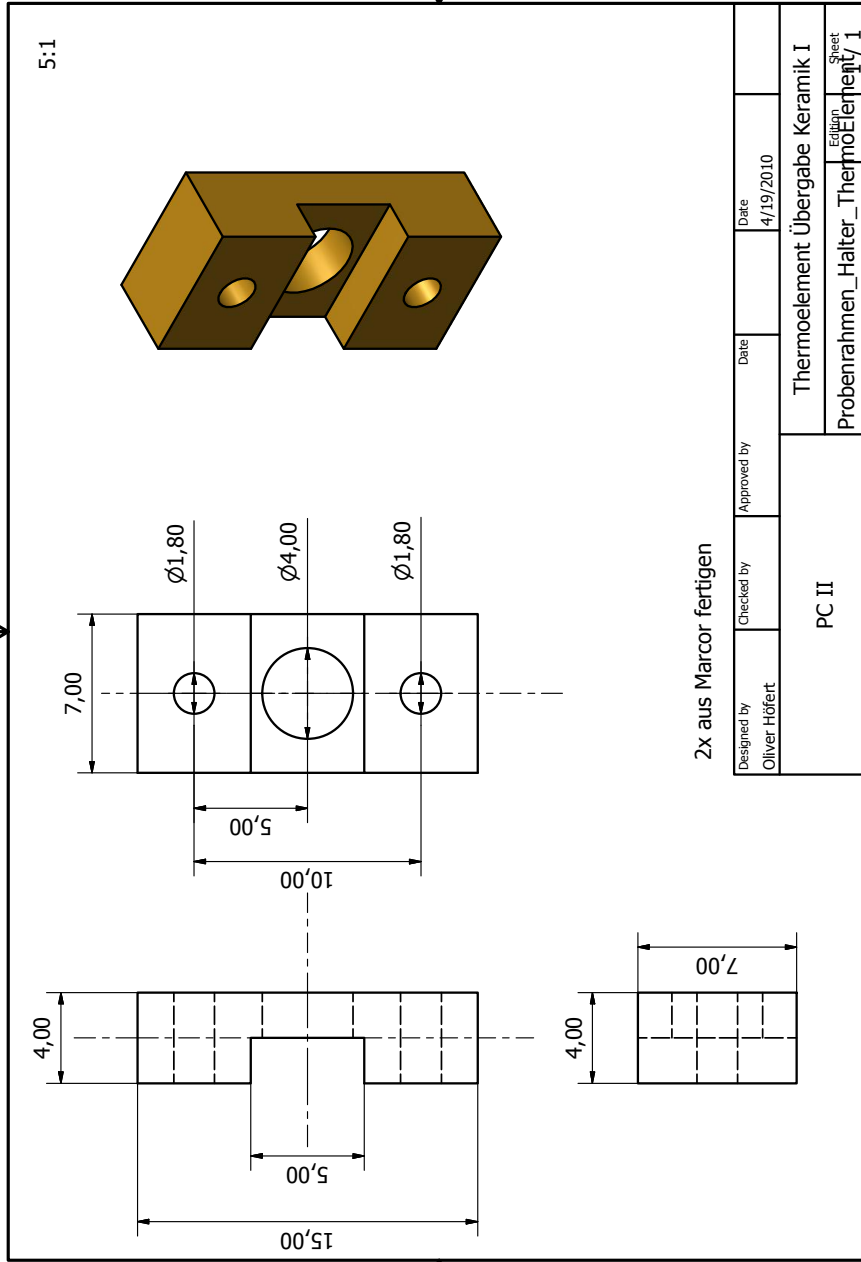






PRODUCED BY AN AUTODESK EDUCATIONAL PRODUCT

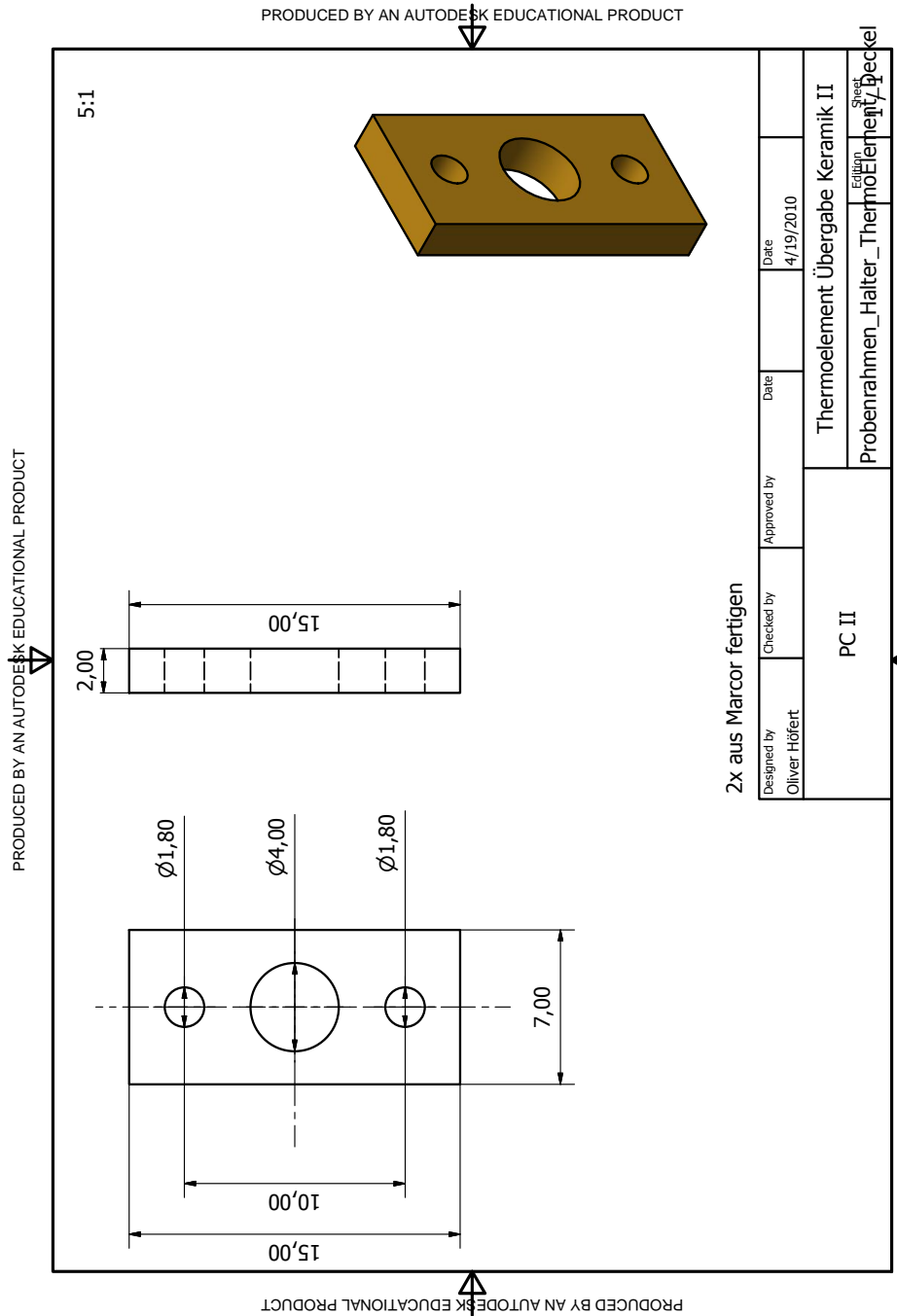
PRODUCED BY AN AUTODESK EDUCATIONAL PRODUCT



PRODUCED BY AN AUTODESK EDUCATIONAL PRODUCT

PRODUCED BY AN AUTODESK EDUCATIONAL PRODUCT

Designed by Oliver Höfert	Checked by	Approved by	Date 4/19/2010
PC II		Thermolement Übergabe Keramik I	
		Probentrahmen_Halter_Thermolement I	
		Sheet 1/1	



PRODUCED BY AN AUTODESK EDUCATIONAL PRODUCT

PRODUCED BY AN AUTODESK EDUCATIONAL PRODUCT

PRODUCED BY AN AUTODESK EDUCATIONAL PRODUCT

7,00  
5,00  
2,00  
M3.5x0.6 - 6H  
10:1

1x aus Chromel fertigen  
1x aus Alumel fertigen

ebenfalls 8x passende Madenschlitzschrauben

Designed by Oliver Höfert	Checked by	Approved by	Date 4/20/2010
PC II		Alumel/Chromel Halter	
		Probenrahmen_Halter_Thermo	Einlage
		Element	Sheet

PRODUCED BY AN AUTODESK EDUCATIONAL PRODUCT

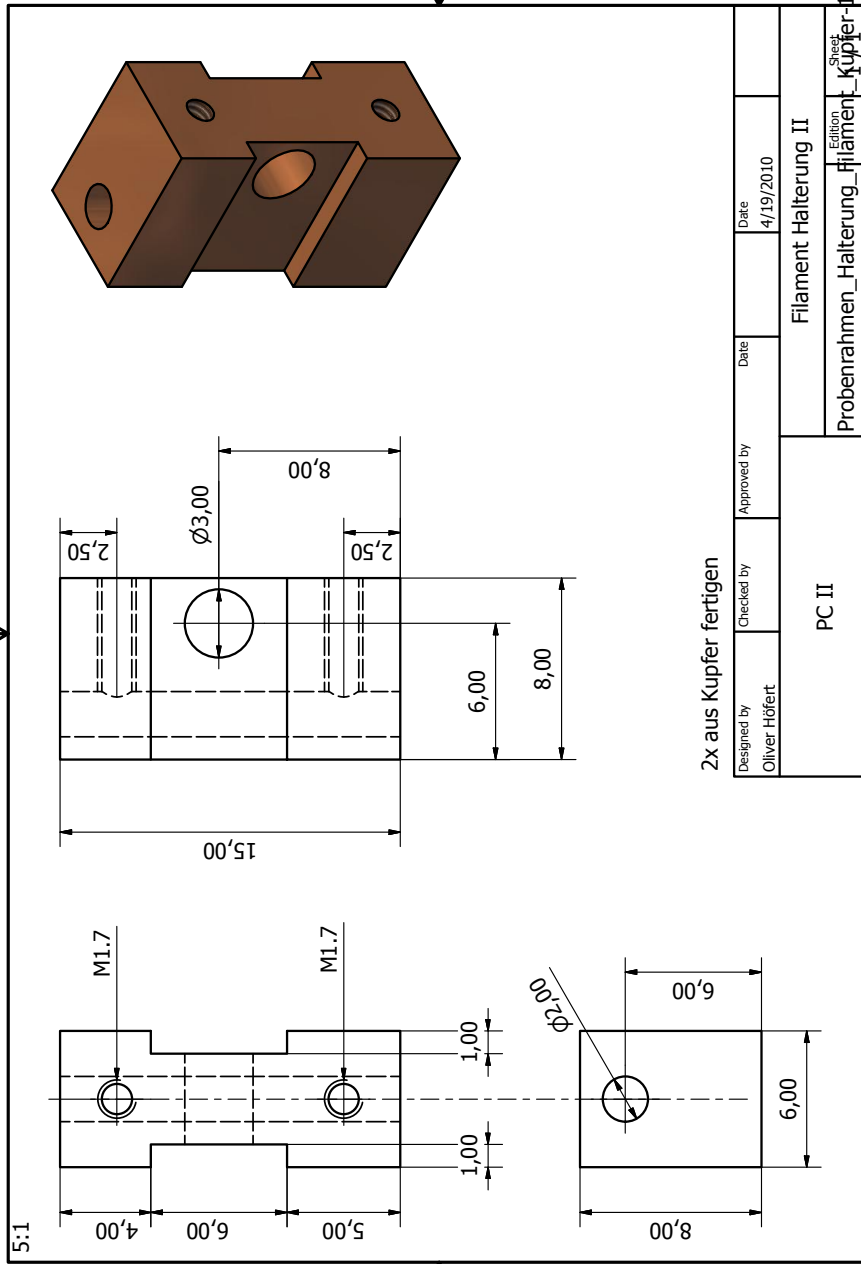
5:1

soweit wie möglich Gewinde schneiden,  
dann mit  $\varnothing 1\text{mm}$  durchbohren

1x aus Edelstahl fertigen

Designed by Oliver Höfert	Checked by	Approved by	Date 4/19/2010	Halterung Filament I
PC II				Probenrahmen_Halterung_Filament I / I Edition Sheet 1 / 1

PRODUCED BY AN AUTODESK EDUCATIONAL PRODUCT

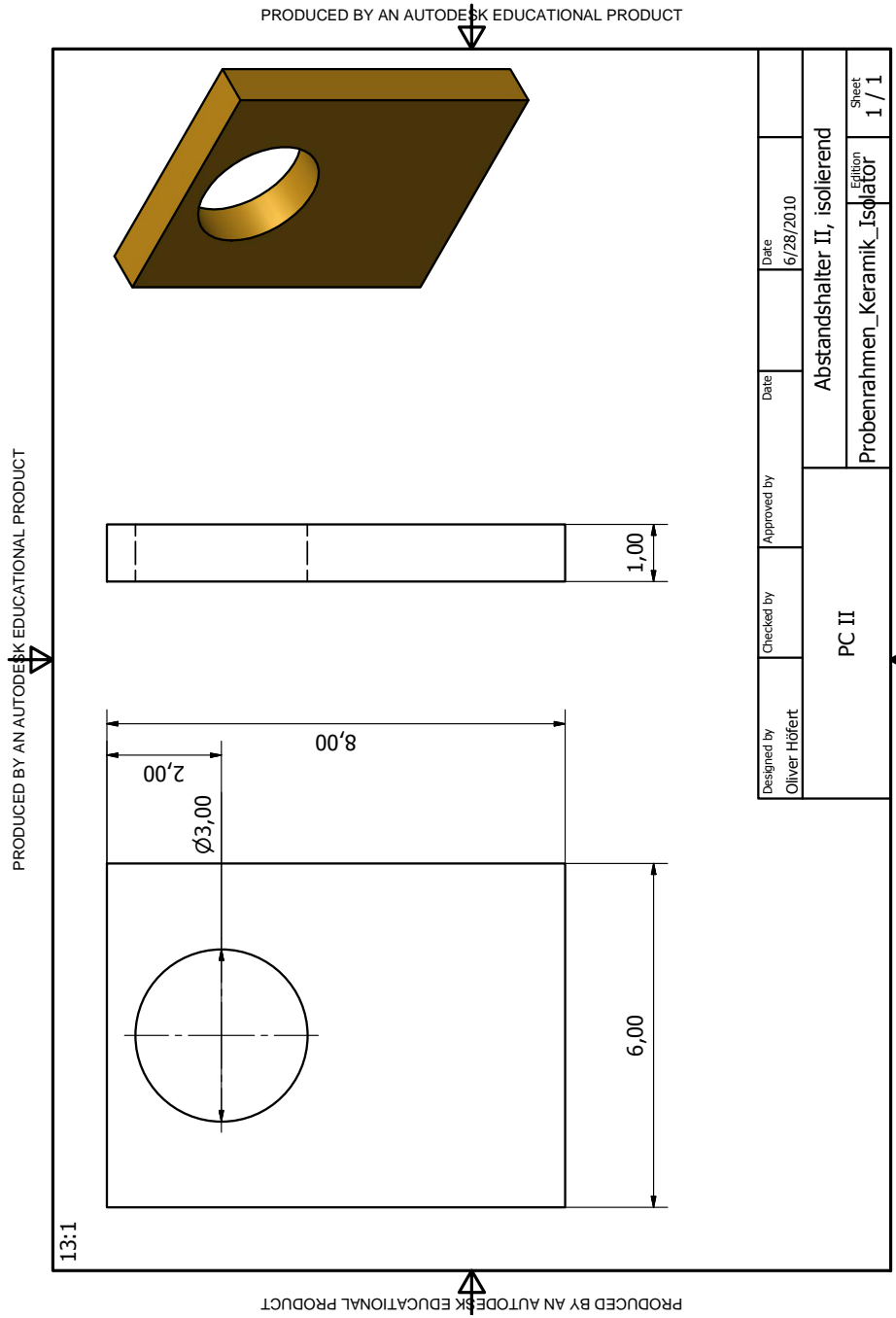


PRODUCED BY AN AUTODESK EDUCATIONAL PRODUCT

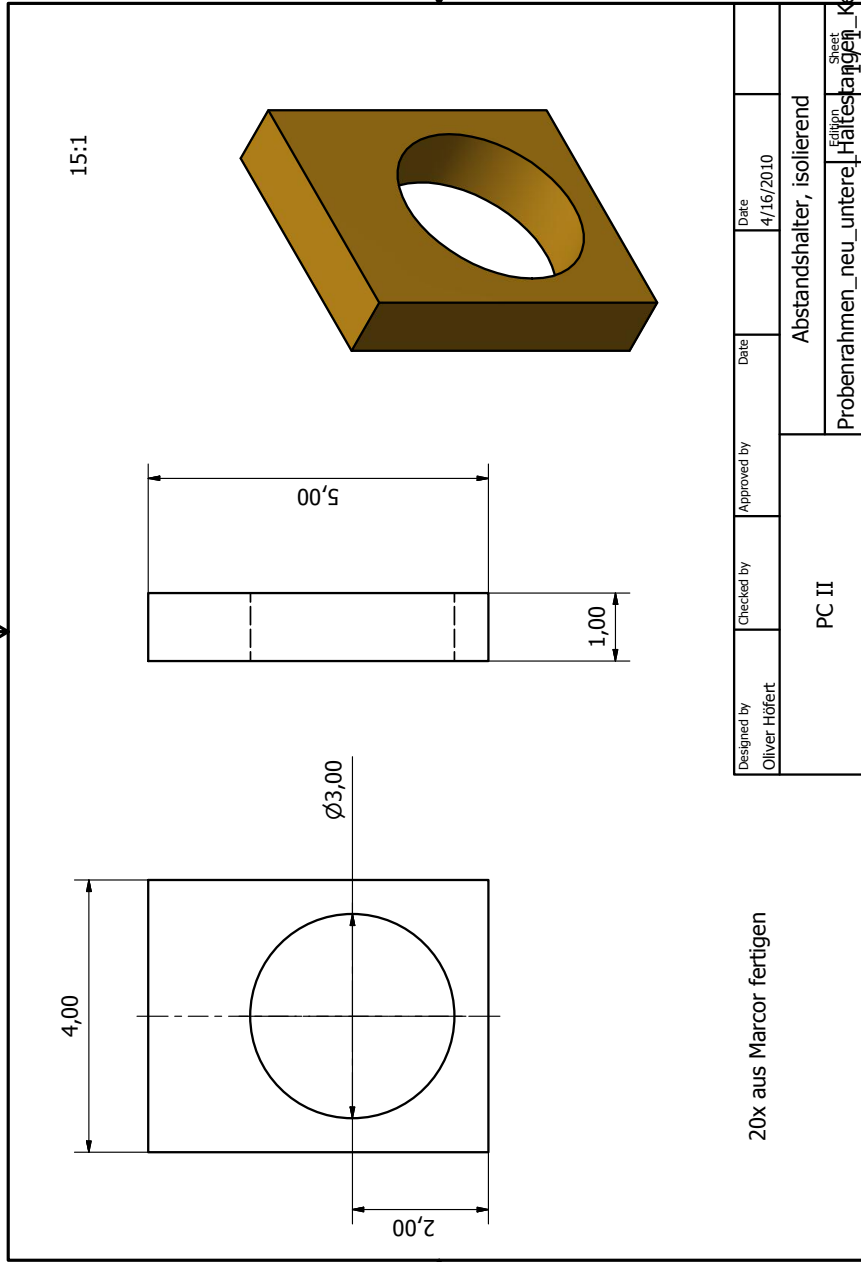
PRODUCED BY AN AUTODESK EDUCATIONAL PRODUCT







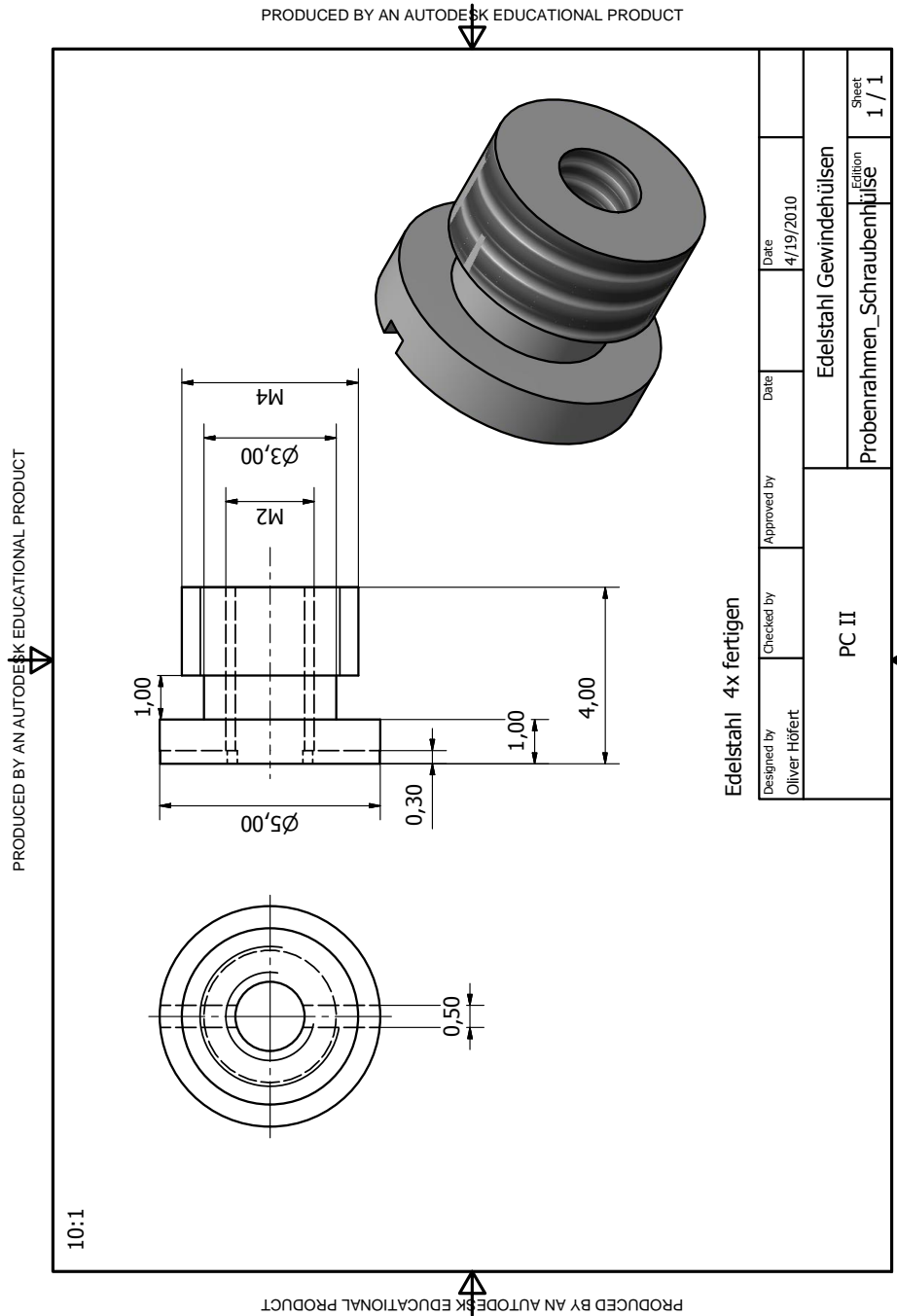
PRODUCED BY AN AUTODESK EDUCATIONAL PRODUCT



PRODUCED BY AN AUTODESK EDUCATIONAL PRODUCT

Designed by Oliver Höfert	Checked by	Approved by	Date 4/16/2010
PC II			Abstandshalter, isolierend
			Probenrahmen_neu_untere Haltestangen
			Sheet: Keramik1

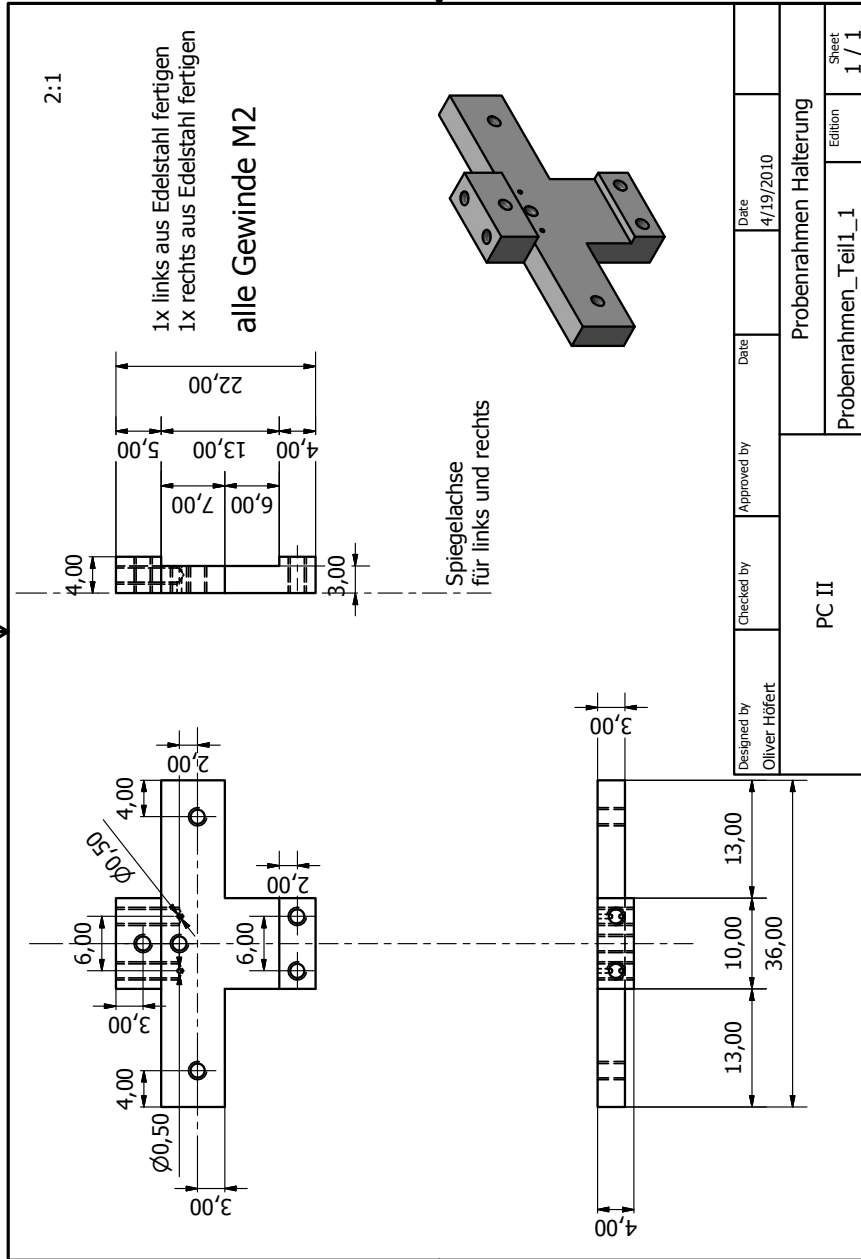
PRODUCED BY AN AUTODESK EDUCATIONAL PRODUCT



PRODUCED BY AN AUTODESK EDUCATIONAL PRODUCT

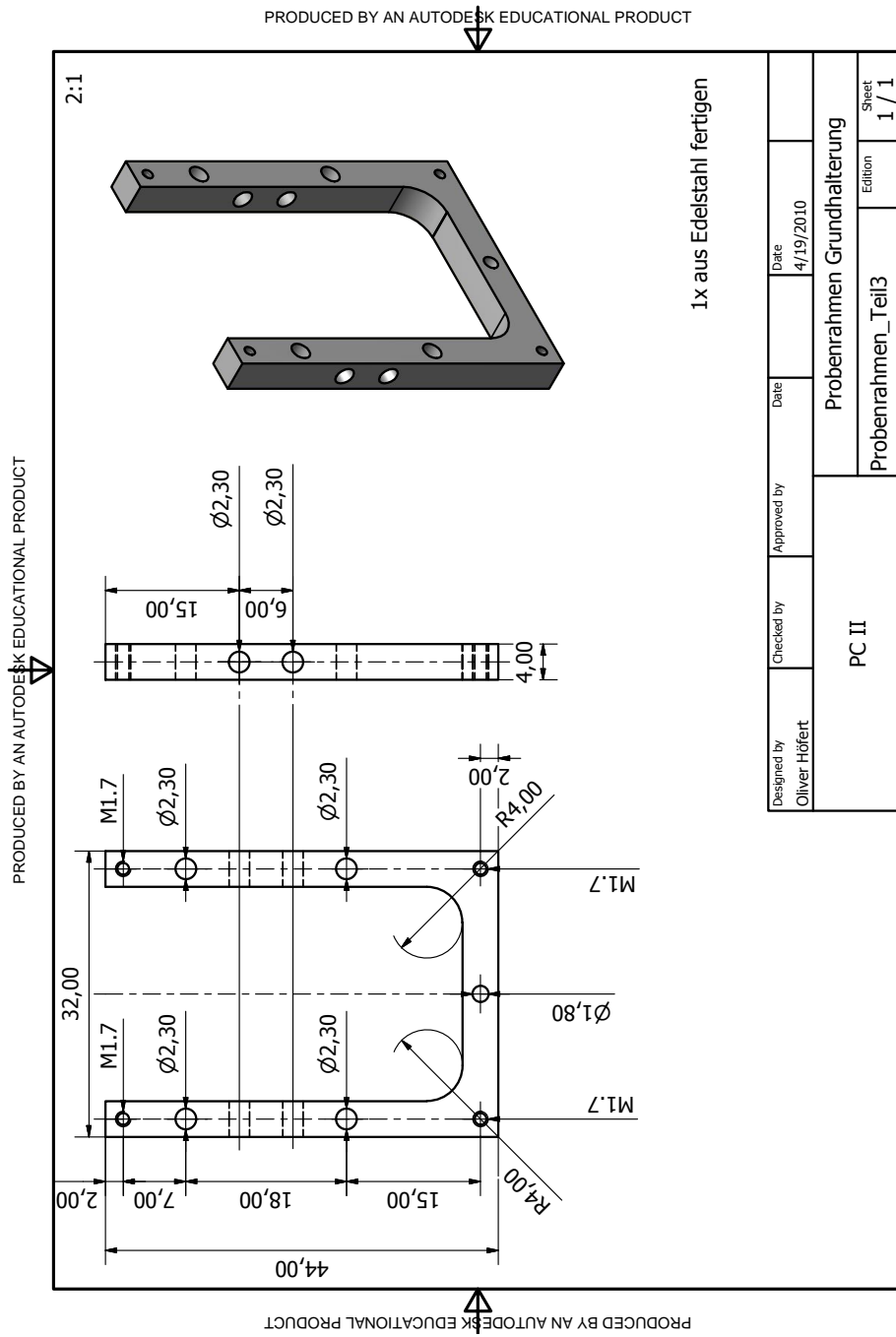
PRODUCED BY AN AUTODESK EDUCATIONAL PRODUCT

PRODUCED BY AN AUTODESK EDUCATIONAL PRODUCT



PRODUCED BY AN AUTODESK EDUCATIONAL PRODUCT

PRODUCED BY AN AUTODESK EDUCATIONAL PRODUCT





# Literature

- [1] G. Ertl, H. Knözinger, J. Weitkamp, *Handbook of Heterogeneous Catalysis* (VCH, Weinheim, 1997).
- [2] M. Zamorano, *Aerotech News and Review* (2006).
- [3] D. Unruh, K. Pabst, and G. Schaub, *Energ. Fuel* **24**, 2634 (2010).
- [4] H. Kato, and A. Kudo, *J. Phys. Chem. B* **105**, 4285 (2001).
- [5] Y. Miseki, H. Kato, and A. Kudo, *Energ. Environ.* **2**, 306 (2009).
- [6] G. Wendt, J. Finster, and R. Schöllner, *Z. anorg. allg. Chem.* **488**, 197 (1982).
- [7] J. R. Sohn, H. W. Kim, M. Y. Park, E. H. Park, J. T. Kim, and S. E. Park, *Appl Catal A: General* **128**, 127 (1995).
- [8] J. R. Sohn, and D. C. Shin, *J. Cat.* **160**, 314 (1996).
- [9] J. R. Sohn, and S. Y. Lee, *Appl Catal A: General* **164**, 127 (1997).
- [10] J. R. Sohn, *Catal Today* **73**, 197 (2002).
- [11] X. Hu, and C. Hu, *J. Chem. Technol. Biot.* **85**, 1522 (2010).
- [12] Lawrie Lloyd, *Handbook of Industrial Catalysts* (Springer Science, 2011).
- [13] A. Zhang, R. Zhang, N. Zhang, S. Hong, and M. Zhang, *Kinet. Catal.+* **51**, 710 (2010).
- [14] Q. Xu, P. Lan, B. Zhang, Z. Ren, and Y. Yan, *Energ. Fuel* **24**, 6456 (2010).

- [15] R. J. Behm, K. Christmann, and G. Ertl, *J. Chem. Phys.* **73**, 2984 (1980).
- [16] R.J. Behm, K. Christmann, and G. Ertl, *Surf. Sci.* **99**, 320 (1980).
- [17] J.-W. He, D.A. Harrington, K. Griffiths, and P.R. Norton, *Surf. Sci.* **198**, 413 (1988).
- [18] D. E. Taylor and R. L. Park, *Surf. Sci.* **125**, L73 (1982).
- [19] G. Ertl, *Surf. Sci.* **299/300**, 742 (1994).
- [20] S. M. Vesecky, X. Xu and D. W. Goodman, *J. Vac. Sci. Technol. A* **12(4)**, 2114 (1994).
- [21] R. Wichtendahl, M. Rodriguez-Rodrigo, U. Härtel, H. Kühlenbeck and H.-J. Freund, *Surf. Sci.* **423**, 90 (1999).
- [22] M.A. Langell, and R. P. Furstenu, *Appl Surf. Sci.* **26**, 445 (1986).
- [23] G.H. Hatzikos, and R.I. Masel, *Surf. Sci.* **185**, 479 (1987).
- [24] Q. Hu, and J. Laskin, *J. Phys. Chem. C* **118**, 2602 (2014).
- [25] R. Streber, B. Tränkenschuh, J. Schöck, C. Papp, H.-P. Steinrück, J.-S. McEwen, P. Gaspard, and R. Denecke, *J. Chem. Phys.* **131**, 064702 (2009).
- [26] Y. Lykhach, V. Johaneck, H. A. Aleksandrov, S. M. Kozlov, M. Happel, T. Skala, P. St. Petkov, N. Tsud, G. N. Vayssilov, K. C. Prince, K. M. Neyman, V. Matolin, and J. Libuda, *J. Phys. Chem. C* **116**, 12103 (2012).
- [27] M. Happel, L. Kylhammar, P.-A. Carlsson, J. Libuda, H. Grönbeck, and M. Skoglundh, *Appl Catal B: Environmental* **91**, 679 (2009).
- [28] Andrea Berlich, Yan-Chun Liu, and Harald Morgner, *Surf. Sci.* **602**, 3737 (2008).
- [29] H.-J. Freund, and G. Pacchioni, *Chem. Soc. Rev.* **37**, 2224 (2008).
- [30] T. Orzali, S. Agnoli, M. Sambri, and G. Granozzi, *Surf. Sci.* **569**, 105 (2004).

- [31] J. Schoiswohl, S. Agnoli, B. Xu, S. Surnev, M. Sambì, M.G. Ramsey, G. Granozzi, and F.P. Netzer, *Surf. Sci.* **599**, 1 (2005).
- [32] S. Agnoli, A. Barolo, P. Finetti, F. Sedona, M. Sambì, and G. Granozzi, *J. Phys. Chem. C* **111**, 3736 (2005).
- [33] S. Agnoli, M. Sambì, A. Atrei, M. Caffio, G. Rovida, and G. Granozzi, *Surf. Sci.* **576**, 1 (2005).
- [34] S. Agnoli, M. Sambì, G. Granozzi, J. Schoiswohl, S. Surnev, F. P. Netzer, M. Ferrero, A. M. Ferrari, and C. Pisani, *J. Phys. Chem. B* **109**, 17197 (2005).
- [35] S. Agnoli, T. Orzali, M. Sambì, J. Schoiswohl, S. Surnev, F.P. Netzer and G. Granozzi, *J. Electron. Spectrosc.* **144-147**, 465 (2005).
- [36] A. Hellman, and H. Grönbeck, *Phys. Rev. Lett.* **100**, 116801 (2008).
- [37] S. Hüfner, *Photoelectron Spectroscopy* (Springer Verlag, 1995).
- [38] R. Denecke, and N. Martensson, *Landolt-Börnstein New Series III/42A4* (Springer Science, 2005).
- [39] H.W. Nesbitt, D. Legrand, and G.M. Bancroft, *Phys Chem Minerals* **27**, 357 (2000).
- [40] L. S. Cederbaum, and W. Domcke, *J. Chem. Phys.* **64**, 603 (1976).
- [41] C. Papp, and H.-P. Steinrück, *Surf. Sci. Rep.* (2013).
- [42] H.-P. Steinrück, T. Fuhrmann, C. Papp, B. Tränkenschuh, and R. Denecke, *J. Chem. Phys.* **125**, 204706 (2006).
- [43] G. Somarjai, *Chemistry in two dimensions: surfaces* (Cornell University Press: Ithaca, 1981).
- [44] R. Denecke, M. Kinne, C. M. Whelan, and H.-P. Steinrück, *Surf. Rev. Lett.* **9**, 797 (2002).
- [45] M. Kinne, *Kinetische Untersuchungen von Oberflächenreaktionen mittels hochaufgelöster Röntgen-Photoelektronenspektroskopie - Oxidation von CO auf Pt(111) und zugehörige Elementarschritte*, PhD thesis, Friedrich-Alexander-Universität Erlangen-Nürnberg, 2003.

- [46] J.-S. McEwen, S. H. Payne, J. J. Kreuzer, M. Kinne, R. Denecke, and H.-P. Steinrück, *Surf. Sci.* **545**, 47 (2003).
- [47] R. Nyholm, M. Qvarford, J. N. Andersen, S. L. Sorensen, and C. Wigren, *J. Phys.: Condens. Matter* **4**, 277 (1992).
- [48] J. N. Andersen, D. Hennig, E. Lundgren, M. Methfessel, R. Nyholm, and M. Scheffler, *Phys. Rev. B* **50**, 17525 (1994).
- [49] G. Zheng, and E.I. Altman, *Surface, Surf. Sci.* **504**, 253 (2002).
- [50] G. W. Simmons, Y.-N. Wang, J. Marcos, and K. Klier, *J. Phys. Chem* **95**, 4522 (1991).
- [51] M.J. Gladys, A.A. El Zein, A. Mikkelsen, J.N. Andersen, and G. Held, *Surf. Sci.* **602**, 3540 (2008).
- [52] P. Uvdal, P.-A. Karlsson, C. Nyberg, S. Andersson and N.V. Richardson, *Surf. Sci.* **202**, 167 (1988).
- [53] J.N. Andersen, M. Qvarford, R. Nyholm, S.L. Sorensen and C. Wigren, *Phys. Rev. Lett.* **67**, 2822 (1991).
- [54] M. Kinne, T. Fuhrmann, C. M. Whelan, J. F. Zhu, J. Pantförder, M. Probst, G. Held, R. Denecke, and H.-P. Steinrück, *J. Phys. Chem.* **117**, 10852 (2002).
- [55] J. Schoiswohl, W. Zheng, S. Surnev, M.G. Ramsey, G. Granozzi, S. Agnoli, and F.P. Netzer, *Surf. Sci.* **600**, 1099 (2006).
- [56] A. M. Ferrari, and C. Pisani, *J. Phys. Chem. B* **110**, 7909 (2006).
- [57] M. Sambì, R. Sensolo, G.A. Rizzi, M. Petukhov, and G. Granozzi, *Surf. Sci.* **537**, 36 (2003).
- [58] M. A. van Veenendaal, and G. A. Sawatzky, *Phys. Rev. Lett.* **70**, 2459 (1993).
- [59] I. Preda, R. J. O. Mossaneck, M. Abbate, L. Alvarez, J. Mendez, A. Gutierrez, and L. Soriano, *Surf. Sci.* **606**, 1426 (2012).
- [60] I. Preda, A. Gutierrez, M. Abbate, F. Yubero, J. Mendez, L. Alvarez, and L. Soriano, *Phys. Rev. B* **77**, 1 (2008).

- [61] L. Soriano, I. Preda, and A. Gutiérrez, S. Palacín, M. Abbate, A. Vollmer, *Phys. Rev. B* **75**, 233417 (2007).
- [62] G.A. Rizzi, M. Petukhov, M. Sambì, and G. Granozzi, *Surf. Sci.* **522**, 1 (2003).
- [63] A. F. Carley, S. D. Jackson, J.N. O'Shea, and M.W. Roberts, *Surf. Sci. Letters* **440**, L868 (1999).
- [64] S. Uhlenbrock, C. Scharfschwerdt, M. Neumann, G. Illing, and H.-J. Freund, *J. Phys.: Condens. Matter* **4**, 7973 (1992).
- [65] S. Tanuma and C. J. Powell and D. R. Penn, *Surf. Interface Anal.* **35**, 268 (2003).
- [66] A. Desikusumastuti, T. Staudt, H. Grönbeck, and J. Libuda, *J. Cat.* **255**, 127 (2008).
- [67] T. X. T. Sayle, S. C. Parker, C. R. A. Catlow, *Surf. Sci.* **316**, 329 (1994).
- [68] A. Tschöpe, W. Liu, M. Flytzani-Stephanopoulos, and J. Y. Ying, *J. Cat.* **157**, 42 (1995).
- [69] E. Aneggi, M. Baoro, C. de Leitenburg, G. Dolcetti, A. Trovarelli, *J. Alloy. Compd.* **408-412**, 1096 (2006).
- [70] E. Aneggi, J. Llorca, M. Baoro, A. Trovarelli, *J. Cat.* **234**, 88 (2005).
- [71] H. Grönbeck, *J. Phys. Chem. B* **110**, 11977 (2006).
- [72] P. Broqvist, I. Panas, and H. Grönbeck, *J. Phys. Chem. B* **109**, 15410 (2005).
- [73] J. Wollschläger, J. Viernow, C. Tegenkamp, D. Erdös, K.M. Schröder, and H. Pfnür, *Appl Surf. Sci.* **142**, 129 (1999).
- [74] S. Agnoli, A. Barolo, G. Granozzi, A.M. Ferrari, and C. Pisani, *J. Phys. Chem. C* **111**, 19066 (2007).
- [75] R. Barlow, and P.J. Grundy, *J. Mat. Sci.* **4**, 797 (1969).
- [76] A. T. Fromhold, and E. L. Cook, *Phy. Rev.* **163**, 650 (1967).

- [77] James E. House, *Principles of Chemical Kinetics* (Academic Press, 2007).
- [78] S. Yamamoto, and I. Matsuda, *J. Phys. Soc. Jpn* **82**, 021003 (2013).
- [79] D. N. Tafen, J. B. Miller, Ö. N. Dogan, J. P. Baltrus, and P. Kondratyuk, *Surf. Sci.* **608**, 61 (2013).
- [80] S. Ramakrishna, and T. Seideman, *J. Phys. B: At. Mol. Opt. Phys.* **45**, 194012 (2012).
- [81] R. Streber, C. Papp, M. P. A. Lorenz, A. bayer, R. Denecke, and H.-P. Steinrück, *Angew. Chem. Int. Edit.* **48**, 9743 (2009).
- [82] K. Gotterbarm, N. Luckas, O. Höfert, M. P. A. Lorenz, R. Streber, C. Papp, F. Vines, and H.-P. Steinrück, and A. Görling, *J. Chem. Phys.* **136**, 094702 (2012).
- [83] L. Gori, R. Tommasini, G. Cautero, D. Giuressi, M. Barnaba, A. Accardo, S. Carrato, and G. Paolucci, *Nucl. Instrum. Meth. A* **431**, 338 (1999).
- [84] D. P. Langstaff, A. Bushell, T. Chase, and D. A. Evans, *Nucl. Instrum. Meth. B* **238**, 219 (2005).
- [85] J.-M. Bussat, C. S. Fadley, B. A. Leudewigt, G. J. Meddeler, A. Nambu, M. Press, H. Spieler, B. Turko, M. West, and G. J. Zizka, *IEEE T. Nucl. Sci.* **51**, 2341 (2004).
- [86] R. Denecke, *Appl Phys A* **80**, 977 (2005).
- [87] I. Nakai, H. Kondoh, A. Resta, J. N. Andersen, T. Ohta, and T. Shimada, *J. Chem. Phys.* **124**, 224712 (2006).
- [88] F. Esch, A. Baraldi, C. Gomelli, S. Lizzit, and M. Kiskinova, *J. Chem. Phys.* **110**, 4013 (1999).
- [89] A. Baraldi, M. Barnaba, B. Brena, D. Cocco, G. Comelli, S. Lizzit, G. Paolucci, and R. Rosei, *J. Elec. Spec. rel. Phen.* **76**, 145 (1995).
- [90] A. Baraldi, G. Comelli, S. Lizzit, D. Cocco, G. Paolucci, and R. Rosei, *Surf. Sci. Letters* **367**, L67 (1996).

- [91] A. Baraldi, *J. Phys.: Condens. Matter* **20**, 093001 (2008).
- [92] N. Luckas, K. Gotterbarm, R. Streber, M. P. A. Lorenz, O. Höfert, F. Vines, C. Papp, A. Görling, and H.-P. Steinrück, *Phys. Chem. Chem. Phys.* **13**, 16227 (2011).
- [93] A. Yoshigoe, and Y. Teraoka, *Appl Surf. Sci.* **190**, 60 (2002).
- [94] Y. Teraoka, and A. Yoshigoe, *Surf. Sci.* **507**, 797 (2002).
- [95] W. Zhao, S. M. Kozlov, O. Höfert, K. Gotterbarm, M. P. A. Lorenz, F. Vines, C. Papp, A. Görling, and H.-P. Steinrück, *J. Phys. Chem. C Letters* **2**, 759 (2011).
- [96] S. Lizzit, and A. Baraldi, *Catal Today* **154**, 68 (2010).
- [97] L. Vattuone, L. Savio, M. Rocca, L. Rumiz, A. Baraldi, S. Lizzit, and G. Comelli, *Phys. Rev. B* **66**, 085403 (2002).
- [98] C. M. Whelan, R. Neubauer, D. Borgmann, R. Denecke, and H.-P. Steinrück, *J. Chem. Phys.* **115**, 8133 (2001).
- [99] C. M. Whelan, R. Neubauer, R. Denecke, and H.-P. Steinrück, *Surf. Rev. Lett.* **9**, 789 (2002).
- [100] A. Stolow, A. E. Bragg, and D. M. Neumark, *Chem. Rev.* **104**, 1719 (2004).
- [101] M. Kamada, S. Tanaka, K. Takahashi, Y.-I. Doi, K. Fukui, T. Kinoshita, Y. Haruyama, S. Asaka, Y. Fujii, and M. Itoh, *Nucl. Instrum. Meth. A* **467-468**, 1441 (2001).
- [102] S. Tanaka, S. D. More, K. Takahashi, M. Kamada, T. Nishitani, and T. Nakanishi, *Surf. Rev. Lett.* **9**, 1297 (2002).
- [103] O. Hemmers, S. B. Whitfield, P. Glans, H. Wang, D. W. Lindle, R. Wehlitz, and I. A. Sellin, *Rev. Sci. Instrum.* **69**, 3809 (1998).
- [104] S. Tanaka, S. D. More, K. Takahashi, and M. Kamada, *J. Phys. Soc. Jpn* **72**, 659 (2003).
- [105] A. Cudok, H. Froitzheim, and M. Schulze, *Phys. Rev. B* **47**, 13682 (1993).

- [106] P. Kisliuk, *J. Phys. Chem. Solids* **3**, 95 (1957).
- [107] V. P. Zhdanov, *Elementary Physicochemical Processes on Solid Surfaces* (Plenum Press, 1991).
- [108] E. M. Stuve, S.W. Jorgensen and R.J. Madix, *Surf. Sci.* **146**, 179 (1984).
- [109] C. Nyberg, C. G. Tengstal, P. Uvdal, and S. Andersson, *J. Elec. Spec. rel. Phen.* **38**, 299 (1986).
- [110] M.A. Henderson, *Surf. Sci. Reports* **46**, 1 (2002).
- [111] G.-C. Wang, S.-X. Tao and X.-H. Bu, *J. Cat.* **244**, 10 (2006).
- [112] J. Li, S. Zhu, Y. Li and F. Wang, *Phys. Rev. B* **76**, 235433 (2007).
- [113] J. Li, S. Zhu, Y. Li and Fuhui Wang, *J. Am. Chem. Soc.* **130**, 11140 (2008).
- [114] M. Schulze, and R. Reissner, *Surf. Sci.* **482**, 285 (2001).
- [115] R. Reissner, and M. Schulze, *Surf. Sci.* **454**, 183 (2000).
- [116] D. J. Simpson, T. Bredow, and A. R. Gerson, *Theor. Chem. Acc.* **114**, 242 (2005).
- [117] N. Yu, W.-B. Zhang, N. Wang, Y.-F. Wang, and B.-Y. Tang, *J. Phys. Chem. C* **112**, 452 (2008).
- [118] D. Cappus, C. Xu, D. Ehrlich, B. Dillmann, C. A. Ventrice Hr, K. Al Shamery, H. Kuhlenbeck, and H.-J. Freund, *Chem. Phys.* **177**, 533 (1993).
- [119] H.-W. Hoppe, and H.-H. Strehblow, *Surf. Interface Anal.* **14**, 121 (1989).
- [120] M. Lorenz, *Interaction of small molecules with thin NiO layers and related metal surfaces studied with high resolution X-ray photoelectron Spectroscopy*, PhD thesis, Friedrich-Alexander-Universität Erlangen-Nürnberg, 2012.

- [121] M. C. Biesinger, B. P. Payne, L. W. M. Lau, A. Gerson and R. St. C. Smart, *Surf. Interface Anal.* **41**, 324 (2009).
- [122] N. Sheppard, *Ann. Rev. Phys. Chem.* **39**, 589 (1988).
- [123] A. F. Lee, K. Wilson, R. L. Middleton, A. Baraldi, A. Goldoni, G. Paolucci, and R. M. Lambert, *J. Am. Chem. Soc.* **121**, 7969 (1999).
- [124] I. Jungwirthova, and L. L. Kesmodel, *J. Phys. Chem B* **105**, 674 (2001).
- [125] A. F. Lee, R. M. Omerod, K. Wilson, R. M. Lambert, A. Goldoni, and A. Baraldi, *Surf. Sci. Letters* **501**, L165 (2002).
- [126] L. L. Kesmodel, G. D. Waddill and J. A. Gates, *Surf. Sci.* **138**, 464 (1984).
- [127] T. G. Rucker, M. A. Logan, T. M. Gentle, E. L. Muettterties, and G. A. Somarjai, *J. Phys. Chem* **90**, 2703 (1986).
- [128] Davy L. S. Nieskens, Francisco Ample-Navarro, Maarten M. M. Jansen, Daniel Curulla-Ferre, Josep Ricart and Hans Niemantsverdriet, *ChemPhysChem* **7**, 1068 (2006).
- [129] A. G. Cabello-Cartagena, J. Vogt and H. Weiss, *J. Chem. Phys.* **132**, 074706 (2010).
- [130] J. P. Camplin, J. K. Eve, and E. M. McCash, *Phys. Chem. Chem. Phys.* **2**, 4433 (2000).
- [131] W. Liu, J. S. Lian, and Q. Jiang, *J. Phys. Chem. C* **111**, 18189 (2007).
- [132] N. Mingo, and K. Makoshi, *Appl Surf. Sci.* **162-163**, 227 (2000).
- [133] B. C. Stipe, M. A. Rezaei, and W. Ho, *Phys. Rev. Lett.* **81**, 1263 (1998).
- [134] B. C. Stipe, M. A. Rezaei, and W. Ho, *Science* **280**, 1732 (1998).
- [135] C. G. P. M. Bernardo, and J. A. N. F. Gomes, *J. Mol. Struct.-Theochem.* **629**, 251 (2003).

- [136] R. Neubauer, C. M. Whelan, R. Denecke, and H.-P. Steinrück, *J. Chem. Phys.* **119**, 1710 (2003).
- [137] W.-H. Hung, and S. L. Bernasek, *Surf. Sci.* **339**, 272 (1995).
- [138] J. M. Heitzinger, S. C. Gebbard and B. E. Koel, *J. Phys. Chem* **97**, 5327 (1993).
- [139] T. M. Gentle, and E. L. Muetterties, *J. Phys. Chem.* **87**, 2469 (1983).
- [140] M. A. Logan, T. G. Rucker, T. M. Gentle, E. L. Muetterties, and G. A. Somarjai, *J. Phys. Chem.* **90**, 2709 (1986).
- [141] S. Doniach, and M. Sunjic, *J. Phys. C: Solid State Phys.* **3**, 285 (1970).
- [142] A. Baraldi, *J. Phys.: Condens. Matter* **20**, 093001 (2008).
- [143] A. Baraldi, S. Lizzit, G. Comelli, M. Kiskinova, R. Rosei, K. Honkala, and J. K. Norskov, *Phys. Rev. Lett.* **93**, 046101 (2004).
- [144] L. Vattuone, Y.Y. Yeo, R. Kose, and D.A. King, *Surf. Sci.* **447**, 1 (2000).
- [145] M. Bowker, C. Morgan, N. Perkins, R. Holroyd, E. Fourre, F. Grillo, and A. MacDowall, *J. Phys. B: At. Mol. Opt. Phys.* **109**, 2377 (2005).
- [146] H. Gabasch, E. Kleimenov, D. Teschner, S. Zafeiratos, M. Hävecker, A. Knop-Gericke, R. Schlögl, D. Zemlyanov, B. Aszalos-Kiss, K. Hayek, and B. Klötzer, *J. Cat.* **242**, 340 (2006).
- [147] X.-C. Guo, and R. J. Madix, *J. Am. Chem. Soc.* **117**, 5523 (1995).
- [148] J. E. Demuth, *Surf. Sci.* **69**, 365 (1977).
- [149] J. E. Demuth, and H. Ibach, *Surf. Sci.* **78**, L238 (1978).
- [150] L. Giordano, J. Goniakowski, and G. Pacchioni, *Phys. Rev. B* **67**, 045410 (2003).
- [151] M. A. van Hove, and G. A. Somorjai, *J. Mol. Catal. A-Chem.* **131**, 243 (1998).
- [152] J. A. Gates, and L. L. Kesmodel, *Surf. Sci.* **124**, 68 (1983).

- [153] E. M. Stuve, and R. Madix, *J. Phys. Chem.* **84**, 105 (1985).
- [154] E. M. Stuve, and R.J. Madix, *Surf. Sci.* **160**, 293 (1985).
- [155] E. M. Stuve, and R. J. Madix, *Surf. Sci.* **152/153**, 532 (1985).
- [156] X.C. Guo, and R. J. Madix, *Surf. Sci. Letters* **391**, 1165 (1997).
- [157] E. W. Hansen, and M. Neurock, *J. Cat.* **196**, 241 (2000).
- [158] N. Lorente, M. F. G. Hedouin, R. E. Palmer, and M. Persson, *Phys. Rev. B* **68**, 155401 (2003).
- [159] F. Mittendorfer, and J. Hafner, *Surf. Sci.* **472**, 133 (2001).
- [160] J. C. Bertolini, G. Dalmai-Imelik, and J. Rousseau, *Surf. Sci.* **67**, 478 (1977).
- [161] A. Nilsson, M. weinelt, T. Wiell, P. Bennich, O. Karis, J. Stöhr, M. G. Samant, and N. Wassdahl, *Phys. Rev. Lett.* **78**, 2847 (1997).
- [162] M. Weinelt, N. Wassdahl, T. Wiell, O. Karis, J. Hasselström, P. Bennich, J. Stöhr, M. Samant, and A. Nilsson, *Phys. Rev. B* **58**, 7351 (1998).
- [163] W.-K. Chen, M.-J. Cao, S.-H. Liu, C.-H. Lu, Y. Xu, and J.Q. Li, *Chem. Phys. Lett.* **417**, 414 (2006).
- [164] R. Zhang, A. J. Hensley, J.-S. McEwen, S. Wickert, E. Darlatt, K. Fischer, M. Schöppke, R. Denecke, R. Streber, M. Lorenz, C. Papp, and H.-P. Steinrück, *Phys. Chem. Chem. Phys.* **15**, 20662 (2013).
- [165] O. Höfert, M. P. A. Lorenz, R. Streber, W. Zhao, A. Bayer, H.-P. Steinrück, and C. Papp, *J. Chem. Phys.* **139**, 164706 (2013).
- [166] Brotherton, Robert J. and Weber, C. Joseph and Guibert, Clarence R. and Little, John L., *Boron Compounds* (Wiley-VCH Verlag GmbH & Co. KGaA, 2000), .
- [167] W. Zhao, J. Gebhardt, K. Gotterbarm, O. Höfert, C. Gleichweit, C. Papp, A. Göring, and H. -P. Steinrück, *J. Phys.: Condens. Matter* **25**, 445002 (2013).

# Danksagung

Als erstes bedanke ich mich bei Herrn Prof. Dr. Steinrück für die Aufnahme in seine Arbeitsgruppe. Insbesondere bedanke ich mich auch für seine Geduld und die vielen hilfreichen Diskussionen.

Der nächste Dank gilt Dr. Christian Papp, für die Betreuung meiner Arbeit und die Unterstützung bei teilweise unkonventionellen Ideen und Methoden und das dadurch mir entgegen gebrachte Vertrauen.

Herrn Prof. Dr. Libuda danke ich für die Übernahme der Zweitkorrektur und die kritischen Fragen während meiner Promotion, welche zur Reife dieser Arbeit beigetragen haben.

Weiterhin bedanke ich mich ganz herzlich bei Carina Bronn-bauer, Johannes Straß und Benjamin Bertleff für das Anfertigen von Abschlußarbeiten, die mir einen Teil der Arbeit abgenommen haben.

Messungen an einer Großforschungsanlage wie das BESSY sind immer Teamarbeit. Daher danke ich hier allen, die mit mir dieses Abenteuer bestritten haben und nicht anderswo erwähnt werden. Um nur einige zu nennen: Dr. Regine Bebensee, Dr. Andreas Bayer, Max Amende und Stefan Schernich.

Aber nicht nur auf Messzeiten ist man auf ein Team angewiesen, sondern auch wenn ein Projekt die eigenen Fähigkeiten übersteigt. Hiermit bedanke ich mich bei der Werkstatt insbesondere Herrn Wölfel, H.P. Bäumler und Bernd Kress für's Handauflegen bei Problemen mit der Technik und für die stets offenen Ohren.

Desweiteren danke ich dem gesamten PC II Lehrstuhl für die hervorragende Atmosphäre, besonders im Hinblick auf das Arbeitsklima. Hier möchte ich Dr. Michael Lorenz, Christoph Gleichweit, Andreas Späth, Udo Bauer und Florian Späth erwähnen. Wei Zhao und Karin Gotterbarm danke ich neben der langjährigen Unterstützung, besonders für den fantastischen Trip nach China.

Ganz besonders meinen Eltern und Freunden von meiner Bürgerschützen-sektion "Die Nachtwache", danke ich für die Unterstützung aus der Ferne.